Development of waveguide filter structures for wireless and satellite communications

Oleksandr Glubokov

School of Electronics and Computer Science

DEVELOPMENT OF WAVEGUIDE FILTER STRUCTURES FOR WIRELESS AND SATELLITE COMMUNICATIONS

OLEKSANDR GLUBOKOV

A thesis submitted in partial fulfilment of the requirements
of the University of Westminster
for the degree of Doctor of Philosophy

March 2011

ABSTRACT

This thesis explores the possibilities of the design and realization of compact conventional and substrate integrated waveguide structures with improved performance taking advantage of recent cross-coupled resonator filters theory achievements such as the modular filter design approach using non-resonating nodes and inline extracted pole filters. Therefore, the core of the thesis presents the following stages of work:

- Solution of electromagnetic problem for wave propagation in rectangular waveguide structures; overview of substrate integrated waveguides.

- Review of available design procedures for cross-coupled resonator filters; realization of coupling matrix synthesis methods by optimization.

- Investigation of the possibility to implement filtering modules using E-plane metallo-dielectric inserts in conventional rectangular waveguides. Application of the modules in configurations of bandpass and dual-band filters. Experimental verification of the filters.

- Implementation of inline extracted pole filters using E-plane inserts in rectangular waveguides. Use of generalized coupling coefficients concept for individual or coupled extracted pole sections. Development of new extracted pole sections. Application of the sections in the design of compact cross-coupled filters with improved stopband performance.

- Application of the techniques developed for conventional rectangular waveguides to substrate integrated technology. Development of a new negative coupling structure for folded substrate integrated resonators. Design of improved modular and extracted pole filters using substrate integrated waveguides.

ACKNOWLEDGEMENT

I would like to give my particular thanks to my director of studies, Dr. D. Budimir for his supervision, encouragement and guidelines throughout this research work. I would also like to thank my supervisor Dr. A. Tarczynski for his useful advice and support.

The financial support provided by School of Electronics and Computer Science, University of Westminster is gratefully acknowledged.

I would like to thank Dr. M. Potrebic for her help with the fabrication and verification of experimental filters.

Special thanks to Dr. B. Shelkovnikov and Dr. O. Shelkovnikov, without whom this work would have never been possible.

On the private side, I am very grateful to my parents Anatolii and Tetiana, my brother Dmytro, and my grandfather Dr. Dmytro Glagola for their faith in me, support and encouragement during the time of my studies. Also I am thankful to my partner Natasha for her understanding, continuous support and patience.

CONTENTS

1. Introduction 1
   1.1. Filters for Wireless Communications 1
   1.2. Rectangular Waveguide Filters 5
   1.3. Substrate Integrated Waveguide Filters 8
   1.4. Aims and Objectives of the Thesis 9
   1.5. Outline of the Thesis 11
   1.6. References 13
2. Rectangular Waveguides 16
   2.1. Introduction 16
   2.2. Electromagnetic Theory of Rectangular Waveguides 17
      2.2.1. Maxwell's Equations 17
      2.2.2. Electromagnetic Modes in Rectangular Waveguide 20
   2.3. Substrate Integrated Waveguides 31
      2.3.1. Conventional Substrate Integrated Waveguides 31
      2.3.2. Folded Substrate Integrated Waveguides 34
      2.3.3. Half-Mode Substrate Integrated Waveguides 36
   2.4. Summary 38
   2.5. References 39
3. Design of Bandpass Filters 41
   3.1. Introduction 41
   3.2. Transfer Function Approximation 42
      3.2.1. Power Transfer Function and Characteristic Polynomials 42
      3.2.2. Butterworth Approximation 45
      3.2.3. Chebyshev Approximation 47
      3.2.4. Generalized Chebyshev Approximation 49
      3.2.5. Elliptic Approximation 52
   3.3. Synthesis of Filter Prototypes 54
      3.3.1. Elements of Filter Prototypes 54

3.3.2. Ladder Networks 58
3.3.3. Multiple Coupled Resonators Circuit Model 62
3.3.3.1. Coupling Matrix Circuit Representation 63
3.3.3.2. Direct Synthesis of the $N \times N$ Coupling Matrix 65
3.3.3.3. Reduction of Coupling Matrix 68
3.3.3.4. Direct Synthesis of the $(N+2) \times (N+2)$ Coupling Matrix 69
3.3.3.5. Coupling Matrix Synthesis by Optimization 72
3.3.3.6. Selection of Topology 74
3.3.4. Extracted Pole Filters 76
3.3.5. Filters With Non-Resonating Nodes 79
3.3.6. Filters with Frequency Dependent Couplings 81
3.4. Frequency Transformation 83
3.4.1. Lowpass-to-Lowpass Transformation 83
3.4.2. Lowpass-to-Highpass Transformation 84
3.4.3. Lowpass-to-Bandpass Transformation 85
3.4.4. Lowpass-to-Bandstop Transformation 87
3.4.5. Lowpass-to-Multiband Transformation 88
3.4.6. Impedance Scaling 89
3.5. Implementation and Optimization 91
3.5.1. Filter Implementation 91
3.5.2. Filter Optimization 93
3.6. Summary 94
3.7. References 95
4. E-plane Cross-Coupled Filters in Conventional Rectangular Waveguide 100
4.1. Introduction 100
4.2. Design of Cross-Coupled Filters Using E-plane Inserts 102
4.2.1. Singlets 102
4.2.1.1. Model of Singlets and Analysis 102
4.2.1.2. Implementation of Singlets 104
4.2.2. Doublets 106
4.2.2.1. Configuration and Frequency Response 106

4.2.2.2. Coupling Scheme and Analysis 107
4.2.3. Higher Order Modules 110
4.3. Coupling Coefficients in Filter Design 114
4.3.1. Coupling Coefficients 114
4.3.2. Extraction of Coupling Coefficients 116
4.3.1.1. Synchronously Tuned Resonators 116
4.3.1.2. Asynchronously Tuned Resonators 117
4.3.1.3. External Quality Factor 118
4.4. Filter Design Examples 120
4.4.1. Design of a 4^{th}-order Filter with Hairpin and I-shaped Resonators 120
4.4.1.1. Approximation and Synthesis 120
4.4.1.2. Implementation 122
4.4.1.3. Experimental Verification 124
4.4.2. Application of E-plane Doublets in Modular Filters 127
4.4.2.1. Inline Filter with NRN 127
4.4.2.2. Dual-Band Filter 128
4.4.2.3. Experimental Verification 129
4.5. Summary 133
4.6. References 134
5. E-plane Extracted Pole Filters in Conventional Rectangular Waveguide 136
5.1. Introduction 136
5.2. Extracted Pole Sections 138
5.3. Generalized Coupling Coefficients for Filters with NRNs 142
5.3.1. Generalized Coupling Coefficients 142
5.3.2. Extraction of GCC for EPS 145
5.3.2.1. Extraction of Internal NRN–Resonator Coupling 145
5.3.2.2. Generalized External Quality Factor 146
5.3.2.3. Coupling Between Adjacent Asynchronously Tuned Sections 147
5.3.2.4. Coupling Between EPS and Resonator 149
5.4. Implementation of EPS in E-plane Waveguide Filters 151
5.4.1. EPS with Embedded S-shaped Resonators 152

5.4.1.1. Effect of NRN's Length Variation 153
5.4.1.2. Effect of S-shaped Resonator's Dimensions Variation 155
5.4.1.3. Effect of Input/Output Septa' Lengths Variation 157
5.4.2. EPS with Embedded Split Ring Resonators 158
5.4.2.1. Effect of NRN's Length Variation 159
5.4.2.2. Effect of SRR's Dimensions Variation 160
5.4.3. EPS with Embedded λ/4-wavelength Resonators 161
5.4.3.1. Effect of NRN's Length Variation 162
5.4.3.2. Effect of λ/4-wavelength Resonator's Dimensions Variation 163
5.4.4. Embedded Stepped-Impedance Resonators 164
5.4.4.1. Stepped-Impedance Resonators 164
5.4.4.2. EPS with Embedded SIR 167
5.4.5. Analysis of Losses and Size Reduction in E-plane Waveguide EPS 169
5.4.6. Analysis of Stopband Performance of E-plane Waveguide EPS 172
5.4.6.1. Comparison of Stopband Performances of EPS 172
5.4.6.2. Theoretical Analysis of Stopband Performance of EPS 173
5.5. Filter Design Examples 176
5.5.1. Design of a 3rd-order Filter with Single Transmission Zero 176
5.5.1.1. Approximation and Synthesis 176
5.5.1.2. Implementation 178
5.5.1.3. Experimental Verification 179
5.5.2. λ/4-wavelength Resonators Based 3rd-order Filter with Three Transmission Zeros in Upper Stopband 182
5.5.2.1. Approximation and Synthesis 182
5.5.2.2. Implementation 183
5.5.2.3. Experimental Verification 185
5.5.3. Filters with S-shaped Resonators and SRR 187
5.5.3.1. 3rd-order Filter with Three Transmission Zeros Using EPS with S-shaped Resonators 187
5.5.3.2. 3rd-order Filter Using EPS with S-shaped Resonators and SRR 190

5.5.4. 4^{th}-order Filter with a Dual-Mode EPS and a Transmission Zero in Lower Stopband 193
5.5.4.1. Dual-Mode EPS with Transmission Zero in Lower Stopband 193
5.5.4.2. Filter with Dual-Mode EPS. Approximation and Synthesis 196
5.5.4.3. Filter with Dual-Mode EPS. Implementation 197
5.5.4.4. Filter with Dual-Mode EPS. Experimental Verification 198
5.6. Summary 201
5.7. References 202
6. Substrate Integrated Waveguide Filter Structures 205
6.1. Introduction 205
6.2. Design of Cross-Coupled SIW Filters 207
6.2.1. SIW Cavity Resonators 207
6.2.1.1. λ/2-wavelength Folded SIW Resonator 208
6.2.1.2. λ/4-wavelength Folded SIW Resonator 210
6.2.2. Coupled FSIW Resonators 212
6.2.2.1. Positive Coupling Structure 212
6.2.2.2. Negative Coupling Structure 213
6.2.3. Filter Design Example 216
6.2.3.1. Coupling Matrix Synthesis 216
6.2.3.2. Implementation 217
6.2.3.3. Simulation and Experimental Results 221
6.3. Design of Modular SIW Filters 224
6.3.1. SIW Filtering Modules 224
6.3.1.1. Singlet 224
6.3.1.2. Doublet 226
6.3.2. Filter Design Example 228
6.4. Design of Inline Extracted Pole SIW Filters 231
6.4.1. SIW Extracted Pole Section 231
6.4.2. Filter Design Example 234
6.5. Summary 237
6.6. References 238

7. Conclusion and Future Work 240
7.1. Conclusion 240
7.2. Contributions of the Thesis 242
7.2.1. Modular Cross-Coupled Filters with NRN 243
7.2.2. E-plane and SIW Extracted Pole Filters 244
7.2.3. Negative Coupling Structure for FSIW Resonators 245
7.3. Suggestions for Future Work 246
Publications 248

LIST OF ACRONYMS

ABCD	Transfer Matrix
ADC	Analog-Digital Converter
BPF	Bandpass Filter
BW	Bandwidth
CAD	Computer-Aided Design
CPW	Coplanar Waveguide
DAC	Digital-Analog Converter
dB	Decibel
DLSIW	Double-Layer Substrate Integrated Waveguide
EBG	Electromagnetic Bandgap
EM	Electromagnetic
EPS	Extracted Pole Section
FBW	Fractional Bandwidth
FIR	Frequency Invariant Reactance
FSIW	Folded Substrate Integrated Waveguide
GCC	Generalized Coupling Coefficient
GHz	Gigahertz
HMSIW	Half-Mode Substrate Integrated Waveguide
LNA	Low Noise Amplifier
LTCC	Low Temperature Co-fired Ceramic
NRN	Non-Resonating Node
PA	Power Amplifier
PCB	Printed Circuit Board
SIR	Stepped-Impedance Ratio
SIW	Substrate Integrated Waveguide
SRR	Split Ring Resonator
TE	Transverse Electric Propagation Mode
TEM	Transverse Electromagnetic Propagation Mode
TM	Transverse Magnetic Propagation Mode

LIST OF FIGURES AND TABLES

Chapter 1

Figure 1-1 Block diagram of a full-duplex superheterodyne transceiver with single conversion stage.

Figure 1-2 Configuration of an improved E-plane resonator with embedded SRR.

Figure 1-3 Typical frequency response of the improved E-plane resonator with embedded SRR.

Chapter 2

Figure 2-1 Configuration of a conventional rectangular waveguide.

Figure 2-2 Field distribution for mode TE_{10} in a rectangular waveguide: (a) electric field; (b) magnetic field.

Figure 2-3 Typical frequency response of a rectangular waveguide.

Figure 2-4 Configuration of a conventional SIW with its dimensions (top view).

Figure 2-5 Cutoff frequencies of the quasi-TE_{10} and quasi-TE_{20} modes of the conventional SIW vs. width *W* for various via diameters *D* [2-9].

Figure 2-6 Configurations of double-layer FSIW: (a) with single folding; (b) with double folding.

Figure 2-7 Configuration of a HMSIW.

Chapter 3

Figure 3-1 Doubly terminated lossless linear network.

Figure 3-2 Maximally flat filter responses for various filter orders *n*.

Figure 3-3 Lowpass prototype filter frequency response of Chebyshev type.

Figure 3-4 Generalized Chebyshev (or pseudo-elliptic) frequency response with three transmission zeros in the upper stopband.

Figure 3-5 Elliptic frequency response.
Figure 3-6 Schematic representations of the commonly used prototype elements: (a) resistor; (b) inductor; (c) capacitor; (d) FIR; (e) inverter.
Figure 3-7 Ladder network.
Figure 3-8 Lowpass filter prototype with impedance/admittance inverters.
Figure 3-9 Ladder prototype network of 4^{th} order elliptic filter with symmetric response: (a) cross-coupled circuit; (b) direct-coupled equivalent circuit.
Figure 3-10 Models of the general coupled-resonator filter: (a) Atia-Williams [3-11]; (b) Cameron [3-10].
Figure 3-11 Lowpass prototype of the multiple-coupled resonators filter.
Figure 3-12 Lowpass prototype of the (N+2) cross-coupled filter.
Figure 3-13 Representation of the N^{th}-order cross-coupled filter as a two-port network.
Figure 3-14 Canonical transversal array network: (a) N^{th}-order circuit with direct source-load coupling; (b) Representation of the k^{th} branch in the transversal array.
Figure 3-15 Schematic representation of a bandstop section.
Figure 3-16 Removal of a transmission line section from the filter network.
Figure 3-17 Removal of a bandstop section from the remaining network.
Figure 3-18 Modules used for cascaded filter design: (a) singlet; (b) square doublet; (c) diamond doublet; (d) extended doublet; (e) scheme of a typical filter based on the modular design concept.
Figure 3-19 Lowpass prototype of a direct-coupled filter with a frequency dependent admittance inverter J_i.

Chapter 4

Figure 4-1 Coupling scheme representation of a singlet.
Figure 4-2 Configurations of E-plane singlets in rectangular waveguide: (a) with O-shaped resonator; (b) with I-shaped resonator.
Figure 4-3 Simulated frequency responses of the proposed singlets.

Figure 4-4 Configuration of an E-plane doublet with two hairpin resonators in rectangular waveguide.
Figure 4-5 Calculated from extracted coupling matrix and simulated frequency responses of the proposed doublet.
Figure 4-6 Coupling scheme representation of the proposed doublet.
Figure 4-7 Configuration of a third-order filtering module using multilayer E-plane insert in rectangular waveguide.
Figure 4-8 Simulated frequency response of a 3rd-order E-plane filtering module.
Figure 4-9 Coupling scheme of the proposed 3rd-order E-plane filtering module.
Figure 4-10 General representation of two coupled resonators.
Figure 4-11 Schematic circuit representation of two synchronously tuned coupled resonators with mixed coupling.
Figure 4-12 Schematic circuit representation of a doubly-loaded resonator.
Figure 4-13 Coupling scheme of a 4th-order filter with two transmission zeros in both stopbands.
Figure 4-14 Configuration of the proposed 4th-order filtering module:
(a) 3D-view; (b) metallo-dielectric insert with stripline resonators.
Figure 4-15 Simulated frequency responses used for extraction of coupling coefficient k_{12}.
Figure 4-16 Extracted coupling coeffcients k_{12} and k_{23} against gaps d_{12} and d_{23}.
Figure 4-17 Photograph of the fabricated filter 4th-order filter.
Figure 4-18 Simulated and experimental frequency responses of the fabricated 4th-order filter with two transmission zeros.
Figure 4-19 Coupling scheme of a doublet-based inline filter with NRN.
Figure 4-20 Configuration of a doublet-based inline filter with NRN.
Figure 4-21 Coupling scheme of a doublet-based dual-band filter.
Figure 4-22 Configuration of a doublet-based dual-band filter.
Figure 4-23 Metallo-dielectric waveguide inserts for implementation of the proposed doublet-based filters.
Figure 4-24 Simulated and measured transmission coefficients of a single doublet.
Figure 4-25 Simulated and measured frequency responses of inline filter with NRN.

Figure 4-26 Simulated and measured transmission coefficients of the doublets-based dual-band filter.

Chapter 5

Figure 5-1 Transformation of a transmission line section in extracted pole filter prototypes.

Figure 5-2 Extracted pole section:
(a) schematic representation; (b) coupling scheme representation.

Figure 5-3 Coupling scheme of a 3rd-order extracted pole filter with two transmission zeros.

Figure 5-4 Schematic representation of a doubly-loaded extracted pole section.

Figure 5-5 Frequency responses of EPS with a transmission zero in:
(a) upper stopband; (b) lower stopband.

Figure 5-6 Possible couplings within a filter with NRNs.

Figure 5-7 Schematic circuit representation of two adjacent EPS coupled through admittance inverter.

Figure 5-8 Schematic representation of EPS coupled with resonator through admittance inverter.

Figure 5-9 Configuration of an E-plane NRN in rectangular waveguide.

Figure 5-10 Configuration of an E-plane EPS with embedded S-shaped resonator in rectangular waveguide.

Figure 5-11 Comparison of frequency responses of an EPS with embedded S-shaped resonator and a hollow E-plane resonator.

Figure 5-12 Effect of variation of L_{NRN} in EPS with embedded S-shaped resonator (L_s = 3 mm; H_s = 5.5 mm; L_{sept} = 5 mm): (a) simulated frequency responses; (b) extracted values.

Figure 5-13 Effect of variation of H_s in EPS with embedded S-shaped resonator (L_s = 3 mm; L_{NRN} = 7 mm; L_{sept} = 5 mm): (a) simulated frequency responses; (b) extracted values.

Figure 5-14 Effect of variation of L_s in EPS with embedded S-shaped resonator (H_s = 5.5 mm; L_{NRN} = 7 mm; L_{sept} = 5 mm): (a) simulated frequency responses; (b) extracted values.

Figure 5-15 Effect of variation of L_{sept} in EPS with embedded S-shaped resonator (H_s = 5.5 mm; L_s = 3 mm; L_{NRN} = 7 mm): (a) simulated frequency responses; (b) extracted Q_{ext} .

Figure 5-16 Configuration of an E-plane EPS with embedded SRR.

Figure 5-17 Comparison of frequency responses of an EPS with embedded SRR (L_{SRR} = 2.7 mm; H_{SRR} = 2.7 mm; g = 0.3 mm; L_{sept} = 1.5 mm; L_{NRN} = 9 mm) and a hollow E-plane resonator.

Figure 5-18 Effect of variation of the length of L_{NRN} in EPS with embedded SRR (L_{SRR} = 2.7 mm; H_{SRR} = 2.7 mm; g = 0.3 mm; L_{sept} = 1.5 mm).

Figure 5-19 Effect of variation of L_{SRR} in EPS with embedded square SRR ($H_{SRR} = L_{SRR}$; L_{NRN} = 8 mm; g = 0.3 mm; L_{sept} = 1.5 mm).

Figure 5-20 Configuration of an E-plane EPS with embedded λ/4-wavelength resonator in rectangular waveguide.

Figure 5-21 Comparison of frequency responses of an EPS with embedded λ/4-wavelength resonator and a hollow E-plane resonator.

Figure 5-22 Effect of variation of L_{NRN} in EPS with embedded λ/4-wavelength resonator (L_{res} = 4 mm; W_{res} = 1.5 mm; L_{sept} = 5 mm).

Figure 5-23 Effect of variation of L_{res} in EPS with embedded λ/4-wavelength resonator (L_{NRN} = 9 mm; W_{res} = 1.5 mm; L_{sept} = 5 mm).

Figure 5-24 Effect of variation of W_{res} in EPS with embedded λ/4-wavelength resonator (L_{NRN} = 9 mm; L_{res} = 4.5 mm; L_{sept} = 5 mm).

Figure 5-25 Stepped impedance resonators: (a) λ/4-type; (b) λ/2-type.

Figure 5-26 Relationship between total electrical length and θ_1 for resonant condition given for different impedance ratios.

Figure 5-27 Configuration of an E-plane EPS with embedded SIR in rectangular waveguide.

Figure 5-28 Comparison of frequency responses of EPS with embedded SIRs for different width combinations (impedance ratios).

Figure 5-29 Effect of variation of SIR's lengths ratio on transmission zero position in EPS with SIR (L_{total} = L_1+L_2 = 6 mm; W_2 = 4 mm; L_{sept} = 5 mm).

Figure 5-30 Frequency responses of EPS of all types used for analysis of losses, size reduction and stopband performance.

Figure 5-31 Coupling scheme representation of an EPS used for stopband performance analysis.

Figure 5-32 Coupling scheme of a 3rd-order extracted pole filter with a single transmission zero.

Figure 5-33 Configuration of the E-plane insert for implementation of the 3rd-order filter with single transmission zero.

Figure 5-34 Dependence of extracted k_{1N}^2 on septum width W_{sept12}.

Figure 5-35 Simulated and experimental frequency responses of the fabricated 3rd-order filter with single transmission zero.

Figure 5-36 Photograph of the fabricated insert and waveguide housing.

Figure 5-37 Coupling scheme of a 3rd-order extracted pole filter with three transmission zeros.

Figure 5-38 Configuration of the E-plane insert for implementation of the 3rd-order filter with three transmission zeros in upper stopband.

Figure 5-39 Extracted GCC as functions of insert dimensions (see Figure 5-38): (a) B_i vs. H_{resi}; (b) k_1^2 vs. L_{NRNi}; (c) k_{ij}^2 vs. L_{septij}; (d) Q_{ext} vs. L_{septS} and L_{septL}.

Figure 5-40 Simulated and experimental responses of the fabricated 3rd-order filter with three transmission zeros in upper stopband.

Figure 5-41 Photograph of the fabricated filter: insert and half of the waveguide housing.

Figure 5-42 Configuration of E-plane filter with three S-shaped resonators.

Figure 5-43 Simulated and measured S-parameters of the 3rd-order filter with S-shaped resonators.

Figure 5-44 Half of waveguide housing with metallo-dielectric insert fabricated for the filter with S-shaped resonators.

Figure 5-45 Configuration of the E-plane filter with two S-shaped resonators and an SRR.
Figure 5-46 Measured and simulated S-parameters of the 3rd-order filter with S-shaped resonators and SRR.
Figure 5-47 Metallo-dielectric insert with S-shaped resonators and SRR embedded in a half of the waveguide housing.
Figure 5-48 Simulated frequency response of an EPS with embedded λ/4-wavelength resonator, generating a transmission zero in lower stopband.
Figure 5-49 Adjustment of positions of poles and zero in EPS by changing geometrical dimensions of its elements: (a) effect of changing W_{res} (L_{NRN} = 25 mm, L_{res} = 7 mm); (b) effect of changing L_{NRN} (W_{res} = 4 mm, L_{res} = 7 mm).
Figure 5-50 Coupling scheme of a dual-mode EPS.
Figure 5-51 Coupling scheme of the 4th-order extracted pole filter with dual-mode EPS.
Figure 5-52 Configuration of E-plane insert for implementation of the 4th-order filter with dual-mode EPS.
Figure 5-53 Photograph of the fabricated filter: insert placed within a channel in a half of the waveguide housing.
Figure 5-54 Simulated and experimental responses of the fabricated 4th-order filter with dual-mode EPS.

Chapter 6

Figure 6-1 Configuration of an SIW cavity resonator and its frequency response.
Figure 6-2 Configuration of a λ/2-wavelength FSIW resonator.
Figure 6-3 Magnetic field distribution in a λ/2-wavelength FSIW resonator.
Figure 6-4 Configuration of a λ/4-wavelength FSIW resonator.
Figure 6-5 Field distribution in a λ/4-wavelength FSIW resonator: (a) electric field; (b) magnetic field.
Figure 6-6 Configuration of coupled λ/4-wavelength FSIW resonators (top view).

Figure 6-7 Folding process of a pair of resonators coupled by inductive iris (cross-section).
Figure 6-8 Phase responses of positively and negatively coupled resonators.
Figure 6-9 Coupling scheme of the proposed FSIW cross-coupled filter.
Figure 6-10 Layout of the proposed FSIW cross-coupled filter (top view).
Figure 6-11 Coupling coefficients k_{12} and k_{34} against iris width W_{12}.
Figure 6-12 Coupling coefficient k_{23} against iris width W_{23}.
Figure 6-13 Coupling coefficient k_{14} against slot length L_{slot}.
Figure 6-14 External Q-factor Q_{ext} against input iris width W_{in}.
Figure 6-15 Photograph of the fabricated FSIW filter.
Figure 6-16 Simulated S-parameters of the FSIW cross-coupled filter.
Figure 6-17 Measured S-parameters of the fabricated FSIW cross-coupled filter.
Figure 6-18 Configuration of a hollow DLSIW.
Figure 6-19 Configuration of a DLSIW singlet with a λ/4-wavelength stripline resonator (top view).
Figure 6-20 Typical S-parameters of a DLSIW singlet.
Figure 6-21 Configuration of a DLSIW doublet with two λ/4-wavelength stripline resonators (top view).
Figure 6-22 Typical S-parameters of a DLSIW doublet.
Figure 6-23 Coupling scheme of the proposed modular DLSIW filter.
Figure 6-24 Layout of the proposed modular DLSIW filter (top view).
Figure 6-25 Simulated frequency response of the proposed modular DLSIW filter.
Figure 6-26 Configuration of a SIW EPS.
Figure 6-27 Typical frequency response of a SIW EPS.
Figure 6-28 Field distribution in the proposed EPS at pole frequency: (a) electric field; (b) magnetic field.
Figure 6-29 Layout of the inline SIW extracted pole filter (top view).
Figure 6-30 Simulated S-parameters of the inline SIW extracted pole filter.

Chapter 4

Table 4-1 Dimensions of the fabricated 4^{th}-order filter (see Figure 4-14).

Table 4-2 Dimensions of the fabricated doublet.

Table 4-3 Dimensions of inline filter with NRN.

Chapter 5

Table 5-1 Comparison of dimensions and *Q*-factors of E-plane resonator and EPS at 10 GHz.

Table 5-2 Dimensions of E-plane insert for the designed filter (see Figure 5-33).

Table 5-3 Dimensions of E-plane insert for the designed filter (see Figure 4-39).

Table 5-4 Dimensions of the designed filter with three S-shaped resonators (see Figure 5-42).

Table 5-5 Dimensions of the designed filter with two S-shaped resonators and an SRR (see Figure 5-45).

Table 5-6 Dimensions of the designed filter with dual-mode EPS (see Figure 4-52).

Chapter 6

Table 6-1 Comparison of SIW resonators based on full-wave EM simulation results (Ansoft HFSS™).

Table 6-2 Dimensions of the designed FSIW filter (see Figure 6-13).

Table 6-3 Dimensions of the inline SIW extracted pole filter (see Figure 6-28).

CHAPTER 1

INTRODUCTION

The commercial success of the telecommunication industry has stimulated the quick development of modern wireless communication technologies. The rapid growth in wireless internet, ultra-wideband systems, mobile and broadband personal communications, satellite navigation and remote sensing systems has created a massive demand for new microwave and millimetre-wave components capable of meeting more stringent requirements. Filters, diplexers and multiplexers responsible for frequency selectivity, play crucial role in these systems. The problem of the efficient utilization of electromagnetic spectrum imposes new challenges to design and realization of microwave and millimetre-wave filters. New solutions and techniques for the design of compact bandpass filters with low insertion loss, high selectivity, and wide stopband are required for the development of the next generation wireless and satellite systems.

1.1. Filters for Wireless Communications

Electronic filters are indispensable components for many wireless systems and applications, where these devices play an important role as discriminators between wanted and unwanted signals [1-1]-[1-4]. In the frequency domain, filters are used to reject signals of certain unwanted frequencies and pass signals of desired frequencies within a frequency band specified for a certain application.

Filters perform a variety of different functions in modern full duplex personal communications systems, which require transmit and receive filters for each transceiver unit at the base station level. These can be illustrated using a block diagram of a full-duplex superheterodyne transceiver with a single conversion stage, as shown in Figure 1-1 [1-5, 1-6].

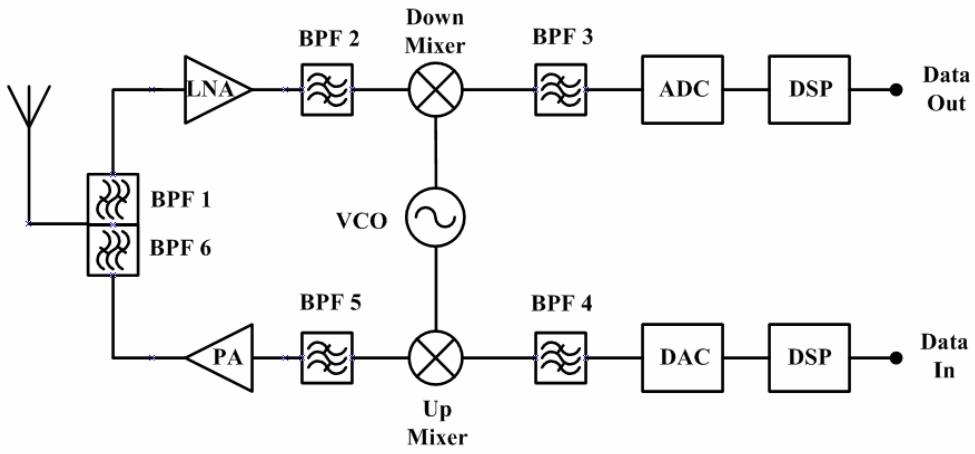

Figure 1-1: Block diagram of a full-duplex superheterodyne transceiver with single conversion stage.

In this scheme, the top sequence of blocks is combined into the receiver, while the bottom sequence constitutes the transmitter. These two systems have a common voltage-controlled oscillator, as well as an antenna with diplexer, which consists of two bandpass filters (BPF): BPF 1 and BPF 6. BPF 1 selects the receiver frequency band signals and removes interference caused by the leakage of the output signal from the transmitter. The main requirements of this particular BPF include low insertion loss and high attenuation at the transmitter band. BPF 6 reduces spurious radiation power from the transmitter and attenuates noise from the receiver band. Hence, this BPF should have low insertion loss and wide stopband. The BPF 2, placed after a low noise amplifier (LNA), is necessary for the suppression of the unwanted image frequency signal, which appears at the same intermediate frequency (IF) as the main signal after down-conversion. BPF 3, whose centre frequency is equal to IF, plays the role of a channel selection filter. Therefore, it should have a narrow bandwidth and a sharp attenuation skirt. In the transmitter part, a narrow-band BPF 4 rejects unwanted components of the baseband signal received from the digital-analog converter (DAC) before upconversion. The up-converting mixer generates unwanted mixing products, which are rejected by the BPF 5, placed before power amplifier (PA). Transmit filters should exhibit low insertion loss and high selectivity in order to prevent out-of-band intermodulation and adjacent channel interferences and satisfy certain

regulatory and efficiency requirements. For cellular systems, a typical transmit filter has an insertion loss of 0.8 dB and return loss of 20 dB in the passband; acceptable levels of adjacent channel interference are specified in GSM standards as C/A > –9 dB.

The evolution of filter design techniques has been driven by the requirements of various wireless systems (for example, military, satellite or cellular). Operating frequencies used in modern communication systems have a very wide range; therefore, various types of resonators and filters have been developed for different frequency bands in order to provide optimal solution based upon certain application requirements [1-3].

Several types of resonators are employed in the implementation of filters operating at microwave and mm-wave frequency ranges. These are usually grouped into three categories [1-1]: lumped-element *LC* resonators, planar resonators, and three-dimensional cavity-type resonators. Lumped-element resonators [1-2] are organized using chip inductors and capacitors. This type of resonators is used at low frequencies and has small size but relatively low *Q*-factor values. Microstrip and stripline resonators [1-4], constructed as sections of transmission lines, terminated in a short or open circuit, form a class of planar resonators. These sections may have various shapes: meander [1-7], hairpin [1-8], ring [1-9] or patch [1-10] configurations. Microstrip and stripline filters are compact, cheap in fabrication and easy to integrate with other components, as they are usually printed on dielectric substrate. However, this type of resonators is quite lossy (*Q*-factors between 50 and 300 at 1 GHz [1-1]) and has limited power handling capability. In contrast, cavity resonators such as coaxial, waveguide and dielectric have very high *Q*-factors (up to 30000) and are capable of handling high power levels. Coaxial and waveguide cavity resonators [1-11]-[1-13] are organized as shorted $\lambda_g/2$-length transmission line sections, while dielectric resonators [1-14] are constructed as pieces of dielectric having different shapes (cube, cylinder, torus etc.), which are mounted on support structures inside metallic housings. The main disadvantage of this type of resonators is that they are massive and require a complex, expensive and time-consuming fabrication process.

With the advent of substrate integrated waveguide (SIW) technology [1-15], it has become possible to combine cheap and simple planar circuits' fabrication processes with the main benefits of the waveguide cavity structures. The same combination can be realized using all-metal or metallo-dielectric inserts in waveguide housings, which may contribute to miniaturization of waveguide resonators and filters [1-16]. The rapid progress in filter design theory, which has resulted in the development of the non-resonating nodes (NRN) concept [1-17, 1-18] for use in cross-coupled filters, has provided new challenges to engineering solutions required to take advantage of the recent theoretical achievements. Improvements of full-wave electromagnetic simulators (EM) based upon quick development of computing techniques and environment enable accurate simulations of the advanced structures. This makes computer-aided design (CAD) tools absolutely indispensable for the efficient design and optimization of high-performance filters for modern wireless communications.

1.2. Rectangular Waveguide Filters

Waveguide theory has been rigorously investigated over the past few decades and has suggested many ways to design various circuits and components, which use rectangular waveguide as the main guiding medium for the propagation of electromagnetic waves. Most filters at the microwave and mm-wave frequencies, therefore, are produced either in waveguide [1-19] (rectangular air-filled metal pipe, dielectric-filled or micromachined air-filled) associated with bulkiness, or image guide and nonradiative dielectric guide [1-20] with high associated loss. Standard configurations of such filters use split block housing with resonating and non-resonating cavities, and corresponding transverse inductive and capacitive irises between them organized in the metallic blocks by milling. Despite the numerous advantages of the waveguide cavities, fabrication process, required for the implementation of these filters, is time-consuming and quite expensive. Moreover, each new filter to be implemented requires a full fabrication cycle in order to build its housing blocks. The dimensions of the cavities, which determine their resonant frequency, appear to be large for use at microwaves as well. This leads to a certain degree of bulkiness (extremely important for satellite applications) and inflexibility in the design, especially taking into account the growing demand for cheap, compact, and mass-producible devices. The classical way of waveguide miniaturization involves the use of a dielectric filling, which reduces the guide wavelength by a square root of its relative permittivity. However, lack of dielectrics with high permittivity and low loss significantly restricts practicability of this approach.

To overcome the issues related to the expensive fabrication process, E-plane waveguide filters have been proposed by Konishi and Uenakada in 1974 [1-21]. This type of filter uses all-metal of metallo-dielectric inserts allocated within the E-plane of rectangular waveguide, represented as two identical halves of housing. These inserts contain a sequence of inductive obstacles, typically septa, at distance of approximately half the wavelength from each other. Such an approach is more flexible, as it does not require complex fabrication of new waveguide housing; same housing can be used for the implementation of

another filter just by replacing the E-plane insert. The inserts can be realized by employing cheap and mass-producible technologies for fabrication of planar structures.

However, stopband performance of E-plane filters may be insufficient for some applications such as diplexers and multiplexers due to the low attenuation level in upper stopband (especially for low-order filters) and spurious resonance, which appears at a frequency of about 1.5 times the centre frequency. The low upper stopband attenuation can be improved by increasing the filter order, but this comes into conflict with the requirement of compactness, since coupling septa may have widths of up to half the length of the resonators, especially for narrow-band filters.

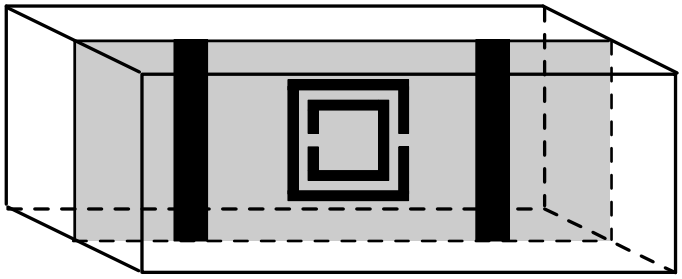

Figure 1-2: Configuration of an improved E-plane resonator with embedded SRR.

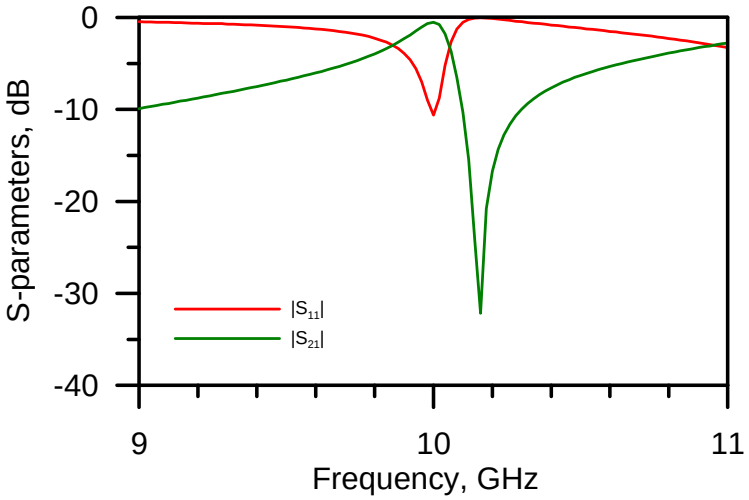

Figure 1-3: Typical frequency response of the improved E-plane resonator with embedded SRR.

It has been shown in [1-22] that the stopband performance of E-plane resonators can be improved by using ridges, which alter the cutoff frequency of the waveguide, and periodically loaded resonators [1-23] embedded within the E-plane resonator, which introduce a lowpass effect. Later, E-plane resonators with embedded split ring resonators (SRR) [1-24] and S-shaped resonators [1-16] capable of generating a transmission zero in the upper stopband have been proposed in order to achieve compactness and stopband improvement. The phenomenon has been related to metamaterial effects produced by periodical lattice composed of SRR and S-shaped resonators. However, it can be seen from the typical configuration of the improved E-plane filter with embedded SRR (shown in Figure 1-2) that there is a single SRR available, which consists of two concentric split rings. Hence, it is impossible to consider the transmission zero, which appears in the upper stopband in the frequency response of this structure (presented in Figure 1-3), as an effect of a periodic lattice employed. Therefore, this structure has to be analyzed using standard filter theory.

1.3. Substrate Integrated Waveguide Filters

Substrate integrated waveguides (SIW) have been developed as a compact, cheap, easy-to-fabricate and mass-producible alternative to conventional rectangular waveguide structures. Rapid growth of the SIW research area has been driven by adaptability of very well developed theory of conventional waveguides. Consequently, the main successful approaches employed in waveguide filter design have been transferred to the SIW platform. It has been found that *Q*-factor and power handling that can be achieved with SIW resonators are much higher than that attainable with traditional planar microstrip or stripline solutions, which made the SIW cavities an attractive object for application in direct- and cross-coupled filters. However, the physical dimensions of SIW circuits may be too large for certain applications, especially those operating at low frequencies. Among the approaches to achieve size reduction of SIW resonators and filters there are ridged SIW [1-26] and EBG-substrate [1-27] concepts. The use of advanced multilayer technologies, such as LTCC, stimulated development of new folded SIW (FSIW) structures, which not only reduce the area occupied by waveguides or resonators on a chip but also offer new engineering solutions to the realization of advanced cross-coupled filters with and without non-resonating nodes (NRN). Two types of compact FSIW resonant cavities have been proposed and compared in [1-28]; a quarter-wavelength FSIW cavity, obtained by the subsequent folding of a conventional $\lambda/2$-wavelength FSIW resonator, has been developed and successfully employed for the implementation of a cross-coupled filter in [1-29]; another miniaturization technique for FSIW resonators has been developed in [1-30], a directional filter based upon a half-mode SIW (HMSIW) has been proposed in [1-31].

At present, development of new SIW cavity resonators for available fabrication processes can be considered as completed. Nevertheless, the combination of SIW with different transmission lines and implementation of internal and external couplings between SIW cavity resonators for the design of cross-coupled filters still remain attractive areas of investigation problems for researchers.

1.4. Aims and Objectives of the Thesis

The aims and objectives of this work are to develop compact filters with improved stopband performance for wireless applications using conventional and substrate integrated waveguide technologies.

The first aim of the project is to develop a design procedure for direct-coupled filters with improved E-plane resonators with embedded S-shaped resonators and SRRs. The achievement of this aim requires the attainment of several objectives. The first objective is to develop a model of the improved E-plane resonators, which is compatible with standard filter synthesis procedures. This requires a comprehensive analysis of the structures; origin of the generated transmission zero in the upper stopband, as well as the origin of the resonant frequency's shift in comparison with standard E-plane resonators are to be determined. The effects of the physical dimensions of the structures on transmission characteristics should be studied. The second objective is to establish the relationships between parameters of the model and behaviour of the real improved E-plane resonators, which requires the development of an extraction procedure. Such a procedure is also needed for parameters' extraction for the model of interacting pairs of improved and conventional E-plane resonators. Next, improved filters with transmission zeros in stopband should be designed according to the design procedure in order to prove the feasibility of the presented model and procedure. Additionally, the possibilities of designing improved E-plane resonators with embedded resonators capable of generating transmission zeros in the lower stopband are to be studied. The opportunities offered by the developed theoretical model should be considered for this purpose.

The second aim of this work is to study possible opportunities of realization of cross-coupled filters with transmission zeros in conventional rectangular waveguides using all-metal and metallo-dielectric E-plane inserts. The first objective is to determine the types of resonators and potential coupling schemes, which can be implemented in conventional rectangular waveguide, taking into account the technological constraints. Then a suitable design procedure should be determined or developed for the realization of the cross-

coupled filter, which involves extraction of appropriate model parameters from simulated data. Another objective is to study the possibility to implement NRN and design cross-coupled filters with NRN using the E-plane approach.

Finally, the third aim of the work is to investigate possible solutions available for realization of cross-coupled filters with or without NRN using SIW technology. The main objective is to create new SIW filters with improved performance using the approaches developed in this work for conventional rectangular waveguides. An additional objective is to study the available SIW filter design and implementation techniques and find potential engineering solutions, which may improve their performance.

1.5. Outline of the Thesis

This thesis presents the work, which has been carried out for a period of almost four years, between 2007 and 2010. It is organized into seven chapters.

Chapter 2 presents a brief introduction into the principles of operation of conventional rectangular waveguide. It includes an overview of the basic electromagnetic field theory with regards to propagation in rectangular waveguides under specific boundary conditions. Analytical expressions for electromagnetic fields and main characteristics are derived for propagating modes. Also, an overview of advanced substrate integrated waveguide structures is given.

Chapter 3 presents an overview of available filter design procedures. The chapter outlines methods of transfer function approximation and focuses on lowpass prototype synthesis techniques for direct- and cross-coupled filters. Coupling matrix representation is introduced for cross-coupled filters; methods of coupling matrix synthesis for filters with and without direct source-load couplings are presented. Advanced techniques employed to generate transmission zeros in filter stopbands are considered. Next, frequency mapping procedure and corresponding circuit transformations for lowpass filter prototypes are outlined. Finally, a brief overview of filter implementation and modern optimization techniques is presented.

Chapter 4 is dedicated to the development of cross-coupled filters with improved stopband performance in conventional rectangular waveguide using E-plane metallo-dielectric inserts. Brief introduction into the concept of coupling coefficients and their extraction from transmission characteristics is given. Several filters based upon a combination of stripline resonators and E-plane septa are designed. Doublet structure for use in modular E-plane filters with non-resonating nodes, which is capable of generating two transmission zeros, is introduced. Dual-band filter based on the doublet structures is realized using E-plane metallo-dielectric inserts.

In chapter 5, a model of the improved E-plane resonators with embedded S-shaped resonators and SRR is developed and investigated. It is shown that the structure can be considered as an extracted pole section with NRN. The concept of generalized coupling coefficients for cross-coupled filters with NRN is outlined and applied to the design of extracted pole filters using the new E-plane structures. The extraction procedure for obtaining the generalized coupling coefficients from frequency responses of single and coupled extracted pole sections is developed. Configurations of new extracted pole sections are proposed as a result of the analysis. Investigations on the effects of dimensions on the generalized coupling coefficients, comparative analysis of stopband performances and losses of the proposed extracted pole sections are carried out. Dual-mode extracted pole section, which generates a transmission zero in the lower stopband, is synthesized based on analysis of the developed model. Finally, several filter design examples are presented in order to validate the analysis.

Chapter 6 illustrates an application of the extracted pole section model in compact SIW filters with improved stopband performance. Singlet and doublet structures generating one and two transmission zeros respectively are proposed for use in SIW filters. Consequently, inline modular filters composed of these modules are designed. Additionally, a negative coupling structure for use in FSIW cross-coupled resonator filters is proposed and investigated. Hence, a bandpass filter with novel structure is designed in order to prove the feasibility of the approach.

Finally, in chapter 7, the main conclusions of the thesis are presented; a summary of contributions of this work is given and some recommendations for future work are offered.

1.6. References

[1-1] R. J. Cameron, C. M. Kudsia, and R. R. Mansour, *Microwave filters for communication systems: fundamentals, design, and applications.* Hoboken, New Jersey: John Wiley & Sons, 2007.

[1-2] G. L. Matthaei, L. Young and E. M. T. Jones, *Microwave filters, impedance matching networks, and coupling structures*, Dedham, MA: Artech House, 1964.

[1-3] I. C. Hunter, *Theory and design of microwave filters*, London, Institution of Electrical Engineers, 2001.

[1-4] J. G. Hong and M. J. Lancaster, *Microstrip Filters for RF/Microwave Applications*, New York: John Wiley & Sons, 2001.

[1-5] F. Ellinger, *Radio Frequency Integrated Circuits and Technologies*, Berlin: Springer, 2007.

[1-6] M. N. S. Swamy and K.-L. Du, *Wireless Communication Systems: From RF Subsystems to 4G Enabling Technologies*, New York: Cambridge University Press, 2010.

[1-7] J. T. Bolljahn and G. L. Matthaei, "A study of the phase and filter properties of arrays of parallel conductors between ground planes," *Proc. IRE*, vol. 50, pp. 299–311, Mar. 1962.

[1-8] E. G. Cristal and S. Frankel, "Hairpin-line and hybrid hairpin line/half-wave parallel-coupled-line filters," *IEEE Trans. Microwave Theory Tech.*, vol. MTT-20, pp. 719–728, Nov. 1972.

[1-9] I. Wolff, "Microstrip bandpass filter using degenerate modes of a microstrip ring resonator," *Electron. Lett.*, vol. 8, no. 12, pp. 302–303, June 1972.

[1-10] J.-S. Hong and S. Li, "Theory and experiment of dual-mode microstip triangular patch resonators and filters," *IEEE Trans. Microwave Theory Tech.*, vol. 52, no. 4, pp. 1237–1243, Apr. 2004.

[1-11] R. Wenzel, "Synthesis of combline and capacitively loaded interdigital bandpass filters of arbitrary bandwidth," *IEEE Trans. Microwave Theory Tech.*, vol. MTT-19, pp. 678–686, Aug. 1971.

[1-12] Ali E. Atia and Albert E. Williams, “Narrow-Bandpass Waveguide Filters”, *IEEE Trans. Microwave Theory Tech.*, vol. 20, pp.258-265, April 1972.

[1-13] S. Amari and U. Rosenberg, “New building blocks for modular design of elliptic and self-equalized filters,” *IEEE Trans. Microwave Theory Tech.*, vol. 52, no. 2, pp. 721–736, Feb. 2004.

[1-14] S. B. Cohn, “Microwave filters containing high-Q dielectric resonators,” *IEEE Trans. Microwave Theory Tech.*, vol. MTT-16, pp. 218–227, Apr. 1968.

[1-15] D. Deslandes and K. Wu, “Integrated microstrip and rectangular waveguide in planar form,” *IEEE Microw. Wireless Compon. Lett.*, vol. 11, no. 2, pp. 68-70, Feb. 2001.

[1-16] N. Suntheralingham and D. Budimir, “Enhanced Waveguide Bandpass Filters Using S-shaped Resonators,” *Int. J. RF and Microwave CAE*, vol. 19, no. 6, pp. 627-633, 2009.

[1-17] H. C. Bell, “Canonical asymmetric coupled-resonator filters,” *IEEE Trans. Microwave Theory Tech.*, vol. 30, pp. 1335–1340, Sept. 1982.

[1-18] S. Amari, U. Rosenberg, and J. Bornemann, “Singlets, cascaded singlets and the nonresonating node model for advanced modular design of elliptic filters,” IEEE Microw. Wireless Compon. Lett., vol. 14, no. 5, pp. 237–239, May 2004.

[1-19] D. Budimir, *Generalized Filter Design by Computer Optimization*, Artech House, 1998.

[1-20] T. Yoneyama and S. Nishida, “Nonradiative dielectric waveguide for millimeter-wave integrated circuits,” *IEEE Trans. Microwave Theory Tech.*, vol. MTT-29, pp. 1188–1192, Nov. 1981.

[1-21] Y. Konishi and K. Uenakada, “The design of a band pass filter with inductive strip planar circuit mounted in waveguide,” *IEEE Trans. Microwave Theory Tech.*, vol. MTT-22, pp. 869–873, Oct. 1974.

[1-22] G. Goussetis and D. Budimir, “Compact ridged waveguide filters with improved stopband performance,” in *IEEE MTT-S Int. Microw. Symp. Dig.*, Jun. 2003, vol. 2, pp. 953–956.

[1-23] G. Goussetis and D. Budimir, “Novel periodically loaded E-plane filters,” *IEEE Microw. Wireless Compon. Lett.*, vol. 13, no. 6, pp. 193–195, Jun. 2003.

[1-24] A. Shelkovnikov and D. Budimir, “Miniaturized Rectangular Waveguide Filters,” *Int. J. RF and Microwave CAE*, vol. 17, no. 4, pp. 398-403, 2007.

[1-25] J. A. Ruiz-Cruz, M. A.E. Sabbagh, K. A. Zaki, J. M. Rebollar, Yunchi Zhang, “Canonical Ridge Waveguide Filters in LTCC or Metallic Resonators,” *IEEE Trans. Microwave Theory Tech.*, vol. 53, pp. 174–182, Jan. 2005.

[1-26] A. Shelkovnikov, D. Budimir, “Novel Compact EBG Waveguide Resonators in Planar Form,” *European Microwave Conference*, vol. 2, 4-6 Oct. 2005.

[1-27] N. Grigoropoulos, B. Sanz Izquierdo, and P. R. Young, “Substrate Integrated Folded Waveguides (SIFW) and filters,” *IEEE Microw. Wireless Compon. Lett.*, vol. 15, no. 12, pp. 829-831, December 2005.

[1-28] J. S. Hong, “Compact folded waveguide resonator,” in *IEEE MTT-S Int. Microw. Symp. Dig.*, Jun. 2004, pp. 213–216.

[1-29] S. K. Alotaibi and J.-S. Hong, “Novel substrate integrated waveguide filter,” *Microw. Opt. Technol. Lett.*, Vol. 50, No. 4, pp. 1111–1114, Apr. 2008.

[1-30] H. H. Lin, “Novel folded resonators and filters,” in *IEEE MTT-S Int. Microw. Symp. Dig.*, Jun. 2007, pp. 1277–1280.

[1-31] Y. Q. Wang, W. Hong, Y. D. Dong, B. Liu, H. J. Tang, J. X. Chen, X. X. Yin, and K. Wu, “Half mode substrate integrated waveguide (HMSIW) bandpass filter,” *IEEE Microw. Wireless Compon. Lett.*, vol. 17, no. 4, pp. 265–267, Apr. 2007.

CHAPTER 2

RECTANGULAR WAVEGUIDES

2.1. Introduction

Rectangular waveguides and components based upon them are widely used in various microwave and millimetre-wave communication systems, especially airborne platforms, communication satellites, earth stations, and wireless base-stations due to their numerous advantages such as high power handling capability and high *Q*-factor values revealed by waveguide cavities. However, conventional waveguides are bulky and unsuitable for high-density integration, which greatly increases the cost of wireless systems. This poses the problem of waveguide miniaturization. An effective solution to this problem requires understanding of electromagnetic processes, which take place within the waveguides.

In this chapter we will be concerned with the main principles of operation of conventional rectangular waveguide and its recently proposed substrate integrated analogues. Section 2.2 presents an overview of the basic electromagnetic field theory with regards to propagation in rectangular waveguides. Maxwell's equations are introduced and analytical expressions for fields in rectangular waveguide are derived on their basis. In section 2.3, an overview of substrate integrated waveguides is given. Configurations of advanced substrate integrated transmission lines are considered. The main properties of several single- and multilayer structures are briefly outlined.

2.2. Electromagnetic Theory of Rectangular Waveguides

2.2.1. Maxwell's Equations

Electric and magnetic fields that vary with time are governed by physical laws described by a set of equations known collectively as Maxwell's equations. The general form of time-varying Maxwell's equations can be written in differential form as [2-1]:

$$\nabla \times \vec{E} = -\frac{\partial \vec{B}}{\partial t}, \tag{2.2-1a}$$

$$\nabla \times \vec{H} = \frac{\partial \vec{D}}{\partial t} + \vec{J}_s, \tag{2.2-1b}$$

$$\nabla \cdot \vec{D} = \rho_\varepsilon, \tag{2.2-1c}$$

$$\nabla \cdot \vec{B} = \rho_m, \tag{2.2-1d}$$

where the variables involved are described as:

$\vec{E}$ (V/m) – Electric field intensity;

$\vec{H}$ (A/m) – Magnetic field intensity;

$\vec{D}$ (C/m^2) – Electric flux density;

$\vec{B}$ (W/m^2) – Magnetic flux density;

$\vec{J}_s$ (A/m^2) – Electric current density;

ρ_ε (C/m^3) – Electric charge density;

Each of the equations in (2.2-1) has its physical meaning. (2.2-1a), also known as Faraday's Law, means that variations of magnetic flux with time or/and fictitious magnetic current play the role of sources of circulating electric field. Equation (2.2-1b) means that time variations of electric flux or/and electric current generate circulating magnetic field. This equation is also known as Ampere's Law. Equation (2.2-1c) is the Gauss's Law, which shows that electric charges are sources of electric field. Gauss's Law for magnetic field is

given in (2.2-1d). Since magnetic charge is known not to exist, magnetic charge density is usually presented as zero.

Another set of equations describes relationships between the above parameters in any medium in terms of its permittivity ε, permeability μ and conductivity σ:

$$\vec{D} = \varepsilon\vec{E} \tag{2.2-2a}$$

$$\vec{B} = \mu\vec{H} \tag{2.2-2b}$$

$$\vec{J} = \sigma\vec{E}\,, \tag{2.2-2c}$$

where $\varepsilon = \varepsilon_r\varepsilon_0$, $\mu = \mu_r\mu_0$. Here, ε_r and μ_r are the relative permittivity and relative permeability of the propagation medium respectively; ε_0 and μ_0 – permittivity and permeability in vacuum.

The presented equations are valid for arbitrary time dependence; however, it is more convenient to consider sinusoidal (harmonic) time dependence with steady-state conditions assumed. In this case, all the field quantities can be represented in a form, where time derivatives get eliminated. Let us consider a sinusoidal electric field with *x*-component of the following form:

$$\vec{E}(x,y,z,t) = \vec{x}A(x,y,z,t)\cos(\omega t + \varphi) \tag{2.2-3}$$

where A is a real magnitude, ω is a radian frequency, φ is a phase reference of the wave at $t = 0$. In phasor form, this field can be written as:

$$\vec{E}(x,y,z,t) = \vec{x}A(x,y,z,t)e^{j\varphi} \tag{2.2-4}$$

Conversion from phasor to real time-varying quantities is given as:

$$\vec{E}(x,y,z,t) = \mathrm{Re}[\vec{E}(x,y,z)\cdot e^{+j\omega t}] \tag{2.2-5}$$

Assuming $e^{+j\omega t}$ time dependence, the time derivatives in expressions (2.2-1) can be replaced with $j\omega$. Therefore, Maxwell's equations in phasor form with harmonic time dependence now become [2-2]:

$$\nabla\times\vec{E} = -j\omega\vec{B} \tag{2.2-6a}$$

$$\nabla\times\vec{H} = j\omega\vec{D} + \vec{J}_s \tag{2.2-6b}$$

$$\nabla\cdot\vec{E} = \rho_\varepsilon \tag{2.2-6c}$$

$$\nabla\cdot\vec{B} = 0 \tag{2.2-6d}$$

2.2.2. Electromagnetic Modes in Rectangular Waveguide

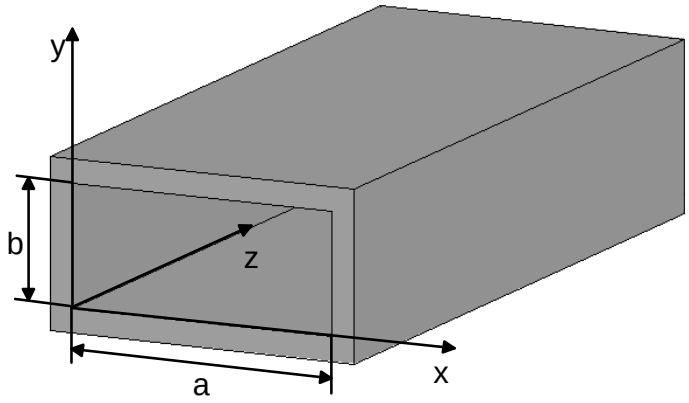

Figure 2-1: Configuration of a conventional rectangular waveguide.

Waveguides normally consist of a hollow or dielectric-filled conducting pipe with arbitrary cross-section. In ideal case, both conductor and dielectric filling of waveguides are assumed to be lossless. Analysis of possible configurations of fields, propagating in waveguides can be accomplished by solution of Maxwell's equations. For steady-state time dependence, in a source-free, linear, isotropic and homogeneous region, Maxwell's equations can be transformed into the following form:

$$\nabla \times \vec{E} = -j\omega\mu\vec{H} \tag{2.2-7a}$$

$$\nabla \times \vec{H} = j\omega\varepsilon\vec{E} \tag{2.2-7b}$$

Taking curl of (2.2-7a) and using substitution from (2.2-7b), these expressions can be converted into Helmholtz equations (wave equations) for electric and magnetic fields:

$$\nabla^2\vec{E} + k^2\vec{E} = 0 \tag{2.2-8a}$$

$$\nabla^2\vec{H} + k^2\vec{H} = 0 \tag{2.2-8b}$$

where constant $k = \omega\sqrt{\mu\varepsilon}$ is called the wavenumber. In free space, $k = k_0 = \omega\sqrt{\mu_0\varepsilon_0}$.

Assuming that the time-varying fields in waveguide structures propagate along the z-axis (see Figure 2-1), the fields can be expressed in terms of the propagation constant γ as $\vec{E}(x,y,z) = f(x,y,z)e^{-\gamma z}$, and the method of separation of variables can be applied to equations (2.2-8). Consequently, the Helmholtz equations can be transformed into:

$$\nabla_t^2 \vec{E} + k_c^2 \vec{E} = 0 \tag{2.2-9a}$$

$$\nabla_t^2 \vec{H} + k_c^2 \vec{H} = 0 \tag{2.2-9b}$$

where $\nabla_t^2 = \frac{\partial^2}{\partial x^2} + \frac{\partial^2}{\partial y^2}$ and $k_c = \sqrt{\gamma^2 + k^2}$, referred to as the cutoff wavenumber.

After applying the derivatives into the Maxwell's curl equations, another form can be obtained, separating transverse electric and magnetic components of the field. Then the transverse field components in terms of E_z and H_z are defined as [2-3]

$$E_x = -\frac{1}{k_c^2}\left(\gamma \frac{\partial E_z}{\partial x} + j\omega\mu \frac{\partial H_z}{\partial y}\right) \tag{2.2-10a}$$

$$E_y = \frac{1}{k_c^2}\left(-\gamma \frac{\partial E_z}{\partial y} + j\omega\mu \frac{\partial H_z}{\partial x}\right) \tag{2.2-10b}$$

$$H_x = \frac{1}{k_c^2}\left(-\gamma \frac{\partial H_z}{\partial x} + j\omega\varepsilon \frac{\partial E_z}{\partial y}\right) \tag{2.2-10c}$$

$$H_y = -\frac{1}{k_c^2}\left(\gamma \frac{\partial H_z}{\partial y} + j\omega\varepsilon \frac{\partial E_z}{\partial x}\right) \tag{2.2-10d}$$

When the longitudinal component (z-component) of the electric field is $E_z \neq 0$, while z-component of the magnetic field $H_z = 0$, a particular set of solutions of equations (2.2-10) can be obtained. In this case it is clear that all the magnetic field components will be transversed to the direction of propagation. The mode of propagation associated with such field structure is, hence, called the transverse magnetic (TM) mode. Similarly, another set of solutions can be obtained when $H_z \neq 0$, while $E_z = 0$. The mode of propagation in this

case does not have an electric field component along the direction of propagation and, therefore, is called transverse electric (TE) mode. Both sets are independent and can be used to characterize fields that propagate along the waveguide. For this purpose, the wave equations should be solved for the longitudinal components of the electromagnetic field with the specific boundary conditions [2-4]. Then, transverse field components can be found from (2.2-10).

According to the method of separation of variables, the solution of Helmholtz equations can now be derived with the substituted E_z and H_z for the variables x and y [2-5]. For a set of solutions when $E_z = 0$,

$$H_z = X(x) \cdot Y(y) \tag{2.2-11}$$

Where $X(x)$ and $Y(y)$ are functions of x and y respectively.

From the new form of wave equations, boundary conditions along x- and y-axis determine the cutoff wavenumber k_c. This number, under such conditions, can only take discrete values, each of which corresponds to a cross-sectional field distribution pattern propagating in the z-direction.

For TM modes propagating in the rectangular waveguide, the solution procedure involves expressing the electric field E_z as a product of three functions, each of which is a function of one of the coordinate variables. Then, from the solutions of the Helmholtz equations, the functions $X(x)$ and $Y(y)$ are given by

$$X(x) = A\sin(k_x x) + B\cos(k_x x) \tag{2.2-12a}$$

$$Y(y) = C\sin(k_y y) + D\cos(k_y y) \tag{2.2-12b}$$

Hence, the complete solution for the longitudinal component of the field component E_z is

$$E_Z = [A\sin(k_x x) + B\cos(k_x x)] \cdot [C\sin(k_y y) + D\cos(k_y y)] \cdot e^{-\gamma z} \qquad (2.2\text{-}13)$$

where

$$k_c^2 = k_x^2 + k_y^2 \qquad (2.2\text{-}14)$$

and A, B, C, D, k_x and k_y can be found by applying boundary conditions on the metallic walls of the waveguide so that the E_z field component on the walls is equal to zero. In this case, substituting $x = 0$, we get $B = 0$; similarly, $y = 0$ leads to $D = 0$; for $x = a$ it can be derived that $k_x a = m\pi$; and $y = b$ yields $k_y b = n\pi$, where m and n are integers. Hence, E_z can be re-written as:

$$E_Z = E_0 \cdot \sin\left(\frac{m\pi x}{a}\right) \cdot \sin\left(\frac{n\pi y}{b}\right) \cdot e^{-\gamma z} \qquad (2.2\text{-}15)$$

where E_0 is an arbitrary amplitude of the electric field to be determined based on the amount of input power to the waveguide, while m and n are the mode numbers, representing the number of sinusoidal half-wave variations in the field in the x and y directions. There is an infinite set of modes, referred to as TM_{mn} modes. It can be shown that

$$k_c^2 = \gamma^2 + k^2 = \left(\frac{m\pi}{a}\right)^2 + \left(\frac{n\pi}{b}\right)^2 \qquad (2.2\text{-}16)$$

where $k = \omega\sqrt{\mu\varepsilon}$.

By considering the cross-section of the waveguide and calculating the number of half sinusoidal variations of the field patterns along the width and the height, we can define the distribution patterns by a recognizable nomenclature. Such field distribution patterns are the waveguide modes. The modes propagate independently and no coupling between them is

observed. This characterizes that they are orthogonal to each other, according to the field patterns, by which they are formed. Therefore, the boundary conditions and physical characteristics of the waveguide, namely the width and the height of the uniform structure, define the number of half sinusoidal variations, also referred to as order of the mode, i.e. define certain values of the wavenumber, independent of the operating frequency of the waveguide. The general solution for the field configurations propagating in waveguides may be obtained from the superposition of the TE and TM modes.

It has been shown in [2-4] that in a lossless waveguide, regardless of its type, wave propagation occurs at frequencies where the propagation constant $\gamma = \alpha + j\beta$ is an imaginary number ($\gamma = j\beta$). If, on the contrary, γ is real ($\gamma = \alpha$), the wave decays with an attenuation factor $e^{-\alpha z}$ along the z-direction. The waveguide, in this case, is characterized by exponentially decaying modes, also referred to as evanescent modes; in real waveguides the propagation constant has a complex value. Thus, in order to provide propagation of waves within the waveguide, the broad (a) and narrow (b) guide inner dimensions, and the frequency of excitation from (2.2-16) should satisfy the condition $k_c^2 < k^2$. The lowest possible excitation frequency for a waveguide to allow propagation is the cutoff frequency, and is obtained when $\beta = 0$ from (2.2-16) as

$$f_c = \frac{k_c}{2\pi\sqrt{\mu\varepsilon}} = \frac{1}{2\pi\sqrt{\mu\varepsilon}}\sqrt{\left(\frac{m\pi}{a}\right)^2 + \left(\frac{n\pi}{b}\right)^2} \tag{2.2-17}$$

It is evident that with the lower mode number, the cutoff frequency is reduced. At frequencies $f > f_c$, the propagation constant is purely imaginary and is called phase constant β. In this case, in terms of the cutoff frequency it may be written by

$$\beta = 2\pi f\sqrt{\mu\varepsilon}\sqrt{1-\left(\frac{f_c}{f}\right)^2} \tag{2.2-18}$$

Below the cutoff frequencies ($f < f_c$), modes attenuate in the z-direction. At the cutoff frequency, modes neither propagate nor attenuate, but a standing wave is formed along the transverse coordinates, also known as transverse resonance. From (2.2-15) it is seen that neither m nor n can be set to zero, as this leads to a trivial solution with all zero components. Thus, the lowest-order TM mode is TM_{11}.

The guide wavelength is defined as the distance in the z-direction of propagation required for a phase change of 2π. Hence, for each propagating mode at operating frequency f_0

$$\lambda_g = \frac{2\pi}{\beta} = \frac{\lambda_0}{\sqrt{1-\left(\frac{f_c}{f}\right)^2}} \tag{2.2-19}$$

where λ_0 is the free space wavelength. The guide wavelength is longer than the length of the wave propagating in free space at the same frequency.

The electromagnetic field transverse components for a propagating mode now can be obtained, using (2.2-15) and substituting γ in equations (2.2-10), for TM modes ($H_z = 0$) as

$$E_x = -\frac{j\beta}{k_c^2}\left(\frac{m\pi}{a}\right)E_0 \cdot \cos\left(\frac{m\pi x}{a}\right)\cdot \sin\left(\frac{n\pi y}{b}\right)\cdot e^{-j\beta z} \tag{2.2-20a}$$

$$E_y = -\frac{j\beta}{k_c^2}\left(\frac{n\pi}{b}\right)E_0 \cdot \sin\left(\frac{m\pi x}{a}\right)\cdot \cos\left(\frac{n\pi y}{b}\right)\cdot e^{-j\beta z} \tag{2.2-20b}$$

$$E_Z = E_0 \cdot \sin\left(\frac{m\pi x}{a}\right)\cdot \sin\left(\frac{n\pi y}{b}\right)\cdot e^{-j\beta z} \tag{2.2-20c}$$

$$H_x = \frac{j\omega\varepsilon}{k_c^2}\left(\frac{n\pi}{b}\right)E_0 \cdot \sin\left(\frac{m\pi x}{a}\right)\cdot \cos\left(\frac{n\pi y}{b}\right)\cdot e^{-j\beta z} \tag{2.2-20d}$$

$$H_y = -\frac{j\omega\varepsilon}{k_c^2}\left(\frac{m\pi}{a}\right)E_0 \cdot \cos\left(\frac{m\pi x}{a}\right)\cdot \sin\left(\frac{n\pi y}{b}\right)\cdot e^{-j\beta z} \tag{2.2-20e}$$

From the transverse field components, the wave impedance for the TM modes can be found. It is evident from (2.2-20) that

$$\frac{E_x}{H_y} = -\frac{E_y}{H_x} = \frac{\beta}{\omega\varepsilon} \tag{2.2-21}$$

The obtained quantity is referred to as the wave impedance of the TM mode:

$$Z_{TM} = \frac{\beta}{\omega\varepsilon} = \eta\sqrt{1-\left(\frac{f_c}{f}\right)^2} \tag{2.2-22}$$

where $\eta = \sqrt{\frac{\mu}{\varepsilon}}$ is the intrinsic wave impedance of a plane wave propagating in an unbounded medium of constitutive parameters μ and ε.

The wave impedance is approaching the intrinsic impedance of the dielectric at infinite frequency and becomes imaginary (reactive) for non-propagating modes. Thus, below the cutoff frequency, where the wave impedance is imaginary, the wave is not capable of producing the average power transfer. At $f = f_c$, wave impedance equals zero and the waveguide is effectively shorted.

The wave impedance concept provides relation between electric and magnetic fields in vector form [2-7]:

$$\vec{H} = \frac{\vec{z} \times \vec{E}_t}{Z_{TM}} \tag{2.2-23}$$

where $\vec{z}$ is the unit vector in the *z*-direction.

For TE modes propagating in the rectangular waveguide, E_z is equal to zero and H_z is finite; solutions for all the transverse components can be obtained in a similar way as for TM modes. The general expression for H_z after separation of variables in this case is given by

$$H_Z = [A\sin(k_x x) + B\cos(k_x x)] \cdot [C\sin(k_y y) + D\cos(k_y y)] \cdot e^{-\gamma z} \qquad (2.2\text{-}24)$$

Applying the boundary conditions on the metallic walls of the waveguide so that the transverse components of the electric field equal zero, H_z can be defined as

$$H_Z = H_0 \cdot \cos\left(\frac{m\pi x}{a}\right) \cdot \cos\left(\frac{n\pi y}{b}\right) \cdot e^{-\gamma z} \qquad (2.2\text{-}25)$$

where H_0 is an arbitrary amplitude of the magnetic field.

The field components for propagating TE modes (E_z = 0, $\gamma = j\beta$), consequently, can be written as

$$E_x = \frac{j\omega\mu}{k_c^2}\left(\frac{n\pi}{b}\right) H_0 \cdot \cos\left(\frac{m\pi x}{a}\right) \cdot \sin\left(\frac{n\pi y}{b}\right) \cdot e^{-j\beta z} \qquad (2.2\text{-}26a)$$

$$E_y = -\frac{j\omega\mu}{k_c^2}\left(\frac{m\pi}{a}\right) H_0 \cdot \sin\left(\frac{m\pi x}{a}\right) \cdot \cos\left(\frac{n\pi y}{b}\right) \cdot e^{-j\beta z} \qquad (2.2\text{-}26b)$$

$$H_x = \frac{j\beta}{k_c^2}\left(\frac{m\pi}{a}\right) H_0 \cdot \sin\left(\frac{m\pi x}{a}\right) \cdot \cos\left(\frac{n\pi y}{b}\right) \cdot e^{-j\beta z} \qquad (2.2\text{-}26c)$$

$$H_y = \frac{j\beta}{k_c^2}\left(\frac{n\pi}{b}\right) H_0 \cdot \cos\left(\frac{m\pi x}{a}\right) \cdot \sin\left(\frac{n\pi y}{b}\right) \cdot e^{-j\beta z} \qquad (2.2\text{-}26d)$$

$$H_Z = H_0 \cdot \cos\left(\frac{m\pi x}{a}\right) \cdot \cos\left(\frac{n\pi y}{b}\right) \cdot e^{-j\beta z} \qquad (2.2\text{-}26e)$$

In order to illustrate the obtained expressions (2.2-26), a simulated distribution of electric and magnetic fields for TE_{10} mode in a rectangular waveguide is presented in Figure 2-2.

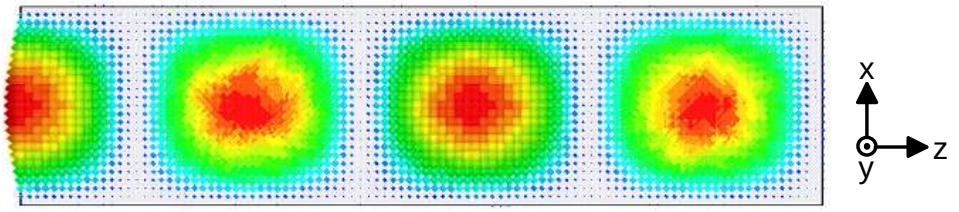

(a)

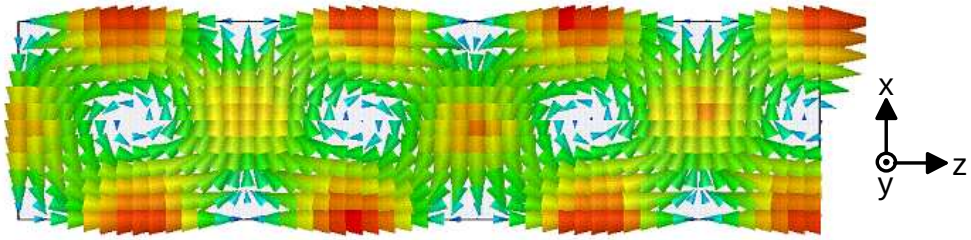

(b)

Figure 2-2: Field distribution for mode TE_{10} in a rectangular waveguide: (a) electric field; (b) magnetic field.

Either *m* or *n* can be equal to zero at once in (2.2-26) but not both. Therefore, taking into account that $a > b$, the lowest cutoff wave mode is the TE_{10} mode. For this mode, the cutoff frequency becomes

$$f_c = \frac{1}{2\pi\sqrt{\mu\varepsilon}}\sqrt{\left(\frac{\pi}{a}\right)^2} = \frac{v}{2a} \tag{2.2-27}$$

where $v = \frac{1}{\sqrt{\mu\varepsilon}}$ is the velocity of light in the dielectric medium, and since $v = \lambda f$, then $\lambda_c = 2a$. Typical frequency response of a rectangular waveguide, which reveals the cutoff frequency at about 30 GHz is shown in Figure 2-3.

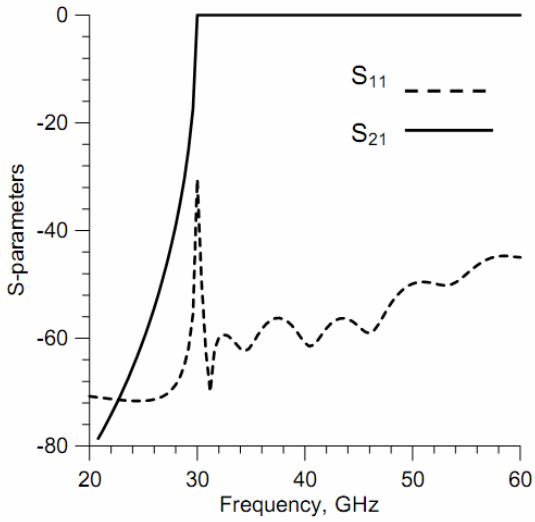

Figure 2-3: Typical frequency response of a rectangular waveguide.

Thus, broad inner dimension (a) of the waveguide with a propagating TE_{10} mode is equal to half the free-space wavelength at the cutoff frequency. Some examples of configurations of the electromagnetic field in a rectangular waveguide and different types of propagating waves are illustrated in [2-7].

The wave impedance for the TE_{10} mode is given by

$$Z_{TE} = \frac{\omega\mu}{\beta} = \frac{\eta}{\sqrt{1-\left(\frac{f_c}{f}\right)^2}} \tag{2.2-28}$$

The corresponding relation between electric and magnetic fields in vector form can be written as

$$\vec{E} = -Z_{TE} \cdot (\vec{z} \times \vec{H}_t) \tag{2.2-29}$$

where $\vec{z}$ is the unit vector in the z-direction.

For both types of the wave modes, the power transfer along the waveguide below the cutoff frequency is zero if the conducting surfaces of the guide are perfect. Above the cutoff, for the propagating modes, power per unit of area transferred by the i^{th} mode along the longitudinal direction of the waveguide is obtained by integrating the *z*-component of the Poynting vector over the cross-section of the waveguide:

$$P^i = \mathrm{Re}\left(\vec{E}_t^i \times \vec{H}_t^i \cdot \vec{z}\right) \tag{2.2-30}$$

where $\vec{E}_t$ and $\vec{H}_t$ are vectors of electric and magnetic field in terms of the transverse *x* and *y* coordinates.

2.3. Substrate Integrated Waveguides

Classical waveguide theory can still be used in order to meet the modern requirements of component parts for communication systems. Rectangular waveguide filters are well-known to be of highly-rated performance due to low losses and high power handling; however, their difficulty in integration and high cost makes them improbable for utilization in low-cost high volume applications. This can be solved by implementing design techniques where rectangular waveguide is integrated with planar circuits on the same substrate. Moreover, introduction of a dielectric substrate results in significant size reduction without considerably degrading its performance.

2.3.1. Conventional Substrate Integrated Waveguides

Design technique, where a rectangular waveguide is integrated with other planar circuits on the same substrate using the microstrip-integrated-circuit (MIC) technology, is known as substrate integrated waveguide (SIW) technology. This approach allows overcoming of the major difficulties of standard rectangular waveguides. SIW structure preserves the guided wave properties of the corresponding conventional rectangular waveguide with certain equivalent width, which allows using the well-developed conventional waveguide techniques for design and analysis of these structures.

Configuration of a SIW, introduced by Deslandes and Wu in [2-8], is presented in Figure 2-4. The structure consists of a microstrip line, a microstrip-to-SIW transition, and a rectangular waveguide section, all integrated on a piece of a dielectric substrate. Generally, various configurations of the transition section are available for realization; in Figure 2-4 a taper transition is shown, which is designed in such a way that the microstrip input and output are 50 Ohm lines and the taper section provides matching by conversion of quasi-TEM mode propagating in microstrip line into the quasi-TE_{10} mode in rectangular waveguide [2-8]. Side walls of the rectangular waveguide section can be realized using arrays of metallic via-posts, metallized grooves, paste side walls or other techniques. Ground plane of the microstrip line becomes the bottom wall of the waveguide, while the tapered microstrip line provides the top one.

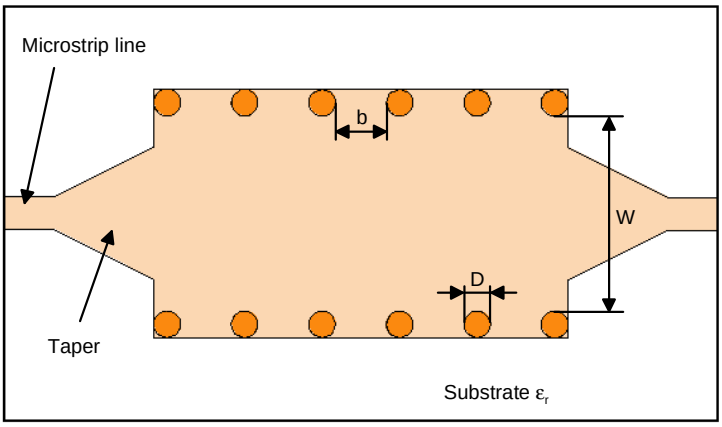

Figure 2-4: Configuration of a conventional SIW with its dimensions (top view).

Characteristics of the SIW have been studied experimentally in [2-9], where cutoff frequencies of the first and the second propagating modes of SIWs have been analyzed. Correspondence between the cutoff frequencies of the quasi-TE_{10} and quasi-TE_{20} modes of the SIW, with respect to diameter of metallized via-posts and spacing between them has been evaluated. Figure 2-5 presents the calculated results for the cutoff frequencies of the quasi-TE_{10} and quasi-TE_{20} modes of the SIW.

The obtained curves can be approximated by the following relations, obtained by the least square approach:

$$f_{cTE_{10}} = \frac{c}{2\sqrt{\varepsilon_r}} \cdot \left(W - \frac{D^2}{0.95 \cdot b} \right)^{-1} \tag{2.3-1}$$

$$f_{cTE_{20}} = \frac{c}{2\sqrt{\varepsilon_r}} \cdot \left(W - \frac{D^2}{1.1 \cdot b} - \frac{D^3}{6.6 \cdot b^2} \right)^{-1} \tag{2.3-2}$$

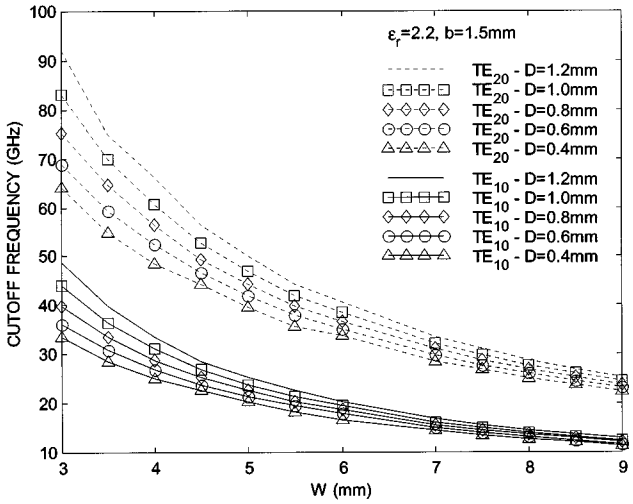

Figure 2-5: Cutoff frequencies of the quasi-TE_{10} and quasi-TE_{20} modes of the conventional SIW vs. width *W* for various via diameters *D* [2-9].

where *c* is the speed of light in free space and *b* is a distance between centers of adjacent metallic posts forming side walls of the SIW. Note that (2.3-1) and (2.3-2) do not depend on thickness of the waveguide. The thickness will only affect the *Q*-factor of SIW resonators, since it is directly proportional to resonator's volume. Inaccuracy of formula (2.3-1) appears to be within 5%. For (2.3-2), the inaccuracy better than +4%/–9% is possible. At the same time, it should be added that the presented approximations are valid for $b < \frac{\lambda_0 \cdot \sqrt{\varepsilon_r}}{2}$ and $b < 4D$.

Consequently, the SIWs are equivalent to conventional rectangular waveguides, and for the fundamental propagating mode they can be analyzed as rectangular waveguides just by using an effective width of the SIW, provided that the spacing between the side wall posts is sufficiently small. This can be derived from (2.3-1) as follows

$$W_{eff} = W - \frac{D^2}{0.95 \cdot b} \tag{2.3-3}$$

2.3.2. Folded Substrate Integrated Waveguides

The concept of folded rectangular waveguides has been proposed and studied theoretically in [2-10] for conventional waveguides, and substrate integrated folded waveguides (FSIW) based upon this approach have been developed in by Grigoropoulos and Young [2-11]. The new structures keep nearly the same propagation and cutoff characteristics as the conventional SIW, and allow saving of almost 50% of area at the cost of introducing additional dielectric layer. The most popular configurations of the FSIW employed in microwave and millimetre-wave circuits using a double-layer substrate can be obtained by single or double folding of a standard SIW along certain longitudinal axes. These configurations are presented in Figure 2-6. The electromagnetic field in the resultant structures undergoes an appropriate folding together with the certain metallic boundaries. Hence, for the FSIW with single folding, its symmetry plane appears in horizontal plane between two dielectric layers, while for the doubly-folded FSIW this retains vertical position. Generally, FSIW with arbitrary folding configurations may exist, which provide saving of more than 50% of area, but these require more substrate layers for implementation. Some multilayer technologies, for example LTCC, give the best fit for this approach.

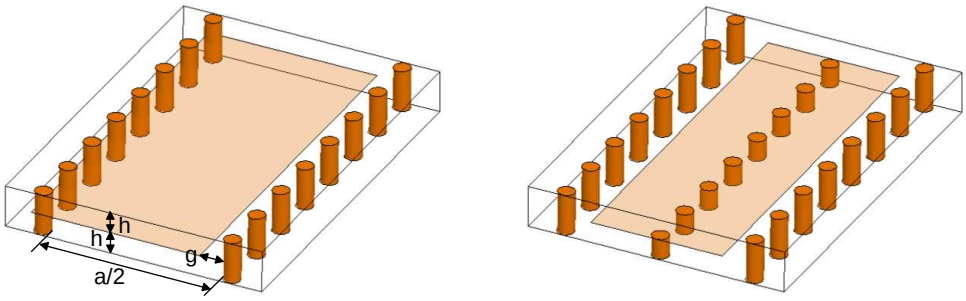

(a) (b)

Figure 2-6: Configurations of double-layer FSIW: (a) with single folding; (b) with double folding.

Transmission characteristics of the singly-folded FSIW, shown in Figure 2-6a, have been studied analytically and experimentally in [2-12]. The FSIW have been considered as a ridged waveguide with septum, represented by the metallization in symmetry plane, and

expressions for propagation constant β and cutoff frequency f_c for quasi-TE_{10} mode have been derived as follows:

$$\beta_{FSIW} = \sqrt{\omega^2 \mu\varepsilon - \left[\frac{2}{a}\cot^{-1}\left(\frac{\mu a h \omega^2}{2\pi} C\right)\right]^2} \tag{2.3-4}$$

$$f_c = \frac{1}{\pi a\sqrt{\mu\varepsilon}}\cot^{-1}\left(4 f_c h\sqrt{\mu\varepsilon}\ln\left[\frac{h}{c_f}\left(\frac{1}{g}-\frac{2}{a}\right)\right]\right) \tag{2.3-5}$$

where $c_f = 1.3$ and

$$C = \frac{4\varepsilon}{\pi}\ln\left[\frac{h\left(1-\frac{2g}{a}\right)}{c_f g}\right] \tag{2.3-6}$$

The formulae (2.3-4) – (2.3-6) provide good accuracy (no more than 2% error) for FSIW with substrate thicknesses and spaces between via posts less than $\lambda_c/20$, where λ_c is the cutoff wavelength of the FSIW.

2.3.3. Half-Mode Substrate Integrated Waveguides

Another modification of the SIW is a half-mode substrate integrated waveguide (HMSIW), which has been proposed by Hong *et al.* in [2-13]. Configuration of the HMSIW, which consists of half of a conventional SIW, is shown in Figure 2-7. Operation of the HMSIW is based on the following principle. For the quasi-TE_{10} mode of a conventional SIW, it is known that the symmetric plane along the direction of propagation (E-plane) is equivalent to a magnetic wall; therefore half of the SIW will keep the half field distribution unchanged if cutting plane is a magnetic wall. In fact, the open side aperture of the HMSIW is nearly equivalent to a perfect magnetic wall due to high ratio between width and height.

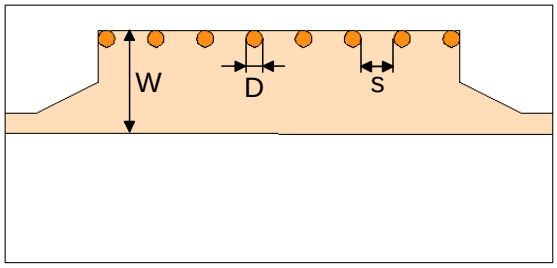

Figure 2-7: Configuration of a HMSIW.

Investigation of propagation properties of the HMSIW has been carried out in [2-14]. It has been shown that only quasi-$TE_{p\text{-}0.5,0}$ (p = 1, 2, …) modes can propagate in the HMSIW due to large width-to-height ratio of HMSIW and discrete arrangement of metallic vias. The dominant mode in the HMSIW is similar to half of the fundamental quasi-TE_{10} mode in the conventional SIW; however mode nomenclature with index 0.5 is used for HMSIW in order to emphasize the half-mode type of the SIW, where this mode propagates.

Despite that one of the narrow walls is removed in HMSIW, this type of SIW still retains the cutoff property in its frequency response. Cutoff frequency of the fundamental mode of the HMSIW can be calculated by

$$f_{c,TE_{0.5,0}} = \frac{c}{4\sqrt{\varepsilon_r} W_{eff,HMSIW}} \tag{2.3-7}$$

where $W_{eff,HMSIW}$ is an effective width of HMSIW, which can be approximated by the following set of empirical expressions

$$W_{eff,HMSIW} = W'_{eff,HMSIW} + \Delta W \tag{2.3-8}$$

$$W'_{eff,HMSIW} = W - 0.54\frac{d^2}{s} + 0.05\frac{d^2}{2W} \tag{2.3-9}$$

$$\frac{\Delta W}{h} = \left(0.05 + \frac{0.3}{\varepsilon_r}\right) \cdot \ln\left(0.79\frac{W'^2_{eff,HMSIW}}{h^3} + \frac{104W'_{eff,HMSIW} - 261}{h^2} + \frac{38}{h} + 2.77\right) \tag{2.3-10}$$

HMSIW allows achieving almost 50% more compact (in terms of occupied PCB area) SIW without addressing to multilayer solutions. At the same time, folded HMSIW using multilayer substrates, which have been recently reported [2-15] as a further development of this type of waveguides, is capable of further improving compactness of HMSIW.

2.4. Summary

In this chapter, an overview of conventional and substrate integrated waveguide structures has been presented.

In section 2.2 Maxwell's equations have been introduced and briefly considered. Next, these equations have been applied to solving the electromagnetic problem for conventional rectangular waveguides. Analytical expressions for electromagnetic fields of TE and TM modes, propagating in rectangular waveguides, have been derived. The main parameters (propagation constant, cutoff frequency, wave impedance) of the fundamental propagating mode TE_{10} have been obtained from analysis.

In section 2.3 the concept of substrate integrated waveguides has been overviewed. Conventional SIW has been introduced as a planar analogue of standard rectangular waveguide. Configurations of the half-mode and multilayer folded modifications of SIW, developed for the purpose of miniaturization, have been presented. The main characteristics and parameters of the SIW have been briefly reported.

2.5. References

[2-1] R. E. Collins, *Foundations for Microwave Engineering*, 2nd ed., IEEE Press, New York, 2001.

[2-2] M. Golio, *The RF and Microwave Handbook*, CRC Press, Boca Raton, 2001.

[2-3] K. Zhang and D. Li, *Electromagnetic Theory for Microwaves and Optoelectronics*, Springer, New York, 1998.

[2-4] M. F. Iskander, *Electromagnetic Fields and Waves*, Prentice-Hall, New Jersey, 1992.

[2-5] J. E. Parton, S. J. T. Owen, M. S. Raven, *Applied Electromagnetics*, 2nd ed., Macmillan, Hong Kong, 1986.

[2-6] I. C. Hunter, *Theory and Design of Microwave Filters*, IEE Press, London, 2001.

[2-7] S. Ramo, J. R. Whinnery, T. van Duzer, *Fields and Waves in Communication Electronics*, 3rd ed., Wiley, New York, 1994.

[2-8] D. Deslandes and K. Wu, "Integrated microstrip and rectangular waveguide in planar form," *IEEE Microw. Wireless Compon. Lett.*, vol. 11, no. 2, pp. 68-70, Feb. 2001.

[2-9] Y. Cassivi, L. Perregrini, P. Arcioni, M. Bressan, K. Wu, and G. Conciauro, "Dispersion characteristics of substrate integrated rectangular waveguide," in *IEEE Microwave Wireless Compon. Lett.*, vol. 12, no. 9, Sep. 2002, pp. 333-335.

[2-10] G. G. Mazumder and P. K. Saha, "Rectangular Waveguide with T-shaped Septa," *IEEE Trans. Microwave Theory Tech.*, vol. 35, no. 2, pp. 201-204, Feb. 1987.

[2-11] N. Grigoropoulos and P. R. Young, "Compact Folded Waveguides," *34th European Microw. Conf.*, vol. 2, pp. 973-976, 13 Oct. 2004.

[2-12] W. Che, G. Liang, D. Kuan and Y. L. Chow, "Analysis and Experiments of Compact Folded Substrate-Integrated Waveguide," *IEEE Trans. Microwave Theory Tech.*, vol. 56, no. 1, pp. 88-93, Jan. 2008.

[2-13] W. Hong, B. Liu, Y. Q. Wang, Q. H. Lai, and K. Wu, "Half mode substrate integrated waveguide: A new guided wave structure for microwave and millimeter

wave application," in *Proc. Joint 31st Int. Infrared Millimeter Wave Conf./14th Int. Terahertz Electron. Conf.*, Shanghai, China, Sep. 2006, pp. 18–22.

[2-14] L. Qinghua, C. Fumeaux, W. Hong and R. Vahldieck, "Characterization of the Propagation Properties of the Half-Mode Substrate Integrated Waveguide," *IEEE Trans. Microwave Theory Tech.*, vol. 57, no. 8, pp. 1996-2004, Aug. 2009.

[2-15] G. H. Zhai, W. Hong, K. Wu, J. X. Chen, P. Chen, J. Wei and H. J. Tang, "Folded Half Mode Substrate Integrated Waveguide 3 dB Coupler," *IEEE Microw. Wireless Compon. Lett.*, vol. 18, no. 8, pp. 512-514, Aug. 2008.

CHAPTER 3

DESIGN OF BANDPASS FILTERS

3.1. Introduction

Filters are key components of modern communication systems, which provide frequency band separation. By passbands, the filters can be classified into five types: lowpass, highpass, bandpass, bandstop and multiband. Filter design is a complex engineering problem, which requires a well developed methodology. Generally, filter design procedure begins from a specification, and contains the following several steps:

- approximation of the transfer function;
- synthesis of the filter prototype;
- scaling and conversion;
- physical implementation.

In this chapter we will be concerned with the available solutions for the first three steps of the filter design procedure. An overview of the transfer function approximation techniques will be presented in Section 3.2. Section 3.3 describes the filter prototype synthesis techniques for direct-coupled and cross-coupled filters. Coupling matrices synthesis techniques are considered. Several different approaches for the realization of transmission zeros in stopband are considered, together with design guidelines. In Section 3.4, the frequency mapping procedure required for transformation of the lowpass prototype is presented. Finally, Section 3.5 briefly describes the filter implementation techniques, together with the main ideas of modern optimization methods for filter design.

3.2. Transfer Function Approximation

The design of a filter usually starts with the determination of the transfer function which satisfies a given filter specification. Since the physical processes in electrical circuits can be represented as integrals and derivatives of currents and voltages, it is convenient to use complex variables for analysis of the circuits with harmonic excitations in frequency domain, and the transfer function can be specified mathematically as a ratio of two polynomials of complex frequency $s = \sigma + j\omega$. The analytical expression of the transfer function provides an interface between the initial specification and a lowpass filter prototype with its cutoff frequency normalized to unity. In this section we will briefly outline the types of polynomials commonly used for approximation of filter's frequency responses.

3.2.1. Power Transfer Function and Characteristic Polynomials

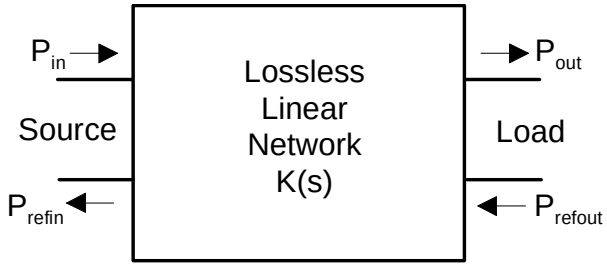

Figure 3-1: Doubly terminated lossless linear network.

Figure 3-1 illustrates a doubly terminated lossless transmission network which can represent a lossless bandpass filter. Assume that P_{in} is the input power to be transmitted through the circuit, while P_{out} is the output power available at the load. Since in passive circuits P_{out} can not exceed P_{in}, it is convenient to denote, that:

$$\frac{P_{in}}{P_{out}} = 1 + \left|K(s)\right|^2_{s=j\omega}, \tag{3.2-1}$$

where $K(s)$ is a rational function in s with real coefficients. On the other hand, the inverted power ratio from (3.2-1) is a squared magnitude of the transmission coefficient, known in transmission line theory as scattering parameter $S_{21}(s)$:

$$\left|S_{21}(s)\right|^2_{s=j\omega} = \frac{1}{1+\left|K(s)\right|^2_{s=j\omega}} \tag{3.2-2}$$

Reflected power is characterized by the reflection coefficient, or scattering parameter $S_{11}(s)$, which is related (for lossless networks) to $S_{21}(s)$ through:

$$\left|S_{11}(s)\right|^2 + \left|S_{21}(s)\right|^2 = 1 \tag{3.2-3}$$

It can be shown that for linear, time-invariant networks $S_{11}(s)$ can be represented as a ratio [3-1]:

$$S_{11}(s) = \frac{F(s)}{E(s)} \tag{3.2-4}$$

Thus, taking into account (3.2-3), for $s = j\omega$ it is correct that:

$$S_{21}(s) = \frac{P(s)}{\varepsilon \cdot E(s)} \tag{3.2-5}$$

$$P(s)\cdot P(-s) = E(s)\cdot E(-s) - \varepsilon^2 \cdot F(s)\cdot F(-s) \tag{3.2-6}$$

Polynomials $E(s)$, $F(s)$ and $P(s)$ are referred to as characteristic polynomials; determination of their coefficients from the given specification poses the approximation problem. Function $K(s)$ is known as the characteristic function, which can be derived from the characteristic polynomials using the following expression:

$$K(s) = \varepsilon \frac{F(s)}{P(s)} \tag{3.2-7}$$

In (3.2-7) the ripple constant ε is employed in order to normalize the maximum amplitude of the filter in passband. In synthesis procedure both polynomials are normalized so that their highest coefficients are unity and the resultant constant factor is absorbed in the ripple constant.

Generally, various characteristic functions are available for approximation; however several classical functions are traditionally noted. These are Butterworth, or maximally flat; Chebyshev and inverse Chebyshev; Cauer, or elliptic; and their modifications. Properties and features of these characteristic functions are discussed in Sections 3.2.2-3.2.5.

3.2.2. Butterworth Approximation

Butterworth, or maximally flat, approximation is the simplest to an ideal lowpass filter. This is an all-pole filter function which shows maximal possible flatness of the insertion loss curve in origin. The approximation is defined by:

$$K(\omega) = \omega^n , \tag{3.2-8}$$

where n is the degree of the prototype network. This suggests that P(s) = 1 and $F(s) = s^n$. S-parameters of the filter prototype are determined as:

$$\left|S_{21}(j\omega)\right|^2 = \frac{1}{1+\omega^{2n}} \tag{3.2-9}$$

$$\left|S_{11}(j\omega)\right|^2 = \frac{\omega^{2n}}{1+\omega^{2n}} \tag{3.2-10}$$

Consequently, the unknown coefficients of the polynomial $E(s)$ can be obtained from [3-2]:

$$s_k = \begin{cases} \exp\left[\frac{j\pi}{2n}(2k-1)\right], n = 2m \\ \exp\left(\frac{j\pi k}{2}\right), n = 2m+1 \end{cases} , \tag{3.2-11}$$

where k = 1, 2, …, 2n.

The calculated maximally flat prototype transmission characteristics corresponding to different circuit orders are illustrated in Figure 3-2.

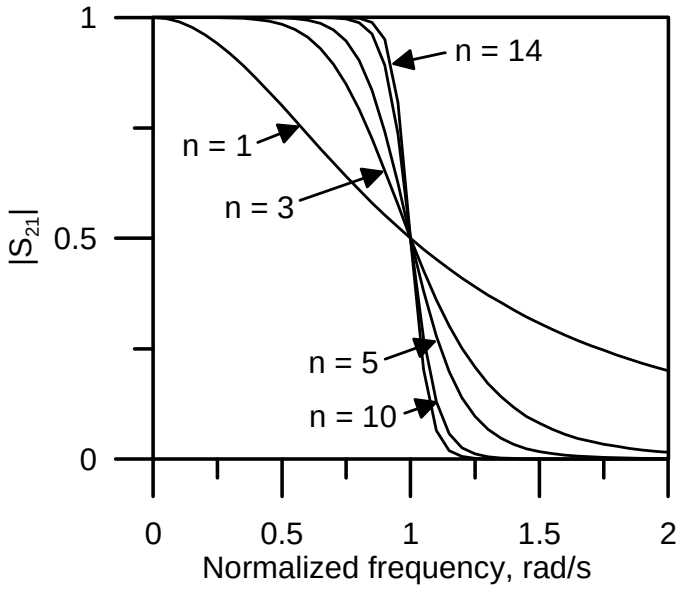

Figure 3-2: Maximally flat filter responses for various filter orders *n*.

3.2.3. Chebyshev Approximation

Chebyshev approximation provides sharper slope for lower filter order n, in comparison with the maximally flat approximation, but introduces equal ripples in passband [3-2, 3-3]. Chebyshev characteristic function is defined as:

$$K(\omega) = \varepsilon \cdot T_n(\omega), \tag{3.2-12}$$

where $T_n(\omega)$ is a Chebyshev polynomial of degree n. Thus, $P(s) = 1$, $F(s) = T_n(s/j)$, and expressions for S-parameters yield:

$$\left|S_{21}(j\omega)\right|^2 = \frac{1}{1+\varepsilon^2 T_n^2(\omega)}, \tag{3.2-13}$$

$$\left|S_{11}(j\omega)\right|^2 = \frac{\varepsilon^2 T_n^2(\omega)}{1+\varepsilon^2 T_n^2(\omega)}. \tag{3.2-14}$$

Chebyshev polynomials can be defined by the following recursion relationship:

$$T_{n+1}(x) = 2xT_n(x) - T_{n-1}(x), \tag{3.2-15}$$

where $T_0(x) = 1$ and $T_1(x) = x$. Alternatively, a trigonometric expression can be used:

$$T_n(x) = \cos(n \cdot \arccos x). \tag{3.2-16}$$

The characteristic polynomial $E(s)$ can be derived as a product of the left half-plane roots (i.e. with $\sigma_k < 0$) $s_k = \sigma_k + j\omega_k$, where:

$$\sigma_k = \pm \sinh\left(\frac{1}{n}\sinh^{-1}\frac{1}{\varepsilon}\right)\sin\frac{\pi}{2}\frac{2k-1}{n}, \tag{3.2-17a}$$

$$\omega_k = \cosh\left(\frac{1}{n}\sinh^{-1}\frac{1}{\varepsilon}\right)\cos\frac{\pi}{2}\frac{2k-1}{n}, \tag{3.2-17b}$$

where $k = 1, 2, \ldots, 2n$.

Typical frequency response of the Chebyshev filter prototype is illustrated in Figure 3-3.

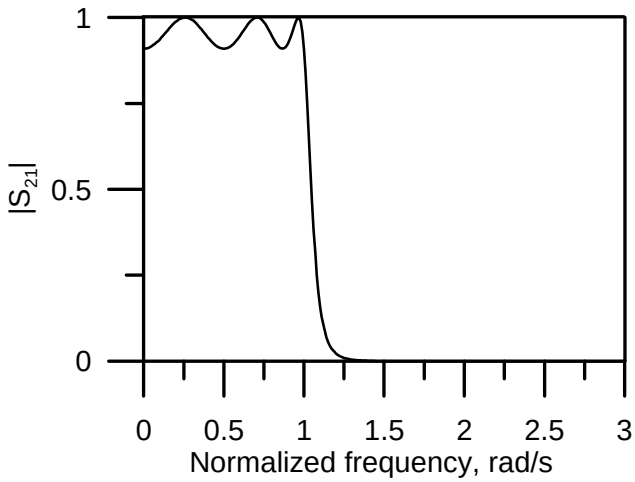

Figure 3-3: Lowpass prototype filter frequency response of Chebyshev type.

3.2.4. Generalized Chebyshev Approximation

Generalized Chebyshev (or pseudo-elliptic) approximation makes possible the realization of the filters with equiripple insertion loss in passband and arbitrary placed transmission zeros in stopband. This enables synthesis of highly selective filters with sharp slopes and asymmetrical frequency responses required for certain applications, for example, base station transmit filters. The location of the transmission zeros is not restricted to being at real frequencies only, and the coefficient of the characteristic polynomials generally become complex values.

The generalized Chebyshev characteristic function is defined as

$$K(\omega) = \varepsilon \cdot C_N(\omega) \tag{3.2-18}$$

where

$$C_N(\omega) = \cosh\left(\sum_{i=1}^{N} \cosh^{-1}(x_i) \right) \tag{3.2-19}$$

$$x_i = \frac{\omega - 1/\omega_{TZi}}{1 - \omega/\omega_{TZi}} \tag{3.2-20}$$

Here, ω is the angular frequency variable and ω_{TZi} is the position of the i^{th} transmission zero to be realized. Consequently, the transmission coefficient is expressed as follows [3-2]:

$$\left|S_{21}(\omega)\right|^2 = \frac{1}{1 + \varepsilon^2 C_N^2(\omega)} \tag{3.2-21}$$

Taking into account the equation (3.2-7), the filtering function $C_N(\omega)$ can be rewritten as a ratio of two polynomials:

$$C_N(\omega) = \varepsilon \frac{F_N(\omega)}{P_N(\omega)}, \tag{3.2-22}$$

with the denominator directly composed from the transmission zeros

$$P_N(\omega) = \prod_{i=1}^{N} (\omega - \omega_{TZi}) \tag{3.2-23}$$

while the numerator $F_N(\omega)$ is calculated using a recursive technique [3-4]:

$$F_N(\omega) = \frac{1}{2}\left[G_N(\omega) + G'_N(\omega)\right] \tag{3.2-24}$$

$$G_N(\omega) = \prod_{i=1}^{N}\left[\left(\omega - \frac{1}{\omega_{TZi}}\right) + \omega'\sqrt{\left(1 - \frac{1}{\omega_{TZi}^2}\right)}\right] \tag{3.2-25}$$

$$G'_N(\omega) = \prod_{i=1}^{N}\left[\left(\omega - \frac{1}{\omega_{TZi}}\right) - \omega'\sqrt{\left(1 - \frac{1}{\omega_{TZi}^2}\right)}\right] \tag{3.2-26}$$

where $\omega' = \sqrt{\omega^2 - 1}$.

In [3-5] an alternative recursive technique for obtaining the characteristic polynomials can be found.

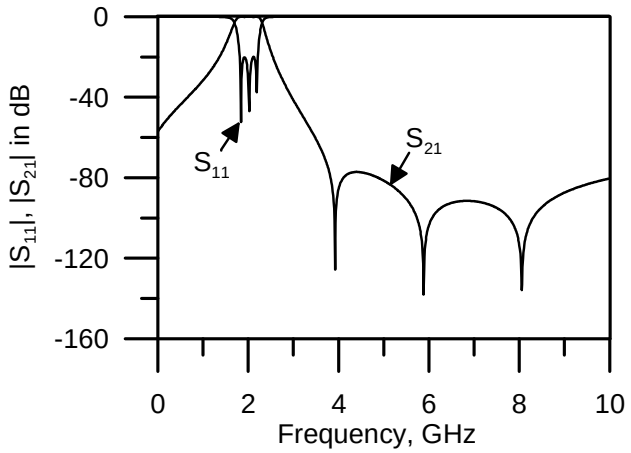

Figure 3-4: Generalized Chebyshev (or pseudo-elliptic) frequency response with three transmission zeros in upper stopband.

An example of a generalized Chebyshev filter prototype frequency response is shown in Figure 3-4. More examples of filters with generalized Chebyshev responses will be given in chapters 4 – 6 of this thesis.

3.2.5. Elliptic Approximation

An elliptic approximation provides a solution with equal ripple of the insertion loss in both passband and stopband. Due to this property it has the sharpest possible attenuation slope. The characteristic function used for this type of approximation is dependent on the Jacobian elliptic function sn(x) and the complete elliptic integral of the first kind K. The characteristic function can be expressed as:

$$K(s) = \varepsilon \cdot s \prod_{v=1}^{(n-1)/2} \frac{\left(s^2 + a_{2v}^2\right)}{\left(s^2 a_{2v}^2 + 1\right)}, \text{ for } n \text{ odd,} \tag{3.2-27}$$

$$K(s) = \varepsilon \prod_{v=1}^{n/2} \frac{\left(s^2 + a_{2v-1}^2\right)}{\left(s^2 a_{2v-1}^2 + 1\right)}, \text{ for } n \text{ even,} \tag{3.2-28}$$

where $a_v = \sqrt{\sin\theta} \cdot \mathrm{sn}\left[vK(\sin\theta)\right]/n$, v = 1, 2, …, n. Here $\sin\theta = \omega_p/\omega_s$; ω_p and ω_s are the cutoff frequencies which determine the rippled intervals in the passband and stopband respectively.

The unknown characteristic polynomial $E(s)$ can be composed of the left half-plane roots calculated from the following equation:

$$1 + \varepsilon^2 K^2(s) = 0 \tag{3.2-29}$$

Eventually, the transmission coefficient of elliptic filter with m zeros (ω_{Z1}… ω_{Zm}) and k poles (ω_{P1}… ω_{Pk}) can be presented in form

$$\left|S_{21}(\omega)\right|^2 = \frac{1}{1 + \dfrac{(\omega^2 - \omega_{P1}^2)...(\omega^2 - \omega_{Pk}^2)}{(\omega^2 - \omega_{Z1}^2)...(\omega^2 - \omega_{Zm}^2)}} \tag{3.2-30}$$

where the location of all the poles and zeros is prescribed by filter specifications and therefore there is no flexibility in comparison with the generalized Chebyshev type.

Comprehensive explanation of filter approximation using elliptic functions can be found in [3-6, 3-7].

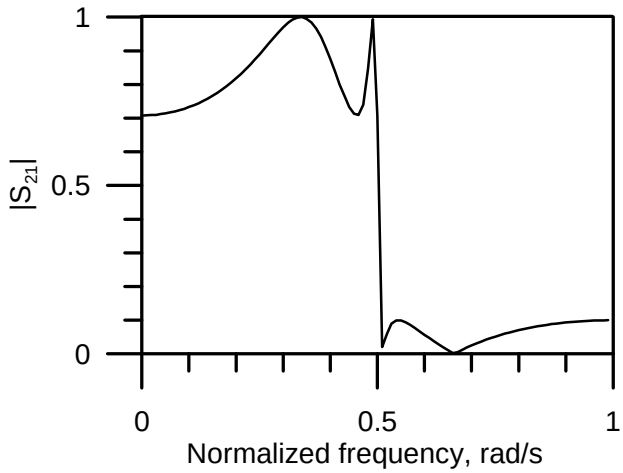

Figure 3-5: Elliptic frequency response.

A typical frequency response of the filter with elliptic approximation is presented in Figure 3-5.

3.3. Synthesis of Filter Prototypes

The next step of the filter design procedure is the synthesis of the equivalent network prototype, which is capable of reproducing the transfer function derived as a result of approximation process. The filter prototype acts as an interface between an abstract filtering function and a structure to be realized. The equivalent circuit should model the electrical performance of the real construction that will implement the filter, so that dimensions of components can be obtained from element values of the prototype. Usually, the normalized lowpass filter prototypes are chosen as equivalent networks, which can further be converted into bandpass, bandstop, or high-pass filter prototypes by applying of the frequency transformation (or frequency mapping) procedure (see Section 3.4). In this section, a brief overview of the most popular equivalent circuits and their elements is given, as well as the available methods for network synthesis are presented.

3.3.1. Elements of Filter Prototypes

Generally, filter prototype networks are synthesized of several standard basic elements, which model electrical characteristics of a corresponding real component. Variety of different circuit elements is currently known to be created for the purpose of convenient filter design in different technologies; however only those elements used below in this thesis will be considered in the current section. The most commonly used elements can be collected in the following list:

- resistors;
- inductors;
- capacitors;
- impedance/admittance inverters;
- frequency independent reactances.

The schematic circuit representations of the elements on the above list are given in Figure 3-6.

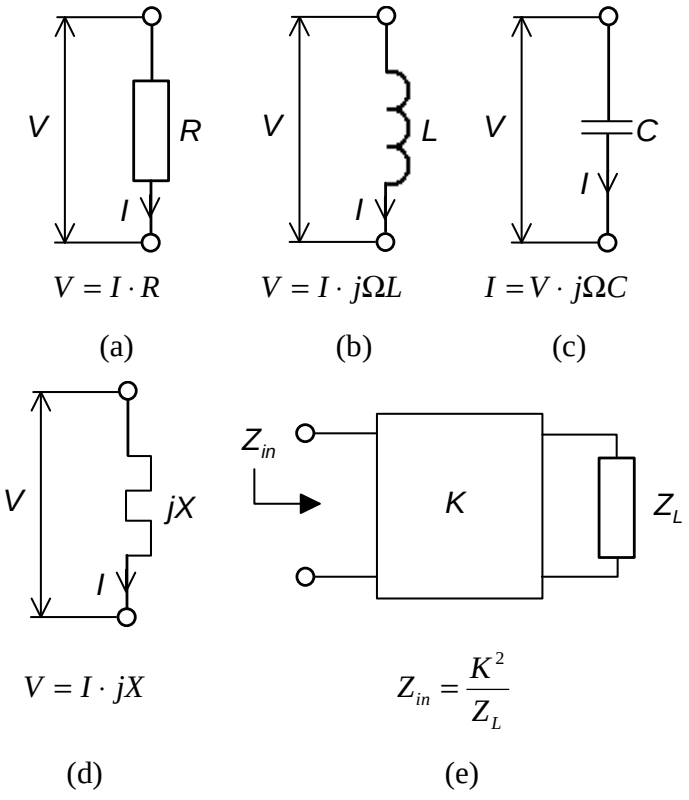

Figure 3-6: Schematic representations of the commonly used prototype elements: (a) resistor; (b) inductor; (c) capacitor; (d) FIR; (e) inverter.

Resistors are usual frequency independent resistive elements, playing the roles of termination loads in filter prototype circuits. Obviously, the resistors are used to account for losses in prototype networks; however, prototypes are considered as lossless circuits in order to simplify analysis of the filters. In advanced lossy filters resistors are deliberately included in prototypes to form the required predistortions [3-8].

Inductors and capacitors represent standard lossless reactances directly and inversely proportional to frequency, with electrical characteristics modeled by formulae presented in Figure 3-6.

Frequency invariant reactance (FIR) is a non-standard element introduced by Baum [3-9] to account for centre frequency shifts of the resonators in asynchronously tuned filters. This is an abstract lossless element with constant reactance throughout the entire frequency range,

which is widely applied in the recently developed concept of the filters with non-resonating nodes (NRN).

An inverter is a lossless, reciprocal, frequency independent, symmetrical two-port network which inverts and scales any impedance connected to its output port, i.e. the impedance seen from the input of the inverter is inversely proportional to the load impedance (see circuit and expression in Figure 3-6). Very often the inverter is defined by its transfer (or *ABCD*-) matrix, which is convenient for analysis of filter circuits using matrix methods:

$$\begin{bmatrix} A & B \\ C & D \end{bmatrix} = \begin{bmatrix} 0 & jK \\ \frac{j}{K} & 0 \end{bmatrix} \tag{3.3-1}$$

Impedance inverters are commonly used in filters based on distributed circuits such as microwave and millimeter wave filters which often can not be realized using lumped elements due to their very small size. It must be noted that impedance inverters with proportionality constant K are usually referred to as K-inverters, while admittance inverters with proportionality constant J are referred to as J-inverters. For admittance inverters loaded with admittance Y_L at output, the following equation is correct:

$$Y_{in} = \frac{J^2}{Y_L} \tag{3.3-2}$$

Consequently, a K-inverter can be considered as a J-inverter using the simple transformation:

$$J = \frac{1}{K} \tag{3.3-3}$$

An impedance/admittance inverter can be realized, for instance, as a discontinuity arranged between two sections of homogeneous transmission line, or as a quarter-wavelength section

of transmission line (known as quarter-wavelength transformer). More information about realization of impedance and admittance inverters can be found in [3-1, 3-2, 3-3].

3.3.2. Ladder Networks

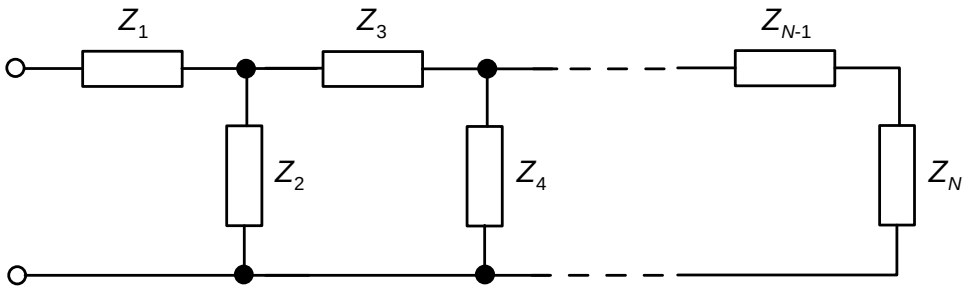

Figure 3-7: Ladder network.

One of the most commonly used circuits for the realization of rational functions in filter design is the ladder network. It is composed of shunt and series impedances in ladder configuration (shown in Figure 3-7). The element values of the prototype can be found from input impedance/admittance of the filter by employing standard analysis technique for ladder circuits [3-2]. Alternatively, for standard filtering functions (Butterworth, Chebyshev types), the element values can be found from tables or promptly computed based upon the main filter specifications.

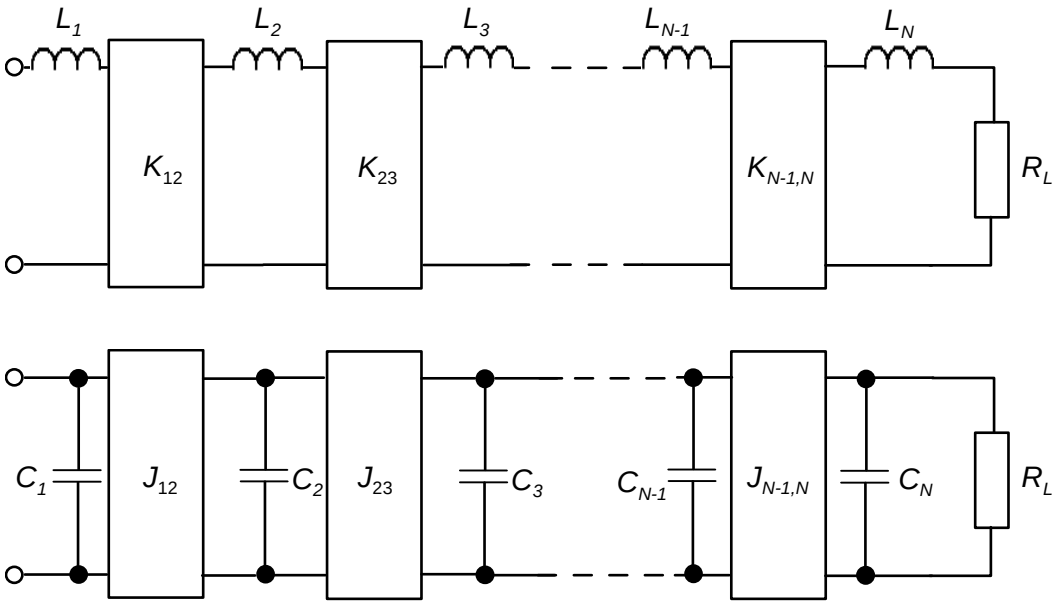

Figure 3-8: Lowpass filter prototype with impedance/admittance inverters.

As mentioned above, at micro- and millimeter waves distributed circuits are preferred rather than lumped elements for simplicity, and thus it is more practical to transform the ladder network into the circuit shown in Figure 3-8, where shunt and series elements are connected through impedance or admittance inverters.

Both types of circuits presented above are time invariant and belong to the class of linear, lossless and passive networks. In addition, the ladder circuits are minimum phase networks, where only one path for energy transmission between source and load is possible. Hence, the networks are capable of realizing frequency responses of Butterworth and Chebyshev types, without any transmission zeros revealed at real frequencies (also referred to as all-pole filters). The continued fraction expansion method applied to the expression of input impedance/admittance is usually used for synthesis of these types of networks [3-3].

For the prototypes of generalized Chebyshev and elliptic filters, the modified inverter-coupled ladder networks, including frequency invariant reactance elements are commonly used. Synthesis of these networks is carried out by employing extracted pole technique [3-2, 3-10]. This synthesis method for the generalized Chebyshev filters with non-resonating nodes will be further discussed in details in Chapter 5.

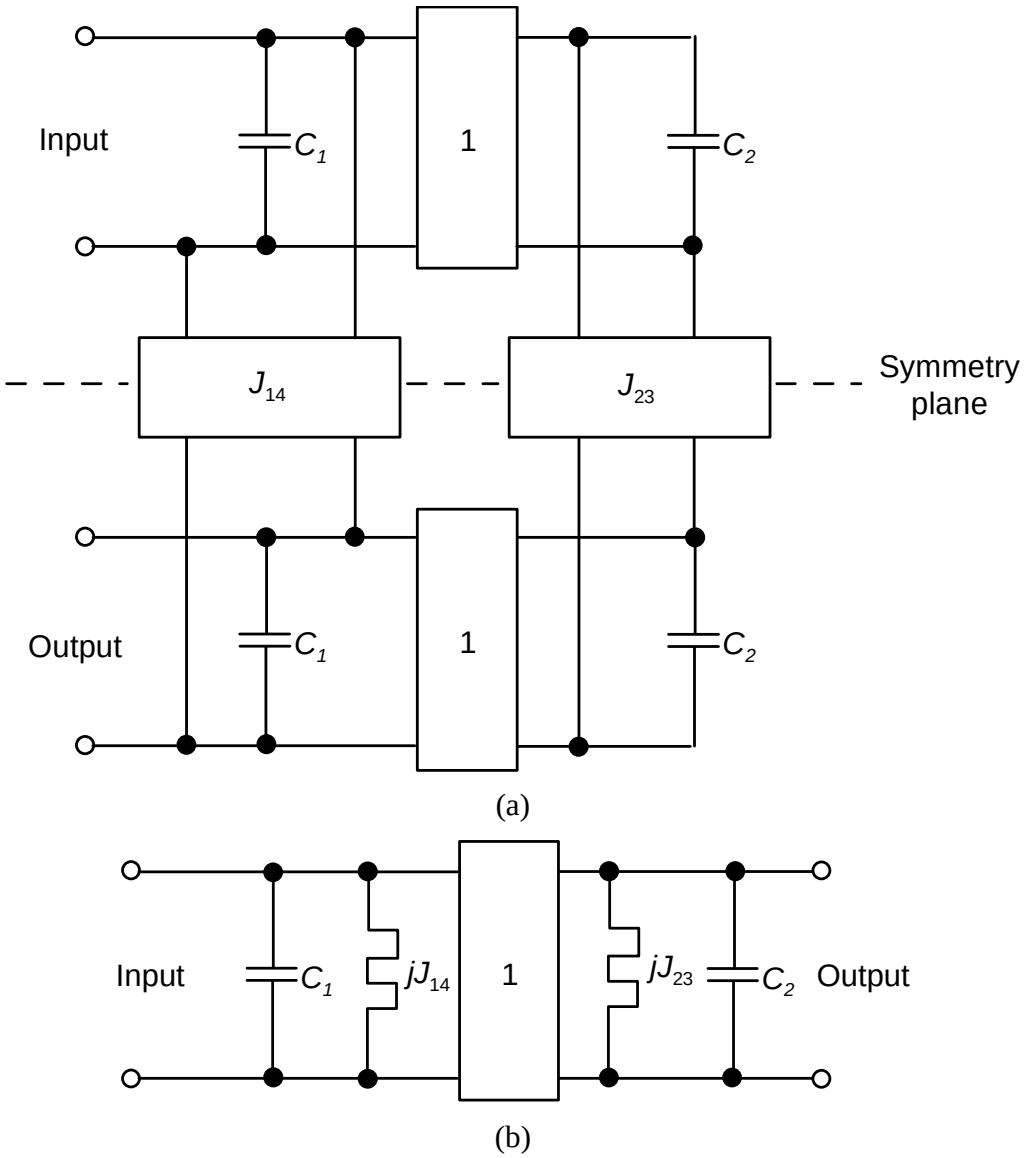

Figure 3-9: Ladder prototype network of 4th order elliptic filter with symmetric response: (a) cross-coupled circuit; (b) direct-coupled equivalent circuit.

An alternative technique of obtaining transmission zeros at finite frequencies is available using cross-coupled network topologies, where more than one path for the signal exists between source and load [3-11]. Transmission zeros are produced by interaction of signals which come to the load with different phase shifts; if the phase shifts at a certain frequency are opposite, then the signals cancel each other and transmission zero appears; alternatively, signals add up and no transmission zero reveals [3-12].

The simplest prototype of elliptic filter with symmetrically located transmission zeros can be realized as cross-coupled ladder network shown in Figure 3-9a. This type of filters can be synthesizes by employing even-odd-mode impedances/admittances technique [3-1, 3-2]. Extraction of the element values of the prototype can be significantly simplified by bisecting the circuit along its symmetry plane, which converts the initial cross-coupled ladder network into the simple inverter-coupled (direct-coupled) ladder circuit with frequency invariant susceptances shown in Figure 3-9b. Even and odd impedance/admittance of the prototype can be derived from the filtering function. More details on synthesis of ladder filter prototype networks can be found in [3-1, 3-2, 3-10].

3.3.3. Multiple Coupled Resonators Circuit Model

As a development of the symmetric cross-coupled network topology, the multiple coupled resonator bandpass prototype circuit has been introduced by Atia and Williams [3-11, 3-13] in 1970s. The proposed model, which consists of *N* resonators coupled by transformers, is shown in Figure 3-10a. Each resonator is represented by capacitor of 1 F in series with the self inductance of 1 H within each loop, so the resonant frequency of all the resonators is 1 rad/s. Generally, each loop couples to every other through mutual couplings between the inductors; all values of the couplings are normalized to a bandwidth of 1 rad/s. This circuit is limited to support filter prototypes with symmetric frequency responses only.

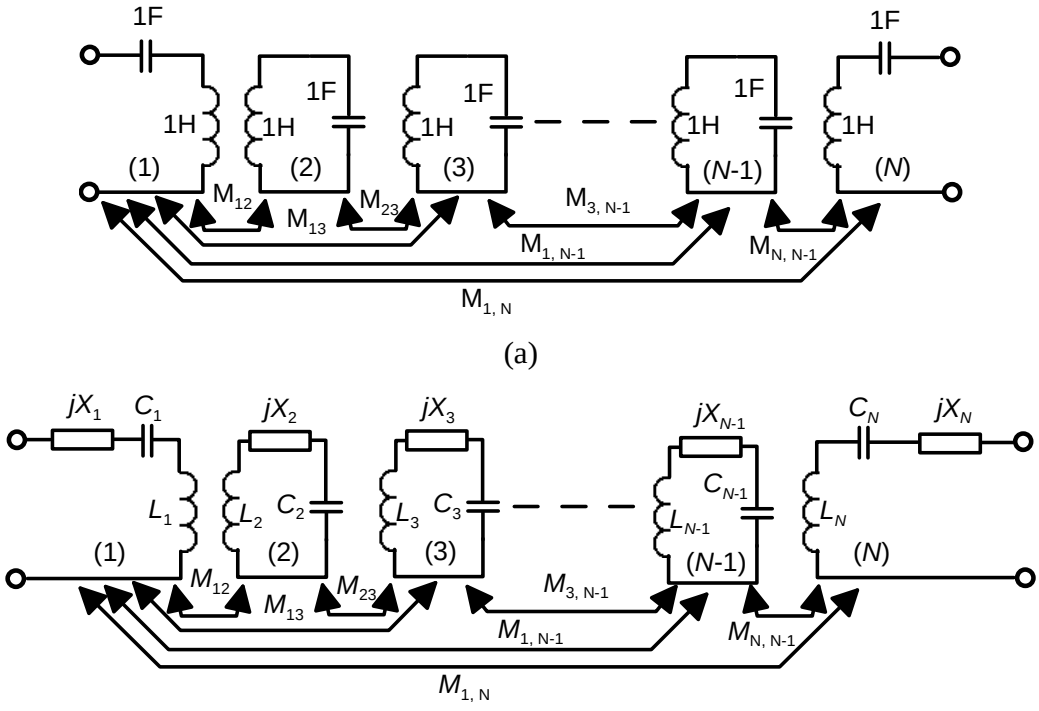

(a)

(b)

Figure 3-10: Models of the general coupled-resonator filter: (a) Atia-Williams [3-11]; (b) Cameron [3-10].

The above model has been further modified by Cameron [3-10]; frequency independent reactance elements have been inserted in each loop in series in order to account for resonant frequency shifts of individual resonators, and enable the circuit to represent asymmetric characteristics. The network with FIR elements is shown in Figure 3-10b.

The multiple coupled resonators filter model can also be represented as a lowpass prototype circuit. In this model, couplings assumed frequency invariant are replaced by the impedance inverters of the same values, while the resonators are replaced by series inductors. Consequently, the FIR elements of the loops become connected in series with inductors. The lowpass prototype model of the cross-coupled filter is shown in Figure 3-11.

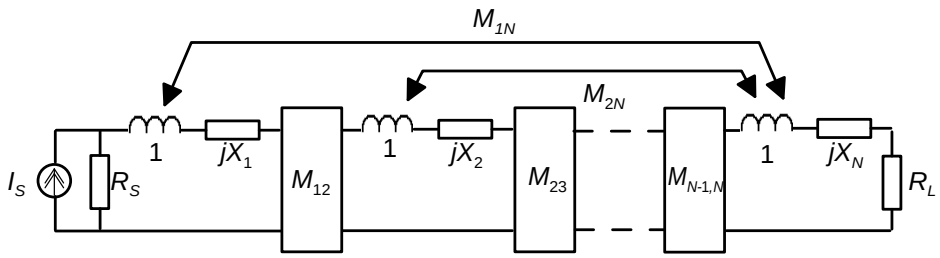

Figure 3-11: Lowpass prototype of the multiple-coupled resonators filter.

Frequency responses of the bandpass and lowpass prototypes are related through the bandpass-to-lowpass frequency transformation, which will be discussed in detail in Section 3.4.

3.3.3.1. Coupling Matrix Circuit Representation

Let us consider the circuit presented in Figure 3-10b, which operates between a voltage source generating E volts with an internal impedance of R_S and a load R_L. By applying the loop currents method (Kirchhoff's equations for each loop) leading to series of equations, the circuit can be represented with the following matrix equation:

$$E \cdot [1, 0, ..., 0]^t = [R + sI + jM] \cdot [i_1, i_2, ..., i_N]^t \tag{3.3-4}$$

where R is the $N \times N$ matrix, which contains the values of the source an load impedances in top left and bottom right corners with all the other entries equal to zero; I is the identity matrix; s is the complex frequency variable ($s = j\omega$); and M is the coupling matrix containing values of mutual couplings between all the resonators:

$$M = \begin{bmatrix} X_1 & M_{12} & M_{13} & \cdots & M_{1N} \\ M_{12} & X_2 & & & \\ M_{13} & & \ddots & & \\ \vdots & & & \ddots & M_{N-1,N} \\ M_{1N} & & & M_{N-1,N} & X_N \end{bmatrix} \tag{3.3-5}$$

Here, the entries of the main diagonal represent the values of the frequency independent reactance elements X_i, also referred to as self-couplings.

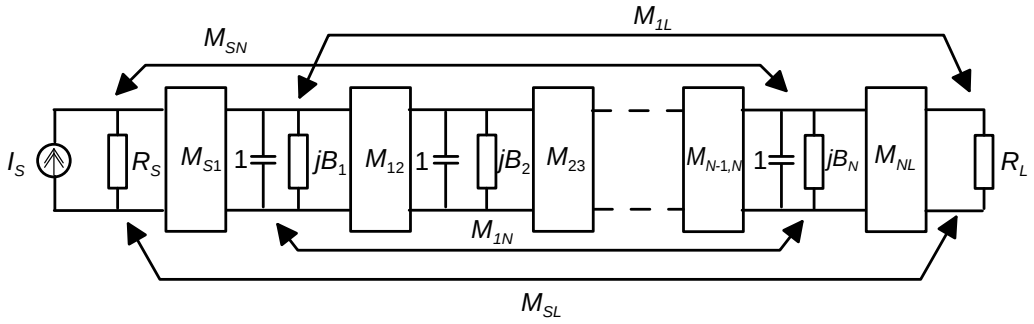

Figure 3-12: Lowpass prototype of the (N+2) cross-coupled filter.

Usually it is more convenient to normalize the source and load impedances to unity connecting them to the first/last resonators through a transformer, or through an inverter for lowpass prototypes. Consequently, in this case the coupling matrix becomes (N+2)×(N+2). Moreover, it is possible to generalize the model by adding couplings between source/load and each other resonator, as well as the direct coupling between source and load. Hence, the generalized lowpass prototype of a cross-coupled filter with direct coupling between input and output can be represented by the network shown in Figure 3-12. The corresponding coupling matrix for the prototype presented in Figure 3-12, takes the following form:

$$M = \begin{bmatrix} 0 & M_{S1} & M_{S2} & \cdots & M_{SL} \\ M_{S1} & B_1 & M_{12} & & \\ M_{S2} & M_{12} & \ddots & & \\ \vdots & & & \ddots & M_{NL} \\ M_{SL} & & & M_{NL} & 0 \end{bmatrix} \tag{3.3-6}$$

3.3.3.2. Direct Synthesis of the N×N Coupling Matrix

The problem of cross-coupled filter design lies in derivation of the coupling matrix *M*, which generates the transfer function able to satisfy the filter specification given in terms of the desired bandwidth, insertion loss, return loss, ripple constants, etc. The transfer function is set explicitly by means of characteristic polynomials discussed in Section 3.2.

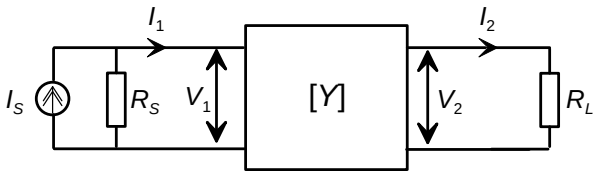

Figure 3-13: Representation of the N^{th} -order cross-coupled filter as a two-port network.

For the coupling matrix synthesis procedure, the prototype network from Figure 3-11 is considered as a two-port block, which operates between a current source of I_S amperes with internal impedance of R_S, and load resistance R_L (see Figure 3-13). The prototype network can be represented using the standard two-port admittance matrix *Y*, defined by equation:

$$\begin{bmatrix} i_1 \\ i_2 \end{bmatrix} = \begin{bmatrix} Y_{11} & Y_{12} \\ Y_{21} & Y_{22} \end{bmatrix} \times \begin{bmatrix} v_1 \\ v_2 \end{bmatrix} \tag{3.3-7}$$

Entries of the *Y*-matrix can be derived from the characteristic polynomials *P*(*s*), *F*(*s*) and *E*(*s*) through *ABCD*-matrix representation, or by employing the standard procedure [3-14], involving complex-even and complex-odd polynomials, to the expression for input impedance/admittance.

On the other hand, it can be shown that the elements of the *Y*-matrix can be written in terms of the $N \times N$ coupling matrix M to be determined [3-15], and the frequency variable $s = j\omega$ as follows:

$$Y_{11}(s) = j\left[-M - \omega I\right]_{11}^{-1} \tag{3.3-8}$$

$$Y_{22}(s) = j\left[-M - \omega I\right]_{NN}^{-1} \tag{3.3-9}$$

$$Y_{12}(s) = Y_{21}(s) = j\left[-M - \omega I\right]_{N1}^{-1} \tag{3.3-10}$$

The matrix M, real and symmetrical about its principal diagonal, can be decomposed using its eigenvalues $\lambda_i, i = \overline{1, N}$:

$$-M = T \cdot \Lambda \cdot T^t \tag{3.3-11}$$

where T – is an $N \times N$ matrix with rows of orthogonal vectors; T^t – is the transpose of T such that $T \cdot T^t = I$; Λ – is a diagonal matrix containing the eigenvalues $\lambda_i, i = \overline{1, N}$:

$$\Lambda = \begin{bmatrix} \lambda_1 & 0 & \cdots & 0 \\ 0 & \lambda_2 & & 0 \\ \vdots & & \ddots & \vdots \\ 0 & 0 & \cdots & \lambda_N \end{bmatrix} \tag{3.3-12}$$

Therefore, the entries of the admittance matrix can be rewritten as follows:

$$Y_{22}(s) = j\left[-T \cdot \Lambda \cdot T^t - \omega I\right]_{NN}^{-1} \tag{3.3-13}$$

$$Y_{21}(s) = j\left[-T \cdot \Lambda \cdot T^t - \omega I\right]_{N1}^{-1} \tag{3.3-14}$$

The solutions of the inverse eigenmatrix problems in equations (3.3-13) and (3.3-14) yield the following partial fraction expansions:

$$Y_{22}(s) = j\sum_{k=1}^{N} \frac{T_{Nk}^2}{\omega - \lambda_k} \tag{3.3-15}$$

$$Y_{21}(s) = j\sum_{k=1}^{N} \frac{T_{Nk}T_{1k}}{\omega - \lambda_k} \tag{3.3-16}$$

It is clear from (3.3-15) and (3.3-16) that the eigenvalues of the coupling matrix, multiplied by *j*, are equal to the roots of the denominator polynomial, common for admittances $Y_{12}(s)$ and $Y_{22}(s)$. On the other hand, the entries of the matrix *T* can be obtained from the residues of the partial fraction expansions of the *Y*-parameters:

$$Y_{22}(s) = j\sum_{k=1}^{N} \frac{r_{22k}}{\omega - \lambda_k} \tag{3.3-17}$$

$$Y_{21}(s) = j\sum_{k=1}^{N} \frac{r_{21k}}{\omega - \lambda_k} \tag{3.3-18}$$

Hence,

$$T_{Nk} = \sqrt{r_{22k}} \qquad \text{and} \qquad T_{1k} = \frac{r_{21k}}{\sqrt{r_{22k}}} \tag{3.3-19}$$

Generally, the terminating resistances are not normalized to unity; however the normalization can be performed by inserting inverters with values $M_{S1} = \sqrt{R_S}$ and $M_{NL} = \sqrt{R_L}$. These parameters can be obtained out of the known entries of the *T*-matrix:

$$M_{S1}^2 = R_S = \sum_{k=1}^{N} T_{1k}^2 \qquad \text{and} \qquad M_{NL}^2 = R_L = \sum_{k=1}^{N} T_{Nk}^2 \tag{3.3-20}$$

The rest of the rows of the *T*-matrix can be reconstructed by applying the Gram-Schmidt orthonormalization process [3-16].

3.3.3.3. Reduction of Coupling Matrix

The $N \times N$ coupling matrix obtained as a result of direct synthesis procedure generally contains all nonzero entries. Physically, this means that every resonator is coupled to each other, which is impossible or extremely difficult to implement by means of a practical circuit. In order to overcome this issue, similarity transformations (or rotations) are applied to the *M*-matrix for annihilation of the unwanted couplings until more convenient form is obtained [3-4]. This procedure preserves the eigenmodes and eigenvectors of the coupling matrix, which means that the transfer characteristics of the filter described by the new coupling matrix remain unchanged in comparison with the initial one. The last statement implies that the certain transfer characteristic may be realized by more than one unique coupling matrix.

Similarity transformation with a pivot [*i, j*] is defined as follows:

$$M_1 = R_1 \cdot M_0 \cdot R_1^t \tag{3.3-21}$$

where M_0 – is the initial coupling matrix; M_1 – transformed coupling matrix; R_1 – the $N \times N$ rotation matrix of the following format:

$$R_m = \begin{bmatrix} 1 & 0 & \cdots & 0 & 0 \\ 0 & \cos\theta_m & 0 & -\sin\theta_m & 0 \\ \vdots & 0 & 1 & 0 & \vdots \\ 0 & \sin\theta_m & 0 & \cos\theta_m & 0 \\ 0 & 0 & \cdots & 0 & 1 \end{bmatrix}, \tag{3.3-22}$$

where $R_{mii} = R_{mjj} = \cos\theta_m$ and $R_{mij} = -R_{mji} = \sin\theta_m$; θ_m – is the rotation angle. For example, the annihilation of a nonzero coupling element M_{ij} (as well as symmetric element M_{ji}) can be carried out by applying rotation with a pivot [*k, j*] with an angle $\theta = -\tan^{-1}\left(M_{kj} / M_{ki}\right)$. More equations for annihilation of specific elements of the coupling matrix are available in [3-10].

The reduction procedure consists of a sequence of similarity transformations which progressively annihilate the unwanted entries of the coupling matrix. Usually the sequences of rotations are applied to certain rows or columns of the matrix, since a single rotation with a pivot [*i*, *j*] affects rows and columns *i* and *j* only; in addition, it is important that zero entries in affected rows and columns remain zero after the transformation.

More information about physical interpretation of the similarity transformations can be found in [3-19]. Example of the coupling matrix derived by similarity transformations will be given further in Section 5.

3.3.3.4. Direct Synthesis of the (N+2)×(N+2) Coupling Matrix

The $(N + 2)\times(N + 2)$ coupling matrix is capable of representing the fully canonical filters, which may realize the maximum of N transmission zeros at finite frequencies for an N^{th}-order network. This can be achieved by introducing a direct coupling between source and load.

The synthesis of the $(N + 2)\times(N + 2)$ coupling matrix is carried out in two steps: first, the initial coupling matrix for a canonical transversal filter prototype is synthesized; then, the obtained transversal coupling matrix is converted to the desired configuration by means of a sequence of the similarity transformations [3-10, 3-17].

The canonical transversal filter prototype network, shown in Figure 3-14a, consists of N lowpass resonators (represented as a capacitor and a FIR connected in parallel), each coupled to source and load by inverters, while not coupled to each other. The equivalent circuit of each lowpass resonator with couplings is shown in Figure 3-14b. Direct coupling between source and load is represented by inverter M_{SL}.

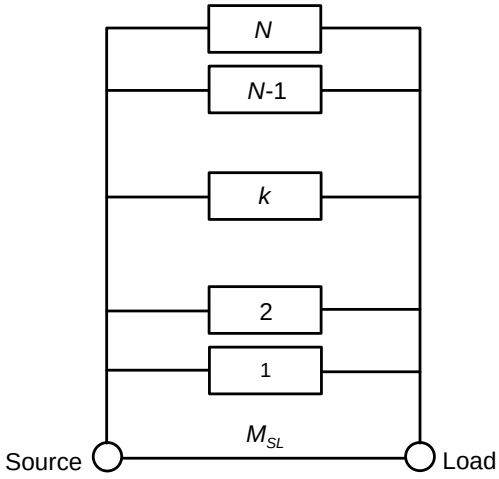

(a)

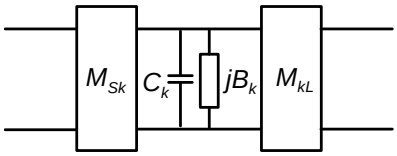

(b)

Figure 3-14: Canonical transversal array network: (a) N^{th}-order circuit with direct source-load coupling; (b) Representation of the k^{th} branch in the transversal array.

It can be easily proved that the admittance matrix Y of the N^{th}-order canonical transversal array network may be written as:

$$Y = j\begin{bmatrix} 0 & M_{SL} \\ M_{SL} & 0 \end{bmatrix} + \sum_{k=1}^{N} \frac{1}{sC_k + jB_k} \begin{bmatrix} M_{Sk}^2 & M_{Sk}M_{Lk} \\ M_{Sk}M_{Lk} & M_{Lk}^2 \end{bmatrix} \tag{3.3-23}$$

On the other hand, the entries of the admittance matrix Y are rational functions, thus these can be represented as partial fraction expansions using poles and residues:

$$Y = j\begin{bmatrix} 0 & K \\ K & 0 \end{bmatrix} + \sum_{k=1}^{N} \frac{1}{s - j\lambda_k} \begin{bmatrix} r_{11k} & r_{12k} \\ r_{21k} & r_{22k} \end{bmatrix} \tag{3.3-24}$$

The constant K is equal to zero for all cases except for the fully canonical. The constant should be extracted from the $Y_{21}(s)$ function, which numerator and denominator are of the same degree. K is evaluated as follows:

$$jK = Y_{21}(s = j\infty) \tag{3.3-25}$$

Consequently, the poles and residues for the equation (3.3-24) can be found from the new expression for the $Y_{21}(s)$:

$$Y'_{21}(s) = Y'_{21}(s) - jK \tag{3.3-26}$$

From comparison of equations (3.3-23) and (3.3-24) it can be concluded that the elements of the canonical transversal network can be straightforwardly relayed to the obtained poles and residues:

$$C_k = 1; \quad B_k = -\lambda_k; \quad M_{Lk} = \sqrt{r_{22k}}; \quad M_{Sk} = \frac{r_{21k}}{\sqrt{r_{22k}}} \tag{3.3-27}$$

The resultant $(N + 2)\times(N + 2)$ fully-canonical coupling matrix M for the transversal array is symmetric about the principal diagonal, and has the following structure:

$$M = \begin{bmatrix} 0 & M_{S1} & M_{S2} & \cdots & M_{Sk} & \cdots & M_{SN} & M_{SL} \\ M_{1S} & B_1 & 0 & & 0 & & 0 & M_{1L} \\ M_{2S} & 0 & B_2 & & 0 & & 0 & M_{2L} \\ \vdots & & & \ddots & & & & \vdots \\ M_{kS} & 0 & 0 & & B_k & & 0 & M_{kL} \\ \vdots & & & & & \ddots & & \vdots \\ M_{NS} & 0 & 0 & & 0 & & B_N & M_{NL} \\ M_{LS} & M_{L1} & M_{L2} & \cdots & M_{Lk} & \cdots & M_{LN} & 0 \end{bmatrix} \tag{3.3-28}$$

The unnecessary couplings between source/load and resonators can be further annihilated by applying the rotation procedure (see Section 3.3.3.3). The similarity transformations employed for the transversal coupling matrix lead to the appearance of nonzero couplings between the resonators and affect their resonant frequencies.

3.3.3.5. Coupling Matrix Synthesis by Optimization

The $(N + 2)\times(N + 2)$ coupling matrix can be synthesized by optimization. The idea of this technique is to determine the coupling matrix M, which generates the frequency response of the filter, which minimizes a cost function composed to account for the difference between the response generated by the coupling matrix and the ideal one [3-5, 3-18].

Standard Newton's optimization procedure begins from determination of the topology capable of reproducing the required number of transmission zeros in the frequency response; hence, the entries of the coupling matrix, which are responsible for interaction of the uncoupled resonators, are set to zero. All the other couplings are generally set to arbitrary but reasonable values. The frequency response generated by the initial matrix is evaluated, as well as the corresponding cost function and gradients. Then, the coupling matrix of the next iteration is composed on the basis of the calculated gradients. The procedure repeats until the cost function is minimized according to a certain criteria.

The optimization technique uses the lowpass coupled resonators model shown in Figure 3-12. Analysis of the model using the loop currents method yields the matrix equation:

$$\left(-jR+\Omega W+M\right)\cdot I = A\cdot I = -j\cdot E \tag{3.3-29}$$

where R is a $(N + 2)\times(N + 2)$ matrix with two unity entries R_{11} and $R_{N+2,\,N+2}$; W is a $(N + 2)\times(N + 2)$ identity matrix, where $W_{11} = W_{N+2,\,N+2} = 0$; Ω is the normalized frequency; I is the vector of loop currents; E is the excitation vector.

Transmission and reflection coefficients of the model can be calculated by

$$S_{21} = -2j \cdot A^{-1}_{N+2,1} \tag{3.3-30}$$

$$S_{11} = 1 + 2j \cdot A^{-1}_{1,1} \tag{3.3-31}$$

The cost function used for optimization is constructed based upon the notion that the filtering functions for the generalized Chebyshev filters are determined by the positions of its poles and zeros; also, the ripple constant should be taken into account. Consequently, the cost function is composed by the following expression:

$$\begin{aligned} CF = &\sum_{i=1}^{NZ} \left|S_{11}(\omega_{Zi})\right|^2 + \sum_{i=1}^{NP} \left|S_{21}(\omega_{Pi})\right|^2 + \\ &+ \left(\left| S_{11}(-1) - \frac{\varepsilon}{\sqrt{1+\varepsilon^2}} \right| \right)^2 + \left(\left| S_{11}(1) - \frac{\varepsilon}{\sqrt{1+\varepsilon^2}} \right| \right)^2 \end{aligned} \tag{3.3-32}$$

where ω_{Zi} and ω_{Pi} are all the *NZ* zeros and *NP* poles of the filtering function.

The gradients of the cost function include the derivatives of the transmission coefficients with respect to the nonzero entries of the coupling matrix. These can be expressed as [3-18]:

$$\frac{\partial S_{11}}{\partial M_{pq}} = -4j \cdot A^{-1}_{1p} \cdot A^{-1}_{q1}, \ \mathrm{p} \neq \mathrm{q} \tag{3.3-33}$$

$$\frac{\partial S_{11}}{\partial M_{pp}} = -2j \cdot A^{-1}_{1p} \cdot A^{-1}_{p1} \tag{3.3-34}$$

$$\frac{\partial S_{21}}{\partial M_{pq}} = 2j \cdot (A^{-1}_{N+2,p} \cdot A^{-1}_{q1} + A^{-1}_{N+2,q} \cdot A^{-1}_{p1}), \ \mathrm{p} \neq \mathrm{q} \tag{3.3-35}$$

$$\frac{\partial S_{21}}{\partial M_{pp}} = 2j \cdot A^{-1}_{N+2,p} \cdot A^{-1}_{p1} \tag{3.3-36}$$

3.3.3.6. Selection of Topology

Topology of a cross-coupled filter is determined by the present couplings between its resonators. In the direct coupling matrix synthesis procedures the topology of the initially obtained matrix is strictly appointed (every resonator is coupled to each other, or coupled to source and load only), and the unwanted couplings can be further annihilated by rotations. In this case the filter topology to be designed can not be chosen in advance. In contrast, for the optimization based matrix synthesis method, the topology is appointed by designers. Thus, it is crucial to determine the topology, which is capable of generating the required filtering function. The problem leads to analysis of different topologies in order to find out the possible number and locations (in upper or lower stopband) of the transmission zeros generated by them.

To find a solution for this problem, physical reasons for appearance of transmission zeros in cross-coupled filters must be examined. It is well known that a reactive electronic circuit introduces a phase shift into the incident signal propagating through it. If a signal flows between source and load through several paths, then, generally, each separate portion of the signal undergoes different phase shift at the load; hence, some signals may come to the load (generally, to a certain node) in phase or out of phase. In the latter case the signals compensate one another and a transmission zero appears.

Therefore, for obtaining the positions of transmission zeros, an analysis of frequency shifts caused by certain pairs of signal paths is required. More information on the algorithm applied to cross-coupled networks for this purpose is given in [3-12].

The fundamental theorem for determining the maximum number of transmission zeros offered by a certain topology has been rigorously proved by Amari and Bornemann [3-20, 3-21]. It states that a cross-coupled filter is capable of producing the maximum number of transmission zeros equal to the maximum number of bypassed resonators between source and load. This implies that an N^{th} order filter with direct coupling between source and load may generate no more than N transmission zeros. If source and load are uncoupled, then the maximum number of possible transmission zeros is reduced to $N - 2$. This rule also clearly

illustrates the fundamental reason why the direct coupled topology is unable to generate any transmission zero: only single path between source and load exists, and no resonators are bypassed. Hence, the direct coupled topology is a network for implementation of all-pole filters.

It must be specially noted that for some topologies the coupling matrix for the realization of a certain filter may be not unique, and many different matrices may reproduce the same filtering function. The solution to the uniqueness problem is available in [3-19], where it has been shown that the transversal matrix is a universal representation of coupled resonator filters of arbitrary orders, topologies and positions of the transmission zeros.

3.3.4. Extracted Pole Filters

Often it is technically difficult or even impossible to realize coupling coefficients with negative values which appear in the synthesized coupling matrix. In these cases extracted pole filter networks are widely used. In these circuits transmission zeros appear due to the bandstop sections removed from the initial filter prototype; the remaining filter circuit does not require any cross-couplings and may be even an inline direct-coupled resonators network [3-22]. The bandstop section consists of a lowpass resonator represented as an inductor connected in series with a FIR element [3-10]. Bandstop section with its equivalent circuit with inverter is presented in Figure 3-15.

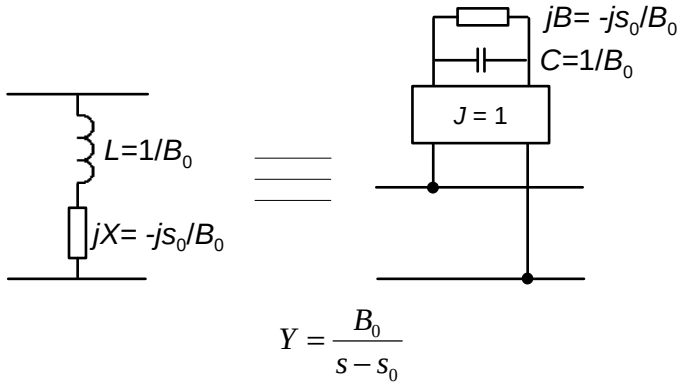

Figure 3-15: Schematic representation of a bandstop section.

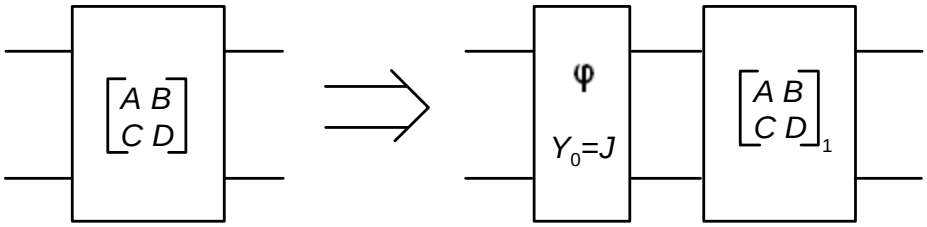

Figure 3-16: Removal of a transmission line section from the filter network.

The bandstop section is extracted out of the two-port *ABCD*-matrix of the filter, which can be easily composed from the known polynomials of the filtering function [3-2]. First, the two-port network is considered as cascade of a transmission line section with a remainder $[ABCD]_1$-matrix, as shown in Figure 3-16.

The entries of the remainder matrix can be calculated as follows [3-10]:

$$\begin{bmatrix} A_1 & B_1 \\ C_1 & D_1 \end{bmatrix} = \begin{bmatrix} A\cos\varphi - j\frac{1}{J}C\sin\varphi & B\cos\varphi - j\frac{1}{J}D\sin\varphi \\ C\cos\varphi - jAJ\sin\varphi & D\cos\varphi - jBJ\sin\varphi \end{bmatrix} \tag{3.3-37}$$

where J is usually taken to be unity for simplification, and

$$\varphi = \tan^{-1}\left.\frac{A}{jC}\right|_{s=s_0} \tag{3.3-38}$$

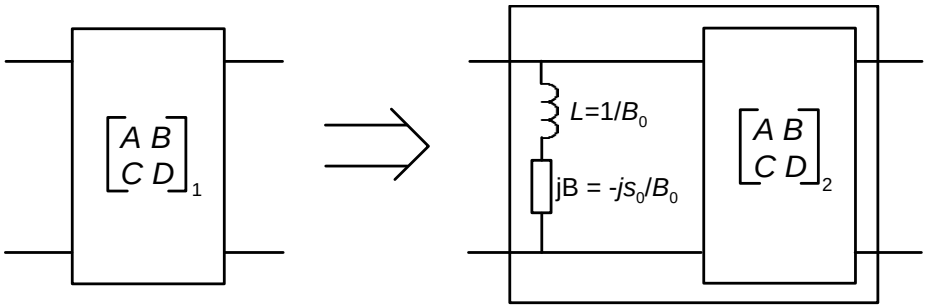

Figure 3-17: Removal of the bandstop section from the remaining network.

Next, the remaining network represented with $[ABCD]_1$-matrix is considered as a bandstop section connected in series with another two-port network described by means of $[ABCD]_2$-matrix (see Figure 3-17). Consequently, the new remainder matrix can be calculated using the following equation:

$$\begin{bmatrix} A_1 & B_1 \\ C_1 & D_1 \end{bmatrix} = \begin{bmatrix} 1 & 0 \\ -\frac{B_0}{s-s_0} & 1 \end{bmatrix} \cdot \begin{bmatrix} A_2 & B_2 \\ C_2 & D_2 \end{bmatrix} \tag{3.3-39}$$

where B_0 can be extracted as a residue

$$B_0 = \left.\frac{(s-s_0)C_1}{A_1}\right|_{s=s_0} \tag{3.3-40}$$

If the rest of the circuit described by the $[ABCD]_2$-matrix contains another bandstop sections to be extracted, then the procedure is repeated until all the poles are removed from the initial network. The remainder circuit, containing no extracted poles, can be synthesized using the techniques illustrated above in this chapter.

3.3.5. Filters With Non-Resonating Nodes

Non-resonating node (NRN) is a shunt FIR element introduced within a prototype network. The NRN offer an opportunity to design cross-coupled filters with maximum number of transmission zeros without direct coupling between source and load. NRN, integrated within a cross-coupled network, introduces constant phase shift and provides new paths for the signal so as to organize more transmission zeros in a certain topology. Another major advantage of the NRNs is ability to reduce the overall size of filters. This happens because strongly detuned resonators with smaller dimensions are often used for implementation of the NRNs.

One of the most attractive applications of the NRNs is the design of inline filters with cascaded topologies. The inline filters are implemented as separately designed modules with own source and load nodes. Then, the load nodes of the modules are connected to the source nodes of the next modules in such a way creating the intermediate NRNs. Use of the separate modules has an important advantage. Each module included in a filter is able to control its own poles and/or transmission zeros; this feature simplifies tuning of cross-coupled filters and reduces their sensitivity to manufacturing tolerances. The described concept of filter design is often referred to as modular design.

Several basic modules for cascading have been introduced in past years. Singlet [3-23], the simplest module (shown in Figure 3-18a), consists of a single resonator bypassed by direct source-load coupling; this scheme produces and controls a pair pole-zero, positions of which may vary depending on signs and values of the available three couplings. Doublet [3-24, 3-25, 3-26] is a more flexible scheme, since two different topological configurations are available (see Figures 3-18b and c), as well as three options for the arrangement of poles and zeros; it is capable of generating and controlling two poles and two zeros. Doublet scheme together with an introduced short resonator constitutes an extended doublet [3-27] (presented in Figure 3-18d); this structure offers three poles and two transmission zeros. The coupling scheme of a typical inline cascaded filter, designed using the modular concept, in given in Figure 3-18e.

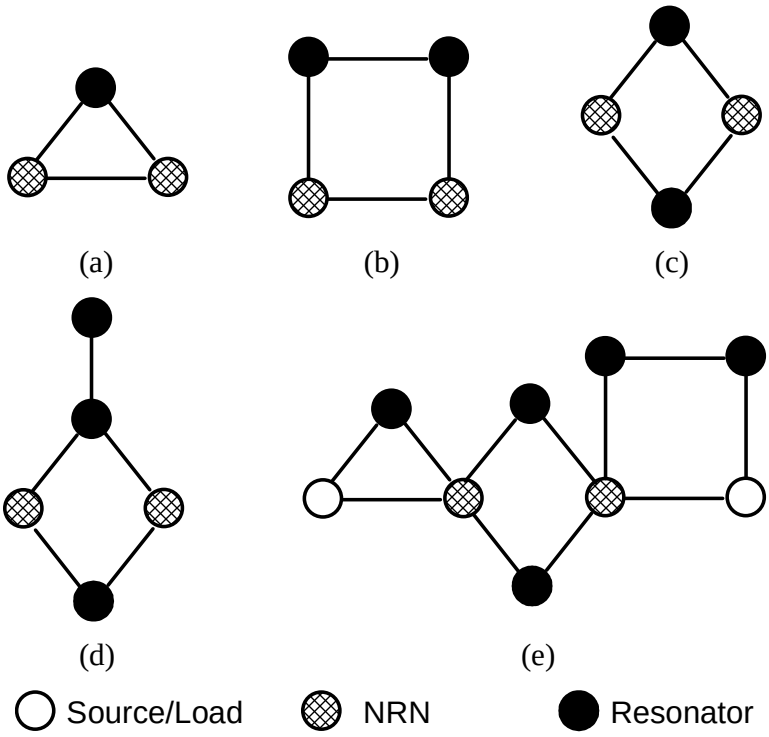

Figure 3-18: Modules used for cascaded filter design:
(a) singlet; (b) square doublet; (c) diamond doublet; (d) extended doublet;
(e) scheme of a typical filter based on the modular design concept.

Filter prototypes with NRNs can be synthesized by direct synthesis [3-28], by node insertion [3-29] or different reconfiguration of already synthesized network [3-23], and by optimization (see Section 3.3.3.5). For synthesis by optimization it is important to note that the coupling scheme of a filter should be selected in advance, as well as that the FIR elements forming NRN are frequency independent. The latter implies that in equation (3.3-29) the entries of the principal diagonal of the matrix *W*, which correspond to the NRNs, should be modified into zeros.

In this thesis several filter structures based upon the modular filter design principle (including singlets, doublets and extracted pole sections) will be demonstrated in chapters 4-6.

3.3.6. Filters with Frequency Dependent Couplings

Use of frequency dependent inter-resonator couplings has become a less popular technique to improve stopband performance by generating transmission zeros. To illustrate the idea of the method, consider an inline admittance inverter-coupled lowpass filter prototype where the value of one of the inverters J_i is frequency dependent: $J_i = J_i(\Omega)$. The circuit is illustrated in Figure 3-19.

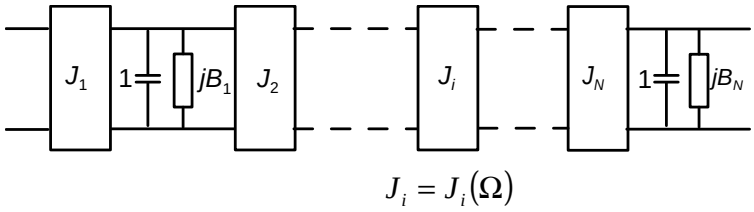

Figure 3-19: Lowpass prototype of a direct-coupled filter with a frequency dependent admittance inverter J_i.

Assume that at a certain normalized frequency Ω_0 the value of inverter J_i turns into infinity. In that case the input impedance of the entire circuit at Ω_0 yields zero, i.e. the circuit becomes short regardless of the values of all the other elements of the network. Hence, propagation of signals through the network becomes impossible at Ω_0, and the transmission zero appears at that frequency.

The design problem for this type of filters lies in the development of coupling elements which are capable of revealing the required frequency dependent properties. In [3-30] frequency dependent irises with two slots for conventional waveguide applications have been introduced. The inverters based upon such irises have linear frequency dependence and generate a single transmission zero in either the upper or lower stopband. The inverters described by linear functions of frequency offer attractive solutions for design of pseudo-elliptic or elliptic filters; it has been shown in [3-31] that the cross-coupled filters which include such inverters can be represented by an equivalent cross-coupled network composed of conventional frequency independent inverters and resonators.

Another approach to introduce transmission zeros in an inline filter by employing the frequency dependent inverters has been realized in [3-32], where a mixture of irises and stubs has been organized for this purpose in a conventional rectangular waveguide section.

Application of the frequency dependent coupling elements in the design of cross-coupled filters is being intensively investigated at the present time. Theoretically, use of such structures may lead not only to generating transmission zeros, but also to the design of a new class of broadband filters; thus, new developments are expected in this field, which makes this area of knowledge very attractive for researchers.

3.4. Frequency Transformation

The lowpass filter prototype networks, previously considered in this chapter, operate between source with unity internal resistance and unity load having the normalized cutoff frequency of $\Omega_c = 1$. However, these restrictions are clearly unpractical for use in real applications; therefore elements of the lowpass prototypes are transformed and scaled into new networks which offer acceptable solutions for certain specifications. In this section frequency transformation (also referred to as frequency mapping) techniques required for conversion of filter responses from the lowpass frequency Ω domain into the real angular frequency ω domain, together with the impedance scaling method, are briefly reviewed.

3.4.1. Lowpass-to-Lowpass Transformation

To transform a lowpass filter prototype into a practical lowpass filter network with cutoff angular frequency of ω_c, the following frequency mapping should be applied [3-2]:

$$\Omega = \frac{\Omega_c}{\omega_c}\omega \tag{3.4-1}$$

Formula (3.4-1) assigns linear scaling; therefore, all the frequency dependent elements of the prototype retain their configuration, getting new values:

$$L \rightarrow L\frac{\Omega_c}{\omega_c} \tag{3.4-2a}$$

$$C \rightarrow C\frac{\Omega_c}{\omega_c} \tag{3.4-2b}$$

Note that the impedance scaling is not included in expressions (3.4-2), as well as in other expressions relevant to the frequency mapping, listed further in this chapter. Additionally, the values of all the frequency independent prototype elements do not change as a consequence of frequency transformations of any type.

3.4.2. Lowpass-to-Highpass Transformation

For highpass filters with real cutoff angular frequency of ω_c, the frequency transformation is defined as [3-2]:

$$\Omega = -\frac{\Omega_c \omega_c}{\omega} \tag{3.4-3}$$

It can be shown that as a result of lowpass-to-highpass transformation the inductors turn into capacitors and vice versa. In this case the new values of inductors and capacitors in the highpass filter network are:

$$L \rightarrow \frac{1}{\Omega_c \omega_c C} \tag{3.4-4a}$$

$$C \rightarrow \frac{1}{\Omega_c \omega_c L} \tag{3.4-4b}$$

3.4.3. Lowpass-to-Bandpass Transformation

By employing the lowpass-to-bandpass transformation, the lowpass filter prototype can be converted into a bandpass filter with a passband of $\omega_2 - \omega_1$, where ω_1 and ω_2 are the passband-edge angular frequencies. The required mapping is defined by the following expression [3-1, 3-2]:

$$\Omega = \frac{\Omega_c \omega_0}{\omega_2 - \omega_1}\left(\frac{\omega}{\omega_0} - \frac{\omega_0}{\omega}\right) \tag{3.4-5}$$

where ω_0 is the center angular frequency calculated as $\omega_0 = \sqrt{\omega_1 \omega_2}$. If this transformation is applied to the inductive and capacitive elements of the lowpass prototype, the inductors are transformed into the series *LC* resonant circuits with the values calculated as:

$$L_{res} = \frac{\Omega_c L}{\omega_2 - \omega_1} \tag{3.4-6a}$$

$$C_{res} = \frac{1}{\omega_0^2} \cdot \frac{\omega_2 - \omega_1}{\Omega_c L} \tag{3.4-6b}$$

Similarly, the capacitors are converted into the parallel *LC* resonant circuits. The new parameters can be obtained from:

$$C_{res} = \frac{\Omega_c C}{\omega_2 - \omega_1} \tag{3.4-7a}$$

$$L_{res} = \frac{1}{\omega_0^2} \cdot \frac{\omega_2 - \omega_1}{\Omega_c C} \tag{3.4-7b}$$

It is evident from equations (3.4-7) that the resonators have the resonance frequency, which coincides with the centre frequency of the filter:

$$\omega_0 = \frac{1}{\sqrt{L_{res} C_{res}}} \tag{3.4-8}$$

In the asynchronously tuned filters the lowpass resonators are often modelled as capacitor *C* connected in parallel with a frequency invariant susceptance *B*; this shifts the centre frequency of the resonator. For these circuits the bandpass transformation leads to the following results:

$$C_{res} = \frac{1}{\omega_0} \cdot \left(\frac{\Omega_c \omega_0 C}{\omega_2 - \omega_1} + \frac{B}{2} \right) \tag{3.4-9a}$$

$$L_{res} = \frac{1}{\omega_0} \cdot \left(\frac{\omega_0 \Omega_c C}{\omega_2 - \omega_1} - \frac{B}{2} \right)^{-1} \tag{3.4-9b}$$

Hence, the angular resonant frequency of a real resonator in the bandpass filter is calculated as [3-1]

$$\omega_{res} = \frac{1}{\omega_0} \cdot \sqrt{1 - \frac{B}{\frac{\omega_0 C}{\omega_2 - \omega_1} + \frac{B}{2}}} \tag{3.4-10}$$

Using the equation (3.4-10), all the angular resonant frequencies of individual resonators which constitute an asynchronously tuned filter can be obtained.

3.4.4. Lowpass-to-Bandstop Transformation

To transform a lowpass filter prototype into bandstop, one needs to apply the mapping scheme of the following form [3-1]:

$$\Omega = \frac{\Omega_c(\omega_2 - \omega_1)}{\omega_0\left(\frac{\omega}{\omega_0} - \frac{\omega_0}{\omega}\right)} \tag{3.4-11}$$

In contrast with the lowpass-to-bandpass transformation, the inductive elements of the lowpass prototype are transformed into parallel *LC* resonant circuits with the values calculated by

$$C_{res} = \frac{1}{(\omega_2 - \omega_1)\Omega_c L} \tag{3.4-12a}$$

$$L_{res} = \frac{\Omega_c L(\omega_2 - \omega_1)}{\omega_0^2} \tag{3.4-12b}$$

The capacitive elements become converted into the series *LC* resonant circuits:

$$L_{res} = \frac{1}{(\omega_2 - \omega_1)\Omega_c C} \tag{3.4-13a}$$

$$C_{res} = \frac{\Omega_c C(\omega_2 - \omega_1)}{\omega_0^2} \tag{3.4-13b}$$

3.4.5. Lowpass-to-Multiband Transformation

Transformation from lowpass prototype to multiband filter can be considered as a superposition of several bandpass and bandstop mappings. Generalized expression for the multiband transformation can be written as follows:

$$\Omega = \Omega_c \left[\sum_{i=1}^{NP} \frac{\omega_{0i}}{\omega_{2i} - \omega_{1i}} \left(\frac{\omega}{\omega_{0i}} - \frac{\omega_{0i}}{\omega} \right) + \sum_{k=1}^{NS} \frac{\omega_{2k} - \omega_{1k}}{\omega_{0k} \left(\frac{\omega}{\omega_{0k}} - \frac{\omega_{0k}}{\omega} \right)} \right] \qquad (3.4\text{-}14)$$

where *NP* is the number of passbands, and *NS* – number of stopbands in the multiband filter.

In practice, the lowpass-to-multiband transformation leads to appearance of several new parallel or series resonant *LC* circuits connected through inverters instead of each lowpass resonator. Individual circuits, obtained as a result of the transformation from lowpass resonators are often referred to as multiband resonators. More information on the application of the multiband frequency mapping can be found in [3-33, 3-34].

3.4.6. Impedance Scaling

Impedance scaling is performed for the normalization of the unity source and load impedances to any required value Z_0 (or inverse value of the termination admittance Y_0). Hong and Lancaster in [3-1] introduce the impedance scaling factor γ_0 for convenience of the procedure:

$$\gamma_0 = \begin{cases} \dfrac{Z_0}{g_0}, & \text{if } g_0 \text{ is the resistance} \\ \dfrac{g_0}{Y_0}, & \text{if } g_0 \text{ is the conductance} \end{cases} \tag{3.4-15}$$

where g_0 is a normalized source or load impedance of the lowpass prototype filter. Consequently, the values of the elements of the filter prototype are scaled using the following rules:

- for impedance: $R \to \gamma_0 R$;
- for admittance: $G \to \dfrac{G}{\gamma_0}$;
- for inductance: $L \to \gamma_0 L$;
- for capacitance: $C \to \dfrac{C}{\gamma_0}$;
- for frequency invariant reactance: $X \to \gamma_0 X$;
- for frequency invariant susceptance: $B \to \dfrac{B}{\gamma_0}$;
- for impedance inverters: $K \to \gamma_0 K$;
- for admittance inverters: $J \to \dfrac{J}{\gamma_0}$.

Note that the impedance scaling procedure should be applied after the transformation of inductors and capacitors into their corresponding elements, in order to avoid possible errors. The scaling procedure does not affect the frequency characteristics of the filter.

3.5. Implementation and Optimization

In the next stage of the design procedure the synthesized bandpass prototype filter should be implemented in a real physical structure. The implementation involves translation of the calculated circuit parameters into physical dimensions of components of the device to be realized. However, in engineering there is no guarantee that the obtained dimensions instantaneously give the perfect solution. This implies that the final dimensions of the filters have to be optimized in order to achieve results suitable for fabrication.

3.5.1. Filter Implementation

At present, a great variety of technologies and their hybrids are available to embody microwave or mm-wave filters (waveguide [3-35], coaxial [3-36], microstrip [3-37], substrate integrated [3-38], dielectric resonator [3-39] etc.); therefore numerous technologies for filter implementation have been developed for the long history of filter design.

In general, the majority of implementation techniques for the class of coupled-resonator filters are built on the design of individual resonators with required resonant frequencies and finding solutions for realization of couplings between them [3-37]. The resonators may be realized as single-, double- or multimode [3-11, 3-22, 3-40]. Usually, sections of transmission lines are used at micro- and millimetre waves as resonators. The resonant frequencies of resonators are determined mainly by size; often, for tuning purpose, perturbations or other elements are included in resonator constructions. Dimensions of the resonators can be calculated for simple shapes, or modelled in electromagnetic simulators.

Couplings, by definition, should be realized by elements capable of providing exchange of energy between resonators. These can be organized by posts [3-34, 3-38], irises [3-22, 3-35], septa [3-41], perturbations [3-11], fringing fields [3-37], and by other means. To obtain dimensions of the coupling elements, corresponding to the coupling coefficient to be implemented, design curves based upon electromagnetic simulations or, rarely, direct

measurements are usually built. Sometimes analytical solutions are available for coupling elements design problem.

In this thesis, several examples of filters implemented in hybrid microstrip and rectangular waveguide technology are presented. Integration of microstrips in the E-plane of a rectangular waveguide, leading to creation of extracted pole sections and other basic cross-coupled modules, suitable for cascade filter design (see Section 3.3) is considered in chapters 4 and 5. In chapter 6 the problem of implementation of couplings between folded substrate integrated waveguide resonators is addressed; a new negative coupling structure for this type of technology is proposed and investigated.

3.5.2. Filter Optimization

Dimensions of real structures obtained as a result of the implementation procedure do not guarantee that the fabricated filter has exactly the same frequency response as initially approximated. Therefore, optimization is necessary for finding new values which show better agreement with the theoretical model.

At present, commercial EM-simulators are widely applied in filter design. These simulate the transmission characteristics of filters by modelling propagation of EM-waves in real structures, which is based upon numerical solving of the Maxwell's equations using the finite element method (FEM), mode matching technique (MMT), finite difference time domain (FDTD) technique and others. Therefore, all filter design procedures, starting from the implementation stage, are carried out with computer aid, i.e. only the fully verified device simulated with high accuracy is eventually fabricated. However, accurate EM-simulation is a time and computational resources consuming process. Hence, gradient-based optimization [3-42] using a full-field solver appears to be difficult and ineffective.

Recently, new effective space mapping optimization techniques for EM-simulators have been proposed, which avoid the direct optimization of accurate (or fine) model by using coarse model as an intermediate step [3-10]. The coarse model offers lower accuracy and is time efficient, while the fine model provides high accuracy, however demands more computational time. The notion of the method lies in establishing the relationship between the parameters of the coarse and fine models, and performing the optimization in the coarse model parameter space. Then, the optimal parameters for the fine model can be found by applying the inversion to the optimal solution for the coarse model. In the first space mapping approach [3-43], linear mapping was assumed between two parameter spaces. More advanced aggressive space mapping approach deals with nonlinear mapping between these spaces; in this case nonlinear equations are solved by available numerical methods. More information on space mapping optimization techniques and examples of its use for filter design can be found in [3-44, 3-45].

3.6. Summary

In this chapter an overview of filter design and optimization procedures has been presented.

In section 3.2 approximation techniques for derivation of the analytical expressions, representing the transfer functions which satisfy the initial filter specifications, have been presented.

Filter prototype synthesis methods have been presented in section 3.3. The prototype circuits are synthesized as ladder or cross-coupled networks; coupling matrices have been introduced as a convenient tool for representation of the cross-coupled filter prototype circuits. Direct and optimization synthesis techniques for $N \times N$ and $(N+2) \times (N+2)$ coupling matrices have been considered, as well as the method of rotations used for elimination of unwanted entries from a coupling matrix. The main topologies of the cross-coupled filters used for the generation of transmission zeros in filter stopband have been presented.

In section 3.4 the frequency mapping techniques applied for conversion of the lowpass prototype filter into practical highpass, bandpass, bandstop and multiband prototype filters have been considered. Transformations of the lowpass prototype elements caused by the frequency mapping process have been presented.

Filter implementation and optimization procedures have been briefly outlined in section 3.5. The problem of implementation will be further addressed in detail in chapters 4-6; more information about the optimization techniques used in filter design can be found in the references.

3.7. References

[3-1] J. S. Hong and M. J. Lancaster, *Microstrip Filters for RF/Microwave Applications*, New York: John Wiley & Sons, 2001

[3-2] I. C. Hunter, *Theory and Design of Microwave Filters*, London: IEE Press, 2001

[3-3] G. L. Matthaei, L. Jones and E. M. T. Jones, *Microwave Filters, Impedance Matching Networks and Coupling Structures*, New York: McGraw-Hill, 1964.

[3-4] R. J. Cameron, "General Coupling Matrix Synthesis Methods for Chebychev Filtering Functions", *IEEE Trans. Microwave Theory Tech*., vol. 47, pp. 433-442, April 1999

[3-5] S. Amari, "Synthesis of Cross Coupled Resonator Filters Using an Analytical Gradient Based Optimization Technique," *IEEE Trans. Microwave Theory Tech*., vol. 48, pp. 1559-1564, September 2000

[3-6] J. D. Rhodes, *Theory of Electrical Filters*. New York: Willey, 1976

[3-7] J. D. Rhodes, "Explicit Formulas for Element Values in Elliptic Function Prototype Networks", *IEEE Trans. Circuit Theory*, vol. 18, pp. 264-276, March 1971

[3-8] A. E. Williams, W. G. Bush, and R. R. Bonetti, "Predistortion Technique for Multicoupled Resonator Filters Methods for Chebyshev Filtering Functions", *IEEE Trans. Microwave Theory Tech.*, vol. 33, pp. 402-407, May 1985

[3-9] R. F. Baum, "Design of Unsymmetrical Band-Pass Filters", *IRE Trans. Circuit Theory*, vol. 4, pp. 33-40, June 1957

[3-10] R. J. Cameron, C. M. Kudsia, and R. R. Mansour, *Microwave Filters for Communication Systems*, Hoboken, New Jersey, John Wiley & Sons, 2007

[3-11] A. E. Atia and A. E. Williams, "Narrow-Bandpass Waveguide Flters," *IEEE Trans. Microwave Theory Tech.*, vol. MTT-20, pp. 258–265, Apr. 1972

[3-12] J. B. Thomas, "Cross-Coupling in Coaxial Cavity Filters – A Tutorial Overview," *IEEE Trans. Microwave Theory Tech.*, vol. MTT-20, pp. 258–265, Apr. 1972

[3-13] A. E. Atia and A. E. Williams, "New Types of Bandpass Filters for Satellite Transponders", *COMSAT Tech. Rev.*, vol. 1, pp. 21-43, 1971.

[3-14] O. Brune, "Synthesis of a Finite Two-Terminal Network Whose Driving Point Impedance is a Prescribed Function of Frequency", *J. Math Phys.*, vol. 10(3), pp. 191 – 236, 1931

[3-15] A. E. Atia, A. E. Williams, and R. W. Newcomb, "Narrow Band Multiple-Coupled Cavity Synthesis," *IEEE Trans. Circuit Syst*., vol. CAS-21, pp. 649-655, Sept. 1974

[3-16] G. H. Golub and C. F. van Loan, *Matrix Computations*, 2nd ed., John Hopkins Univ. Press, Baltimore, 1989

[3-17] R. J. Cameron, "Advanced Coupling Matrix Synthesis Techniques for Microwave Filters", *IEEE Trans. Microwave Theory Tech*., vol. 51, pp. 1-10, Jan. 2003

[3-18] S. Amari, U. Rosenberg, and J. Bornemann, "Adaptive Synthesis and Design of Resonator Filters With Source/Load-Multiresonator Coupling," *IEEE Trans. Microwave Theory Tech*., vol. 50, pp. 1969-1978, August 2002

[3-19] S. Amari, and M. Beckheit, "Physical Interpretation and Implications of Similarity Transformations in Coupled Resonator Filter Design," *IEEE Trans. Microwave Theory Tech*., vol. 55, pp. 1139-1153, June 2007

[3-20] S. Amari, "On the Maximum Number of Finite Transmission Zeros of Coupled Resonator Filters With a Given Topology," *IEEE Microwave Wireless Components Lett*., vol. 9, pp. 354-356 , Sept. 1999

[3-21] S. Amari and J. Bornemann, "Maximum Number of Finite Transmission Zeros of Coupled Resonator Filters With Source/Load Multi-Resonator Coupling and a Given Topology," *Microwave Conference 2000 Asia Pacific*, pp. 1175-1177, Dec. 2000

[3-22] J. D. Rhodes, and R. J. Cameron, "General Extracted Pole Synthesis Technique With Applications to Low-Loss TE_{011} Mode Filters," *IEEE Trans. Microwave Theory Tech*., vol. 28, pp. 1018-1028, Sept. 1980

[3-23] S. Amari, U. Rosenberg and J. Bornemann, "Singlets, Cascaded Singlets, and the Nonresonating Node Model for Advanced Modular Design of Elliptic Filters," *IEEE Microwave and Wireless Components Letters*, vol. 14, pp. 237–239, May 2004.

[3-24] S. Amari and U. Rosenberg, “The Doublet: A New Building Block for the Modular Design of Elliptic Filters,” in *Eur. Microwave Conf.* Milan, Italy, vol. 2, pp. 123-125, 2002

[3-25] O. Glubokov and D. Budimir, “Compact E-plane Doublet Structures for Modular Filter Design,” in *Eur. Microwave Conf.*, Paris, France, pp. 1253-1256, 2010

[3-26] S. Amari and U. Rosenberg, “A Universal Building Block for Advanced Modular Design of Microwave Filters,” *IEEE Microwave and Wireless Components Letters*, vol. 13, pp. 541–543, Dec. 2003

[3-27] S. Amari and U. Rosenberg, “New Building Blocks for Modular Design of Elliptic and Self-Equalized Filters,” *IEEE Trans. Microwave Theory Tech.*, vol. 52, pp. 721-736, Feb. 2004

[3-28] G. Macchiarella and S. Amari, “Direct Synthesis of Prototype Filters With Non-Resonating Nodes,” in *Eur. Microwave Conf.* Amsterdam, The Netherlands, pp. 305-308, 2004

[3-29] H. C. Bell, “Cascaded Singlets Realized by Node Insertions,” in *IEEE MTT-S Int. Microw. Symp. Dig.*, Long Beach, CA, Jun. 2005, pp. 107–110

[3-30] U. Rosenberg, S. Amari, and F. Seyfert, “Pseudo-Elliptic Direct-Coupled Resonator Filters Based on Transmission-Zero-Generating Irises,” in *Eur. Microwave Conf.*, Paris, France, pp. 962-965, 2010

[3-31] S. Amari, M. Bekheit, and F. Seyfert, “Notes of Bandpass Filters Whose Inter-Resonator Coupling Coefficients are Linear Functions of Frequency”, accepted for presentation at *IEEE Inter. Microwave Symposium*, Atlanta, USA, June 2008

[3-32] S. Amari and J. Bornemann, “Using Frequency-Dependent Coupling to Generate Finite Attenuation Poles in Direct-Coupled Resonator Bandpass Flters,” *IEEE Microw. Guided Wave Lett.,* vol. 9, no. 10, pp. 404–406, Oct. 1999

[3-33] G. Macchiarella and S. Tamiazzo, “Design techniques for dual-passband filters,” *IEEE Trans. Microwave Theory Tech.*, vol. 53, pp. 3265-3271, Nov. 2005

[3-34] X.-P. Chen, K. Wu, and Z.-L. Li, “Dual-Band and Triple-Band Substrate Integrated Waveguide Filters With Chebyshev and Quasi-Elliptic Responses,” *Microwave Theory and Techniques, IEEE Transactions on*, vol. 55, pp. 2569-2578, Dec. 2007

[3-35] J. D. Rhodes, "The Generalized Direct-Coupled Cavity Linear Phase Filter," *Microwave Theory and Techniques, IEEE Transactions on*, vol. 18, pp. 308-313, Jun. 1970

[3-36] Y. Wang and M. Yu, "True Inline Cross-Coupled Coaxial Cavity Filters," *Microwave Theory and Techniques, IEEE Transactions on*, vol. 57, pp. 2958-2965, Dec. 2009

[3-37] J.-S. Hong and M. J. Lancaster, "Couplings of Microstrip Square Open-Loop Resonators for Cross-Coupled Planar Microwave Filters," *Microwave Theory and Techniques, IEEE Transactions on*, vol. 44, no. 11, pp. 2099-2109, Nov. 1996

[3-38] X.-P. Chen and K. Wu, "Substrate Integrated Waveguide Cross-Coupled Filter With Negative Coupling Structure," *Microwave Theory and Techniques, IEEE Transactions on*, vol. 56, pp. 142-149, Jan. 2008

[3-39] S. B. Cohn, "Microwave Bandpass Filters Containing High-Q Dielectric Resonators," *Microwave Theory and Techniques, IEEE Transactions on*, vol. 16, no. 4, pp. 218-227, Apr. 1968

[3-40] I. C. Hunter, J. D. Rhodes, and J. Dassonville, "Triple Mode Dielectric Resonator Hybrid Reflection Filters," *Microwaves, Antennas and Propagation, IEE Proc.*, vol. 145, no. 4, pp. 337-343, Aug. 1998

[3-41] V. Postoyalko and D. S. Budimir, "Design of Waveguide E-plane Filters With All-Metal Inserts by Equal Ripple Optimization," *Microwave Theory and Techniques, IEEE Transactions on*, vol. 42, no. 2, pp. 217-222, Feb. 1994

[3-42] J. W. Bandler, S. H. Chen, S. Daijavad, and K. Madsen, "Efficient Optimization With Integrated Gradient Approximations," *Microwave Theory and Techniques, IEEE Transactions on*, vol. 36, no. 2, pp. 444-455, Feb. 1988

[3-43] J. W. Bandler, R. M. Biernacki, S. H. Chen, P. A. Grobelny, and R. H. Hemmers, "Space Mapping Technique for Electromagnetic Optimization," *Microwave Theory and Techniques, IEEE Transactions on*, vol. 42, no. 12, pp. 2536-2544, Dec. 1994

[3-44] J. W. Bandler, R. M. Biernacki, S. H. Chen, R. H. Hemmers, and K. Madsen, "Electromagnetic Optimization Exploiting Aggressive Space Mapping," *Microwave Theory and Techniques, IEEE Transactions on*, vol. 43, no. 12, pp. 2874-2882, Dec. 1995

[3-45] J. Amari, C. LeDrew and W. Menzel, “Space Mapping Optimization of Planar Coupled Resonators Filters,” *Microwave Theory and Techniques, IEEE Transactions on*, vol. 54, no.5, pp. 2153-2159, May 2006

CHAPTER 4

E-PLANE CROSS-COUPLED FILTERS IN CONVENTIONAL RECTANGULAR WAVEGUIDE

4.1. Introduction

The standard E-plane waveguide filters are organized by means of the direct-coupled topology which provides a single path between source and load; this implies that these filters may have all-pole frequency responses, and transmission zeros can not be generated. Interaction between adjacent resonators in the E-plane filters is provided by metallic septa which, being combined, form E-plane inserts to be arranged within a waveguide. The inserts can be all-metal (for example, cut out of copper foil) or metallo-dielectric; the latter usually is a piece of dielectric substrate with septa etched on top metallization layer, while the bottom metallization is removed. However, bottom metallization can be used to realize cross-couplings in E-plane filters. For this purpose, a stripline resonator can be etched on the bottom side, opposite to a top side septum. This will introduce two new couplings with adjacent waveguide resonators, forming a triplet [4-1, 4-2] – the filtering module capable of generating a single transmission zero at finite frequency.

This approach can be further generalized by substituting the waveguide resonators by NRN, which yields a singlet, the simplest filtering module introduced in [4-3]. More complex modules can be obtained by employing additional stripline resonators on the bottom side. Use of NRN makes possible arrangement of the filtering modules into a modular cross-coupled filter, whose poles and zeros can be controlled independently by adjusting parameters of individual modules.

In this chapter a problem of modular filter design using E-plane inserts in rectangular waveguide will be addressed. In section 4.2 several filtering modules composed of septa and stripline resonators are proposed. Their configurations and main properties are

outlined. Section 4.3 gives an overview of coupling coefficients traditionally used in the design of cross-coupled filters for characterization of degree of interaction between adjacent resonators. Methods of extraction of coupling coefficients from simulated or measured frequency responses are discussed. In section 4.4 design examples of single filtering modules and cross-coupled filters composed of these modules, and implemented in E-plane technology, are presented. Bandpass filters containing NRN are fabricated and tested in order to prove feasibility of the proposed approach.

4.2. Design of Cross-Coupled Filters Using E-plane Inserts

In this section several modules for E-plane cross-coupled filters composed of septa and stripline resonators, and implemented using metallo-dielectric inserts, will be discussed.

4.2.1. Singlets

Singlet is the simplest filtering module which consists of a single resonator and generates a pole-zero pair due to bypass source-load coupling.

4.2.1.1. Model of Singlets and Analysis

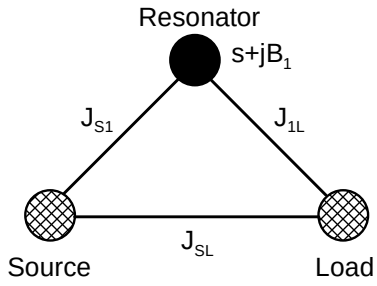

Figure 4-1: Coupling scheme representation of a singlet.

The coupling scheme of a singlet is presented in Figure 4-1. It contains three nodes representing source, load and a resonator. Solid lines connecting the nodes represent couplings between them; two of these couplings constitute the main path (source-resonator and resonator-load); the third one is a bypass coupling between source and load. According to Amari and Bornemann [4-4, 4-5], this coupling scheme generates a single transmission zero as only one resonator is bypassed. Coupling matrix of an arbitrary singlet, corresponding to the coupling scheme, has the following form:

$$M = \begin{bmatrix} 0 & J_{S1} & J_{SL} \\ J_{S1} & B_1 & J_{1L} \\ J_{SL} & J_{1L} & 0 \end{bmatrix} \tag{4.2-1}$$

For symmetrical singlets the matrix can be simplified by $J_{S1} = J_{1L}$.

Frequency domain performance of the singlet's lowpass prototype equivalent scheme can be analyzed by applying formulae (3.3-30) and (3.3-31) to matrix *M*. The following expressions for S-parameters of an arbitrary singlet have been obtained:

$$S_{11} = -\frac{(1-J_{SL}^2)(\Omega+B_1)+2J_{S1}J_{1L}J_{SL}+j(J_{S1}^2-J_{1L}^2)}{(1+J_{SL}^2)(\Omega+B_1)-j(J_{S1}^2+J_{1L}^2)-2J_{S1}J_{1L}J_{SL}} \tag{4.2-2}$$

$$S_{21} = -2j\frac{J_{SL}(\Omega+B_1)-J_{S1}J_{1L}}{(1+J_{SL}^2)(\Omega+B_1)-j(J_{S1}^2+J_{1L}^2)-2J_{S1}J_{1L}J_{SL}} \tag{4.2-3}$$

where Ω – is a lowpass frequency variable.

It is clear that variation of constant value of FIR B_1 (variation of resonant frequency of the resonator in real-frequency domain) leads to corresponding shift of transmission characteristics, and the expressions can be analyzed for B_1 equal to zero for simplicity.

The singlet's model has a transmission zero at Ω_Z and a pole at Ω_P:

$$\Omega_Z = \frac{J_{S1}J_{1L}}{J_{SL}} \tag{4.2-4}$$

$$\Omega_P = -\frac{2J_{S1}J_{1L}J_{SL}+j(J_{S1}^2-J_{1L}^2)}{1-J_{SL}^2} \tag{4.2-5}$$

Positions of singlet's pole and transmission zero are determined by all three couplings available in its coupling scheme; the transmission zero always appears at a real frequency. If values of all the couplings are positive, then the transmission zero is located in the upper stopband, while its location in the lower stopband requires an odd number of negative couplings. From (4.2-5) it is clear that a general singlet has its pole at a complex frequency. However, it can be noticed that the pole frequency moves to real frequency for those singlets where $|J_{S1}| = |J_{1L}|$.

Discrepancy between positions of pole and zero for a singlet with its eigenmodes located at real frequencies can be evaluated as follows

$$\Omega_Z - \Omega_P = \frac{J_{S1}J_{1L}}{J_{SL}} \cdot \frac{1+J_{SL}^2}{1-J_{SL}^2} \tag{4.2-6}$$

This illustrates the flexibility of transmission zeros positioning with respect to passband offered by singlets, which is important for singlet-based modular filter design for a variety of applications.

4.2.1.2. Implementation of Singlets

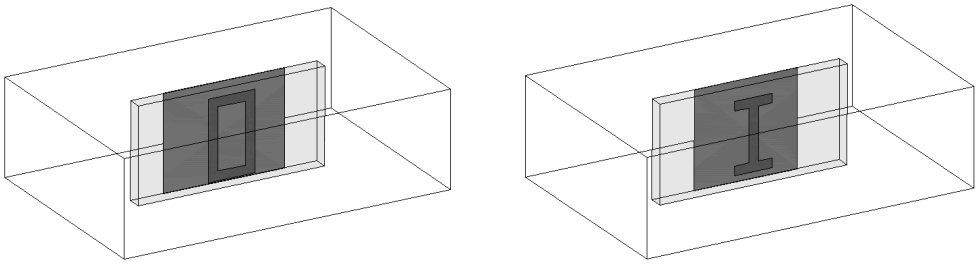

(a) (b)

Figure 4-2: Configurations of E-plane singlets in rectangular waveguide: (a) with O-shaped resonator; (b) with I-shaped resonator.

Two configurations of E-plane singlets are presented in Figure 4-2. Both of the singlet structures consist of a metallo-dielectric insert arranged in the E-plane of a conventional rectangular waveguide. The inserts are dielectric slabs of rectangular shape with a resonator etched on top side, and metallic septum placed on the other one. Separate all-metal insert can be used for realization of the septum as well. The septum acts as inverter and implements the direct source-load coupling. Resonators can be organized as a section of stripline of arbitrary shape. Couplings between source, load and the resonator are implemented by interaction between the resonating mode in resonator and the mode propagating in the waveguide; if the resonator is narrower than the septum, then evanescent mode in the septum region is utilized for this purpose.

In Figure 4-2 two variations of singlets with O-shaped and I-shaped resonators are shown. Generally, more variations including S-shaped, C-shaped and other resonators are available. The difference between these resonators is in their ability to provide various combinations of external couplings (J_{S1} and J_{1L}); hence, selection of resonator for use in singlets mainly depends on external coupling required for a certain design.

Simulated frequency responses of the proposed singlets, obtained using Ansoft HFSS™ EM solver, are presented in Figure 4-3. The S-parameters of the structures indicate that the singlets generate a transmission zero which is located at a frequency higher than the pole frequency. The singlets have been designed to exhibit the same pole frequency using septa of the same width for the purpose of comparison. Hence, it can be concluded from the simulated curves that transmission zero of singlet with O-shaped resonator is located further in the upper stopband than the transmission zero of the one with I-shaped resonator. This effect can be explained by the fact that the fast decaying evanescent mode, propagating in the waveguide through the septum region, interacts with the O-shaped resonator stronger than with the I-shaped resonator, as the O-shaped resonator is located closer to the septum's ends than the I-shaped one. In support of this statement, formula (4.2-6) suggests that for singlets with constant bypass coupling the distance between pole and zero grows with increase external couplings.

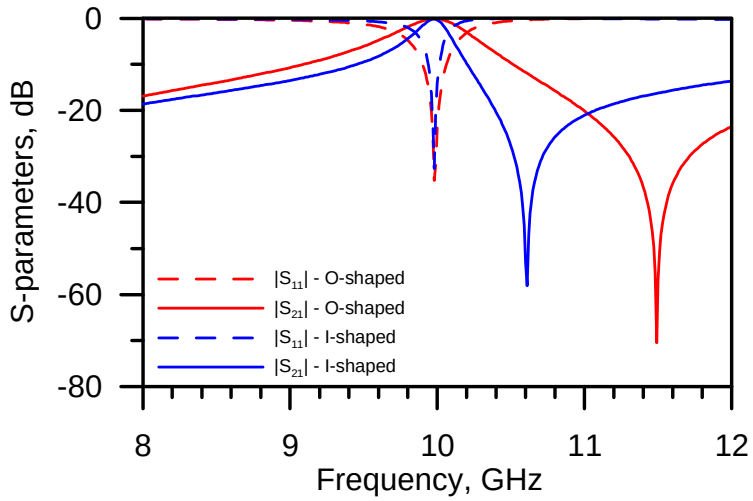

Figure 4-3: Simulated frequency responses of the proposed singlets.

4.2.2. Doublets

Doublet is a filtering module capable of generating two poles and two transmission zeros. The generation of transmission zeros in lower stopband using E-plane singlets presents some difficulty. E-plane doublet, introduced in this section, provides a neat solution for this problem.

4.2.2.1. Configuration and Frequency Response

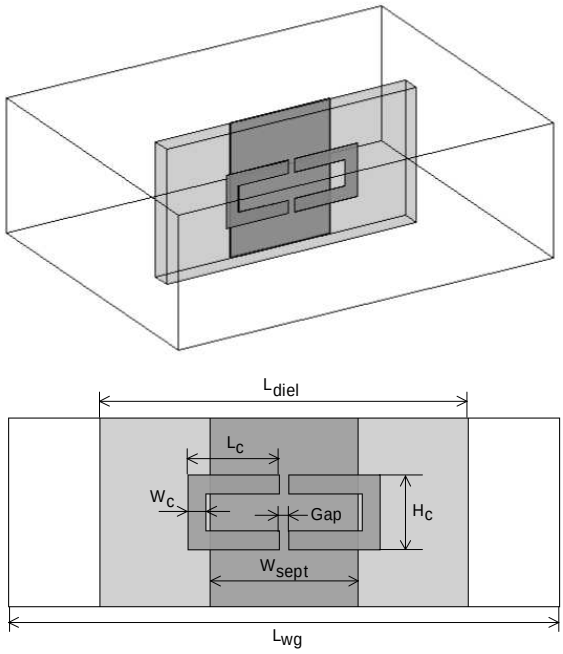

Figure 4-4: Configuration of an E-plane doublet with two hairpin resonators in rectangular waveguide.

Configuration of the proposed E-plane doublet is shown in Figure 4-4. The structure consists of a metallo-dielectric E-plane insert arranged within a conventional rectangular waveguide. The insert is a rectangular piece of dielectric substrate with two hairpin resonators etched on its top side so that their open ends face one another. On the other side of the dielectric slab a metallic septum is placed which can be implemented by either etching bottom side of the dielectric substrate or by a piece of metallic foil placed between

two halves of waveguide housing. The septum is an inductive discontinuity which acts as an inverter in combination with short transmission line sections [4-6]–[4-8].

Transmission characteristics of the proposed doublet, simulated in commercial finite-element-based electromagnetic solver Ansoft HFSS™, are presented in Figure 4-5. The obtained frequency response shows that the doublet structure acts as a bandpass filter with two poles and two transmission zeros placed asymmetrically in the upper and lower stopbands with respect to the doublet's centre frequency.

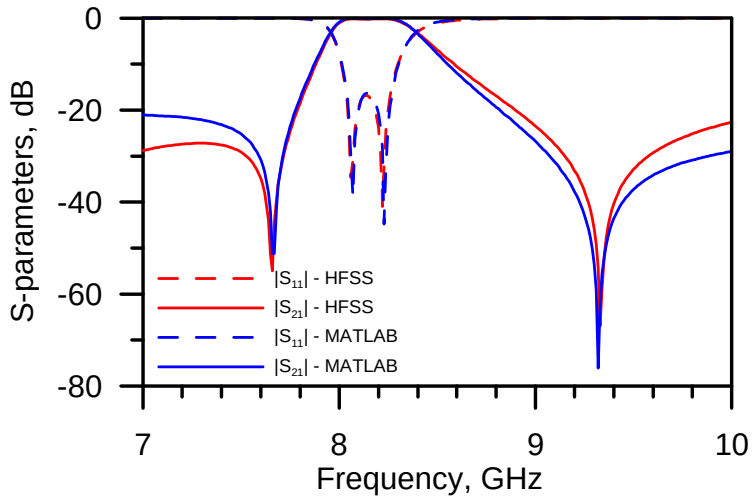

Figure 4-5: Calculated from extracted coupling matrix and simulated frequency responses of the proposed doublet.

4.2.2.2. Coupling Scheme and Analysis

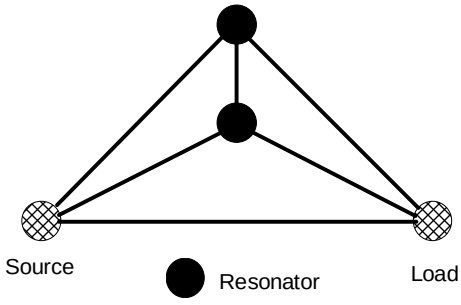

Figure 4-6: Coupling scheme representation of the proposed doublet.

The behaviour of the doublet in the frequency domain can be analyzed using its coupling scheme presented in Figure 4-6. It contains four nodes which represent source, load and two hairpin resonators. Couplings between them are shown as solid lines; it is evident that all the couplings in the doublet have non-zero values. Its coupling matrix has the following form:

$$M = \begin{bmatrix} 0 & J_{S1} & J_{S2} & J_{SL} \\ J_{S1} & B_1 & J_{12} & J_{1L} \\ J_{S2} & J_{12} & B_2 & J_{2L} \\ J_{SL} & J_{1L} & J_{2L} & 0 \end{bmatrix} \tag{4.2-7}$$

For doublets with symmetrical geometry the matrix can be simplified by using equalities $J_{S1} = J_{2L}$, $J_{S2} = J_{1L}$, $B_1 = B_2 = 0$.

Generalized doublets described by the coupling matrix M have been investigated theoretically in [4-9]. It has been shown that transmission zeros generated by the doublet may be arranged in different combinations according to values and signs of entries of coupling matrix M. General expressions for S-parameters of the doublet can be obtained by applying formula (3.3-30) and (3.3-31) to matrix M:

$$S_{11} = \frac{(1-J_{SL}^2)\Omega^2 + 4J_{S1}J_{S2}J_{SL}\Omega + (J_{S1}^2 - J_{S2}^2)^2 - J_{12}^2(1-J_{SL}^2) - 2J_{12}J_{SL}(J_{S1}^2 + J_{S2}^2)}{\det(M)} \tag{4.2-8}$$

$$S_{21} = -2j\frac{J_{SL}\Omega^2 - 2J_{S1}J_{S2}\Omega + (J_{12}J_{S1}^2 + J_{12}J_{S2}^2 - J_{SL}J_{12}^2)}{\det(M)} \tag{4.2-9}$$

The resultant expressions are complex for comprehensive analysis; however some important conclusions can be made. First of all, it is seen from (4.2-8) and (4.2-9) that the network always reveals two poles and two zeros if coupling between source and load J_{SL} is non-zero; at the same time it is evident that non-zero value of J_{S2} results in asymmetrical location of poles and zeros with respect to centre frequency, in contrast with symmetrical location for $J_{S2} = 0$. Degree of this asymmetry can be evaluated by discrepancy between vertices of parabola given by numerator polynomials in (4.2-8) and (4.2-9):

$$\Delta_{asym} = \Omega_{vertex,Z} - \Omega_{vertex,P} = \frac{J_{S1}J_{S2}}{J_{SL}} \cdot \frac{1+J_{SL}^2}{1-J_{SL}^2} \tag{4.2-10}$$

The proposed doublet structure has several design constraints which limit the variety of possible combinations. For example, inverter J_{SL} implemented by a solid septum may have only positive values; consequently, the value of J_{12} will be always negative as it is implemented by capacitive coupling between hairpin resonators. This can be illustrated by extraction of coupling matrix elements from the simulated frequency response of a doublet using optimization technique outlined in section 3.3.3.5. The coupling matrix, corresponding to the calculated S-parameters presented in Figure 4-5, has been derived in MATLAB™:

$$\begin{bmatrix} 0 & 1.086 & 0.099 & 0.039 \\ 1.086 & 0 & -1.436 & 0.099 \\ 0.099 & -1.436 & 0 & 1.086 \\ 0.039 & 0.099 & 1.086 & 0 \end{bmatrix} \tag{4.2-11}$$

4.2.3. Higher Order Modules

The approach used for the implementation of doublet in the previous section can be extended to higher order modules. In the doublet structure hairpin resonators are coupled directly by means of capacitive interaction at the ends of stripline section. The idea of realization of higher order modules consists in placing additional resonators between the first and last ones. In that way, number of resonators in the main path grows thus increasing the order of the obtained filter. At the same time, bypass coupling implemented by a septum creates another path for the signal and makes possible generation of transmission zeros. However, not only these two paths are available in the structure being proposed. Evanescent mode which propagates between the septum and side wall of the waveguide, interacts with all resonators in the main path before extinction. As a result, additional couplings appear which introduce uncontrollable transmission zeros, sometimes located in the passband.

To avoid this issue, the added resonators can be shielded by another septum arranged in parallel with the present one. Introduction of the additional septum reduces inductance of the system of parallel septa and alters its properties as an inverter. However, in a qualitative sense, these septa still provide direct coupling between source and load. The new septum can be implemented either as a separate all-metal insert or as a metallo-dielectric insert, combined with the present one or separated from it. The combined insert requires a multilayer structure with three metallization layers; top and bottom layers contain septa, while the middle one contains all the resonators which thus can be considered as symmetric stripline resonators. Use of separate insert leads to the same configuration but two dielectric slabs can be split. Configuration of a typical module with multilayer E-plane insert in rectangular waveguide is presented in Figure 4-7. The 3rd-order module shown in this figure contains an I-shaped resonator between two hairpins. This resonator interacts with the adjacent ones using electric coupling at its open ends. It is shown in [4-10] that this interaction can be characterized by negative coupling coefficient (considered in more detail in section 4.3).

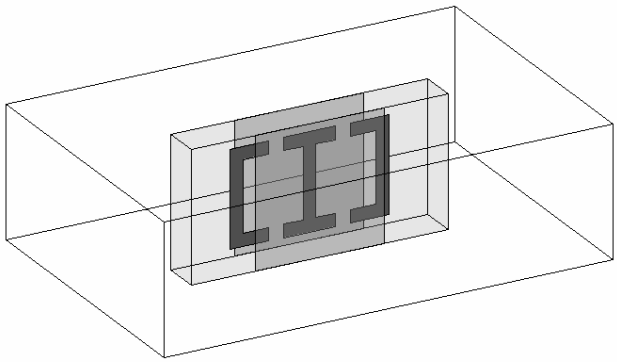

Figure 4-7: Configuration of a 3rd-order filtering module using multilayer E-plane insert in rectangular waveguide.

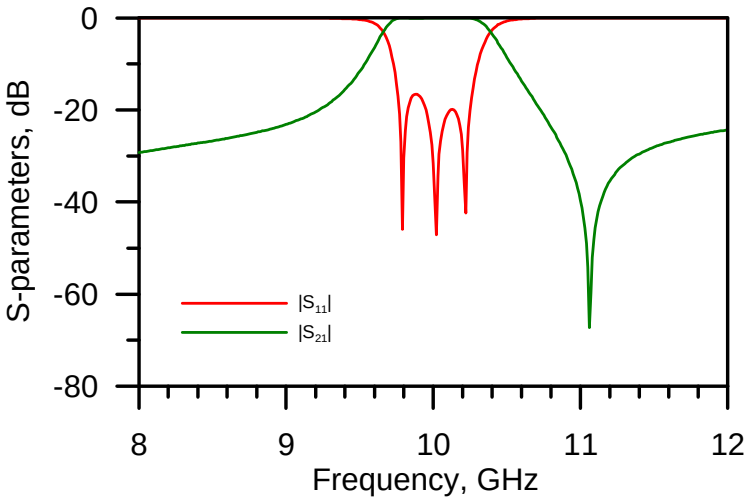

Figure 4-8: Simulated frequency response of a 3rd-order E-plane filtering module.

The simulated frequency response of the 3rd-order module, shown in Figure 4-7, is presented in Figure 4-8. The characteristic displays three poles and a single transmission zero in the upper stopband. It can be noticed that, in comparison with the response of the doublet considered in the previous section, the lower stopband transmission zero has disappeared after introducing an I-shaped resonator between two hairpins. The origin of this effect can be found by analysis of phase shifts caused by sequences of coupled resonators in the main paths of the two structures; this method, introduced by Thomas in 2003 [4-11], makes possible the determination of the number of transmission zeros which

an arbitrary coupling scheme may produce. Also, it can be found whether these transmission zeros are located in the lower or upper stopband.

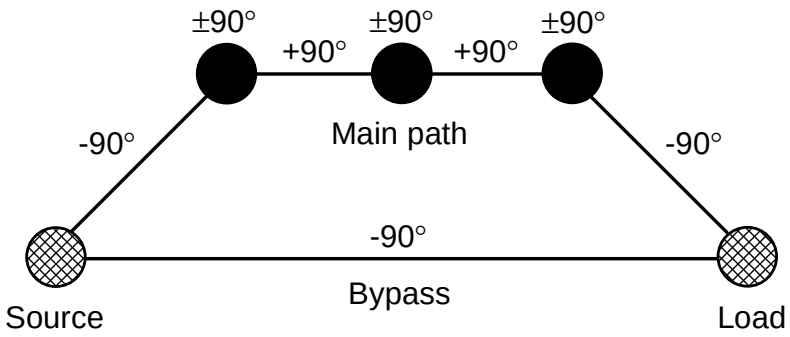

Figure 4-9: Coupling scheme of the proposed 3rd-order E-plane filtering module.

The coupling scheme of the proposed 3rd-order module with corresponding phase shifts caused by its elements is depicted in Figure 4-9. It is seen that the phase shift in the main path for frequencies below the resonance is 270°; for frequencies above the resonance it is equal to –270°. Taking into account that the phase shift provided by direct source-load coupling is equal to –90°, it is clear that signals from both paths reach the load in phase at frequencies lower than resonant, but out of phase at frequencies higher than resonant (in fact, this condition is satisfied at a certain frequency where the transmission zero appears). Hence, the 3rd-order module generates a single transmission zero in the upper stopband.

Coupling scheme of a doublet can be obtained from the scheme of the 3rd-order module by removing the middle resonator and one of its couplings to adjacent resonators. In this case, phase shift in lower stopband drops by 180°, while in upper stopband it retains its value in comparison with the initial shifts calculated for the 3rd-order module. This leads to appearance of another transmission zero in lower stopband, as signals are out of phase at these frequencies. Similarly, if another I-shaped resonator is added in the main path, phase shifts lower than resonant frequency increase by 180°, and remain unaffected higher than resonance; consequently, the new 4th-order module will generate two transmission zeros. Design example of such a module will be presented in section 4.4.1. Generally, for the class of structures with I-shaped and hairpin resonators being considered, it can be shown that

modules with even order generate one transmission zero in each stopband, while modules of odd order generate only one zero in the upper stopband.

4.3. Coupling Coefficients in Filter Design

4.3.1. Coupling Coefficients

In lowpass filter prototypes, discussed in section 3.3, coupling matrices described cross-coupled filters with unity bandwidth at zero centre frequency in terms of normalized frequency variable Ω. Consequently, entries M_{ij} of a coupling matrix characterize the degree of interaction between adjacent resonators required to satisfy these conditions. However, real filters are designed to perform at a certain centre frequency f_0 with a specified bandwidth *BW*. Therefore, in order to provide link between the model and reality, coupling values are normalized to fractional bandwidth $FBW = BW / f_0$. Values obtained as a result of this normalization are referred to as coupling coefficients.

At the schematic circuit level, coupling coefficient between two resonators connected through admittance inverter J_{ij} is introduced as follows [4-12]

$$k_{ij} = FBW \cdot \frac{J_{ij}}{\sqrt{B_i \cdot B_j}} \tag{4.3-1}$$

where

$$B_k = \frac{1}{2} \cdot \left. \frac{\partial B_k(\omega)}{\partial \omega} \right|_{\omega=\omega_0}, \qquad k = i, j \tag{4.3-2}$$

represents total susceptance of the k^{th} resonator.

External couplings are defined by the external quality factor:

$$Q_{ext,i} = \frac{G_0}{FBW \cdot J_{0,i}^2} \tag{4.3-3}$$

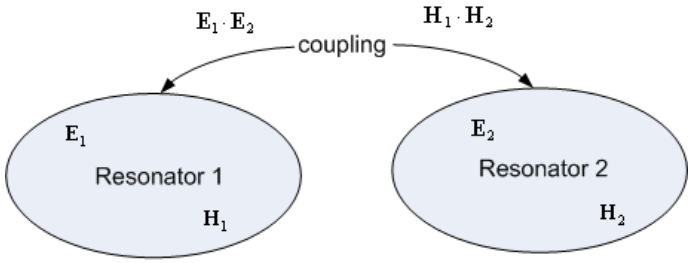

Figure 4-10: General representation of two coupled resonators.

On the other hand, at the electromagnetic level, coupling is considered as transfer of power from one circuit to another. Hence, the coupling coefficient between two resonators is defined as a ratio of coupled energy to stored energy [4-13]:

$$k_{12} = \frac{\iiint \varepsilon \vec{\mathbf{E}}_1 \cdot \vec{\mathbf{E}}_2 dv}{\sqrt{\iiint \varepsilon \left|\vec{\mathbf{E}}_1\right|^2 dv \times \iiint \varepsilon \left|\vec{\mathbf{E}}_2\right|^2 dv}} + \frac{\iiint \mu \vec{\mathbf{H}}_1 \cdot \vec{\mathbf{H}}_2 dv}{\sqrt{\iiint \mu \left|\vec{\mathbf{H}}_1\right|^2 dv \times \iiint \mu \left|\vec{\mathbf{H}}_2\right|^2 dv}} \qquad (4.3\text{-}4)$$

Here, $\vec{\mathbf{E}}$ and $\vec{\mathbf{H}}$ are vectors of electric and magnetic fields of resonators as it is shown in Figure 4-10. The fields are determined at resonance, and volume integrals are taken over the entire effective region with permittivity ε and permeability μ. Generally, the resonators 1 and 2 may have different resonant frequencies. The first term in equation (4.3-4) represents electric coupling component, while the second one – magnetic coupling component. Coupling coefficient may possess positive or negative values due to dot multiplication of fields' space vectors.

4.3.2. Extraction of Coupling Coefficients

Coupling coefficients play very important role in filter design. In development of coupled resonators filters, a general technique is employed in order to relate values of coupling coefficients obtained theoretically to physical dimensions of structures which implement the couplings. Coupling between two resonators, synchronously or asynchronously tuned, can be characterised by two eigen frequencies that can be indentified by experiment or full wave EM simulation. Coupling coefficients extraction procedure from frequency responses for synchronously and asynchronously tuned resonators can be found in [4-14], [4-15].

4.3.1.1. Synchronously Tuned Resonators

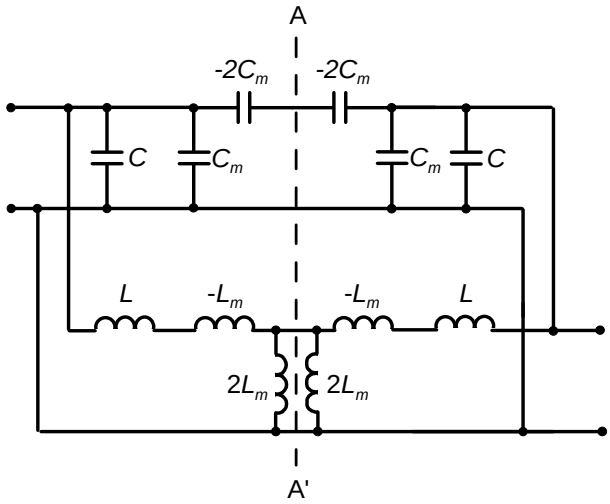

Figure 4-11: Schematic circuit representation of two synchronously tuned coupled resonators with mixed coupling.

Network representation of two identical resonators with both capacitive and inductive couplings is presented in Figure 4-11, where C, L, C_m, and L_m are the self-capacitance, the self-inductance, the mutual capacitance, and the mutual inductance of the resonators respectively. Taking advantage of the circuit's symmetry, electric and magnetic walls can be inserted in the symmetry plane A-A', and even-odd mode technique can be applied to the schematic circuit. As a result of the analysis, two resonant frequencies of the equivalent circuit can be found as follows

$$f_e = \frac{1}{2\pi\sqrt{(L-L_m)(C-C_m)}} \tag{4.3-5a}$$

$$f_m = \frac{1}{2\pi\sqrt{(L+L_m)(C+C_m)}} \tag{4.3-5b}$$

Coupling coefficient *k* between these resonators is calculated as a superposition of its electric and magnetic components as

$$k = k_e + k_m = \frac{L_m}{L} + \frac{C_m}{C} \tag{4.3-6}$$

assuming that couplings are weak, which implies $L_m C_m << LC$. Combining equations (4.3-5) and (4.3-6), an expression for extraction of coupling coefficient between synchronously tuned resonators can be obtained:

$$k = \frac{f_e^2 - f_m^2}{f_e^2 + f_m^2} \tag{4.3-7}$$

4.3.1.2. Asynchronously Tuned Resonators

A similar method as shown in the previous section can be used for analysis of coupling coefficient between a pair of asynchronously tuned resonators. Assuming that one of the resonators has its self-resonant frequency at $f_{01} = \frac{1}{2\pi\sqrt{L_1 C_1}}$ and another one – at $f_{02} = \frac{1}{2\pi\sqrt{L_2 C_2}}$, coupling coefficient *k* between them can be calculated as follows

$$k = \pm\frac{1}{2}\left(\frac{f_{02}}{f_{01}} + \frac{f_{01}}{f_{02}}\right)\sqrt{\left(\frac{f_2^2 - f_1^2}{f_2^2 + f_1^2}\right)^2 - \left(\frac{f_{02}^2 - f_{01}^2}{f_{02}^2 + f_{01}^2}\right)^2} \tag{4.3-8}$$

where f_2 and f_1 are resonant frequencies of the obtained system of coupled resonators.

4.3.1.3. External Quality Factor

External *Q*-factor of a resonator can be extracted by determining its 3dB-bandwidth from its frequency response. Consider an equivalent schematic circuit of a doubly-loaded resonator presented in Figure 4-12.

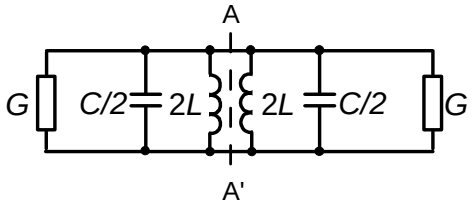

Figure 4-12: Schematic circuit representation of a doubly-loaded resonator.

In this figure, *A–A'* represents the symmetry plane and the single *LC* resonator has been separated into two symmetrical parts. Applying even-odd mode technique, one can obtain the following expressions for even- and odd-mode reflection coefficients [4-13]:

$$S_{11e} = \frac{1 - jQ_e \Delta\omega/\omega_0}{1 + jQ_e \Delta\omega/\omega_0} \tag{4.3-9a}$$

$$S_{11o} = -1 \tag{4.3-9b}$$

where $\omega_0 = 1/\sqrt{LC}$ and $\omega = \omega_0 + \Delta\omega$ with approximation $\Delta\omega = (\omega^2 - \omega_0^2)/(2\omega)$, and singly-loaded external *Q*-factor is denoted by

$$Q_e = \frac{\omega_0 C}{G} \tag{4.3-10}$$

Therefore, after several manipulations, magnitude of transmission coefficient can be written as follows

$$|S_{21}| = \frac{1}{\sqrt{1 + (Q_e \Delta\omega/\omega_0)^2}} \tag{4.3-11}$$

It can be noticed from (4.3-11) that $|S_{21}|$ equals to 0.707 (or –3dB) when

$$Q_e \frac{\Delta\omega}{\omega_0} = \pm 1 \tag{4.3-12}$$

Hence, 3dB-bandwidth and singly-loaded external *Q*-factor can be calculated as

$$\Delta\omega_{3dB} = \frac{2\omega_0}{Q_e} \tag{4.3-13}$$

$$Q_e = \frac{2\omega_0}{\Delta\omega_{3dB}} \tag{4.3-14}$$

Doubly-loaded external *Q*-factor is a half of the singly loaded one, and it can be extracted from frequency response as

$$Q'_e = \frac{\omega_0}{\Delta\omega_{3dB}} \tag{4.3-15}$$

Another extraction technique for the singly-loaded external *Q*-factor based on analysis of phase characteristic of reflection coefficient has been reported in [4-13]. In this case

$$Q_e = \frac{\omega_0}{\Delta\omega_{\pm 90^\circ}} \tag{4.3-16}$$

where $\Delta\omega_{\pm 90^\circ}$ – is the absolute bandwidth between $\pm 90^\circ$ points in phase response of reflection coefficient S_{11} against frequency.

4.4. Filter Design Examples

In this section, two design examples of filters based upon the modules introduced previously in this chapter are presented.

4.4.1. Design of a 4th-order Filter with Hairpin and I-shaped Resonators

To demonstrate the design of an E-plane filtering module introduced in section 4.2.3, a fourth-order bandpass filter which, as shown previously, has two transmission zeros in both stopbands is implemented in conventional rectangular waveguide. The filter is designed to satisfy the following specifications:

- centre frequency: 10.4 GHz;
- ripple passband: 10.1 – 10.7 GHz;
- return loss: 30 dB;
- transmission zeros: 9.6 GHz and 11.9 GHz.

4.4.1.1. Approximation and Synthesis

Frequency response of the filter has been approximated by means of the standard technique for pseudo-elliptic filters, presented in section 3.2.4. The filter specifications yield the following expressions for the S-parameters of the lowpass prototype:

$$S_{11}(s)=\frac{F(s)}{E(s)}, \qquad S_{21}(s)=\frac{P(s)}{\varepsilon \cdot E(s)} \tag{4.4-1}$$

$$P(s)=s^2 - j1.907s + 13.0149 \tag{4.4-2}$$

$$F(s)=s^4 + j0.0783s^3 + 1.0085s^2 + j0.0591s + 0.1293 \tag{4.4-3}$$

$$\begin{aligned}\varepsilon \cdot E(s)=3.1471\cdot(s^4+(3.1764+j0.0783)s^3+(6.0532+j0.3312)s^2+\\ +(6.8307+j0.7164)s+(4.0611+j0.7917))\end{aligned} \tag{4.4-4}$$

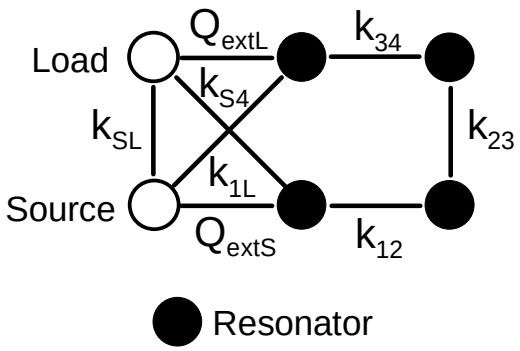

Figure 4-13: Coupling scheme of a 4th-order filter with two transmission zeros in both stopbands.

Coupling scheme of the filter with corresponding coupling coefficients is shown in Figure 4-13. The scheme has been obtained using analysis of physical structures proposed in section 4.2.3. It consists of five mainline couplings between adjacent resonators, a bypass direct source-load coupling, and two parasitic couplings between first and last resonators and source/load. The origin and effect of this coupling have been considered in section 4.2.2. Coupling matrix of the filter has been obtained by optimization, using an adaptive algorithm (see section 3.3.3.5) realized in MATLAB™ by author. The denormalized matrix has the following form:

$$M = \begin{bmatrix} 0 & 1.2727 & 0 & 0 & 0.0311 & 0.0247 \\ 1.2727 & 0 & -1.1952 & 0 & 0 & 0.0311 \\ 0 & -1.1952 & 0 & -0.8746 & 0 & 0 \\ 0 & 0 & -0.8746 & 0 & -1.1952 & 0 \\ 0.0311 & 0 & 0 & -1.1952 & 0 & 1.2727 \\ 0.0247 & 0.0311 & 0 & 0 & 1.2727 & 0 \end{bmatrix} \quad (4.4\text{-}5)$$

Thereafter, coupling coefficients can be calculated from formulae (4.3-1) and (4.3-3). These values are: $Q_{extS} = Q_{extL} = 10.701$, $k_{12} = k_{34} = -0.069$, $k_{23} = -0.05$, $k_{SL} = 0.0014$, $k_{S4} = k_{1L} = 0.0018$.

4.4.1.2. Implementation

The filter has been implemented using two hairpin and two I-shaped resonators etched in the middle layer of a metallo-dielectric insert placed between two septa, arranged in the E-plane of a conventional rectangular waveguide. Configuration of the filter, together with a view of the metallo-dielectric insert containing stripline resonators, is presented in Figure 4-14.

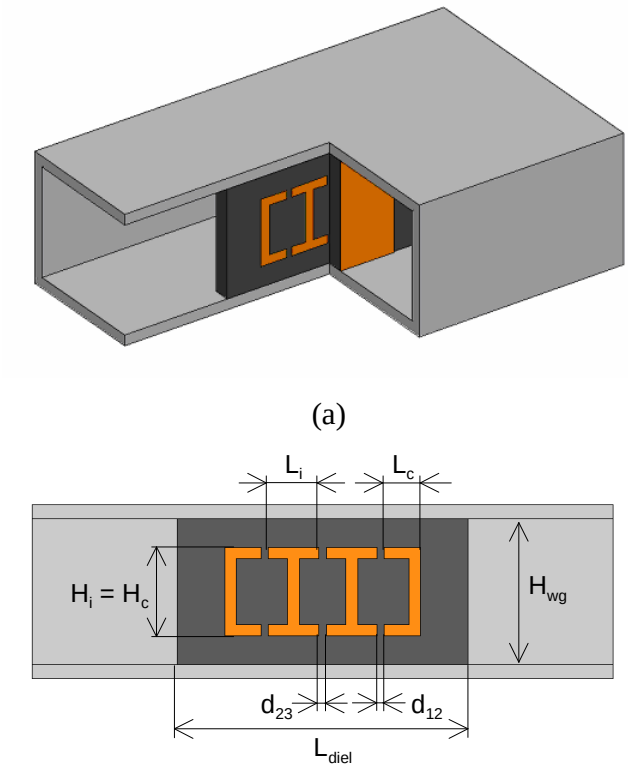

Figure 4-14: Configuration of the proposed 4th-order filtering module: (a) 3D-view; (b) metallo-dielectric insert with stripline resonators.

Design of the filter begins with determination of the required width of the double septum. This can be done by extraction of value of inverter implemented by the septum from its simulated reflection coefficient using the following expression:

$$J_{SL} = \sqrt{\frac{1-S_{11}}{1+S_{11}}} \tag{4.4-6}$$

To obtain the corresponding coupling coefficient k_{SL}, the extracted value should be multiplied by *FBW*.

Determination of dimensions of resonators has been done by analysis of frequency responses of doubly loaded hairpin and I-shaped resonators. I-shaped resonators have been examined as a stripline resonator with capacitive external couplings through a gap. Hairpin resonators are not pure stripline resonators as these are partially located between two septa; in this application, hairpin resonators can be considered as stepped-impedance resonators. Resonant frequency of these resonators depends on length of their fractions located between septa. For analysis of the hairpin resonator's resonant frequency, it has been considered as a network operating between rectangular waveguide input and stripline output. For analysis of external *Q*-factor of these resonators, the stripline output has been removed, so the structure has been analyzed as a single-port network, and external *Q*-factor has been extracted using expression (4.3-16).

Gaps d_{12} and d_{23} between the resonators have been determined by plotting dependencies of certain coupling coefficients, extracted from full-wave simulations, against physical dimensions of the insert's elements for certain pairs of adjacent resonators. The coupled resonators have been simulated as two-port networks with stripline inputs for I-shaped resonators and rectangular waveguide inputs for hairpin resonators; it should be noted that the resonators should be weakly coupled to the inputs in order to keep accuracy of the procedure. A set of frequency responses used for extraction of coupling coefficient between hairpin and I-shaped resonators is presented in Figure 4-15. Coupling coefficients have been extracted from the frequency response using formula (4.3-7). Dependencies of extracted coupling coefficients against gaps d_{12} and d_{23} are shown in Figure 4-16.

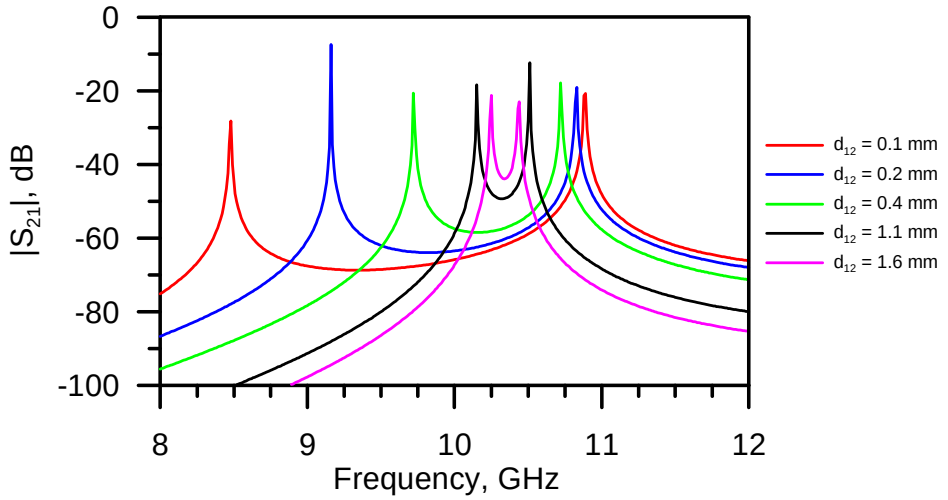

Figure 4-15: Simulated frequency responses used for extraction of coupling coefficient k_{12}.

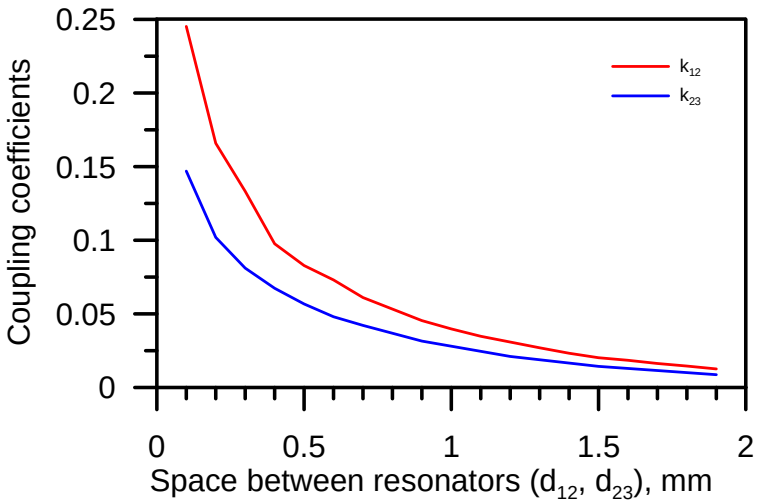

Figure 4-16: Extracted coupling coeffcients k_{12} and k_{23} against gaps d_{12} and d_{23}.

The described procedure based upon coupling coefficients extraction gives initial dimensions of the filter structure for further optimization (see section 3.5.2) which, for this filter, has been carried in full-wave EM simulator Ansoft HFSS™ using quasi-Newton procedure.

4.4.1.3. Experimental Verification

The structure has been fabricated in order to demonstrate performance of the proposed filter and prove its feasibility. Due to restrictions of the available manufacturing technology, the

entire device has been realized using four separate components: two identical septa have been cut out of a sheet of copper foil with thickness T_{Cu} = 0.1 mm; and two pieces of dielectric have been cut out of a slab of Rogers Duroid RT/5880™ substrate (ε_r = 2.2, tanδ = 0.0009; thickness T_{diel} = 1.5 mm). One side of both dielectric pieces have been etched: the pattern with hairpin and I-shaped resonators has been formed on the first piece, while the second piece has been patterned by a copper strip repeating the shape of septa in order to simplify the assembling process. The four components have been arranged between two halves of brass housing, in the E-plane of a standard waveguide WR90 (22.86×10.16 mm^2). Photograph of the components and assembled halves of the filter is presented in Figure 4-17. Dimensions of the filter are given in Table 4-1.

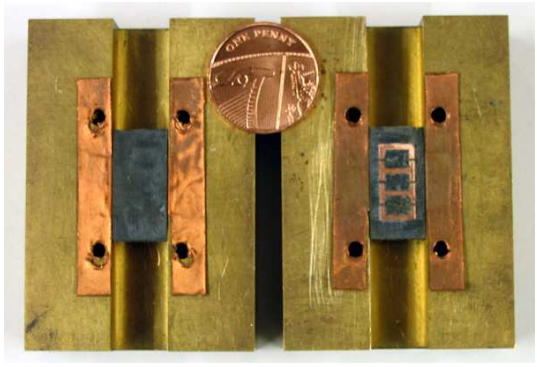

Figure 4-17: Photograph of the fabricated filter 4th-order filter.

Parameter	Value, mm
H_c	5.5
H_i	5.45
L_c	2.6
L_i	3.5
d_{12}	0.5
d_{23}	0.5
L_{sept}	10.4
L_{diel}	20

Table 4-1: Dimensions of the fabricated 4th-order filter (see Figure 4-14).

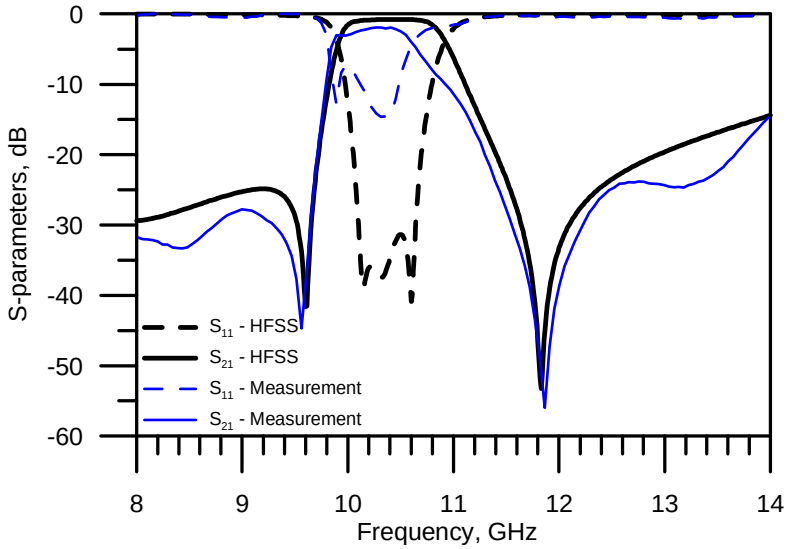

Figure 4-18: Simulated and experimental frequency responses of the fabricated 4th-order filter with two transmission zeros.

The filter has been tested using the Agilent Technologies E8361A network analyzer. Measured S-parameters are shown in Figure 4-18 in comparison with simulation results. Agreement of the curves is reasonable taking into account fabrication and measurement inaccuracies. The reason of good agreement of the simulated and measured transmission zeros is that their positions are mainly determined by the length of two septa which have been fabricated using the accurate PCB cutting process. On the other hand, the laboratory did not possess enough milling tools to remove the top and bottom metallization layers of the PCB slabs with high accuracy. Consequently, the metallization has been removed manually. As a result of this less accurate process, the hairpin resonators have been slightly damaged. This caused the shift of their resonant frequencies. At the same time, use of the separate copper inserts caused the issue of inaccurate alignment between the septa and the dielectric pieces, which has also resulted in shift of the hairpin resonators' resonant frequencies. Taking into account high sensitivity of the filter to fabrication tolerances (particularly, to the resonators' dimensions), the above issues have resulted in the severe degradation of the inband performance.

4.4.2. Application of E-plane Doublets in Modular Filters

Doublets, as well as singlets, can be used as units for modular filter design which allows overcoming issues related with high sensitivity of cross-coupled filters to manufacturing tolerances. The doublet structure introduced in section 4.2.2 can be applied as a module to more complicated frequency selective devices. There are two possible ways to arrange two doublets in space in order to obtain advanced filter structure. Unit sections can be connected in series or in parallel.

4.4.2.1. Inline Filter with NRN

Connecting modules based on hairpin resonators and septum in series, an inline bandpass filter with four transmission zeros and four poles can be obtained. Since input and output nodes of doublets are non-resonating, cascading of modules has to be performed via NRN, role of which can be played by sections of waveguide with electrical length longer than wavelength about the centre frequency of the filter. For a bandpass filter composed of two doublets, design leads to the functional scheme presented in Figure 4-19.

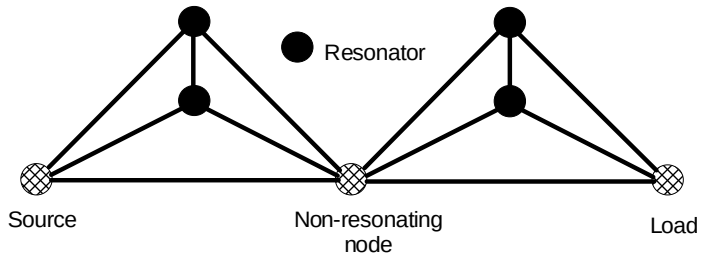

Figure 4-19: Coupling scheme of a doublet-based inline filter with NRN.

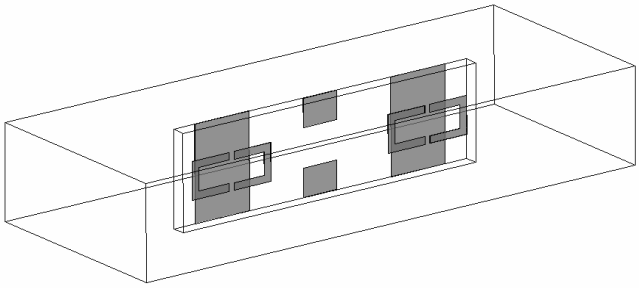

Figure 4-20: Configuration of a doublet-based inline filter with NRN.

Configuration of the inline filter with two doublets designed for centre frequency of 10.2 GHz with 900 MHz bandwidth is shown in Figure 4-20. The structure contains two identical doublets connected via an NRN which is represented by a waveguide resonator with E-plane ridge, added in order to lower the spurious resonance frequency and thus improve lower stopband of the filter, maintaining its compactness.

4.4.2.2. Dual-Band Filter

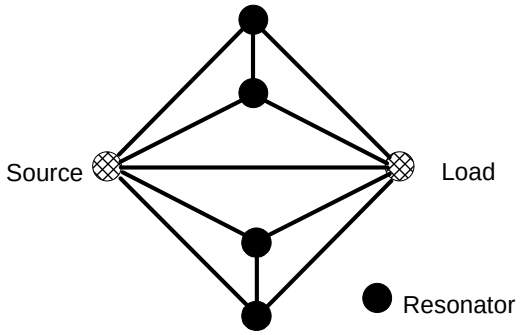

Figure 4-21: Coupling scheme of a doublet-based dual-band filter.

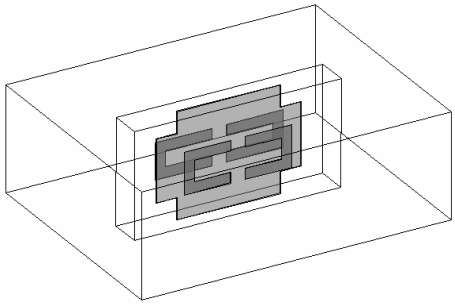

Figure 4-22: Configuration of a doublet-based dual-band filter.

Utilization of the doublet's septum as a shield makes it possible to apply connection of doublets in parallel. Two pairs of capacitively coupled hairpin resonators placed on both sides of the septum can act independently and without interaction between different pairs due to shielding effect of the septum. As a result, resonant frequency of one of coupled pairs can be moved higher or lower maintaining the coupling scheme and signs of coupling

coefficients. Thus, two doublets are organized at different central frequencies simultaneously, and the structure acts as a dual-band filter with four poles and four transmission zeros. Coupling scheme of the filter is given in Figure 4-21. View of the dual-band filter's Ansoft HFSS™ model with passbands at 7.9 – 8.4 GHz and 10.4 – 10.8 GHz is presented in Figure 4-22. It must be noted that septum has additional fragments attached to its sides in order to prevent parasitic coupling between shielded resonators.

4.4.2.3. Experimental Verification

The proposed doublet inserts have been fabricated by etching the top side of a 1.524 mm thick Rogers RT/Duroid 5880 substrate (ε_r = 2.2, tanδ = 0.0009) with 0.017 mm copper cladding using a standard PCB process. Copper metallization has been completely removed from the bottom side of the dielectric inserts. The septum has been cut out of a copper foil sheet with thickness of 0.1 mm. Finished insertions have been placed into the E-plane of a rectangular waveguide WR90 (22.86×10.16 mm^2) composed of two housing halves made of brass. Photograph of the E-plane inserts and septa used for experimental verification are presented in Figure 4-23.

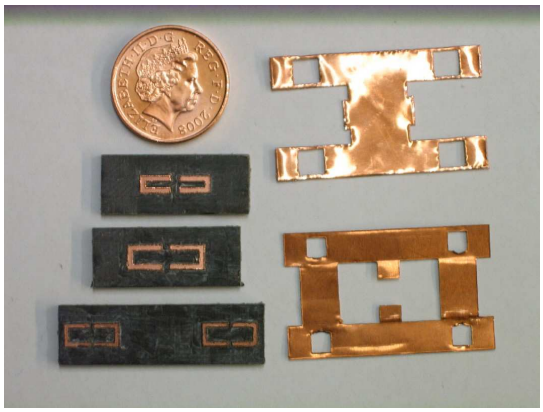

Figure 4-23: Metallo-dielectric waveguide inserts for implementation of the proposed doublet-based filters.

Frequency responses of the doublets and filters have been measured with Agilent PNA (E8361A) network analyzer. Experimental frequency responses of the structures have been compared to those simulated in Ansoft HFSS™. In Figure 4-24 simulated and experimental transmission coefficients of the doublet with a passband of 7.9–8.4 GHz are presented.

Dimensions of the structure are given in Table 4-2. Experimental curve appears to be shifted upper by 0.25 GHz and to exhibit insertion loss of 1.5 dB.

Parameters	Dimensions, mm
Width of septum, W_{sept}	11.5
Length of hairpin resonator, L_c	6
Height of hairpin resonator, H_c	4.3
Line width of hairpin resonator, W_c	1
Gap between resonators, *Gap*	1.1
Length of dielectric slab, L_{diel}	25
Length of waveguide section, L_{wg}	60

Table 4-2: Dimensions of the fabricated doublet.

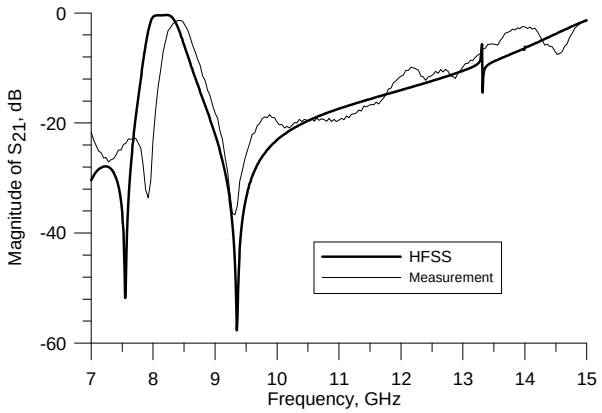

Figure 4-24: Simulated and measured transmission coefficients of a single doublet.

Comparison of measurement and simulation results for the inline filter is shown in Figure 4-25. Dimensions of the filter are given in Table 4-3. The measured curve is again shifted to upper frequencies; the structure has all four predicted transmission zeros and shows insertion loss of 2 dB in passband.

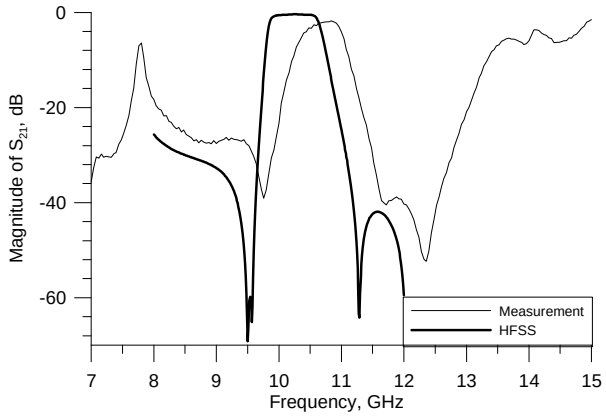

Figure 4-25: Simulated and measured frequency responses of inline filter with NRN.

Parameters	Dimensions, mm
Width of septa, W_{sept}	6.5
Length of hairpin resonator, L_c	4.4
Height of hairpin resonator, H_c	4
Line width of hairpin resonator, W_c	0.8
Gap between resonators, *Gap*	0.6
Length of non-resonating node, L_{nrn}	16.9
Length of dielectric slab, L_{diel}	35
Length of waveguide section, L_{wg}	60

Table 4-3: Dimensions of inline filter with NRN.

Dielectric slab with two hairpins has been added to the structure depicted in Figure 4-4 in order to realize a dual-band filter. Dimensions of the smaller hairpins are given as follows: L_c = 5.3 mm, H_c = 3 mm, *Gap* = 1.4 mm. In Figure 4-26 simulated and experimental responses of the dual-band filter are presented. Measured response is shifted and upper passband exhibits extra 2 dB insertion loss in comparison with simulation.

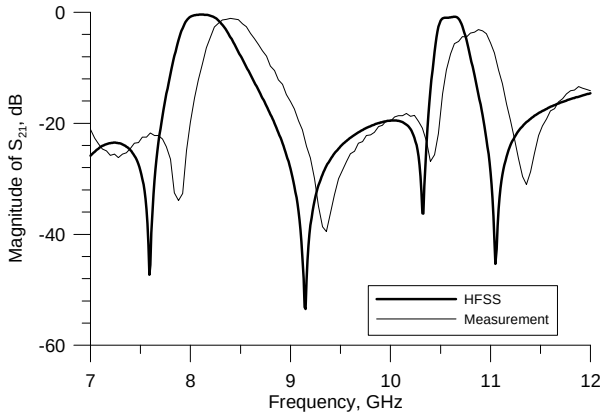

Figure 4-26: Simulated and measured transmission coefficients of the doublets-based dual-band filter.

It can be concluded from comparison of simulated and experimental results that agreement is quite good taking into account inaccuracies of manufacturing and measurement. However it can be suggested that experimental responses displays an offset to higher frequencies in all the plots. This can be explained by accuracy of a mill used and alteration of effective permittivity in waveguide due to removal of a quite thick layer of dielectric substrate by etching machine together with cladding. Higher insertion loss in the upper band of the dual-band filter occurred due to a fabrication error. Metallization of the dielectric inserts of the filter was first removed using the PCB milling machine, and then, in the areas where milling was unsuccessful, copper was removed manually. Frequency response of the filter in the upper passband is determined by the insert containing two small hairpin resonators (see Figure 4-23). In the area between the hairpin resonators the metallization was removed manually which resulted in shortening of the left resonator due to error. Therefore, the resonant frequency of the left resonator has shifted upper and this mismatch lead to increase of the insertion loss in passband.

4.5. Summary

In this chapter the problem of cross-coupled filters design using metallo-dielectric E-plane inserts in rectangular waveguides has been considered.

In section 4.2 E-plane singlets, doublets and higher order filtering modules capable of generating transmission zeros in upper and lower stopbands have been introduced. Coupling schemes and corresponding coupling matrices of the modules have been analyzed theoretically. Implementation technique for the E-plane modules using stripline resonators and septa has been proposed. The introduced concept allows designing simple and compact filters with improved stopband performance in rectangular waveguides without using negative coupling elements.

In section 4.3 the concept of coupling coefficients between coupled resonators has been discussed. Methods of coupling coefficients extraction from simulated or measured frequency responses of the coupled resonators have been derived for synchronously and asynchronously tuned resonators.

Finally, in section 4.4 several design examples of cross-coupled filters have been presented. A compact 4^{th}-order filter with two transmission zeros has been designed and implemented using a multilayer E-plane insert with hairpin and I-shaped stripline resonators. Utilization of doublets as basic modules for advanced cross-coupled filters has been illustrated by design of a 4^{th}-order bandpass filter with NRN, which has four transmission zeros, the maximum possible number. Also, a dual-band filter realized using two doublets connected in parallel has been proposed. The filters have been fabricated and tested in order to prove adequacy of the introduced ideas. Frequency responses of all the fabricated filters have suffered from inaccurate fabrication process. The numerous errors have been related to lack of practical experience at the machine PCB fabrication, as well as to unavailability of tools required for the process. Unavailability of suitable waveguide housing with a thick channel has become an additional difficulty. Despite that, the obtained experimental results have shown reasonable agreement with the simulated data and prove validity of the approach.

4.6. References

[4-1] R. Hershtig, R. Levy, and K. Zaki, “Synthesis and design of cascated trisection (CT) dielectric resonator filters,” in *Proc. European Microwave Conf.*, pp. 784–791, 1997

[4-2] R. Levy and P. Petre, “Design of CT and CQ filters using approximation and optimization,” in *IEEE MTT-S Int. Microwave Symp. Dig.*, Phoenix, AZ, pp. 1467–1470, May 2001

[4-3] S. Amari, U. Rosenberg, and J. Bornemann, “Singlets, cascaded singlets and the nonresonating node model for advanced modular design of elliptic filters,” *IEEE Microw. Wireless Compon. Lett.*, vol. 14, no. 5, pp. 237–239, May 2004

[4-4] S. Amari, “On the Maximum Number of Finite Transmission Zeros of Coupled Resonator Filters With a Given Topology,” *IEEE Microw. Wireless Compon. Lett.*, vol. 9, pp. 354-356 , Sept. 1999

[4-5] S. Amari and J. Bornemann, “Maximum Number of Finite Transmission Zeros of Coupled Resonator Filters With Source/Load Multi-Resonator Coupling and a Given Topology,” *Microwave Conference 2000 Asia Pacific*, pp. 1175-1177, Dec. 2000

[4-6] Y. Konoshi, and K. Uenakada, “The design of a bandpass filterwith inductive strip-planar circuit mounted in waveguide,” *IEEE Trans. Microwave Theory Tech.*, vol. MTT-22, pp. 869-873, Oct.1974

[4-7] Y. C. Shih, “Design of waveguide E-plane filters with all-meial inserts,” *IEEE Trans. Microwave Theory Tech.*, vol. MTT-32, pp. 695-704, 1984

[4-8] I. C. Hunter, *Theory and Design of Microwave Filters*, London, U.K.: IEE Press, 2001

[4-9] S. Amari and U. Rosenberg, “A universal building block for advanced modular design of microwave filters,” *IEEE Microw. Wireless Compon. Lett.*, vol. 13, pp. 541–543, Dec. 2003

[4-10] J.-S. Hong and M. J. Lancaster, “Cross-coupled microstrip hairpin-resonator filters,” *IEEE Trans. Microwave Theory Tech.*, vol. 46, pp. 118–122, Jan. 1998

[4-11] J. B. Thomas, “Cross-Coupling in Coaxial Cavity Filters – A Tutorial Overview,” *IEEE Trans. Microwave Theory Tech.*, vol. 51, no. 4, pp. 1368–1376, Apr. 2003

[4-12] G. L. Matthaei, L. Jones and E. M. T. Jones, *Microwave Filters, Impedance Matching Networks and Coupling Structures*, New York: McGraw-Hill, 1964

[4-13] J.-S. Hong and M. J. Lancaster, *Microstrip Filters for RF/Microwave Applications*. New York: Wiley, 2001

[4-14] J.-S. Hong, "Couplings of asynchronously tuned coupled microwave resonators," *Proc. Inst. Elect. Eng.– Microw., Antennas, Propag.*, vol. 147, no. 5, pp. 354–358, Oct. 2000

[4-15] J.-S. Hong and M. J. Lancaster, "Couplings of microstrip square open-loop resonators for cross-coupled planar microwave filters," *IEEE Trans. Microwave Theory Tech.*, vol. 44, no. 11, pp. 2099–2109, Nov. 1996

CHAPTER 5

E-PLANE EXTRACTED POLE FILTERS IN CONVENTIONAL RECTANGULAR WAVEGUIDE

5.1. Introduction

Inline extracted pole filters with NRN have become very popular in recent years due to their ability to produce the maximum number of transmission zeros equal to the order of the filter without direct coupling between source and load. The filters exhibit the property of modularity, since positions of transmission zeros can be controlled independently by adjusting parameters of separate extracted pole sections (EPS).

In rectangular waveguide technology, extracted pole filters are implemented by means of coupled resonating and non-resonating cavities [5-1]–[5-3]. This approach is inflexible, as it excessively consumes time and resources due to fabrication of waveguide housing for each individual filter. In contrast, E-plane technology [5-4], where all-metal or metallo-dielectric inserts are arranged in the E-plane of rectangular waveguides, offers more design flexibility due to its simplicity, inexpensiveness and the fact that it allows implementation of varieties of filters through utilizing the same housing. As long as E-plane inserts are arranged in longitudinal direction, the extracted pole filters with inline topology make the ideal solution suitable for implementation in the E-plane technology. However, to present day, very few works have been dedicated to the design of extracted pole filters in E-plane technology. In [5-5] the E-plane bandpass filter was implemented with EPS connected directly to input and output; internal EPS were used in [5-6] for realization of a bandstop filter.

During the last decade, several investigations into methods of miniaturizing conventional E-plane filters, as well as making improvements to their stopband performance have been carried out. It has been shown that split ring resonators (SRR) [5-7], [5-8] and S-shaped

resonators [5-9], embedded within the E-plane resonators, cause shifting of fundamental resonance of the structure to lower frequencies and generate a transmission zero in upper stopband. The observed phenomena have been speculatively explained by metamaterial effects which occur in periodical lattices composed of SRRs or S-shaped resonators. However, no convincing explanations of the effects based upon the filter theory have been given yet. In this chapter, a comprehensive theoretical explanation of the observed effects is given; the E-plane resonator with embedded SRR of S-shaped resonator is considered as an EPS, capable of generating a single pole-transmission zero pair.

In section 5.2 EPS containing NRNs are introduced as key components of inline extracted pole filters. Main properties of the circuit are outlined. Abstract generalized coupling coefficients, applied for design of filters with NRNs, are presented in section 5.3. Extraction techniques for generalized coupling coefficients within EPS and between them are given. In section 5.4 realization of EPS in E-plane technology is discussed. Several potential implementations are proposed. It is shown that the E-plane resonators with embedded resonators act as EPS; generalized coupling coefficients of the EPS are investigated as functions of physical dimensions. Finally, in section 5.5 several design examples of inline extracted pole filters implemented in E-plane technology are presented. Compact filters with transmission zeros in both lower and upper stopbands are designed and fabricated. Experimental verification of theoretical results and simulations is carried out in order to prove adequacy of the proposed model.

5.2. Extracted Pole Sections

Extracted pole sections originate from reconfiguration of the inline extracted pole filter prototype network discussed in section 3.3.4. The transmission line section, removed at the first stage of the synthesis procedure, can be represented as an equivalent circuit composed of an inverter and two FIR elements. Details of the transformation are presented in Figure 5-1.

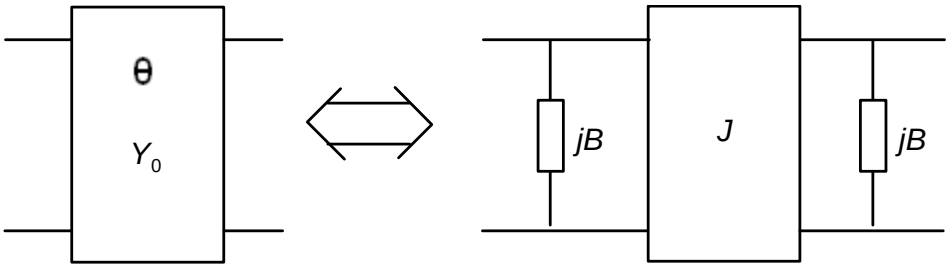

Figure 5-1: Transformation of a transmission line section in extracted pole filter prototypes.

As a result of the above transformation, the prototype of the extracted pole filter can be reconfigured into an inline inverter-coupled network, which consists of EPS and single resonators. The EPS are composed of a bandstop section connected in parallel with an FIR element, as shown in Figure 5-2a. The shunt FIR element is also referred to as a non-resonating node, and in coupling schemes it is usually denoted by a special symbol. In Figure 5-2b, an equivalent representation of an EPS is given as a coupling scheme composed of two resonating and non-resonating nodes. The inverter is presented as a line connecting the nodes. Generally, EPS may be removed from the circuit not only at the ends of the direct-coupled network, but also can be formed in the middle of a filter prototype [5-1, 5-2, 5-10]. The entire coupling scheme of a 3rd-order extracted pole filter with two transmission zeros is depicted in Figure 5-3.

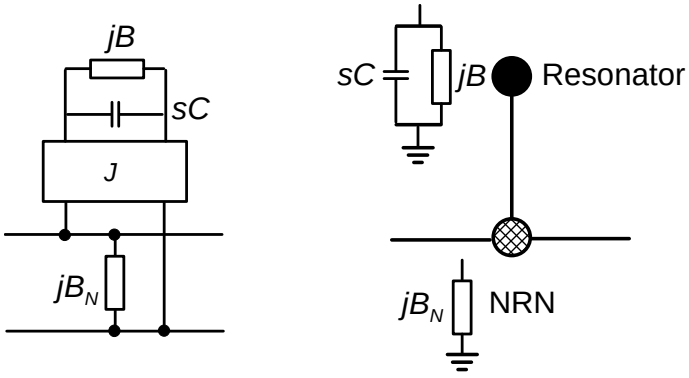

(a) (b)

Figure 5-2: Extracted pole section: (a) schematic representation; (b) coupling scheme representation.

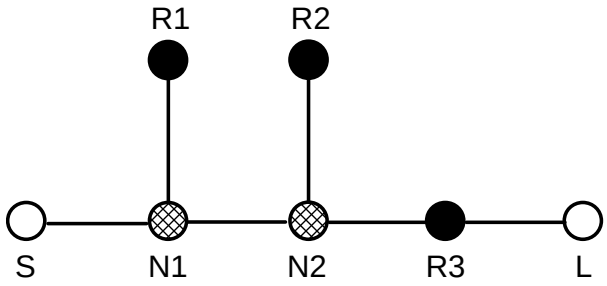

Figure 5-3: Coupling scheme of a 3rd-order extracted pole filter with two transmission zeros.

Direct-coupled extracted pole filters can also be synthesized from input impedance/admittance rational functions by applying the direct synthesis technique, which is explained in [5-10, 5-11] in details.

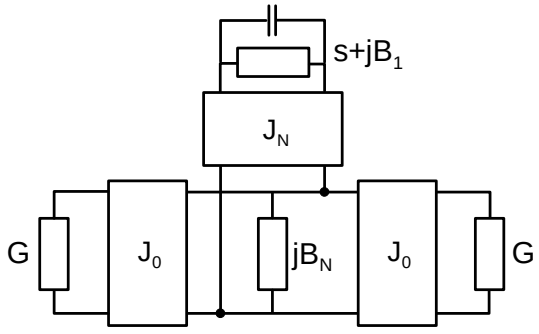

Figure 5-4: Schematic representation of a doubly-loaded extracted pole section.

In Figure 5-4 an equivalent schematic circuit of single doubly-loaded EPS is presented, where J_0 and J_N represent admittance inverters, the resonator is modelled as unity capacitance connected in parallel with frequency invariant susceptance B_1. Another frequency invariant susceptance B_N represents a non-resonating node. The circuit is doubly loaded with unity loads G. Taking advantage of the circuit's symmetry, even-odd mode technique can be applied to analyze the prototype. The reflection coefficient can be calculated as follows:

$$S_{11}(\Omega) = \frac{1}{1 - jF(\Omega)}, \tag{5.2-1}$$

Where

$$F(\Omega) = \frac{2J_0^2(\Omega + B_1)}{B_N\left(\Omega + B_1 - \frac{J_N^2}{B_N}\right)} \tag{5.2-2}$$

Here, Ω is a lowpass prototype frequency variable which can be obtained from real frequency f by standard bandpass to lowpass transformation:

$$\Omega = \frac{1}{FBW}\left(\frac{f}{f_0} - \frac{f_0}{f}\right), \tag{5.2-3}$$

where f_0 is centre frequency of the filter to be designed and FBW – its fractional bandwidth.

The frequency response of the prototype circuit has a transmission zero at Ω_Z and a pole at Ω_P:

$$\Omega_Z = -B_1 \tag{5.2-4}$$

$$\Omega_P = -B_1 + \frac{J_N^2}{B_N} \tag{5.2-5}$$

Typical frequency responses of doubly loaded EPS which generate transmission zeros in upper and lower stopbands are shown in Figure 5-5.

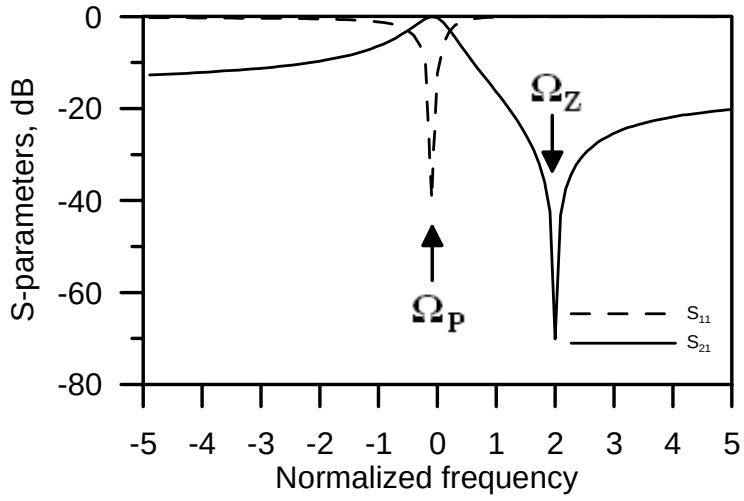

(a)

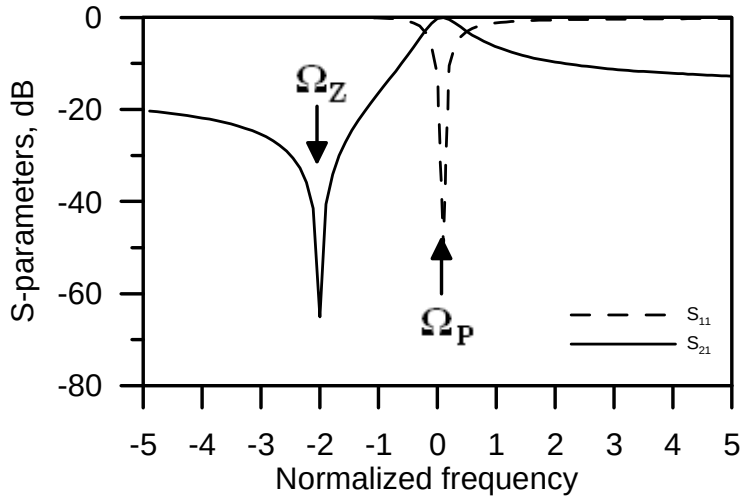

(b)

Figure 5-5: Frequency responses of EPS with a transmission zero in:
(a) upper stopband; (b) lower stopband.

5.3. Generalized Coupling Coefficients for Filters with NRN

Classical coupling coefficients (see section 4.3) can not be used for denormalization of filter prototypes which include NRN, as these become meaningless due to the fact that the couplings involve FIR elements. In 2008, Macchiarella [5-12] introduced generalized coupling coefficients (GCC) which can be used for account of couplings between pairs of NRN and resonators. The parameters can be evaluated from the synthesized lowpass prototype of a filter with NRN, and then used for dimensioning of the physical structure similarly to the classical coupling coefficients.

5.3.1. Generalized Coupling Coefficients

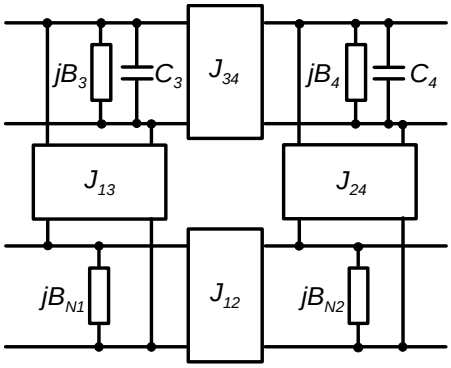

Figure 5-6: Possible couplings within a filter with NRN.

Generalized coupling coefficients are abstract parameters which keep their values when a denormalized filter prototype with NRN is scaled. It has been recently found that in some circuits such as cascaded extracted pole filters these coefficients may be effectively used as design parameters. Figure 5-6 shows all the kinds of couplings possible in a cross-coupled filter with NRN: between two resonators (through inverter J_{12}), between two NRN (inverter J_{34}) and between resonator and NRN (inverters J_{13} and J_{24}). According to Macchiarella [5-12], GCC k_{ij} for these couplings is introduced as follows:

$$k_{ij} = \frac{J_{ij}}{\sqrt{B_i \cdot B_j}} \tag{5.3-1}$$

where B_i and B_j are susceptances of the corresponding resonators or NRN. It should be noted that the variables B_i and B_j have different meanings in eq. (4.3-1) and (5.3-1). In eq. (4.3-1) B_i and B_j are determined by the value of the derivative of the total susceptance at the resonant frequency (see eq. (4.3-2)). In case of the NRN this derivative is always zero, thus the denominator of eq. (4.3-1) equals zero and the entire expression becomes meaningless.

To account couplings with external loads, a generalized external quality factor is defined by

$$Q_{ext,i} = \frac{B_i \cdot G_0}{J_{0,i}^2} \tag{5.3-2}$$

where G_0 is the external conductance.

The GCC k_{ij} and external Q-factor $Q_{ext,i}$ retain properties of the classical coupling coefficients keeping their values during denormalization of a prototype; this means that the GCC fully describe a prototype with NRN up to scaling factor.

To calculate GCC of a certain normalized prototype, fractional bandwidth FBW of the filter should be taken into account. Assume a lowpass prototype, where resonators are represented by a pair of frequency invariant susceptance B_i and capacitance C_i; NRN are defined solely by a frequency invariant susceptance B_j; and couplings are represented by admittance inverters J_{ij}. In this case the GCC can be calculated as follows:

$$k_{ij} = FBW \frac{J_{ij}}{\sqrt{C_i \cdot C_j}} \text{ – resonator-resonator coupling} \tag{5.3-3}$$

$$k_{ij} = \sqrt{FBW} \frac{J_{ij}}{\sqrt{C_i \cdot |B_j|}} \text{ – resonator-NRN coupling} \tag{5.3-4}$$

$$k_{ij} = \frac{J_{ij}}{\sqrt{|B_i| \cdot |B_j|}} \text{ – NRN-NRN coupling} \tag{5.3-5}$$

The generalized external Q-factor for resonating node i can be calculated by

$$Q_{ext,i} = \frac{C_i}{J_{0,i}^2 \cdot FBW} \tag{5.3-6}$$

If node i is NRN, the expression for the generalized external Q-factor yields

$$Q_{ext,i} = \frac{|B_i|}{J_{0,i}^2} \tag{5.3-7}$$

5.3.2. Extraction of GCC for EPS

GCC can be calculated from the synthesized normalized prototype; and also, these values can be extracted from full-wave simulations of the real structures to implement the filter, or from measurement results. The design problem lies in matching calculated and extracted values of the GCC. Solution to this problem gives the initial dimensions of the required filter. In this section, expressions for direct extraction of internal and external GCC of EPS from frequency response are derived.

5.3.2.1. Extraction of Internal NRN–Resonator Coupling

It can be noticed from (5.2-1) and (5.2-2) that the circuit from Figure 5-4 can be completely described by three parameters: two ratios J_N^2 / B_N, J_0^2 / B_N and a frequency invariant susceptance B_1. In terms of GCC, the first ratio connotates the squared coupling coefficient between resonating and non-resonating nodes, whereas the second ratio shows the reverse external quality factor:

$$k_N^2 = \frac{J_N^2}{B_N} \tag{5.3-8}$$

$$Q_{ext} = \frac{B_N}{J_0^2} \tag{5.3-9}$$

Taking into account expressions (5.2-4) and (5.2-5), B_1 and k_N can be extracted from measured or simulated frequency responses using the following expressions:

$$B_1 = -\Omega_Z \tag{5.3-10}$$

$$k_N^2 = \Omega_P - \Omega_Z \tag{5.3-11}$$

It can be concluded from (5.3-8) and (5.3-11) that susceptance of the non-resonating node B_N should be negative to arrange a transmission zero above the filter's passband, and positive to place it below passband. At the same time, expression (5.3-11) shows that separation between two eigenmodes is determined by the absolute value of the GCC k_N. By

finding solutions which allow obtaining higher k_N, stopband performance of the designed filters can be improved by placing additional transmission zeros further from passband.

5.3.2.2. Generalized External Quality Factor

Similarly to the conventional resonators case [5-13], the generalized external quality factor can be extracted from evaluation of the 3dB-bandwidth of a single EPS. It is seen from (5.2-1) that magnitude of S_{11} equals –3dB when $|F(\Omega_{3dB})| = 1$, and therefore the external quality factor can be rewritten as:

$$Q_{ext} = \pm \frac{2\left(\Omega_{3dB} - \Omega_Z\right)}{\Omega_{3dB} - \Omega_P} \tag{5.3-12}$$

Taking into account that half of the 3dB-bandwidth can be approximated as $\Delta\Omega_{3dB}/2 \approx |\Omega_{3dB} - \Omega_P|$, equation (5.3-12) can be simplified to:

$$Q_{ext} \approx \frac{4k_N^2}{\Delta\Omega_{3dB}} \tag{5.3-13}$$

Equations (5.3-10), (5.3-11) and (5.3-13) form a set of expressions for complete characterization of a single EPS with arbitrary implementation. This is particularly important for structures, in which values of inverters or susceptances can not be calculated directly or these calculations are bulky. Examples of such structures will be discussed in section 5.4.

5.3.2.3. Coupling Between Adjacent Asynchronously Tuned Sections

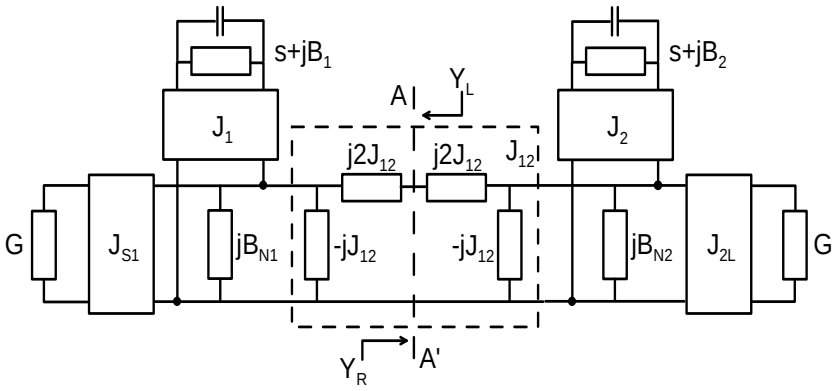

Figure 5-7: Schematic circuit representation of two adjacent EPS coupled through admittance inverter.

Assume that two arbitrary EPS are connected through admittance inverter of value J_{12} as shown in Figure 5-7. For analysis the inverter is replaced with its equivalent Π-network, and condition for natural resonance of the circuit can be written as:

$$\frac{1}{Y_R}+\frac{1}{Y_L}=0\,, \tag{5.3-14}$$

where Y_R and Y_L are the input admittances when we look at the right and the left of the reference plane *A–A'* in Figure 5-7. The input admittances can be expressed as follows:

$$\frac{1}{Y_L}=\frac{1}{2jJ_{12}}+\frac{1}{Y_1-jJ_{12}+\frac{J_{S1}^2}{G}} \tag{5.3-15}$$

$$\frac{1}{Y_R}=\frac{1}{2jJ_{12}}+\frac{1}{Y_2-jJ_{12}+\frac{J_{2L}^2}{G}} \tag{5.3-16}$$

where

$$Y_i = jB_{Ni}\frac{\Omega + B_i - \frac{J_i^2}{B_{Ni}}}{\Omega + B_i}, i = 1, 2 \qquad (5.3\text{-}17)$$

Let us denote the positions of poles and zeros revealed by both single sections examined individually as Ω_{P1}, Ω_{Z1}, Ω_{P2} and Ω_{Z2} respectively. Assuming that external couplings of the structure are very weak, i.e. $J_{S1} = J_{2L} \approx 0$, and applying substitutions from (5.2-4), (5.2-5) in (5.3-17), after several manipulations the following equation can be obtained:

$$\frac{(\Omega - \Omega_{P1})(\Omega - \Omega_{P2})}{(\Omega - \Omega_{Z1})(\Omega - \Omega_{Z2})} = k_{12}^2 \qquad (5.3\text{-}18)$$

where

$$k_{12}^2 = \frac{J_{12}^2}{B_{N1}B_{N2}} \qquad (5.3\text{-}19)$$

is defined as squared GCC k_{12} between two asynchronously tuned EPS.

Roots Ω_1 and Ω_2 of equation (5.3-18) correspond to two self resonances of the system in terms of normalized frequency. Solving (5.3-18) and combining roots, we obtain the expression for experimental evaluation of the squared GCC k_{12}:

$$k_{12}^2 = \frac{\Omega_1\Omega_2 - \Omega_{P1}\Omega_{P2}}{\Omega_1\Omega_2 - \Omega_{Z1}\Omega_{Z2}} \qquad (5.3\text{-}20)$$

5.3.2.4. Coupling Between EPS and Resonator

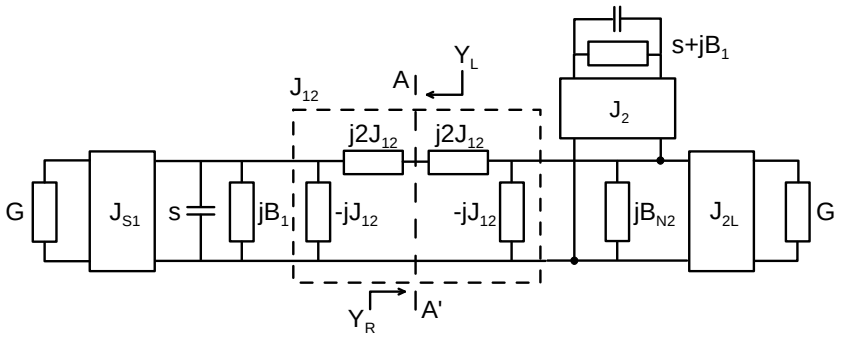

Figure 5-8: Schematic representation of EPS coupled with resonator through admittance inverter.

Schematic circuit used for extraction of GCC between arbitrary resonator with resonant frequency at normalized frequency $\Omega_1 = -B_1$ and an EPS connected through admittance inverter J_{12} is shown in Figure 5-8.

The circuit can be solved using the technique applied in the previous section, and formula (5.3-14)–(5.3-16) are correct for this case, as well as expression (5.3-17) is correct for $i = 2$. However, here we use $Y_1 = j(\Omega + B_1)$ in (5.3-15) to represent the resonating node.

Making assumption that external couplings are weak, the initial eigenmode equation can be converted into the following one:

$$\frac{(\Omega - \Omega_{P1})(\Omega - \Omega_{P2})}{\Omega - \Omega_{Z2}} = k_{12}^2 \tag{5.3-21}$$

where

$$k_{12}^2 = \frac{J_{12}^2}{B_{N2}} \tag{5.3-22}$$

is the squared GCC between resonating node and NRN of EPS.

Expression for extraction of the GCC can be obtained by combining two roots Ω_1 and Ω_2 of equation (5.3-21):

$$k_{12}^2 = \frac{\Omega_1\Omega_2 - \Omega_{P1}\Omega_{P2}}{\Omega_{Z2}} \tag{5.3-23}$$

5.4. Implementation of EPS in E-plane Waveguide Filters

Since EPS consist of pairs of resonators and NRN, it is convenient to implement the NRN as a strongly detuned standard E-plane resonator, which reveals the required susceptance at a certain narrow band, where this susceptance can be considered as frequency invariant. The E-plane resonator (referred to as the E-plane NRN below) contains homogeneous waveguide section between input and output septa. The configuration is presented in Figure 5-9.

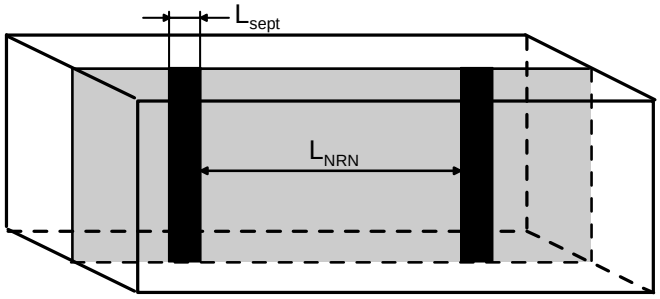

Figure 5-9: Configuration of an E-plane NRN in rectangular waveguide.

The other part of an EPS is a resonator, which can be conveniently embedded within the E-plane NRN, between two septa. This type of structures with embedded split ring resonators (SRRs) and S-shaped resonators has been investigated previously [5-9, 5-14], however the phenomena observed during the investigation were rather related to effects of metamaterials, and EPS were not addressed.

In this section, EPS based upon E-plane NRN with several embedded resonators are considered. Investigation of dependences between extracted GCC and real dimensions is carried out. Then, the aspect of losses in the proposed EPS is discussed. Finally, stopband performance of EPS is studied theoretically. Comparison of the proposed E-plane structures by losses and stopband performance is done using full-wave simulations.

5.4.1. EPS with Embedded S-shaped Resonators

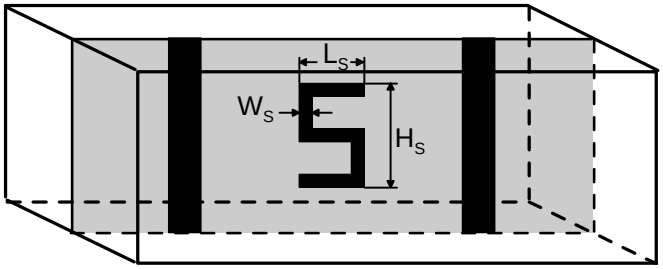

Figure 5-10: Configuration of an E-plane EPS with embedded S-shaped resonator in rectangular waveguide.

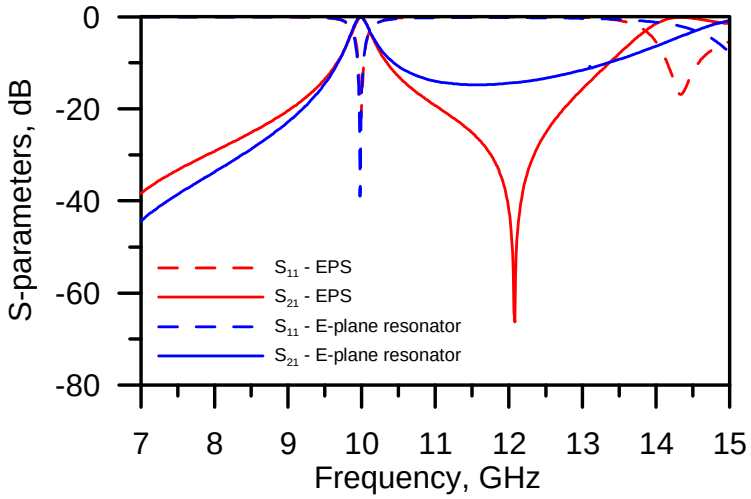

Figure 5-11: Comparison of frequency responses of an EPS with embedded S-shaped resonator and a hollow E-plane resonator.

Configuration of an EPS with S-shaped resonator in rectangular waveguide is shown in Figure 5-10. The S-shaped resonator, located in the middle of the E-plane NRN, can be considered as a $\lambda_g/2$-long section of stripline folded into the S-shaped structure, which maintains field distribution of a conventional $\lambda_g/2$-wave stripline resonator: electric field has its maximum magnitude at the ends on the resonator, while maximum of magnetic field occurs at the middle. Due to angle discontinuities in the loop the S-shaped resonator reveals slightly lower resonant frequency than conventional $\lambda_g/2$-wave stripline resonator of the same length.

The structure can be realized using a metallo-dielectric slab with the S-shaped resonator and septa etched on its top side, which can then be inserted within the E-plane of a rectangular waveguide, between two halves of its housing. Typical simulated frequency response of the configuration is presented in Figure 5-11. It is evident from the plot, that the structure reveals two widely separated resonant modes and a transmission zero between them. Considering the low-frequency mode as a main resonance and high-frequency mode as a higher-order resonance, it can be concluded that the transmission zero improves attenuation at the upper stopband in comparison with the hollow E-plane resonator case (compared response shown in Figure 5-11). On the other hand, the pair of the first pole and zero can be considered as generated by the EPS being introduced. In this case, the higher-order resonating mode can be explained by cross-couplings of two interacting resonators, one of which is the E-plane NRN. This effect will be comprehensively illustrated in section 5.4.6.

In the next several subsections, effects produced by variation of different dimensions of elements of the EPS with S-shaped resonators to its frequency response and GCC are investigated.

5.4.1.1. Effect of NRN's Length Variation

To examine the effects caused by variation of the length of NRN in the EPS with embedded S-shaped resonator, a model of the EPS based upon a real structure has been developed. S-parameters of the E-plane EPS with metallo-dielectric insert organized within a rectangular waveguide have been simulated in full-wave electromagnetic simulator CST Microwave Studio™ for several values of L_{NRN}, while all the other dimensions have been fixed. The resultant family of curves is presented in Figure 5-12a. Key parameters of lowpass prototype of EPS have been extracted from the obtained responses using expressions for GCC extraction derived in section 5.3. Lowpass prototype values have been calculated for the centre frequency of 9.45 GHz and 0.4 GHz bandwidth, which will appear as filter specifications in section 5.5.3. Dependences of resonator's frequency invariant susceptance B_1 and squared internal GCC between NRN and resonator k_N^2 on the length of NRN L_{NRN} is shown in Figure 5-12b.

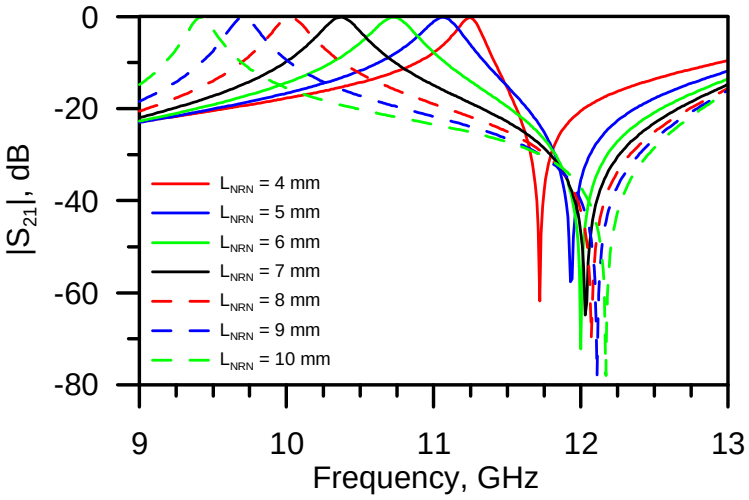

(a)

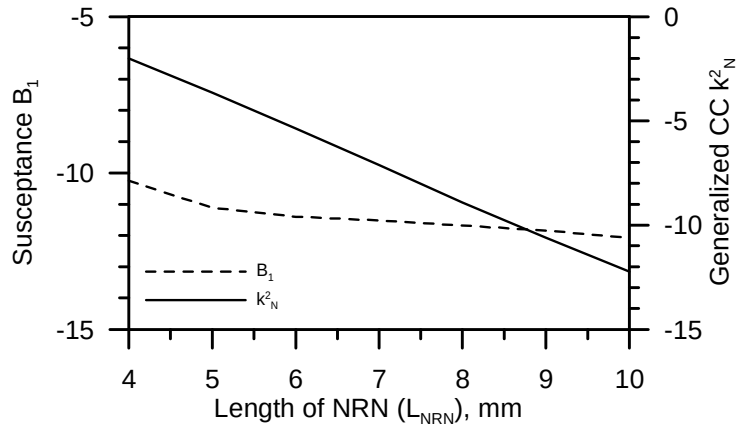

(b)

Figure 5-12: Effect of variation of L_{NRN} in EPS with embedded S-shaped resonator (L_s = 3 mm; H_s = 5.5 mm; L_{sept} = 5 mm): (a) simulated frequency responses; (b) extracted values.

It can be observed from Figure 5-12 that the value of B_1 remains almost unchanged for NRN's longer than 5 mm, where this parameter very slowly decreases with increasing L_{NRN}. Considerable increase of B_1 for NRN shorter than 5 mm originates from capacitive interaction between input/output septa and embedded resonator, which results in decrease of its resonant frequency. From Figure 5-12b it is clear that the GCC k_N^2 decreases linearly with stretching of the NRN.

5.4.1.2. Effect of S-shaped Resonator's Dimensions Variation

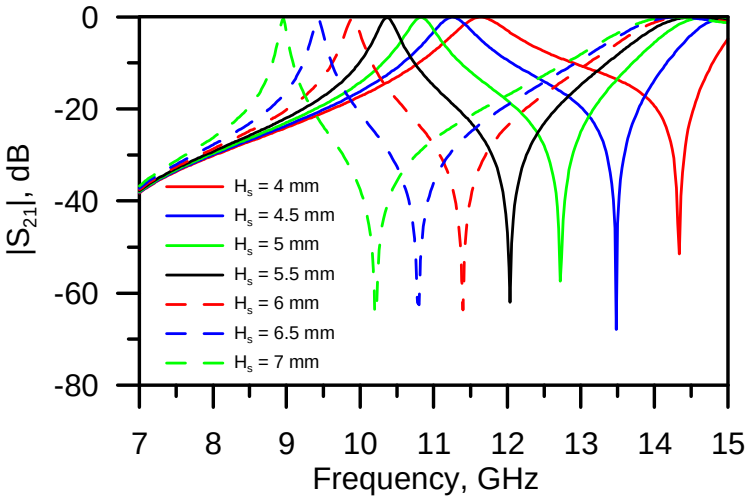

(a)

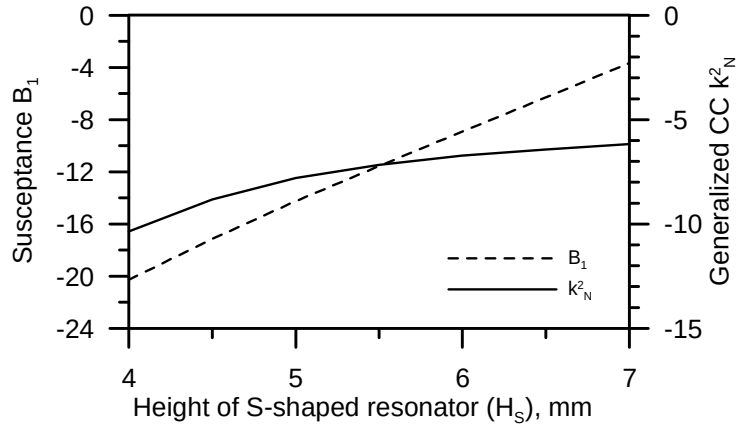

(b)

Figure 5-13: Effect of variation of H_s in EPS with embedded S-shaped resonator (L_s = 3 mm; L_{NRN} = 7 mm; L_{sept} = 5 mm): (a) simulated frequency responses; (b) extracted values.

Effects of varying the dimensions of S-shaped resonator in EPS are illustrated in Figures 5-13 and 5-14. It can be noticed from comparison of extracted values of B_1 in Figures 5-13b and 5-14b that increasing the height and length of S-shaped resonator causes similar linear increase of its resonant frequency and thus leads to an increase in the value of the susceptance. Comparison of dependences of GCC k_N^2 on S-shaped resonator's dimensions suggests that the value of GCC decreases with decreasing of both parameters. However,

variation of S-shaped resonator's length L_S appears to have more influence on the extracted GCC, particularly for realization of low resonant frequencies.

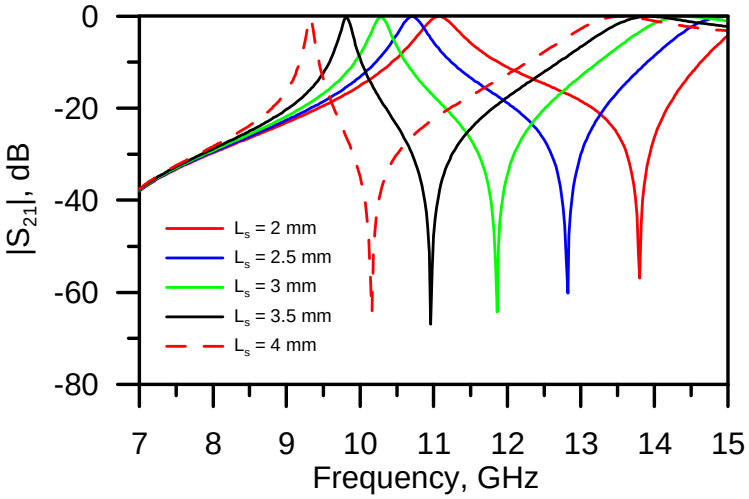

(a)

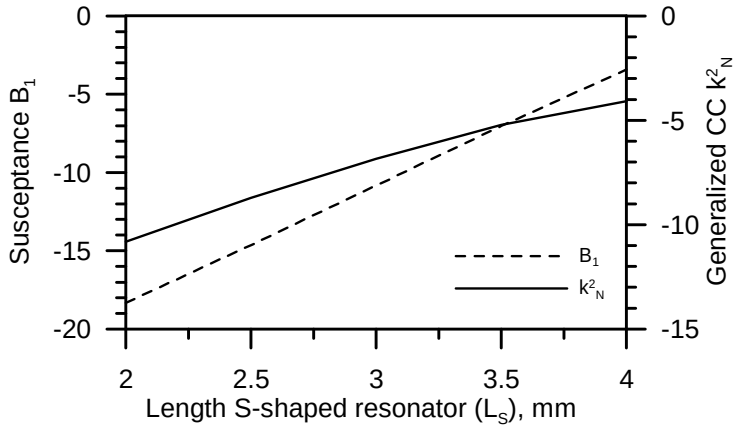

(b)

Figure 5-14: Effect of variation of L_s in EPS with embedded S-shaped resonator (H_s = 5.5 mm; L_{NRN} = 7 mm; L_{sept} = 5 mm): (a) simulated frequency responses; (b) extracted values.

5.4.1.3. Effect of Input/Output Septa' Lengths Variation

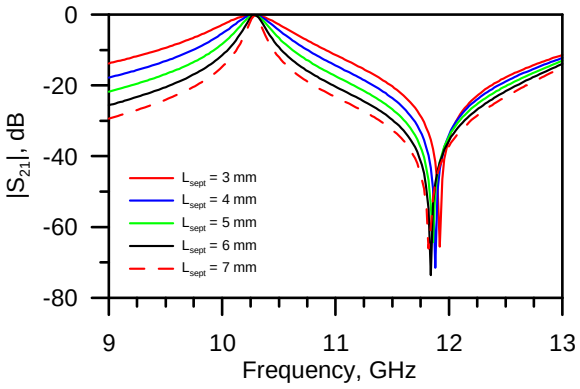

(a)

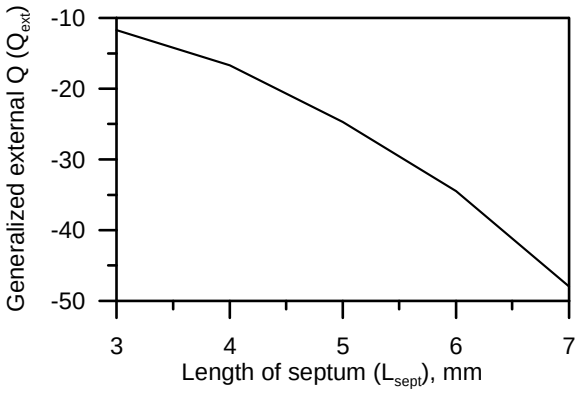

(b)

Figure 5-15: Effect of variation of L_{sept} in EPS with embedded S-shaped resonator (H_s = 5.5 mm; L_s = 3 mm; L_{NRN} = 7 mm): (a) simulated frequency responses; (b) extracted Q_{ext}.

In Figure 5-15 an effect caused by alteration of input and output septa lengths in EPS with embedded S-shaped resonator is presented. Variation of the septa' length modifies the energy flow from the source to the system of the resonator and the NRN, and causes the same effect as in a doubly loaded resonator, which results in widening the 3dB-passband with decrease of the septa' length. It is evident from Figure 5-15b that a wide range of generalized external Q-factors can be realized by changing the values of lengths of input/output septa. The Q_{ext} shows a nonlinear decrease with increase of L_{sept}. Also it can be noticed from Figure 5-15a that position of transmission zero remains practically unchanged, slightly drifting to higher frequencies with septa' enlarging.

5.4.2. EPS with Embedded Split Ring Resonators

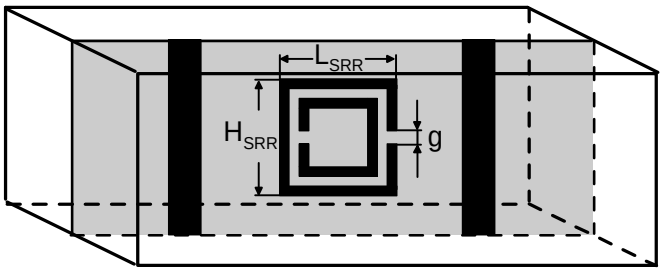

Figure 5-16: Configuration of an E-plane EPS with embedded SRR.

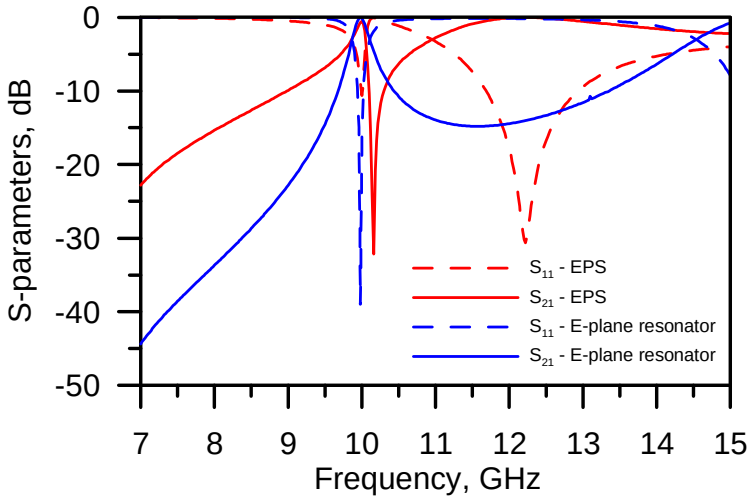

Figure 5-17: Comparison of frequency responses of an EPS with embedded SRR (L_{SRR} = 2.7 mm; H_{SRR} = 2.7 mm; g = 0.3 mm; L_{sept} = 1.5 mm; L_{NRN} = 9 mm) and a hollow E-plane resonator.

Similar results can also be achieved when the S-shaped resonator is replaced with a square-shaped SRR in the middle of the E-plane NRN. An SRR is constructed as two concentric rings terminated by a narrow gap in their middle. Such a structure has found wide applications in metamaterial techniques [5-15] – [5-17] as arrays of SRR exhibit negative permeability in a narrow band. However, a single SRR does not possess metamaterial properties and in waveguide this structure should be analyzed as a system of two strongly coupled ring resonators, thus having two widely separated low- and high-frequency resonant modes. Also it is reasonable to pay attention to the low-mode only, as the high-mode appears at a frequency above the cutoff frequency of the TE_{20} mode.

In an EPS with SRR, the SRR is usually arranged between two coupling septa on the top side of a dielectric slab as shown in Figure 5-16. Alternative configurations are also available, such as split rings arranged on different sides of the substrate [5-18]; however, this approach is more complex to realize. A simulated transmission coefficient of an EPS with SRR is shown in Figure 5-17 along with the previously considered frequency response of the hollow E-plane resonator. It is evident from the plot that the E-plane resonator with SRR insertion reveals a response similar to the one obtained using S-shaped resonator, where a transmission zero is located between two poles. However, stopband performance of this EPS is much worse than that of the EPS with S-shaped resonator.

5.4.2.1. Effect of NRN's Length Variation

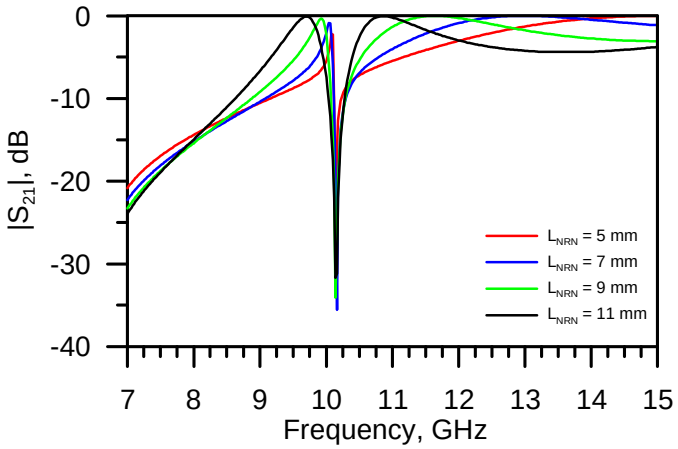

Figure 5-18: Effect of variation of the length of L_{NRN} in EPS with embedded SRR (L_{SRR} = 2.7 mm; H_{SRR} = 2.7 mm; g = 0.3 mm; L_{sept} = 1.5 mm).

Effects caused by variation of NRN's length in EPS with embedded SRR have been studied based on the same principle that has been discussed in section 5.4.1.1. Figure 5-18 presents a family of frequency responses of the EPS simulated for different values of L_{NRN}. It can be concluded from analysis of the figure that separation between pole and zero slightly increases with enlarging the NRN, while the transmission zero retains its position. This suggests that the absolute values of GCC k_N^2 in EPS with embedded SRR are smaller and

insensitive to variations of L_{NRN} in comparison with the previously considered EPS with S-shaped resonator.

5.4.2.2. Effect of SRR's Dimensions Variation

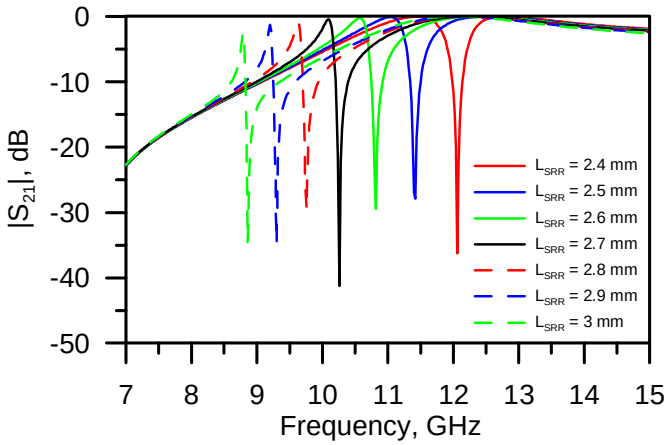

Figure 5-19: Effect of variation of L_{SRR} in EPS with embedded square SRR ($H_{SRR} = L_{SRR}$; L_{NRN} = 8 mm; g = 0.3 mm; L_{sept} = 1.5 mm).

Observation into the effects caused by varying the length of SRR in EPS has been carried out. Simulations for different values of L_{SRR} have been conducted using CST Microwave Studio™. The resultant family of transmission characteristics is shown in Figure 5-19. It is noticeable from the simulated results that reduction of the SRR's length leads to the transmission zero being drifted to higher frequencies. Due to numerous folds and, thus, the compactness of the SRR, position of the transmission zero is very sensitive to tolerances on SRR's size, which may result in reproducibility issues at the fabrication stage. It should be noted that SRR of square shape has been chosen to illustrate this investigation, as effects of variation of H_{SRR} and L_{SRR} have appeared to be identical. Therefore, in general, it is possible to vary the ratio between height and length of SRR in order to generate a transmission zero at the required frequency, taking into account various design constraints, such as the height of the basic waveguide or length of NRN.

The effect of input/output septa' width for the EPS with SRR is similar to the one previously discussed in section 5.4.1.3. This effect is common for all the resonators to be considered below, thus it will not be analyzed in detail.

5.4.3. EPS with Embedded λ/4-wavelength Resonators

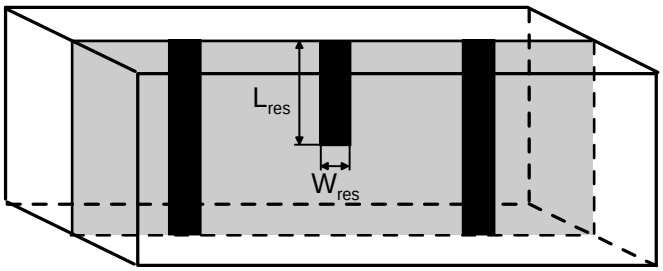

Figure 5-20: Configuration of an E-plane EPS with embedded λ/4-wavelength resonator in rectangular waveguide.

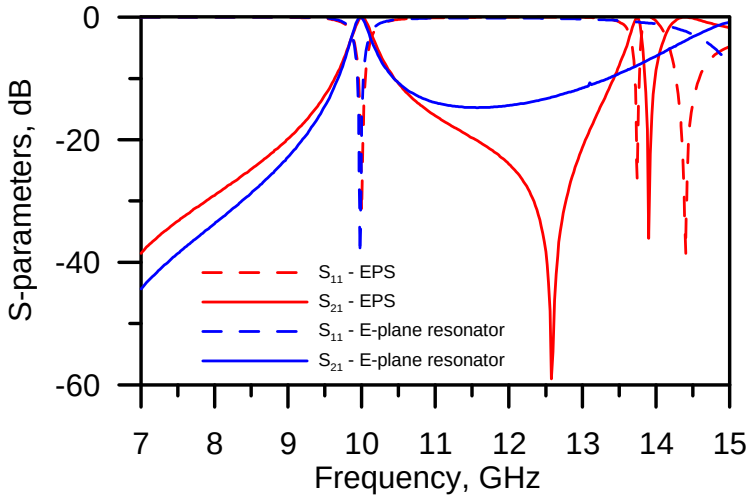

Figure 5-21: Comparison of frequency responses of an EPS with embedded λ/4-wavelength resonator and a hollow E-plane resonator.

Practicability of the use of S-shaped resonators and, especially, SRRs in the EPS is ambiguous. On the one hand, for realization of transmission zeros at high frequencies, these structures should be very small, which require precise fabrication process; on the other hand, for use at lower frequencies, these become large structures, occupying significant area. In this case, the width of these elements constraints the range of possible values of the length of NRN, which determines how close to the passband transmission zeros may be located.

The problems related to the resonators' size can be overcome by using quarter-wavelength resonators, which consist of a λ/4-wavelength microstrip section with one of the ends open, and the other one shorted to the ground plane. The resonant frequency of this type of resonators is determined by their electrical length. Since the E-plane of rectangular waveguides crosses its top and bottom grounded walls, it is convenient to connect an end of the λ/4-wavelength resonator to one of these walls, as it is shown in Figure 5-20. Resonators of the λ/4-wavelength type have been widely used in filters using distributed commensurate and non-commensurate lines [5-19]–[5-22]. Simulated frequency response of an EPS with λ/4-wavelength resonator is compared to the one of a standard E-plane resonator in Figure 5-21, from which it is evident that the behaviour characteristic to EPS with S-shaped resonators is retained, as the pair of pole and transmission zero are clearly available.

5.4.3.1. Effect of NRN's Length Variation

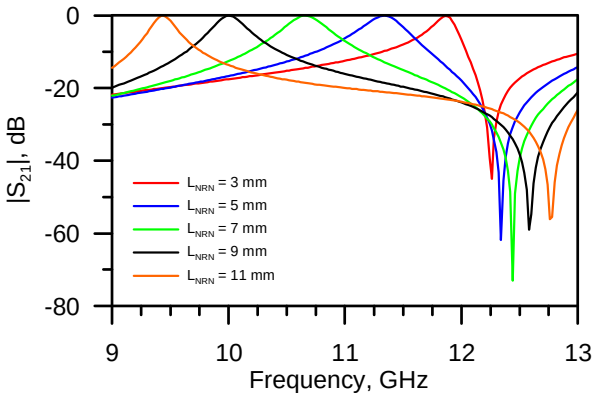

Figure 5-22: Effect of variation of L_{NRN} in EPS with embedded λ/4-wavelength resonator (L_{res} = 4 mm; W_{res} = 1.5 mm; L_{sept} = 5 mm).

Figure 5-22 illustrates the effect of variation of the NRN's length in EPS with embedded λ/4-wavelength resonator. The effect is similar to the effect of varying the same parameter of the EPS with S-shaped resonator discussed in section 5.4.1.1. Increasing L_{NRN} leads to slight drift of transmission zero due to decrease of parasitic capacitance between the embedded resonator and septa, which results in reducing the resonant frequency of the λ/4-wavelength resonator.

Simultaneously, space between pole and zero constantly widens with growth of L_{NRN}. This can be explained by increase of interaction of electric fields together with corresponding decrease of magnetic coupling between the resonator and NRN due to alteration of their structure with variation of geometry.

5.4.3.2. Effect of λ/4-wavelength Resonator's Dimensions Variation

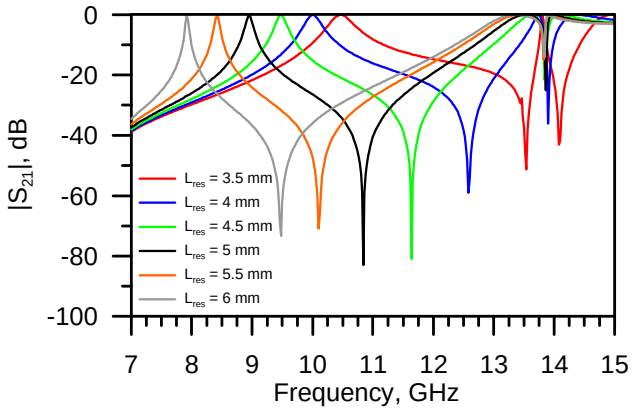

Figure 5-23: Effect of variation of L_{res} in EPS with embedded λ/4-wavelength resonator (L_{NRN} = 9 mm; W_{res} = 1.5 mm; L_{sept} = 5 mm).

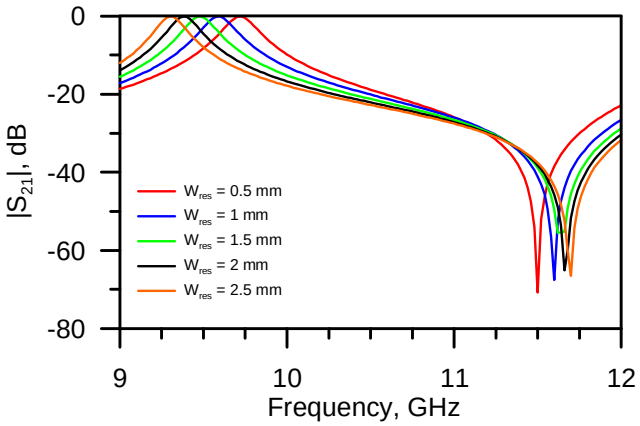

Figure 5-24: Effect of variation of W_{res} in EPS with embedded λ/4-wavelength resonator (L_{NRN} = 9 mm; L_{res} = 4.5 mm; L_{sept} = 5 mm).

Illustrations of effects of variation of L_{res} and W_{res} of λ/4-wavelength resonator in EPS are given in Figures 5-23 and 5-24. It is seen that variation of L_{res} leads to the effect observed in section 5.4.1.2. At the same time, the EPS is not that sensitive to variations of W_{res}, which can be used in tuning of filters with EPS.

5.4.4. Embedded Stepped-Impedance Resonators

Stepped-impedance resonators (SIR) are often used in the design of microstrip bandpass filters. SIRs are employed to achieve miniaturization of resonators without degradation of the *Q*-factor. This feature can be used in E-plane EPS in order to generate transmission zeros at lower frequencies.

5.4.4.1. Stepped-Impedance Resonators

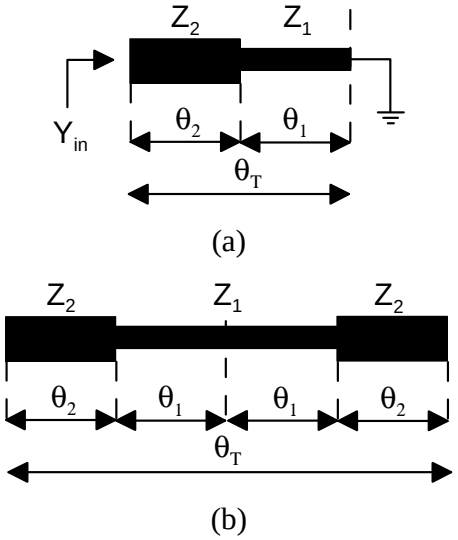

Figure 5-25: Stepped impedance resonators: (a) λ/4-type; (b) λ/2-type.

Stepped impedance resonator is a transmission line resonator that consists of two or more lines with different characteristic impedance [5-23]. Two most popular SIR are short-circuited λ/4-type and open-circuited λ/2-type resonators shown in Figure 5-25. It is evident from this figure that the λ/4-type SIR consists of a short-ended line with characteristic impedance Z_1 and electrical length θ_1 connected to an open-ended line with characteristic impedance Z_2 and electrical length θ_2. This structure can be considered as a fundamental element of SIR; the λ/2-type resonators consist of two such elements connected to each other by short-circuited ends with grounding replaced by this connection.

The input admittance of the λ/4-type SIR, shown in Figure 5-25a can be written as:

$$Y_{in} = jY_2 \frac{Y_2 \tan\theta_1 \cdot \tan\theta_2 - Y_1}{Y_2 \tan\theta_1 + Y_1 \tan\theta_2} \tag{5.4-1}$$

Short-circuited λ/4-type resonators behave like a parallel resonant circuit. Hence, the parallel resonance condition $Y_{in} = 0$ applied to them, yields:

$$\tan\theta_1 \cdot \tan\theta_2 = Y_1/Y_2 = Z_2/Z_1 = R_z \tag{5.4-2}$$

Expression (5.4-2) shows that the resonant condition of SIR is determined by electrical lengths θ_1, θ_2, and impedance ratio R_Z. Comparing to conventional uniform λ/4-wavelength resonators, analyzed in section 5.4.3, the resonance condition of which is solely determined by the electrical length, SIRs have an extra degree of freedom that can be used in future designs.

Total electrical length of resonator, given in Figure 5-25a as θ_T, for resonant condition (5.4-2) is equal to:

$$\theta_T = \theta_1 + \theta_2 = \theta_1 + \tan^{-1}\left(R_Z/\tan\theta_1\right) \tag{5.4-3}$$

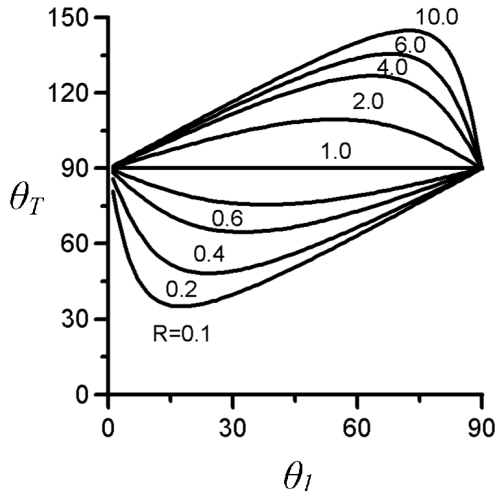

Figure 5-26: Relationship between total electrical length and θ_1 for resonant condition given for different impedance ratios.

Figure 5-26 illustrates total electrical length of SIR in terms of θ_1 for different impedance ratios R_Z. It can be seen that total electrical length of resonator has maximum value when $R_Z \geq 1$ and minimum value when $R_Z \leq 1$. Condition for these maximum and minimum values has been derived as [5-24]:

$$\theta_1 = \theta_2 = \tan^{-1}\sqrt{R_Z} \tag{5.4-4}$$

Condition $\theta_1 = \theta_2$ is a special condition which gives the maximum and minimum length of SIR which can be expressed as [5-25]:

$$\theta_{T\min} = \theta_{T\max} = \tan^{-1}\left(\frac{2\sqrt{R_Z}}{1-R_Z}\right) \tag{5.4-5}$$

Equation (5.4-5) provides minimum value for θ_T when $0 < R_Z < 1$ and $0 < \theta_T < \pi/2$, and maximum value for θ_T when $R_Z > 1$ and $\pi/2 < \theta_T < \pi$. In practice, for microstrip SIRs, this means that the shorted section should be narrower than the open one in order to obtain lower resonant frequency, and wider than the open section to increase resonant frequency.

The distinct feature of SIR in comparison with uniform ones is that the SIRs' length can be controlled by changing impedance ratio R_Z. This can be used for designing SIRs, which are shorter then their conventional counterparts, resonating at the same fundamental resonance frequency. At the same time, SIRs can be employed to control the first spurious passband of bandpass filters. More information about this feature of the SIRs can be found in [5-26, 5-27].

5.4.4.2. EPS with Embedded SIR

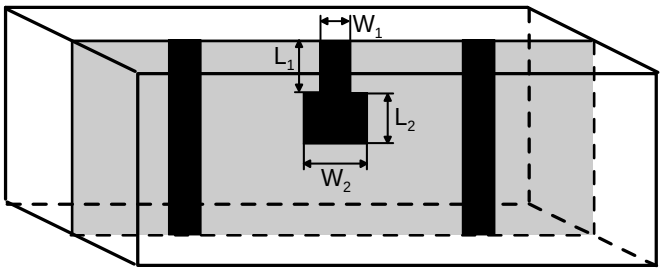

Figure 5-27: Configuration of an E-plane EPS with embedded SIR in rectangular waveguide.

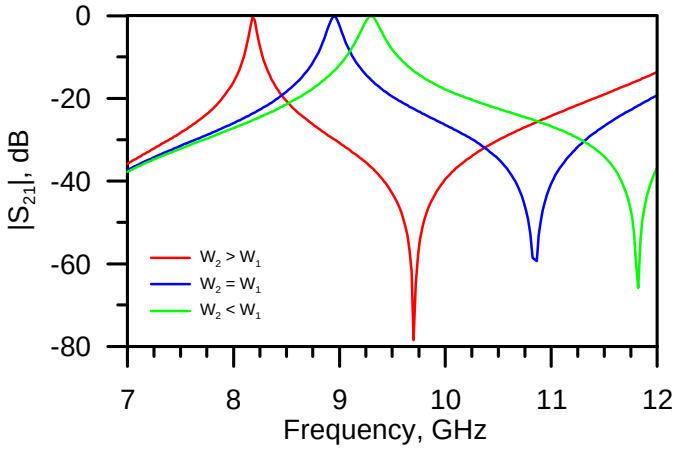

Figure 5-28: Comparison of frequency responses of EPS with embedded SIRs for different width combinations (impedance ratios).

Configuration of an EPS with embedded SIR is presented in Figure 5-27. It is seen from this figure that the SIR is implemented as two sections of microstrip lines with different widths on top layer of dielectric substrate inserted in the waveguide's E-plane. One of the sections is connected to the top ground plane of the waveguide just as the λ/4-wavelength resonator discussed in the previous section, and the other is left open.

Let us consider an EPS with embedded SIR composed of two sections with the same electrical lengths ($\theta_1 = \theta_2$, the condition from (5.4-4) is fulfilled), but different widths ($W_1 \neq W_2$). According to equation (5.4-5), if $W_1 < W_2$, the resonant frequency should decrease, therefore the transmission zero of the EPS should move towards lower frequencies; if $W_1 >$

W_2, the resonant frequency should decrease, hence the transmission zero shifts towards the higher frequencies; if $W_1 = W_2$, then the SIR turns into the conventional λ/4-wavelength resonator. For the latter case, the resonant frequency and the corresponding transmission zero appears between the transmission zeros for $W_1 < W_2$ and $W_1 > W_2$. The argumentation is illustrated by simulation results presented in Figure 5-28.

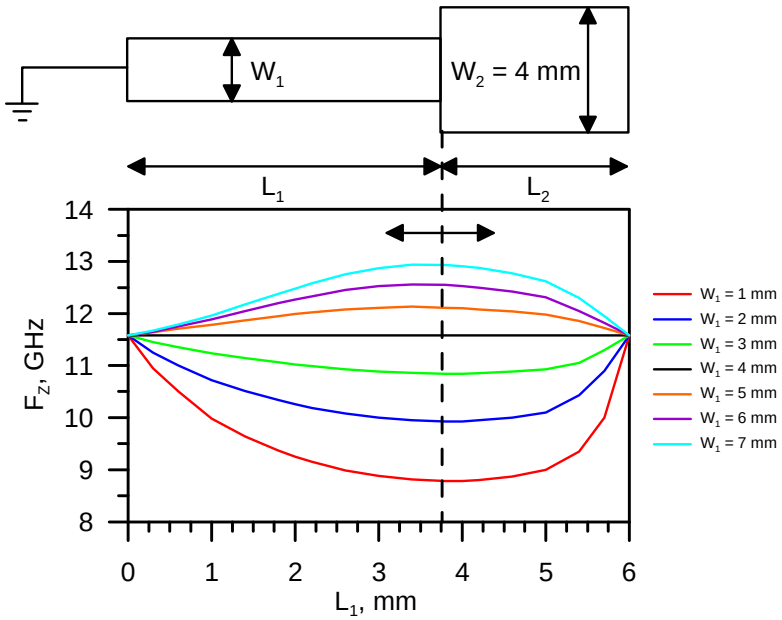

Figure 5-29: Effect of variation of SIR's lengths ratio on transmission zero position in EPS with SIR ($L_{total} = L_1+L_2 = 6$ mm; $W_2 = 4$ mm; $L_{sept} = 5$ mm).

To study the effect of variation of lengths ratio in SIR, an EPS with 6 mm long SIR has been simulated for different widths and lengths of open and shorted sections and positions of the transmission zeros have been retrieved from the simulation results. Dependences of SIR's resonant frequency on the length of the shorted section L_1 for variable W_1 and constant W_2 and L_{total} are shown in Figure 5-29. It is evident that the form of the family of curves is similar to the one presented in Figure 5-26. However, the condition $L_1 = L_2$ for maximum and minimum electrical lengths is not retained in this case; in real structure this condition is fulfilled for $L_1 > L_2$ due to the effect of parasitic capacitive load not considered theoretically in section 5.4.4.1.

5.4.5. Analysis of Losses and Size Reduction in E-plane Waveguide EPS

In order to carry out an analysis of losses in the previously introduced EPS and degree of size reduction achieved by them in comparison with a standard E-plane resonator, all the EPS in this section are considered as single resonators with main resonance at the pole frequency, while the transmission zero is ignored. This is required for applying the standard *Q*-factor approach commonly used for characterization of losses in resonant circuits [5-28].

The analysis includes comparison of different EPS by unloaded Q-factors and other characteristic parameters. In order to keep consistency of comparison, EPS with embedded S-shaped resonator, SRR, λ/4-wavelength resonator and SIR, as well as a standard E-plane resonator have been designed to reveal the same pole frequency of 10 GHz and have the same 3dB-bandwidth, which may vary within 10%. This means that EPS may have different input and output septa lengths as well as the lengths of NRN section. All the structures have been analyzed in a full-wave electromagnetic simulator CST Microwave Studio™. The resultant transmission characteristics of the EPS are presented in Figure 5-30.

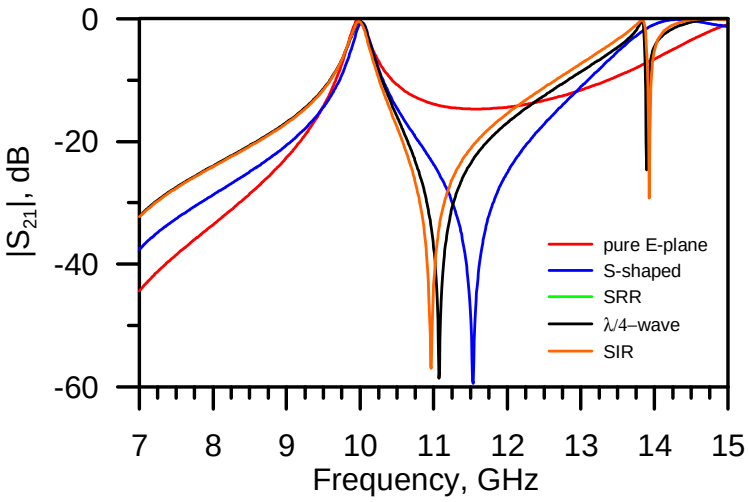

Figure 5-30: Frequency responses of EPS of all types used for analysis of losses, size reduction and stopband performance.

The following parameters of the resonators have been extracted from the available simulated frequency responses: the loaded *Q*-factor Q_L; the unloaded *Q*-factor Q_U, which

describes losses in resonators; and the external *Q*-factor, Q_{ext}, which shows the external coupling properties of resonators. *Q*-factors have been extracted from the simulated data using the well-known expressions [5-22]:

$$Q_L = \frac{f_{res}}{\Delta f_{3dB}} \tag{5.4-6}$$

$$Q_U = \frac{Q_L}{1 - S_{21}(f_{res})} \tag{5.4-7}$$

$$\frac{1}{Q_L} = \frac{1}{Q_U} + \frac{1}{Q_{ext}} \tag{5.4-8}$$

Summary of the *Q*-factors extracted from all the structures is presented in Table 5-1 together with their total lengths, which show the degree of size reduction achieved by employing EPS approach.

Parameter	E-plane resonator	Type of resonator embedded in EPS			
		S-shaped	SRR	λ/4-wave	SIR
NRN's length*, mm	13.8	7.2	9.1	5.9	6.0
Total length, mm	24.8	17.1	13.5	13.9	14
Unloaded *Q*	2660	674.6	309.7	1042	904.3
Loaded *Q*	39.9	43.6	40.3	41.7	41.6
External *Q*	40.5	46.6	46.3	43.4	43.6

*Length of resonator excluding input/output septa for hollow E-plane resonator

Table 5-1: Comparison of dimensions and *Q*-factors of E-plane resonator and EPS at 10 GHz.

It is evident from the table that lengths of the EPS are reduced by 31–43% in comparison with the length of hollow E-plane resonator, while unloaded *Q*-factor dropped by 61–88%. Losses in the EPS are concentrated in the embedded resonators realized by means of narrow striplines. The hollow E-plane resonator has the highest *Q*-factor as it does not contain any embedded resonator. Ohmic and skin-effect losses in the septa mainly

contribute into the overall losses in this case. In the EPS with $\lambda/4$-wavelength resonator additional high ohmic and skin-effect losses appear in the resonator. Therefore, the *Q*-factor of the EPS drops significantly. In the SIR resonator losses also occur due to the square corners. In the S-shaped resonator current flows twice longer distance than in the $\lambda/4$-wavelength resonator, therefore the ohmic and skin-effect losses are almost twice as higher. The SRR has the lowest *Q*-factor due to the narrower conductors used in the rings (in order to reduce the SRRs' size) and additional losses related to the proximity effect. The losses can be reduced by cutting off the available right angles and increasing conductor widths; however this approach leads to inability to realize small resonators for high resonant frequencies.

Analysis of the values of external *Q*-factors suggests that for the EPS with SRR, the same external coupling can be realized by using narrower septa, which leads to additional size reduction of filters.

5.4.6. Analysis of Stopband Performance of E-plane Waveguide EPS

In section 5.2 a model of EPS has been considered, which takes into account only one pole and one transmission zero produced by the EPS. However, real structures do not display ideal behaviour. In bandpass filters this becomes apparent as spurious resonances in stopband. In this section, stopband performance of the introduced EPS will be compared. Analysis of the effects in the stopband caused by resonant character of NRN used in E-plane EPS will be presented.

5.4.6.1. Comparison of Stopband Performances of EPS

Comparison of stopband performances of different EPS and a standard E-plane resonator have been carried out based upon the same principle as the comparison of *Q*-factors and lengths discussed in the previous section. All the EPS introduced in section 5.4 have been tuned to the same main resonant frequency of 10 GHz, and position of the second-order resonance has been extracted from the simulated frequency responses of these structures as an attribute showing the stopband performance. Therefore, Figure 5-30 can be used for the purpose of comparison of stopband performances of EPS. It is evident from this figure that transmission zeros in upper stopband significantly improve the stopband of EPS in comparison with the hollow E-plane resonator in the frequency range between two resonating modes. However, each of the proposed EPS exhibits the second-order resonant frequency lower than the first spurious resonance of the hollow E-plane resonator, which is located at a frequency slightly above 15 GHz. From Figure 5-30 it can be noticed that spurious resonance of the EPS with embedded S-shaped resonator appears at about 14.3 GHz, which is the best result for the considered types of EPS. λ/4-wavelength resonator and SIR based EPS reveal their spurious resonances at 13.7 GHz, which are accompanied by a transmission zero at 14 GHz. This pair of pole and zero appears because of the second-order resonance of the embedded resonator which forms another, spurious EPS, in combination with the NRN. EPS with embedded SRR shows the worst stopband performance as its spurious resonance appears at only 11.7 GHz. Theoretical explanation of observed behaviour of the considered EPS is given in the next section.

5.4.6.2. Theoretical Analysis of Stopband Performance of EPS

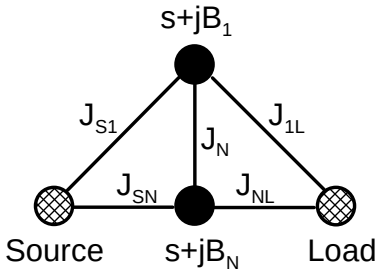

Figure 5-31: Coupling scheme representation of an EPS used for stopband performance analysis.

The higher-order resonances in EPS are determined by parasitic effects, which are not taken into account in the circuit model of EPS discussed in section 5.2. A more accurate model for analysis of spurious resonances should take into consideration the resonating character of the NRN represented by a strongly detuned standard E-plane resonator and parasitic couplings, taking place between source/load nodes and the embedded resonator. Therefore, the new model for analysis of stopband performance of EPS includes two resonators: the main E-plane resonator and the inserted one. The resonators are coupled to source, load and each other, while the only weak direct coupling between source and load is neglected. Coupling scheme of the resultant EPS is depicted in Figure 5-31. Couplings between elements of the functional scheme are defined by means of the following coupling matrix:

$$M = \begin{bmatrix} 0 & J_{S1} & J_{S2} & 0 \\ J_{S1} & B_N & J_N & J_{1L} \\ J_{S2} & J_N & B_1 & J_{2L} \\ 0 & J_{1L} & J_{2L} & 0 \end{bmatrix} \tag{5.4-9}$$

Analytical expression for S-parameters of the network can be obtained by processing the coupling matrix using the technique discussed in section 3.3.3.5. Applying formula (3.3-30) and (3.3-31) to the coupling matrix *M*, and assuming that the network under consideration is symmetrical (which implies $J_{S1} = J_{1L}$ and $J_{SN} = J_{NL}$), positions of poles $\Omega_{P1,2}$ and zeros Ω_Z of the network can be calculated analytically as:

$$\Omega_{P1,2} = -\frac{B_1 + B_N}{2} \pm \frac{1}{2}\sqrt{(B_1 - B_N)^2 + 4J_N^2} \tag{5.4-10}$$

$$\Omega_Z = \frac{2J_N J_{SN} J_{S1} - J_{SN}^2 B_1 - J_{S1}^2 B_N}{J_{SN}^2 + J_{S1}^2} \tag{5.4-11}$$

From (5.4-10) it is clear that locations of poles depend on self-resonance frequencies of both resonators, and on coupling between them. Separation between two global resonant modes of the considered doublet widens as the degree of detuning of the two resonators is increased, as well as with the increase of J_N regardless of sign of coupling. The latter is particularly useful as it allows creation of a wide stopband without modifying the E-plane resonator, solely adjusting parameters of the embedded resonator, such as self-resonance frequency and shape in order to obtain the highest possible coupling coefficient.

Concerning the EPS structures, which stopband performance has been compared in the previous section, it can be suggested, that the S-shaped resonator is strongly coupled with the E-plane resonator (NRN), as the available two poles are widely separated. This is because the S-shaped resonator is located in the area, where electric field of the E-plane resonator is concentrated. Thus, magnetic fields of two resonators are scarcely overlapping, and interaction between them becomes strongly capacitive. Same explanation is correct for the EPS with λ/4-wavelength resonator and SIR. In contrary, coupling coefficient of SRR with the E-plane resonator is smaller because the coupling coefficient has larger magnetic component due to stronger magnetic coupling of split rings and E-plane resonator's mode. At the same time, electric coupling component becomes weaker as the gaps in split rings are shifted from the middle of NRN, where electric field is concentrated. Hence the resultant coupling coefficient decreases and the gap between two poles becomes much narrower.

Equation (5.4-11) shows that position of transmission zero can be generally shifted by changing external coupling coefficients, keeping available poles unaffected. However, if (5.4-11) is simplified for analysis by division of numerator and denominator by J_{SN}^2, it can

be seen that the position of transmission zero is fully described by four parameters: inverter value J_N, values of susceptances B_1 and B_N, and ratio J_{S1}/J_{SN}:

$$\Omega_Z = \frac{2J_N \frac{J_{S1}}{J_{SN}} - B_1 - \frac{J_{S1}^2}{J_{SN}^2} B_N}{1 + \frac{J_{S1}^2}{J_{SN}^2}} \tag{5.4-12}$$

It is evident from (5.4-12) that weak parasitic coupling J_{S1} and strong main line coupling J_{SN} lead to the same effect: the position of transmission zero Ω_Z tends to $-B_1$ in terms of lowpass prototype normalized frequency. In practice, both weak J_{S1} and strong J_{SN} are combined and it can be assumed that the position of transmission zero is determined by the resonant frequency of the embedded resonator.

Another important consequence of expressions (5.4-10) and (5.4-11) is that the transmission zero always appears between two poles. In can be easily proven that the following inequality is always true for the network under consideration:

$$-\frac{B_1 + B_N}{2} - \frac{1}{2}\sqrt{(B_1 - B_N)^2 + 4J_N^2} \le -B_1 \le -\frac{B_1 + B_N}{2} + \frac{1}{2}\sqrt{(B_1 - B_N)^2 + 4J_N^2} \tag{5.4-13}$$

Equation (5.4-13) also suggests that in order to design an EPS with transmission zero in lower stopband, the second-order resonance should be considered as the main resonance, while the first-order resonance becomes unwanted. Practically, a transmission zero in lower stopband can be obtained by changing the sign of the NRN's susceptance, which can be realized by increasing its length. Therefore, the NRN's self-resonance frequency decreases significantly, and the unwanted resonance appears in lower stopband.

5.5. Filter Design Examples

It has been shown in the previous section that use of E-plane EPS in rectangular waveguide results in improvement in size and selectivity in comparison with standard E-plane resonators. In this section, several design examples of extracted pole filters with the considered EPS are presented. The examples are organized according to the standard filter design procedure described in chapter 3.

5.5.1. Design of a 3rd-order Filter with Single Transmission Zero

To demonstrate the design of inline extracted pole filter by extraction of GCC between hollow E-plane resonators and EPS, a third-order bandpass filter with a single transmission zero in upper stopband is implemented in conventional rectangular waveguide. The filter is designed to satisfy the following specifications:

- center frequency: 9.45 GHz;
- ripple passband: 9.28 – 9.62 GHz;
- return loss: 18 dB;
- transmission zero: 11.33 GHz.

5.5.1.1. Approximation and Synthesis

Approximation of the required filter response has been carried out using the standard technique for filters with generalized Chebyshev response, discussed in details in section 3.2.4. The filter specifications yield the following expressions for the S-parameters of the lowpass prototype:

$$S_{11}(s)=\frac{F(s)}{E(s)}, \qquad S_{21}(s)=\frac{P(s)}{\varepsilon \cdot E(s)} \tag{5.5-1}$$

$$P(s)=s-j10.1413 \tag{5.5-2}$$

$$F(s)=s^3-j0.0495s^2+0.7494s-j0.0247 \tag{5.5-3}$$

$$\varepsilon \cdot E(s)=5.1389\cdot(s^3+(2.1114-j0.0492)s^2+(2.9788-j0.1513)s+ \\ +(1.9597-j0.2348)) \tag{5.5-4}$$

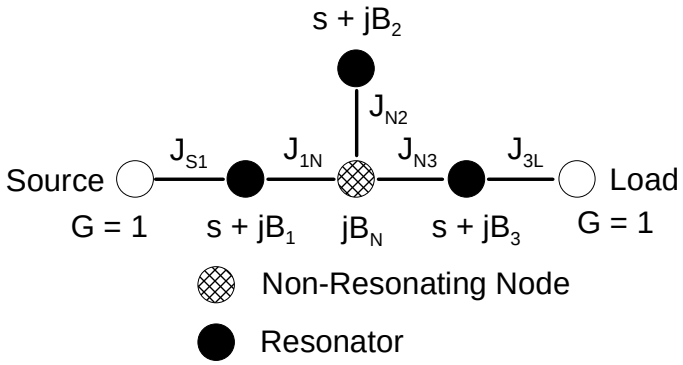

Figure 5-32: Coupling scheme of a 3rd-order extracted pole filter with a single transmission zero.

Equivalent circuit synthesis procedure and extraction of values of admittance inverters and frequency invariant susceptances have been made using the direct synthesis technique for inline filters with non-resonating nodes presented in [5-29], which results in the coupling scheme presented in Figure 5-32 with values of the circuit elements arranged in the following coupling matrix:

$$\begin{bmatrix} 0 & J_{S1} & 0 & 0 & 0 & 0 \\ J_{S1} & B_1 & J_{1N} & 0 & 0 & 0 \\ 0 & J_{1N} & B_N & J_{N2} & J_{N3} & 0 \\ 0 & 0 & J_{N2} & B_2 & 0 & 0 \\ 0 & 0 & J_{N3} & 0 & B_3 & J_{3L} \\ 0 & 0 & 0 & 0 & J_{3L} & 0 \end{bmatrix} =$$

$$= \begin{bmatrix} 0 & 1.0275 & 0 & 0 & 0 & 0 \\ 1.0275 & -0.0697 & 1 & 0 & 0 & 0 \\ 0 & 1 & -10.9481 & 10.441 & 1 & 0 \\ 0 & 0 & 10.441 & -10.1413 & 0 & 0 \\ 0 & 0 & 1 & 0 & -0.0697 & 1.0275 \\ 0 & 0 & 0 & 0 & 1.0275 & 0 \end{bmatrix} \qquad (5.5\text{-}5)$$

Thereafter, GCC to be realized can be calculated from formula (5.3-4), (5.3-6) and (5.5-5). Computed values of the GCC are: $Q_{extS} = Q_{extL} = 26.33$, $k_{1N}^2 = k_{N3}^2 = -0.091$, $k_{N2}^2 = -0.1$.

Note that calculation of the GCC between NRN and resonators has been carried out without applying the fractional bandwidth *FBW* for simplicity.

5.5.1.2. Implementation

The filter has been implemented using two hollow E-plane resonators and an EPS with embedded SIR (see section 5.4.4). Configuration of insert, placed in the E-plane of rectangular waveguide in order to obtain the required coupling scheme is shown in Figure 5-33.

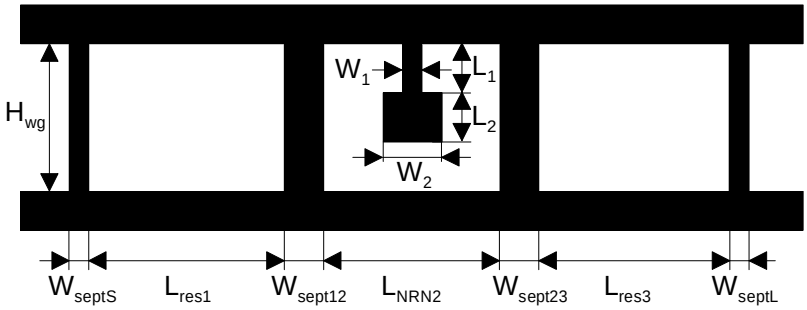

Figure 5-33: Configuration of the E-plane insert for implementation of the 3rd-order filter with single transmission zero.

Determination of geometrical measurements of the insert is carried out by plotting dependencies of the required GCC, extracted from full-wave simulations, on dimensions of insert's elements. Alternatively, the lengths of E-plane resonators and input/output septa can also be calculated using the standard approach described in [5-30]. Firstly, the resonator in EPS is designed by adjusting the widths and lengths of shorted and open sections of SIR, so the transmission zero is located at the required frequency. Then, the NRN's length is adjusted until the required value of k_{N2}^2 is reached. The value of k_{N2}^2 is extracted from simulation results using expression (5.3-11). The resultant plots for this step of the design procedure are not shown in this section because these are similar to the results of EPS' investigation made in section 5.4. It must be stressed that extraction of all the GCC here and below (except generalized external *Q*-factor) should be performed under weak external coupling condition.

Next, the width of coupling septa between EPS and E-plane resonators must be found. For this purpose, the pair of interacting components has been simulated with different values of the coupling septum. GCC k_{1N}^2 has been extracted from the obtained frequency responses using formula (5.3-23). The dependence of the extracted k_{1N}^2 on the width of the septum W_{sept12} is presented in Figure 5-34. From this plot, a value of W_{sept12}, which corresponds to the required value of k_{1N}^2 = –0.091, should be determined.

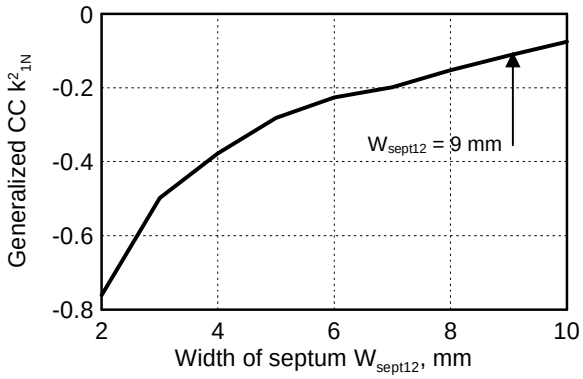

Figure 5-34: Dependence of extracted k_{1N}^2 on septum width W_{sept12}.

After the initial dimensions of the E-plane insert are found, the entire filter structure undergoes the optimization procedure in a full-wave electromagnetic simulator (see Section 3.5.2 about optimization). The optimization of the filter under consideration has been carried out in Ansoft HFSS™ using quasi-Newton procedure.

5.5.1.3. Experimental Verification

The designed filter structure has been realized in standard E-plane waveguide technology. All-metal E-plane insert with the optimized dimensions, summarized in Table 5-2, has been cut out of copper foil ($\sigma = 5.8\times10^7$ Sm/m) with the thickness of T = 0.1 mm, and placed between two halves of rectangular waveguide housing (WG-90, cross-section: 22.86×10.16 mm^2) made of brass.

Parameter	Value, mm
L_1	1.0
L_2	3.4
W_1	1.0
W_2	4.8
W_{septS}, W_{septL}	2.0
W_{sept12}, W_{sept23}	7.0
L_{res1}, L_{res3}	15.85
L_{NRN2}	8.7
L_{total}	58.4

Table 5-2: Dimensions of E-plane insert for the designed filter (see Figure 5-33).

In order to validate the design procedure, the bandpass filter has been fabricated and tested. S-parameters of the filter, measured with an Agilent E8361A vector network analyzer, are shown in Figure 5-35 together with the simulation results for the purpose of comparison. The measured curves show insertion loss of 1.6 dB, and exhibit overall good agreement with the simulated ones, taking into account the manufacturing tolerances and fabrication errors. Photograph of the fabricated insert and waveguide housing is shown in Figure 5-36.

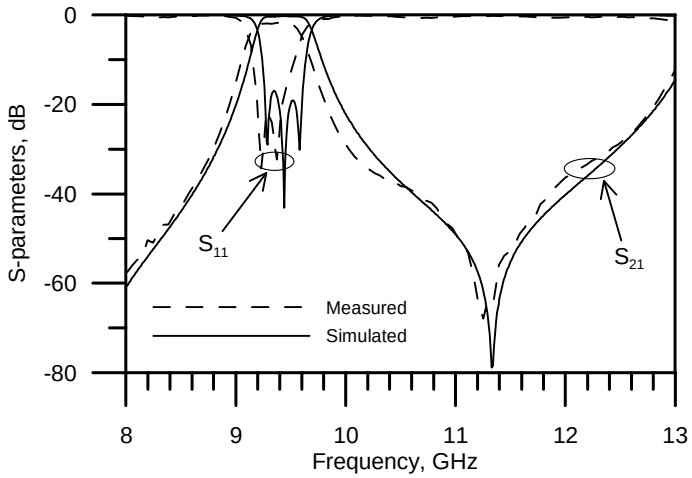

Figure 5-35: Simulated and experimental frequency responses of the fabricated 3rd-order filter with single transmission zero.

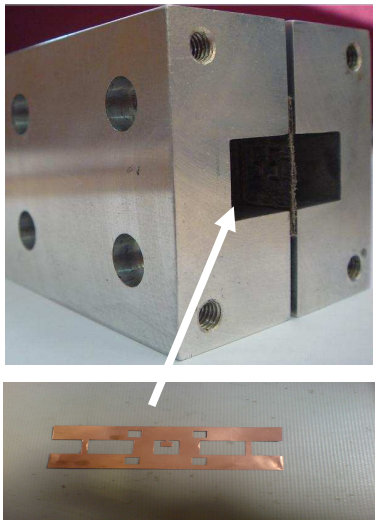

Figure 5-36: Photograph of the fabricated insert and waveguide housing.

In order to demonstrate the filter size reduction achieved by the proposed extracted pole filter, comparison with an equivalent filter containing only conventional E-plane resonators with the same filter order, passband and ripple is made. The total length of the conventional E-plane filter and proposed filter are 66.4 mm and 58.4 mm respectively. Therefore, size reduction of more than 12% is achieved by employing a single EPS.

5.5.2. λ/4-wavelength Resonators Based 3rd-order Filter with Three Transmission Zeros in Upper Stopband

In order to demonstrate how inline extracted pole filters can be designed by extraction of GCC between individual EPS, a third-order bandpass filter with three transmission zeros is synthesized and implemented as an E-plane insert within a conventional rectangular waveguide. The filter specifications are defined as follows:

- center frequency: 9.45 GHz;
- ripple passband: 9.3 – 9.6 GHz;
- return loss: 20 dB;
- transmission zeros: 10.6 GHz, 11.6 GHz, 12.7 GHz.

5.5.2.1. Approximation and Synthesis

The generalized Chebyshev approximation technique applied to the filter specifications leads to the following characteristic polynomials:

$$P(s) = s^3 - j39.1s^2 - 477s + j1781.7 \tag{5.5-6}$$

$$F(s) = s^3 - j0.1342s^2 + 0.7427s - j0.0667 \tag{5.5-7}$$

$$\varepsilon \cdot E(s) = 711.23 \cdot (s^3 + (2.358 - j0.1343)s^2 + (3.5202 - j0.4972)s + \\ + (2.3661 - j0.8255)) \tag{5.5-8}$$

Extraction of admittance inverters' and frequency invariant susceptances' values from the derived characteristic polynomials, using the direct synthesis procedure for inline extracted pole filters with NRN [5-29], leads to the equivalent network presented in Figure 5-37 with the following values of the denoted element: J_{S1} = 1, B_{N1} = –11.15, J_1 = 11.981, B_1 = –13.005, J_{12} = 1, B_{N2} = –7.988, J_2 = 7.535, B_2 = –7.251, J_{23} = 1, B_{N3} = –16.168, J_3 = 17.425, B_3 = –18.894, J_{3L} = 1.0. Corresponding GCC to be physically realized can be calculated from the prototype values by applying formula (5.3-4), (5.3-5) and (5.3-7). The values of the GCC (which have the same indices as the corresponding *J*-inverters) and external Q-

factors have been calculated from the synthesis results as follows: Q_{extS} = –11.15, Q_{extL} = –16.168, k_1^2 = –12.873, k_2^2 = –7.83, k_3^2 = –16.07, k_{12}^2 = 0.0112, k_{23}^2 = 0.0077.

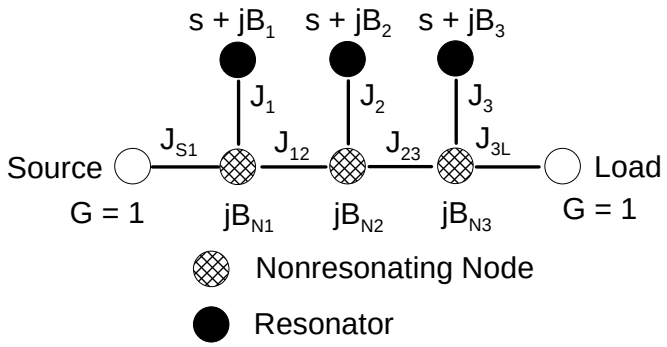

Figure 5-37: Coupling scheme of a 3rd-order extracted pole filter with three transmission zeros.

5.5.2.2. Implementation

3rd-order filter with three transmission zeros in upper stopband has been implemented by three direct coupled EPS with embedded λ/4-wavelength resonators discussed in section 5.4.3. Configuration of the corresponding E-plane insert is presented in Figure 5-38.

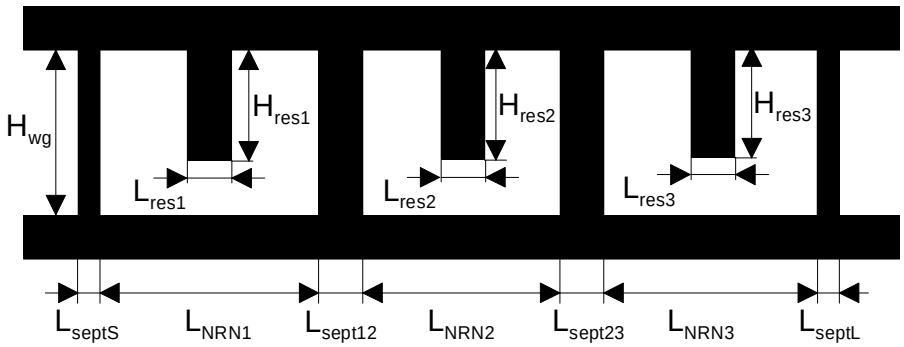

Figure 5-38: Configuration of the E-plane insert for implementation of the 3rd-order filter with three transmission zeros in upper stopband.

Determining the dimensions of each EPS and septa responsible for internal and external couplings is similar to the procedure used for filter implementation in the previous section. GCC within EPS or between adjacent EPS are extracted using expressions (5.3-10), (5.3-11), (5.3-13) and (5.3-20) from their simulated frequency responses as functions of certain

geometrical parameters. GCC extraction is carried out according to the following procedure. First, dependence of the position of transmission zero versus the resonator's height is examined for single symmetric EPS with arbitrary septa and length of NRN. Then, H_{resi} are fixed for all three sections, and L_{NRNi} are adjusted until the projected coupling coefficient k^2_i is reached. After this, external Q-factors are adjusted for input/output sections by changing lengths of input/output septa. Finally, coupling coefficients between adjacent sections are examined for the corresponding couplings by changing lengths of septa between them. Results of extraction for the designed filter are shown in Figure 5-39.

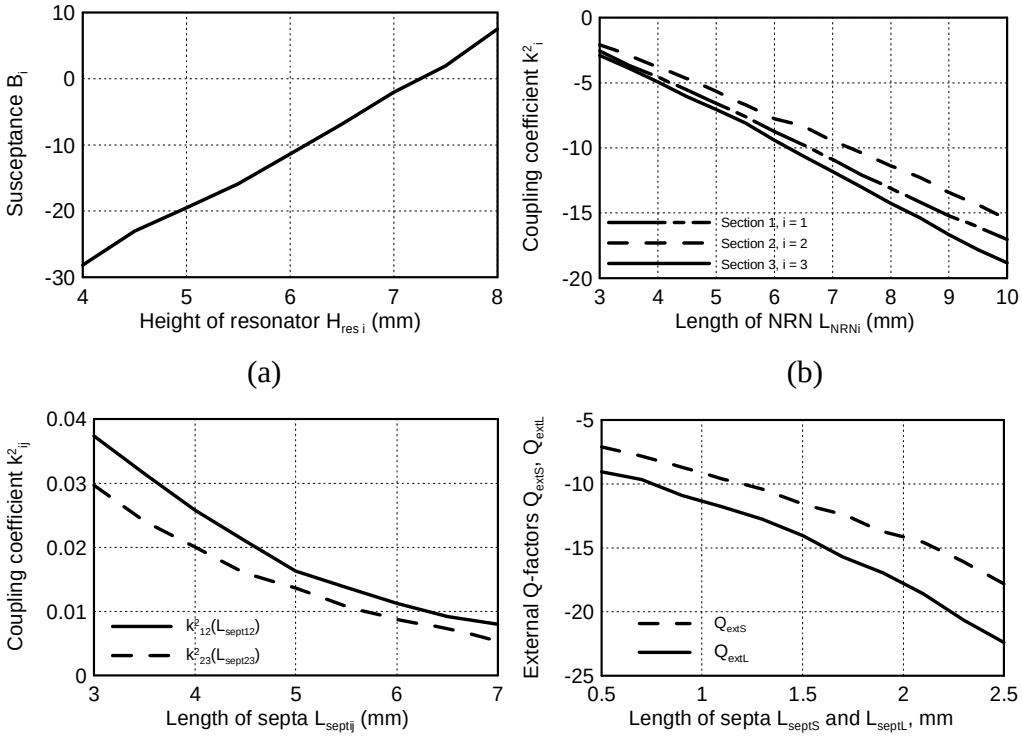

Figure 5-39: Extracted GCC as functions of insert dimensions (see Figure 5-38): (a) B_i vs. H_{resi}; (b) k_1^2 vs. L_{NRNi}; (c) k_{ij}^2 vs. L_{septij}; (d) Q_{ext} vs. L_{septS} and L_{septL}.

From the dependencies plotted as a result of extraction, the initial dimensions of the filter have been obtained. Filter with initial dimensions has been then optimized with respect to the manufacturing tolerances by means of the full-wave simulator CST Microwave Studio™. From comparison of initial and optimized dimensions of the designed filter,

presented in Table 5-3, it is evident that the design procedure based upon the proposed extraction of GCC provides good initial approximation of dimensions of the E-plane insert.

Parameters	Initial	Optimized
L_{septS}	1.3	1.5
L_{sept12}	5.9	5.5
L_{sept23}	6.4	5.2
L_{septL}	1.7	1.0
L_{NRN1}	7.4	7.8
L_{NRN2}	5.8	5.9
L_{NRN3}	9.8	10
H_{res1}	5.8	5.9
H_{res2}	6.4	6.4
H_{res3}	5.3	5.3
L_{resi}, i = 1..3	2.0	2.0
L_{total}	38.3	36.9

Table 5-3: Dimensions of E-plane insert for the designed filter (see Figure 4-39).

5.5.2.3. Experimental Verification

In order to validate the analysis and confirm the introduced design approach, the filter structure has been realized using standard E-plane waveguide technology. The insert of the shape shown in Figure 5-38 has been cut out of copper foil ($\sigma = 5.8\times10^7$ Sm/m) with thickness of T = 0.1 mm and placed between two halves of brass rectangular waveguide housing (WG-90, cross-section: 22.86×10.16 mm^2).

S-parameters of the filter have been measured using Agilent E8361A vector network analyzer. Figure 5-40 shows simulated and measured responses of the fabricated filter. The computed response reveals all three reflection and three transmission zeros, while experimental curve does not depict one of the poles. It is also clear that all three transmission zeros observed are close to that of the frequencies expected. The measured insertion loss at centre frequency is 1.2 dB. Required return loss of greater than 20 dB at the passband has been successfully achieved. Overall agreement between computed and experimental responses is very good taking into account potential fabrication tolerances and measurement errors. Photograph of the fabricated structure is shown in Figure 5-41.

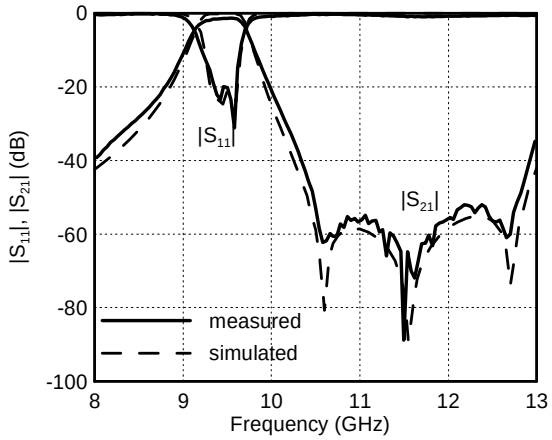

Figure 5-40: Simulated and experimental responses of the fabricated 3rd-order filter with three transmission zeros in upper stopband.

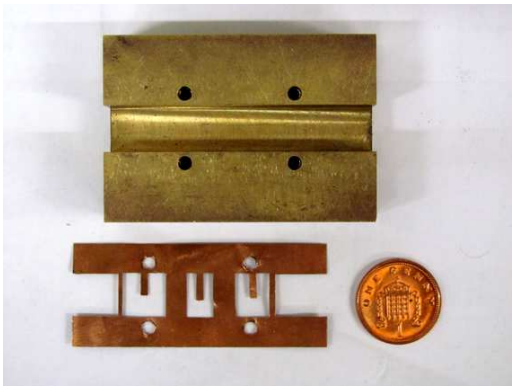

Figure 5-41: Photograph of the fabricated filter: insert and half of the waveguide housing.

5.5.3. Filters with S-shaped Resonators and SRR

In this section, feasibility of the EPS with embedded S-shaped resonators and SRR is proven by fabrication of the corresponding 3rd-order filters with three transmission zeros in upper stopband. Detailed implementation procedure is not provided in this section, as this entirely coincides with the one used in Section 5.5.2.

5.5.3.1. 3rd-order Filter with Three Transmission Zeros Using EPS with S-shaped Resonators

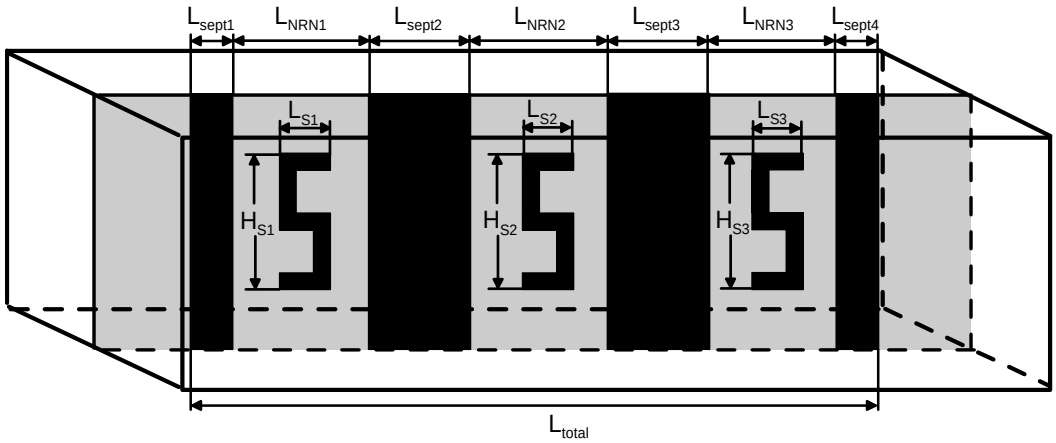

Figure 5-42: Configuration of E-plane filter with three S-shaped resonators.

Configuration of the designed 3rd-order extracted pole bandpass filter with S-shaped resonators is presented in Figure 5-42. The filter has been designed to meet the following specifications:

- center frequency: 9.45 GHz;
- ripple passband: 9.25 – 9.65 GHz;
- return loss: 22 dB;
- transmission zeros: 10.5 GHz, 11.35 GHz, 11.65 GHz.

The lowpass prototype of the filter has been obtained by direct synthesis technique, and the resultant coupling scheme is shown in Figure 5-37. Prototype elements in this network have

the following values: $J_{S1} = 1$, $B_{N1} = -4.117$, $J_1 = 4.533$, $B_1 = -4.988$, $J_{12} = 1$, $B_{N2} = -9.471$, $J_2 = 9.074$, $B_2 = -8.705$, $J_{23} = 1$, $B_{N3} = -8.318$, $J_3 = 9.137$, $B_3 = -9.961$, $J_{3L} = 1$.

The filter has been implemented using three EPS with S-shaped resonators and four septa, arranged as an E-plane metallo-dielectric insert. The dielectric block etched on its top side with the pattern has been placed in the E-plane of standard rectangular waveguide, between two halves of its housing. Dimensions of the metallo-dielectric insert, which have been found by extraction of GCC and optimization, are presented in Table 5-4.

Parameters	Values, mm
L_{sept1}	1.0
L_{sept2}	4.6
L_{sept3}	4.8
L_{sept4}	1.0
L_{NRN1}	8.4
L_{NRN2}	7.0
L_{NRN3}	9.6
H_{S1}	5.9
H_{S2}	6.4
H_{S3}	5.5
L_{Si}, $i = 1..3$	3.0
L_{total}	36.4

Table 5-4: Dimensions of the designed filter with three S-shaped resonators (see Figure 5-42).

For experimental validation of the proposed structure, the metallo-dielectric insert has been fabricated using the standard PCB process (Rogers Duroid RT/5880™ substrate with relative permittivity $\varepsilon_r = 2.2$, $\tan\delta = 0.0009$ and thickness $T_{sub} = 0.8$ mm has been used; metallization thickness – $T_{metal} = 0.017$ mm) and mounted inside a brass housing of the standard rectangular waveguide WG-90 (22.86 mm×10.16 mm). Frequency response of the fabricated filter has been measured using the Agilent PNA (E8361A) vector network analyzer. Corresponding measured insertion and return losses along with the simulated ones are shown in Figure 5-43. It is evident from this figure that measured results demonstrate a good agreement with the results of simulation. However, it is evident that one of the poles

is slightly shifted towards higher frequencies. At the same time, the first transmission zero is also slightly shifted from the predicted location. These shifts can be explained by a fabrication error in the area where the second S-shaped resonator is located, which would have resulted in an alteration of the S-shaped resonator's resonant frequency.

Photograph of the cross-section of waveguide housing with the metallo-dielectric insert containing the pattern for implementation of the 3rd-order filter with three S-shaped resonators is shown in Figure 5-44.

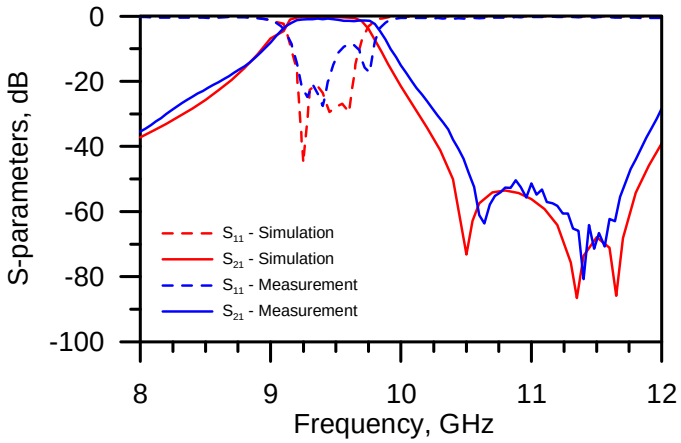

Figure 5-43: Simulated and measured S-parameters of the 3rd-order filter with S-shaped resonators.

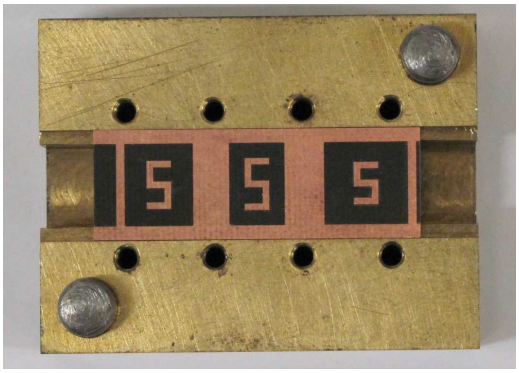

Figure 5-44: Half of waveguide housing with metallo-dielectric insert fabricated for the filter with S-shaped resonators.

5.5.3.2. 3rd-order Filter Using EPS with S-shaped Resonators and SRR

In order to show feasibility of EPS with SRRs, a 3rd-order extracted pole filter with S-shaped resonators and SRR has been designed to meet the following specifications:

- center frequency: 9.45 GHz;
- ripple passband: 9.25 – 9.65 GHz;
- return loss: 20 dB;
- transmission zeros: 10.5 GHz, 11.2 GHz, 11.8 GHz.

Approximation and synthesis procedures result in a lowpass prototype with the coupling scheme shown in Figure 5-37 with the following element values: $J_{S1} = 1$, $B_{N1} = -3.79$, $J_1 = 4.344$, $B_1 = -4.988$, $J_{12} = 1$, $B_{N2} = -8.551$, $J_2 = 8.297$, $B_2 = -8.066$, $J_{23} = 1$, $B_{N3} = -8.104$, $J_3 = 9.29$, $B_3 = -10.58$, $J_{3L} = 1$. The filter has been implemented in E-plane technology using a metallo-dielectric insert with two EPS with S-shaped resonators and a single EPS with SRR. Configuration of the E-plane insert for realization of the 3rd-order filter is presented in Figure 5-45. The EPS with SRR is arranged between the EPS with S-shaped resonators; however, generally an arbitrary sequence can be chosen.

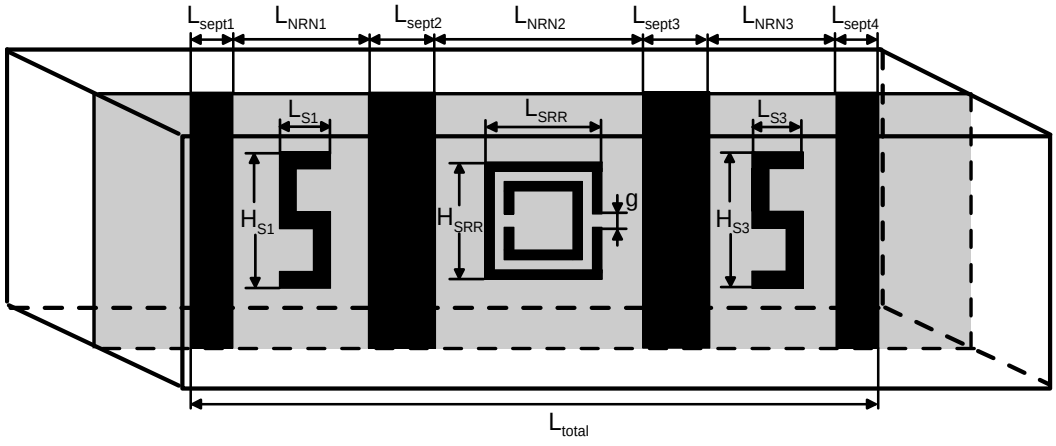

Figure 5-45: Configuration of the E-plane filter with two S-shaped resonators and an SRR.

Dimensions of the metallo-dielectric insert, obtained by extraction of GCC between EPS and refined by further optimization, are presented in Table 5-5.

Parameters	Values, mm
L_{sept1}	1.0
L_{sept2}	4.5
L_{sept3}	4.2
L_{sept4}	1.0
L_{NRN1}	9.6
L_{NRN2}	7.0
L_{NRN3}	8.4
H_{S1}	5.5
H_{S3}	5.9
L_{Si}, i = 1, 3	3.0
H_{SRR}	7.6
L_{SRR}	5.2
g	0.6
L_{total}	38.6

Table 5-5: Dimensions of the designed filter with two S-shaped resonators and an SRR (see Figure 5-45).

The metallo-dielectric insert has been fabricated using the same procedure as mentioned in the previous section. The frequency response of the fabricated filter, measured by the Agilent PNA (E8361A) vector network analyzer is shown in Figure 5-46, along with the corresponding simulated response. Measurement results demonstrate good agreement with the results of simulation, taking into account the shift of a pole and the first transmission zero to a higher frequency. The origin of this shift is suspected to be in fabrication errors occurred in the middle EPS containing the SRR, which is very sensitive to manufacturing tolerances. The pole available at 10.5 – 10.8 GHz frequency range is referred to the spurious resonance of the EPS with embedded SRR (see section 5.4.6).

Photograph of the metallo-dielectric insert with etched EPS and septa, fabricated for implementation of the 3rd-order filter with S-shaped resonators and SRR and placed in a channel within a half of the waveguide housing is shown in Figure 5-47.

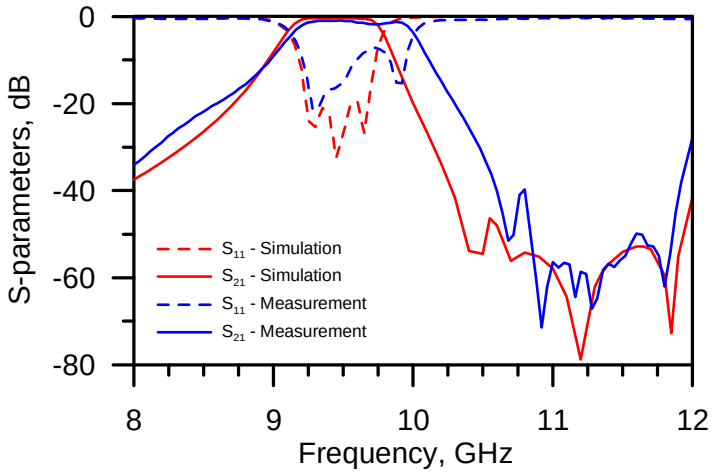

Figure 5-46: Measured and simulated S-parameters of the 3rd-order filter with S-shaped resonators and SRR.

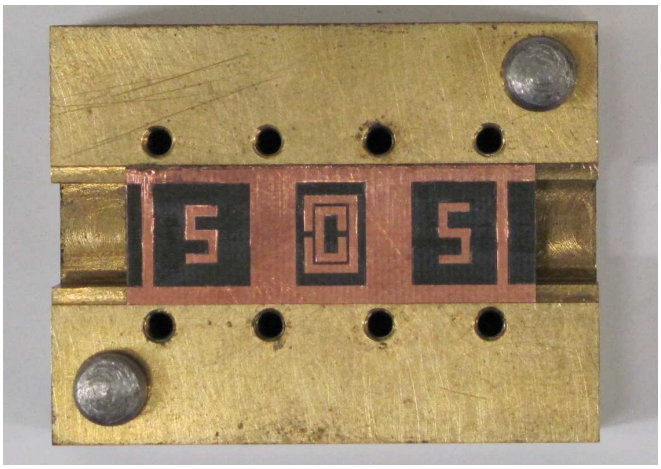

Figure 5-47: Metallo-dielectric insert with S-shaped resonators and SRR embedded in a half of the waveguide housing.

5.5.4. 4th-order Filter with a Dual-Mode EPS and a Transmission Zero in Lower Stopband

In section 5.2 it has been mentioned that EPS are capable of generating a transmission zero not only in upper stopband, but in lower as well. In section 5.4.6 it has been shown theoretically that a real EPS reveals at least two poles and a transmission zero, which is always located between them. Expressions (5.2-4) and (5.2-5) suggest that to generate a transmission zero in lower stopband, it is necessary to realize an NRN with positive frequency invariant susceptance B_N instead of the negative B_N used for upper stopband transmission zeros in the previous filter design examples. In this section a development of an EPS with a transmission zero in the lower stopband compatible with E-plane insert technology is considered. A filter with transmission zeros in both lower and upper stopbands is designed based on the developed EPS.

5.5.4.1. Dual-Mode EPS with Transmission Zero in Lower Stopband

A strongly detuned standard E-plane resonator, which acted as an NRN in the previously reported designs, has negative susceptance at frequencies lower than self-resonant frequency and, on the other hand, positive susceptance at frequencies higher than self-resonant frequency. This suggests that it is necessary to increase the length of the NRN in order to obtain much lower resonant frequency and, therefore, a positive value of B_N. An embedded resonator in EPS, which determines the position of a transmission zero, retains the same configuration as in ordinary EPS.

Let us examine a frequency response of an EPS with embedded λ/4-wavelength resonator, which has an enlarged NRN in order to obtain the lower stopband transmission zero. General configuration of this type of EPS is presented in Figure 5-20. Corresponding S-parameters of the EPS, simulated in CST Microwave Studio™ are shown in Figure 5-48. It is evident from the frequency response of the EPS that beside the pair of pole and zero, an additional pole has appeared in the frequency range under consideration. Simulated field distribution at the pole frequencies suggests that the additional resonance corresponds to the second-order resonance (quasi-TE_{102} mode) of the E-plane resonator used as NRN. The second pole is the one produced by the EPS. Generally, the transmission zero still appears

between two poles generated by the EPS as it has been previously predicted in section 5.4.6.2 (see eq. (5.4-13)). The lower-mode pole is located at a very low frequency and is not shown in Figure 5-48.

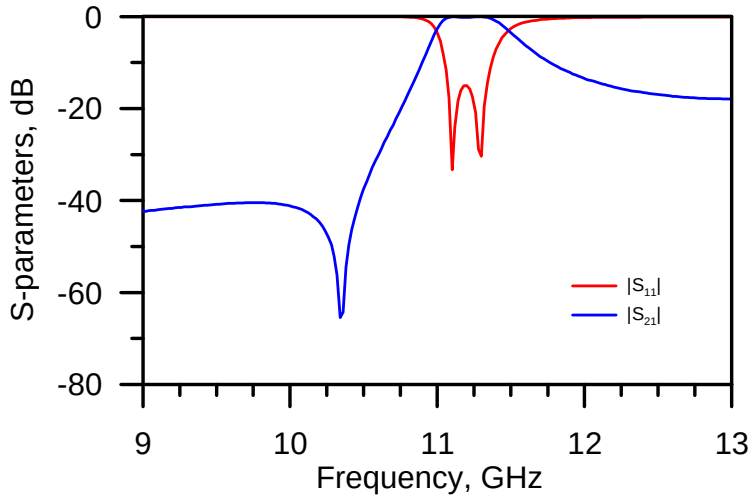

Figure 5-48: Simulated frequency response of an EPS with embedded λ/4-wavelength resonator, generating a transmission zero in lower stopband.

It has been found that positions of the poles can be adjusted by changing the width of embedded λ/4-wavelength resonator W_{res} and the length of the NRN L_{NRN}. Investigation of this property is illustrated in Figure 5-49.

Variation of the W_{res} causes alteration of position of one of the poles, which becomes shifted by the same frequency as the transmission zero (see Figure 5-49a). At the same time, the other pole, which corresponds to the NRN's self-resonance, retains its position. This effect can be explained by shifting of resonant frequency of the λ/4-wavelength resonator due to alteration of its internal inductance and capacitance.

From Figure 5-49b it is evident that with variation of L_{NRN} the transmission zero undergoes slight shifting due to alteration of capacitance between both septa and the resonator. At the same time, increasing L_{NRN} leads to reduction of distance between the transmission zero and poles, as well as distance between the poles. Taking advantage of the considered effects, a real EPS can be tuned in order to achieve the desired performance.

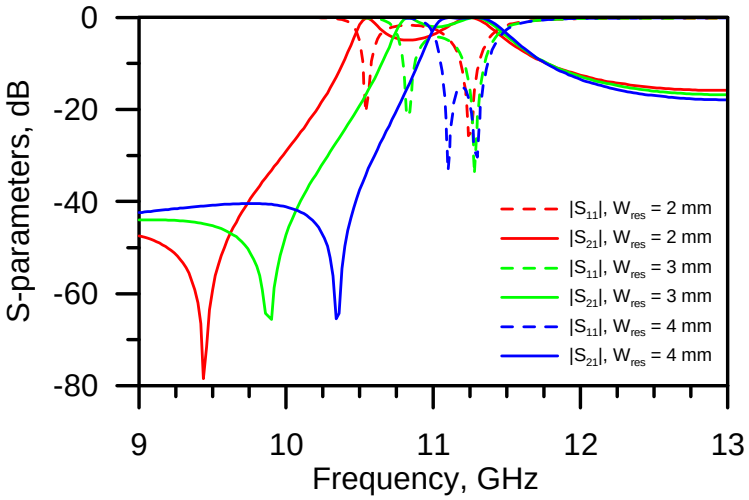

(a)

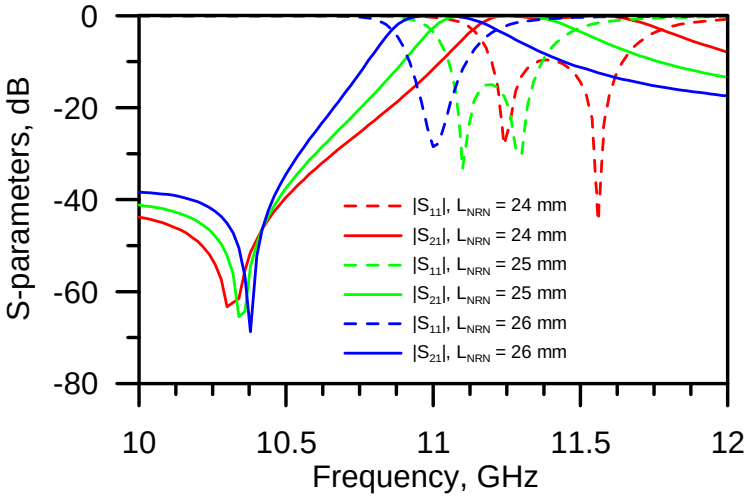

(b)

Figure 5-49: Adjustment of positions of poles and zero in EPS by changing geometrical dimensions of its elements: (a) effect of changing W_{res} (L_{NRN} = 25 mm, L_{res} = 7 mm); (b) effect of changing L_{NRN} (W_{res} = 4 mm, L_{res} = 7 mm).

The EPS which exhibits two very closely located poles and a transmission zero in lower stopband can be defined as a dual-mode EPS. This structure has the properties of a standard EPS connected in cascade with a resonator. Therefore, it can be modelled using a lowpass prototype network with a coupling scheme presented in Figure 5-50.

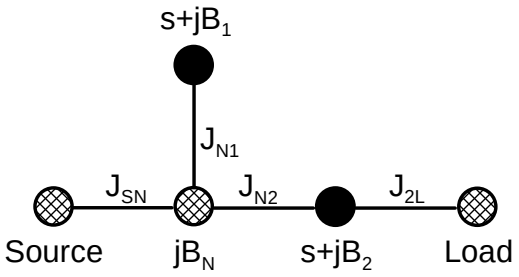

Figure 5-50: Coupling scheme of a dual-mode EPS.

Analysis of the dual-mode EPS is a complex problem as the structure generates two resonating modes which can not be separated. Thus, GCC can not be extracted using the technique given in section 5.3, because it is generally impossible to distinguish the origin of two poles generated by the circuit. However, analysis and design of dual-mode EPS can be effectively carried out by optimization. Example of such an approach has been reported in [5-11].

5.5.4.2. Filter with Dual-Mode EPS. Approximation and Synthesis

A 4th-order inline extracted pole bandpass filter with a transmission zero in lower stopband has been designed and implemented in E-plane technology in order to demonstrate the use of dual-mode EPS. Specifications of the filter are given as follows:

- center frequency: 11 GHz;
- ripple passband: 10.75 – 11.25 GHz;
- return loss: 18 dB;
- transmission zeros: 10.3 GHz, 11.7 GHz, 12 GHz.

Characteristic polynomials $P(s)$ and $F(s)$ of the filter have been derived using generalized Chebyshev approximation. When the roots of $F(s)$ have been found, these can be used for coupling matrix synthesis by optimization (see Section 3.3.3.5) as well as the known transmission zeros (roots of $P(s)$). The gradient-based optimization procedure applied to the polynomials leads to obtaining the lowpass prototype equivalent network shown in Figure 5-51. Elements of the prototype have the following values: $J_{S1} = 1.0$, $B_{N1} = -2.064$, $J_{N1} = 2.599$, $B_1 = -2.895$, $J_{12} = 1.0$, $B_{N2} = 3.131$, $J_{N2} = 2.657$, $J_{23} = 0.827$, $B_2 = 2.716$, $B_3 = 0.243$,

J_{34} = 0.884, B_{N4} = –3.324, J_{N4} = 3.558, B_4 = –3.833, J_{4L} = 1.0. Therefore, corresponding GCC can be calculated as: Q_{extS} = –2.064, Q_{extL} = –3.3244, k_1^2 = –3.272, k_2^2 = 2.255, k_4^2 = –3.809, k_{12}^2 = –0.155, k_{23}^2 = 0.218, k_{34}^2 = –0.235.

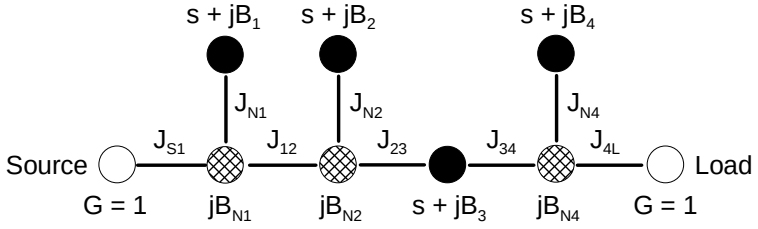

Figure 5-51: Coupling scheme of the 4th-order extracted pole filter with dual-mode EPS.

5.5.4.3. Filter with Dual-Mode EPS. Implementation

The filter has been implemented by three direct coupled EPS with embedded λ/4-wavelength resonators. Two of these sections are conventional EPS with negative B_N, used for implementation of the filter in Section 5.5.2, each producing a transmission zero in upper stopband. The remaining section is the dual-mode EPS, responsible for the transmission zero in lower stopband. Configuration of the E-plane insert for this filter is presented in Figure 5-52.

Dimensions of both single-mode EPS and input/output septa have been obtained by extraction of the corresponding GCC from simulated frequency responses of each individual EPS. Plots used for extraction are not shown here in order to save space, as the GCC' extraction procedure has been explained in details in Section 5.5.2. Initial length of the embedded resonator in dual-mode EPS has been obtained by tuning H_{res2} until the required position of transmission zero is reached. The remaining dimensions of the insert have been found by gradient optimization carried out with respect to the manufacturing tolerances in full-wave simulator CST Microwave Studio™. The dimensions of the insert obtained as a result of optimization process are summarized in Table 5-6.

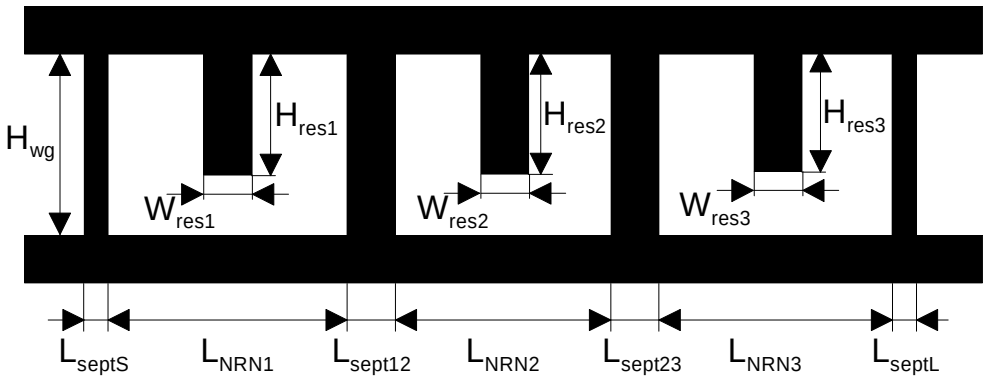

Figure 5-52: Configuration of E-plane insert for implementation of the 4th-order filter with dual-mode EPS.

Parameter	Value	Parameter	Value
L_{septS}	0.7	H_{res1}	4.5
L_{sept12}	7.3	H_{res2}	6.3
L_{sept23}	7.5	H_{res3}	4.3
L_{septL}	0.5	W_{res1}, W_{res3}	1.5
L_{NRN1}	3.9	W_{res2}	2.5
L_{NRN2}	25.6	H_{wg}	10.16
L_{NRN3}	4.8	L_{total}	50.3

Table 5-6: Dimensions of the designed filter with dual-mode EPS (see Figure 4-52).

5.5.4.4. Filter with Dual-Mode EPS. Experimental Verification

Feasibility of the dual-mode EPS and adequacy of the proposed approach have been verified experimentally. For this purpose the pattern presented in Figure 5-52 has been etched on the top side of a rectangular piece of standard PCB (Rogers Duroid RT/5880™ substrate with relative permittivity ε_r = 2.2, tanδ = 0.0009 and thickness T_{sub} = 0.8 mm; metallization thickness – T_{metal} = 0.017 mm), while the bottom side of the substrate has been completely cleaned of metallization. The resultant metallo-dielectric insert has been placed in a channel within the E-plane of a standard rectangular waveguide (WG-90; cross-section: 22.86×10.16 mm^2), between two separate halves of a brass housing. Photograph of the fabricated structure is shown in Figure 5-53.

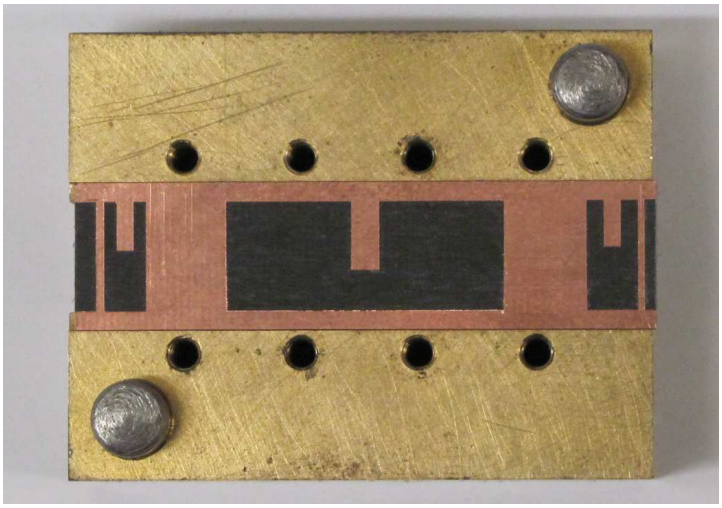

Figure 5-53: Photograph of the fabricated filter: insert placed within a channel in a half of the waveguide housing

S-parameters of the filter have been measured using the Agilent E8361A vector network analyzer. Comparison of simulated and measured responses of the fabricated filter is presented in Figure 5-54.

The measured curves clearly display all three transmission zeros, however two zeros and two poles of four are shifted from the predicted positions due to high sensitivity of resonant frequencies of λ/4-wavelength resonators to fabrication tolerances. The measured insertion loss at centre frequency is 2.05 dB. Required return loss in the passband of better than 18 dB is successfully achieved. Overall agreement of computed and experimental responses is satisfactory taking into account fabrication tolerances.

The second band of the filter is primarily determined by the cutoff frequency of the second propagation mode TE_{20} of the waveguide which appears at about 13 GHz for the waveguide WG-90 with the dielectric insert. It is clear that the second band is located too close to the passband of the filter. However the choice of the filter's centre frequency which strictly determines the total length of the filter was limited by the available housing with the special channel for convenient arrangement of the dielectric insert. Use of a longer housing and/or

use of all-metal inserts will improve the stopband performance of the filter, as well as allow lowering the centre frequency of the filter. It should be noted that influence of fabrication tolerances should be less for filters designed for lower centre frequency.

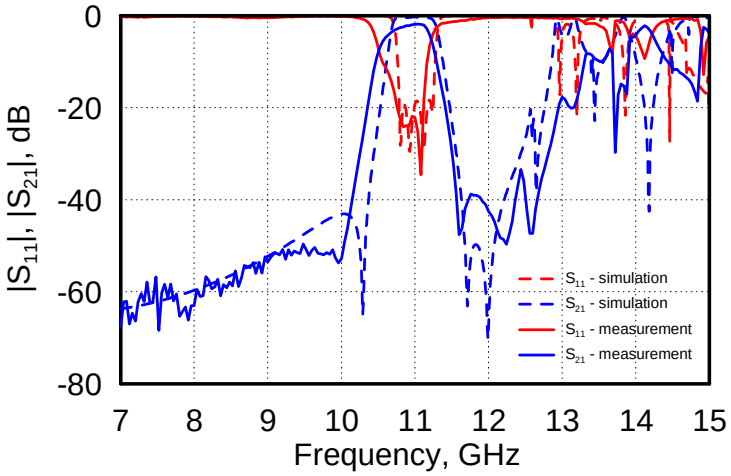

Figure 5-54: Simulated and experimental responses of the fabricated 4th-order filter with dual-mode EPS.

5.6. Summary

In this chapter the problem related to extracted pole filters design using E-plane inserts in rectangular waveguides has been thoroughly discussed.

In section 5.2 extracted pole sections have been introduced as modules which constitute inline extracted pole filters. Equivalent lowpass prototype and main properties of frequency responses of the EPS have been demonstrated.

Generalized coupling coefficients have been introduced in section 5.3 as a convenient tool for representation and design of filters with NRN. Expressions for extraction of GCC from simulated or measured frequency responses of single EPS, EPS interacting with another EPS or resonator have been derived analytically for the first time.

In section 5.4 several EPS with embedded resonators have been studied. Effects caused to frequency responses of EPS by varying of geometrical dimensions of its elements have been investigated using electromagnetic simulations. It has been found that position of the transmission zero may vary in a wide range which makes it possible to improve stopband performance of the filters drastically. Analysis of the EPS' performance has shown that *Q*-factor of the EPS with embedded resonators drops by more than 60% in comparison with hollow E-plane resonators, while total element's length is reduced by more than 40%.

In section 5.5 a set of inline extracted pole filters with EPS has been designed using the novel GCC extraction technique and fabricated. It has been found that this technique provides good initial values for CAD optimization of the filter structures. Experimental verification has shown excellent agreement for the filter with all-metal insert, while the filters with metallo-dielectric inserts have suffered from errors due to high sensitivity of the structures to fabrication tolerances. Additionally, a novel dual-mode EPS capable of generating a transmission zero in lower stopband has been achieved as a result of theoretical investigation. The results confirm the proposed ideas and prove adequacy of the EPS model and the filter design approach using the novel GCC extraction technique.

5.7. References

[5-1] J. R. Montejo-Garai, J. A. Ruiz-Cruz, J. M. Rebollar, M. J. Padilla-Cruz, A. Onoro-Navarro, and I. Hidalgo-Carpintero, "Synthesis and Design of In-Line N-Order Filters With N Real Transmission Zeros by Means of Extracted Poles Implemented in Low-Cost Rectangular H-Plane Waveguide," *IEEE Trans. Microwave. Theory & Tech.*, vol. 53, no. 5, pp. 1636–1642, May 2005.

[5-2] M. Fahmi, J. A. Ruiz-Cruz, R. R. Mansur, and K. A. Zaki, "Compact Ridge Waveguide Filters Using Non-Resonanting Nodes," *2007 IEEE MTT-S International Microwave Symposium Dig.*, pp. 1137-1340, June 2009.

[5-3] G. Macchiarella and Marco Politi, "Use of Generalized Coupling Coefficients in the Design of Extracted-Poles Waveguide Filters with Non-Resonating Nodes," *2009 IEEE MTT-S International Microwave Symposium Dig.*, pp. 1341-1344, June 2009.

[5-4] Y.-C. Shih, and T. Itoh, "E-Plane Filters with Finite-Thickness Septa," *IEEE Trans. Microwave. Theory & Tech.*, vol. 31, no. 12, pp. 1009–1013, Dec. 1983.

[5-5] D. Young and I. C. Hunter, "Integrated E-Plane Filters with Finite Frequency Transmission Zeros,," *24th European Microwave Conference, 1994*, vol. 1, pp. 460-465, 5-9 Sept. 1994.

[5-6] R. Lopez-Villarroya and G. Goussetis, "Novel Topology for Low-Cost Dual-Band Stopband Filters," *Asia Pacific Microwave Conference, 2009*, pp. 933-936, 7-10 Dec. 2009.

[5-7] A. Shelkovnikov and D. Budimir, "Miniaturized Rectangular Waveguide Filters," *Int. J. RF and Microwave CAE*, vol. 17, no. 4, pp. 398-403, 2007.

[5-8] A. Shelkovnikov and D. Budimir, "Left-Handed Rectangular Waveguide Bandstop Filters," *Microwave Opt. Technol. Lett.*, Vol. 48, No. 5, pp. 846–848, 2006.

[5-9] N. Suntheralingham and D. Budimir, "Enhanced Waveguide Bandpass Filters Using S-shaped Resonators," *Int. J. RF and Microwave CAE*, vol. 19, no. 6, pp. 627-633, 2009.

[5-10] S. Amari and U. Rosenberg, "Synthesis and Design of Novel In-Line Filters With One or Two Real Transmission Zeros," *IEEE Trans. Microwave Theory Tech.*, vol. 52, pp. 1464-1478, May 2004.

[5-11] S. Amari and U. Rosenberg, "New In-Line Dual- and Triple-Mode Cavity Filters With Nonresonating Nodes," *IEEE Trans. Microwave Theory Tech.*, vol. 53, pp. 1272-1279, April 2005.

[5-12] G. Macchiarella, "Generalized Coupling Coefficient for Filters With Nonresonant Nodes," *IEEE Microwave and Wireless Components Letters*, Vol. 18, No. 12, pp. 773-775, Dec. 2008.

[5-13] J.-S. Hong and M. J. Lancaster, *Microstrip Filters for RF/Microwave Applications*. New York: Wiley, 2001.

[5-14] A. Shelkovnikov, N. Suntheralingam and D. Budimir, "Novel SRR Loaded Waveguide Bandstop Filters," *IEEE AP-S/USRI Int. Symp. Dig.*, pp. 4523-4526, Albuquerque, USA, 9-14 July, 2006.

[5-15] J. B. Pendry, A. J. Holden, D. J. Robbins, and W. J. Stewart, "Magnetism from Conductors and Enhanced Nonlinear Phenomena," *IEEE Trans. Microw. Theory Tech.*, vol. 47, no. 11, pp. 2075–2084, Nov. 1999.

[5-16] D. R. Smith, W. J. Padilla, D. C. Vier, S. C. Nemat-Nasser, and S. Schultz, "Composite Medium with Simultaneously Negative Permeability and Permittivity," *Phys. Rev. Lett.*, vol. 84, pp. 4184-4187, May 2000

[5-17] R. Marques, J. Martel, F. Mesa, and F. Medina, "Left-Handed-Media Simulation and Transmission of EM Waves in Subwavelength Split-Ring-Resonator-Loaded Metallic Waveguides," *Phys. Rev. Lett.*, vol. 89, no. 18, Oct. 28, 2002.

[5-18] A. A. Glubokov and B. N. Shelkovnikov, "Waveguide Filter Using Ring Resonators," *Microwave and Telecommunication Technology, 2006. CriMiCo'06. 16th International Crimean Conference*, vol. 2, pp. 525-526, Sept. 2006.

[5-19] G. L. Matthaei, "Interdigital Band-Pass Filters", *Microwave Theory and Techniques, IRE Transactions on*, vol. MTT-10, pp. 479–491, Nov. 1962.

[5-20] R. J. Wenzel, "Exact Theory of Interdigital Band-Pass Filters and Related Coupled Band-Pass Structures", *Microwave Theory and Techniques, IEEE Transactions on*, vol. 13, pp. 559-575, Sep. 1965.

[5-21] R. Levy, S. B. Cohn, "A History of Microwave Filter Research, Design, and Development", *Microwave Theory and Techniques, IEEE Transactions on*, pp. 1055–1067, vol. 32, 1984.

[5-22] I. C. Hunter, *Theory and Design of Microwave Filters*, London, U.K.: IEE Press, 2001.

[5-23] M. Sagawa, M. Makimoto, and S. Yamashita, "Geometrical Structures and Fundamental Characteristics of Microwave Stepped-Impedance Resonators," *Microwave Theory and Techniques, IEEE Transactions on*, vol. 45, pp. 1078-1085, 1997.

[5-24] M. Makimoto and S. Yamashita, "Compact Bandpass Filters Using Stepped Impedance Resonators," *Proceedings of the IEEE*, vol. 67, pp. 16-19, 1979.

[5-25] M. Makimoto, *Microwave Resonators and Filters for Wireless Communication*, Springer, 2001.

[5-26] M. Makimoto and S. Yamashita, "Bandpass Filters Using Parallel Coupled Stripline Stepped Impedance Resonators," *Microwave Theory and Techniques, IEEE Transactions on*, vol. 28, pp. 1413-1417, 1980.

[5-27] A. A. A. Apriyana and P. Zhang Yue, "A Dual-Band BPF for Concurrent Dual-Band Wireless Transceiver," presented at Electronics Packaging Technology, 2003 5th Conference (EPTC 2003), 2003.

[5-28] D. M. Pozar, *Microwave engineering / David M. Pozar*. New York; Chichester: Wiley, 2004.

[5-29] S. Amari and G. Macchiarella, "Synthesis of Inline Filters With Arbitrary Placed Attenuation Poles by Using Nonresonating Nodes," *IEEE Trans. Microwave. Theory & Tech.*, vol. 53, no. 10, pp. 3075–3081, Oct. 2005.

[5-30] V. Postoyalko and D. S. Budimir, "Design of Waveguide E-plane Filters with All-Metal Inserts by Equal Ripple Optimization," *IEEE Trans. Microwave. Theory & Tech.*, vol. 42, no. 2, pp.217-222, Feb 1994.

CHAPTER 6

SUBSTRATE INTEGRATED WAVEGUIDE FILTER STRUCTURES

6.1. Introduction

Active development of modern telecommunication technologies has created colossal demand for compact, inexpensive and high-performance bandpass filters with good selectivity and low insertion loss. Recently developed planar structures – substrate integrated waveguides (SIW), able to meet present specifications, have been proposed as a replacement of conventional rectangular waveguides which are expensive, difficult to fabricate and integrate [6-1]. SIW resonators have become attractive for design of microwave filters using cross-coupled topologies with elliptic and pseudo-elliptic responses [6-2], which have found wide application in microwave and mm-wave systems lately due to their ability to produce transmission zeros at predicted frequencies and create sharp slopes.

Methods of miniaturization of SIW resonators have been thoroughly examined recently. Several techniques of size reduction for resonators and filters have been proposed: use of EBG-substrate structures [6-3]; ridged SIW resonators [6-4]; folded SIW (FSIW) resonators which occupy only half an area of equivalent SIW resonators [6-5]. Filter based on quarter-wavelength SIW cavities have been designed in [6-6], and another approach to miniaturization by folding has been developed and investigated in [6-7, 6-8].

In chapters 4 and 5 it has been shown that conventional waveguide filters can be miniaturized by employing modular filter design and extracted pole technique, taking advantage of using combinations of stripline resonators and rectangular waveguide transmission line. Historically, evolution of SIW structures has been driven by achievements made in research of conventional rectangular waveguides. Therefore,

application of the methods previously proposed in this thesis to SIW technology may lead to development of new planar filters retaining the advantages of their conventional waveguide analogues.

In this chapter, attention will be paid to design of miniaturized SIW cross-coupled filters. In section 6.2 FSIW resonators are introduced; a new structure for implementation of negative coupling between FSIW resonators is proposed. The design example of a 4^{th}-order cross-coupled filter based on half- and quarter-wavelength FSIW resonators is presented. Section 6.3 focuses on design of modular SIW filters. In this section, singlet and doublet modules with $\lambda/4$-wavelength stripline resonators are proposed for realization in multilayer SIW technology. Modular filter with NRN, which has three transmission zeros in both stopbands is designed. Finally, in section 6.4, an extracted pole section for multilayer SIW technology is introduced. Design example of inline extracted pole filter with NRN using the substrate integrated EPS is presented.

6.2. Design of Cross-Coupled SIW Filters

6.2.1. SIW Cavity Resonators

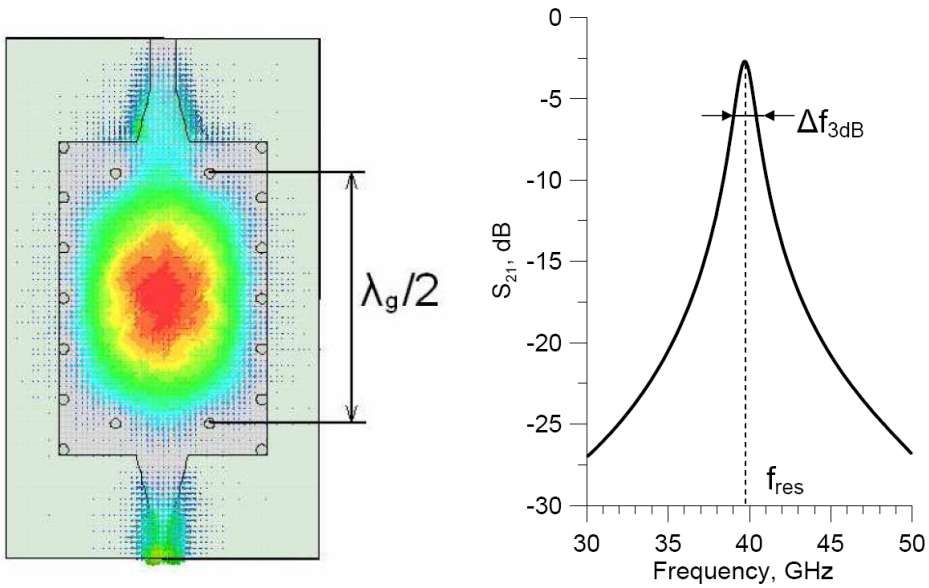

Figure 6-1: Configuration of a SIW cavity resonator and its frequency response.

Waveguide cavity resonators are usually organized as a λ/2-wavelength section of a transmission line limited by conductive walls with slots for the purpose of excitation. Figure 6-1 shows a general configuration of a λ/2-wavelength SIW cavity resonator. If SIW is used as a basic transmission line, the conductive walls of the resonator are formed by via holes connecting top and bottom ground planes. Role of the excitation slot is performed by a gap in the wall, between vias. Side walls of the SIW can be realized within its substrate, either as an array of metallized posts, metallized grooves, or paste side walls. Feeding of the structure is realized by means of microstrip inputs; microstrip-to-SIW transition is organized using tapers [6-1, 6-9] which provide effective modal energy conversion from TE_{10} mode in waveguide to TEM propagating in microstrip line, and vice versa.

Resonant wavelength λ_{res} of SIW resonators is related to their length L_{res} through the following equation:

$$L_{res} = \frac{\lambda_g}{2} = \frac{\lambda_{res}}{2 \cdot \sqrt{1 - \left(\frac{\lambda_{res}}{2 \cdot W_{eff}} \right)}} \tag{6.2-1}$$

where W_{eff} is given by (2.3-3). Hence, the resonant frequency can be derived as

$$f_{res} = \frac{c\sqrt{W_{eff}^2 + L_{res}^2}}{2W_{eff}L_{res}} \tag{6.2-2}$$

6.2.1.1. λ/2-wavelength Folded SIW Resonator

In [6-10] Grigoropoulos and Young introduced a concept of new folded substrate-integrated waveguides (FSIW). Further research have indicated that, when the width of FSIW is nearly half of width of original unfolded SIW, and its E-plane gap width is nearly the height of the SIW, the FSIW reveals nearly the same propagation and cutoff characteristics of the SIW structure. In this way, it is possible to design novel RF/microwave circuits using this new platform. Comprehensive theoretical investigation and experimental verification of FSIW can be found in [6-11].

Consider a λ/2-wavelength long section of SIW folded along its longitudinal axis while maintaining its standing waves. Having two layers, the obtained structure occupies only half the area comparing to the conventional SIW resonator and is referred to as FSIW λ/2-wavelength cavity resonator. Complete resonator contains a guiding part with a longitudinal slot made near the side wall which consists of several metallic posts. Some via connectors organize input and output apertures which are connected to input/output striplines. Typical configuration of a SIFW λ/2-wavelength resonator is presented in Figure 6-2.

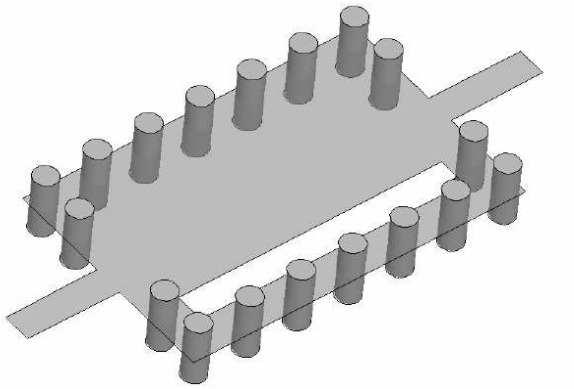

Figure 6-2: Configuration of a λ/2-wavelength FSIW resonator.

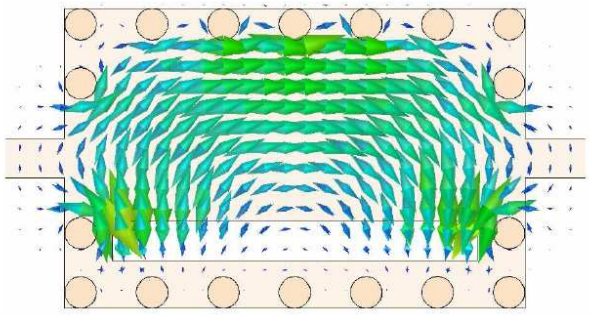

Figure 6-3: Magnetic field distribution in a λ/2-wavelength FSIW resonator.

In Figure 6-3, distribution of magnetic field in the resonator at its resonant frequency is presented. It is seen that magnetic field has its maximum near the side walls. The field structure forms a magnetic line which passes the region near the side walls on top layer clockwise, goes through the slot near the resonator's input, than passes the bottom side walls region anticlockwise returning to the top layer through the slot near the resonator's output.

FSIW resonator occupies half an area of a SIW resonator but requires stacking of two layers of substrate. Due to unusual field distribution, the FSIW resonators give new opportunities in design of microwave and mm-wave filters.

6.2.1.2. λ/4-wavelength Folded SIW Resonator

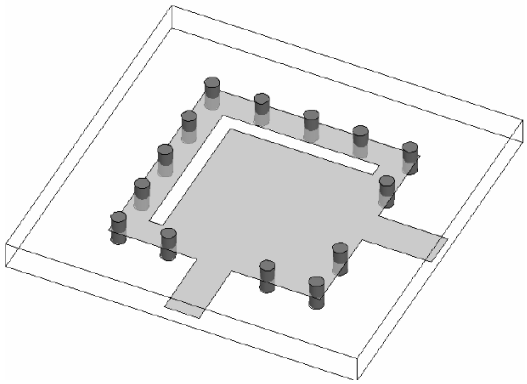

Figure 6-4: Configuration of a λ/4-wavelength FSIW resonator.

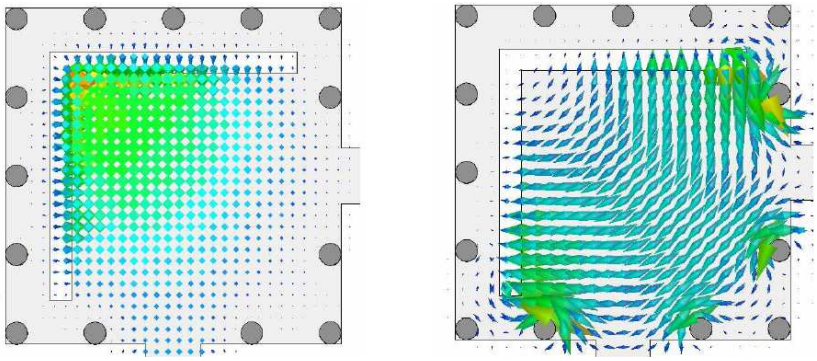

(a) (b)

Figure 6-5: Field distribution in a λ/4-wavelength FSIW resonator: (a) electric field; (b) magnetic field.

New structure of λ/4-wavelength FSIW resonator can be obtained by folding the λ/2-wavelength FSIW resonator by 90° in the plane of substrate. The new FSIW resonator has been proposed in [6-12]. It has been recently shown that the novel type of compact FSIW resonators, stemming from the concept of folding standing waves of a conventional TE_{101}-mode SIW resonator, retains similar high *Q*-factor property of SIW resonator but has only a quarter of its footprint.

Configuration of the λ/4-wavelength FSIW resonator is presented in Figure 6-4. Complete resonator contains a guiding part with L-shaped slot made near the side walls realized as metallized via-holes. Input/output striplines are used for feeding of the resonator through

input/output apertures in side walls. Distribution of electric and magnetic fields in the resonator at its resonant frequency, simulated in Ansoft HFSS™, is presented in Figure 6-5. Electric field is concentrated at the region of slot, while the magnetic field has its maximum near side walls where electric field has its minimum. Magnetic line has the same topology as the one for the λ/2-wavelength FSIW resonator case; its form is distorted due to the appropriate 90° folding. Direction of the line is clockwise in top dielectric layer and anticlockwise in bottom layer.

Comparison of main parameters of conventional SIW, λ/2-wavelength and λ/4-wavelength FSIW resonators, adjusted for the same resonant frequency f_{res} of 10 GHz is presented in Table 6-1. Calculation of unloaded *Q*-factor of the resonators has been performed using formulae (5.4-6) and (5.4-7). It is evident from the table that the λ/4-wavelength FSIW resonator occupies the smallest area, while the λ/2-wavelength FSIW resonator has the highest unloaded *Q*-factor.

Parameter	Type of resonator		
	Standard SIW	λ/2-wave FSIW	λ/4-wave FSIW
Width, mm	12	11.5	8.9
Length, mm	15	8.9	8.9
Area, mm^2	180	102.4	79.2
Unloaded *Q*-factor	255.2	389.4	356.1

Table 6-1: Comparison of SIW resonators based on full-wave EM simulation results (Ansoft HFSS™).

6.2.2. Coupled FSIW Resonators

Some types of cross-coupled filters require pairs of resonators which have positive and negative coupling coefficients. Several techniques are usually used for realization of the specified coupling coefficients. The simplest of them is coupling through irises in walls between integrated cavities.

6.2.2.1. Positive Coupling Structure

To realize a positive coupling coefficient between two folded resonators by means of coupling iris, it is sufficient to design a conventional pair of single-layer SIW resonators [6-2] and fold them around their longitudinal axes.

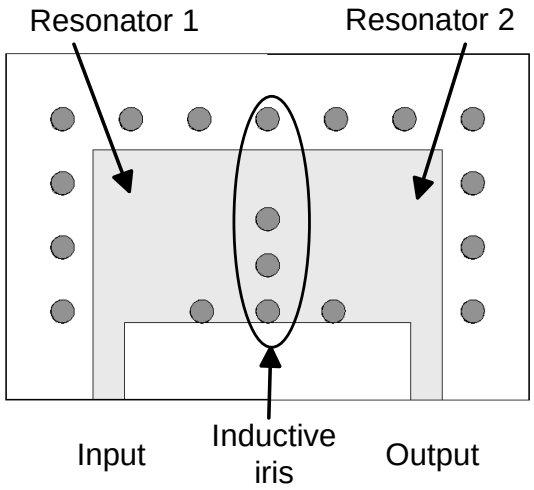

Figure 6-6: Configuration of coupled λ/4-wavelength FSIW resonators (top view).

In case of direct coupling, the gap in the middle metallization layer runs from one resonator to another, while two halves of coupling iris formed using plated vias are located one upon another in different layers. This principle is used for coupling of λ/4-wavelength FSIW resonators, shown in Figure 6-6. Direct coupling can be also realized by the principle used for design of conventional E-plane filters in rectangular waveguide [6-13], where a septum placed in the E-plane acts as an inductive discontinuity. Taking into account that the E-plane of a folded waveguide coincides with the gap in the middle layer, the coupling septum can be easily applied. However, realization of low coupling coefficients requires septa with significant widths. Nevertheless, narrow septa can be used in combination with

coupling irises to regulate values of coupling coefficients. In case of side coupling, folding does not affect the coupling iris and the coupling is provided by an inductive iris in regular way.

6.2.2.2. Negative Coupling Structure

Electric coupling provides negative coupling coefficient and it can be realized with a slot or gap at a region of a FSIW resonator, where maximum of electric field and minimum of magnetic field magnitudes appear. However, for the case of considered FSIW resonators, maximum of electric field appears in the slot and direct realization of the negative coupling coefficient is possible only if slots of two adjacent resonators are located by a common side wall. Such configuration becomes inapplicable when filter's layout must be built so that the slots are located by opposite side walls. To overcome the issue, use of magnetic coupling through a slot between top and bottom layers of adjacent resonators is proposed in this thesis instead of electric coupling.

It can be concluded from analysis made by Thomas in [6-14] that in two positively coupled resonators fields oscillate in phase at low resonant mode and have a shift of 180º at high mode. In contrast, in a pair of negatively coupled resonators fields are out of phase at low mode and not shifted at high mode. Consequently, the waves which have equal phases at the inputs of negative and positive coupling structures will be out of phase at the outputs. Thus, a negative coupling structure can be obtained from the positive one by reversing polarity at the output. One of advantages of folded resonators is that this effect can be achieved by folding both SIW resonators anticlockwise or clockwise (in the same direction) which is equal to swapping top and bottom ground planes of the output resonator. This procedure is also equivalent to swapping top and bottom layers of the second resonator. It should be emphasized that such approach is valid only for narrow-band circuits such as coupled resonators.

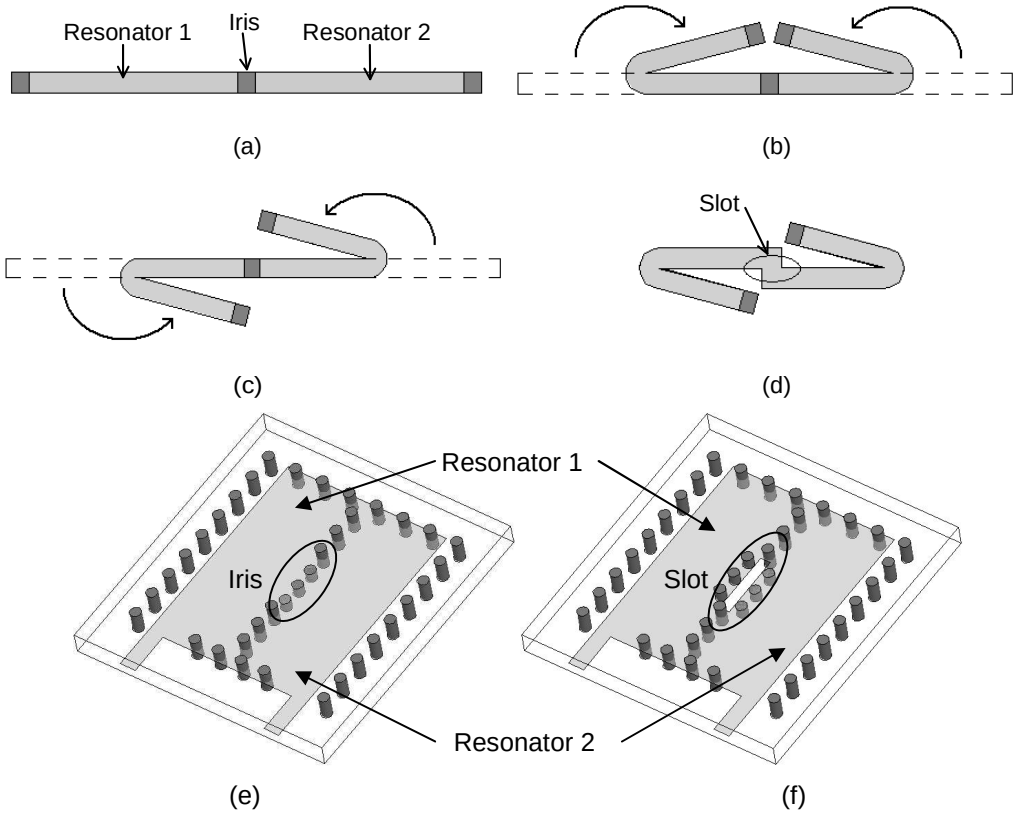

Figure 6-7: Folding process of a pair of resonators coupled by inductive iris (a–d: cross-section; e,f: 3-D view).

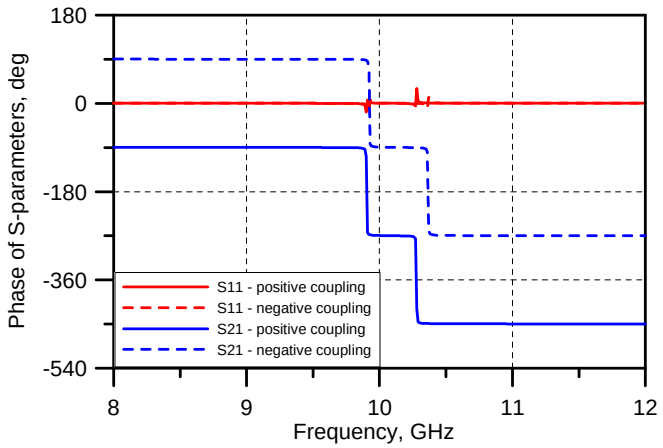

Figure 6-8: Phase responses of positively and negatively coupled resonators.

Consider a pair of single-layer SIW resonators positively coupled by an iris in common side wall (Figure 6-7a). To create a positively coupled pair of double-layer FSIW

resonators, it is necessary to fold up both resonators around their axes of symmetry clockwise and anticlockwise (in opposite directions) as it is shown in Figure 6-7b. 3-D view of the positively coupled SIW resonators is shown in Figure 6-7e. Swapping of layers of the second resonator can be performed by folding it clockwise (in the same direction, Figure 6-7c). Resultant structure consists of three layers; their number can be reduced by shifting one of resonators up or down by thickness of substrate. Such procedure will cause deformation of area where the coupling iris is located, so the iris becomes a slot in the middle metallization layer (Figure 6-7d). It is extremely important that despite the deformation of the iris area, all the waves and currents keep their structures and the folding condition [6-5] is satisfied. 3-D view of the negatively coupled SIW resonators is shown in Figure 6-7f. The structure has the properties of a pair of negatively coupled resonators. This can be proven by comparison of phase responses of positive and negative coupling structures which have weak external couplings (Figure 6-8). Indeed, at the neighbourhood of the resonant modes, phases of S_{21} are shifted by 180º, while phases of S_{11} remain equal. Feasibility of the upside-down negative coupling structure in cross-coupled filter will be proven in section 6.2.3 by a filter design example.

6.2.3. Filter Design Example

4th-order bandpass filter with λ/2- and λ/4-wavelength FSIW resonators has been designed in order to demonstrate feasibility of the negative coupling structure introduced in the previous section. The filter has been designed to satisfy the following specifications:

- centre frequency: 10 GHz;
- ripple passband: 9.75 – 10.25 GHz;
- return loss: 30 dB;
- transmission zeros: 9.2 GHz and 10.8 GHz.

6.2.3.1. Coupling Matrix Synthesis

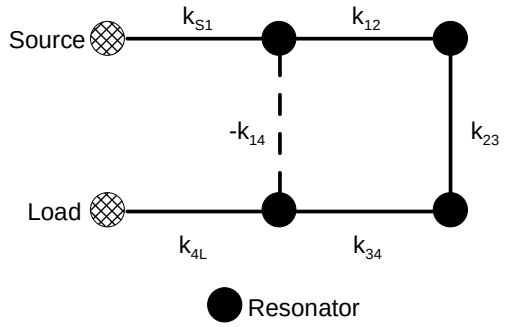

Figure 6-9: Coupling scheme of the proposed FSIW cross-coupled filter.

Synthesis of a cross-coupled filter with synchronously tuned resonators lies in derivation of a coupling matrix for its lowpass prototype from known initial specifications. For pseudo-elliptic filters, the matrix can be derived by optimization using the procedure presented in [6-15]. Coupling scheme chosen to realize the lowpass prototype of the corresponding filter (shown in Figure 6-9) with four poles and two transmission zeros at $\pm j3.2$ leads to the following generalized coupling matrix M:

$$M = \begin{bmatrix} & S & 1 & 2 & 3 & 4 & L \\ S & 0 & 1.219 & 0 & 0 & 0 & 0 \\ 1 & 1.219 & 0 & 1.105 & 0 & -0.112 & 0 \\ 2 & 0 & 1.105 & 0 & 0.857 & 0 & 0 \\ 3 & 0 & 0 & 0.857 & 0 & 1.105 & 0 \\ 4 & 0 & -0.112 & 0 & 1.105 & 0 & 1.219 \\ L & 0 & 0 & 0 & 0 & 1.219 & 0 \end{bmatrix} \quad (6.2\text{-}3)$$

Program for calculation of the coupling matrix has been developed in MATLAB™ by author.

Matrix M is then denormalized with respect to the required centre frequency f_0 and bandwidth Δf to obtain coupling coefficients k_{ij} and external quality factor Q_{ext} using the following formulae:

$$k_{ij} = \frac{\Delta f}{f_0} M_{ij} \quad (6.2\text{-}4)$$

$$Q_{ext} = \frac{f_0}{\Delta f \cdot M_{S1}^2} = \frac{f_0}{\Delta f \cdot M_{4L}^2} \quad (6.2\text{-}5)$$

Therefore, the following design parameters can be obtained for the filter: $k_{12} = k_{34} = 0.055$; $k_{23} = 0.043$; $k_{14} = -0.006$; $Q_{ext} = 13.46$.

6.2.3.2. Implementation

When the coupling matrix is obtained, correspondence between theoretical coupling coefficients and dimensions of coupling slots and irises is to be established. This can be done using plots of coupling coefficients against the slot/gap dimensions made for various types of couplings between pairs of resonators, built during preliminary analysis. Alternative method is calculation of corresponding slot/gap dimensions theoretically. However, this approach usually leads to bulky calculations.

To determine how coupling coefficients depend on dimensions of the irises and slots, coupled resonators have been simulated in EM full-wave simulator Ansoft HFSS™, and frequency responses have been obtained. Then, from each curve two peak frequencies have been identified as low mode f_{low} and high mode f_{high} frequencies. Coupling coefficients can be extracted using the modified expression (4.3-7):

$$k_{ij} = \pm \frac{f_{high}^2 - f_{low}^2}{f_{high}^2 + f_{low}^2} \tag{6.2-6}$$

The filter contains three positive coupling structures which produce the main path for signal in combination with all four resonators. Among the resonators, two between which negative coupling is to be realized (1 and 4) have been chosen to be λ/2-wavelength for the reason of simple organization of input and output transitions. The rest (2 and 3) have been chosen to be quarter-wavelength due to their location at the bend of the structure. Top view of the filter layout is given in Figure 6-10.

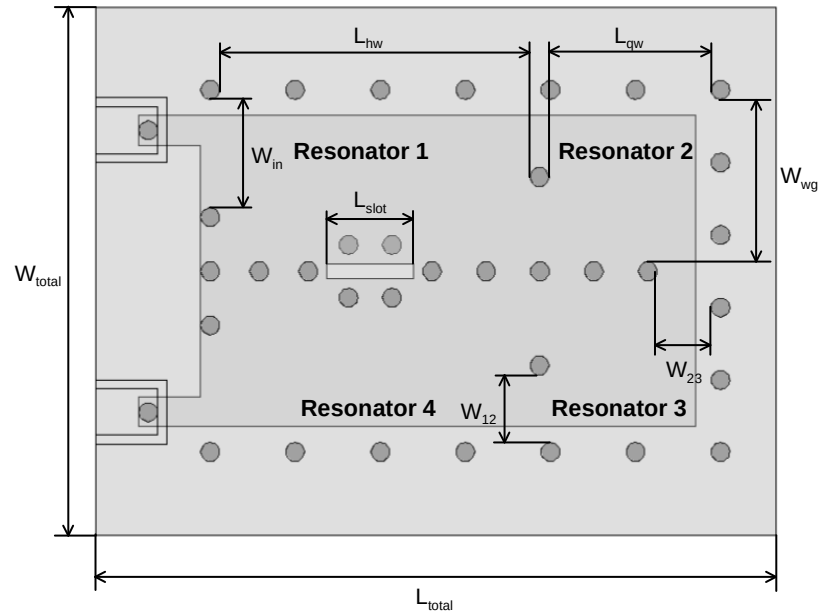

Figure 6-10: Layout of the proposed FSIW cross-coupled filter (top view).

Coefficients k_{12} and k_{34} can be obtained from analysis of coupled λ/2- and λ/4-wavelength resonators. In this case, direct iris coupling without septum is used and the coupling is controlled by width W_{12} of the iris. Curve obtained as a result of this analysis is shown in Figure 6-11.

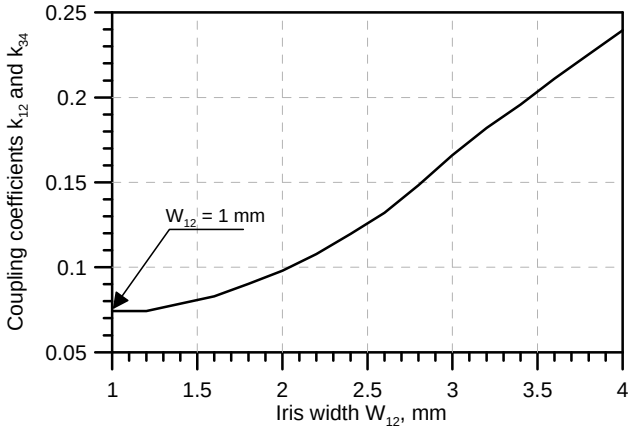

Figure 6-11: Coupling coefficients k_{12} and k_{34} against iris width W_{12}.

Analysis of iris-coupled λ/4-wavelength resonators (depicted in Figure 6-6) gives a similar curve for coupling coefficient k_{23}, which is shown in Figure 6-12. Here, coupling control is realized by the iris of the width W_{23}.

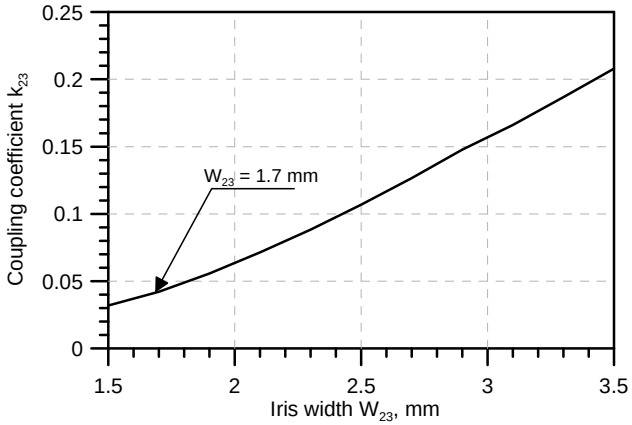

Figure 6-12: Coupling coefficient k_{23} against iris width W_{23}.

As it has been mentioned in section 6.2.2, the proposed negative coupling structure is also based on magnetic coupling but in this case coupling element is a rectangular slot of length

L_{slot} between top layer part of resonator 1 and bottom layer part of resonator 4. Dependence of coupling coefficient k_{14} on L_{slot} is shown in Figure 6-13.

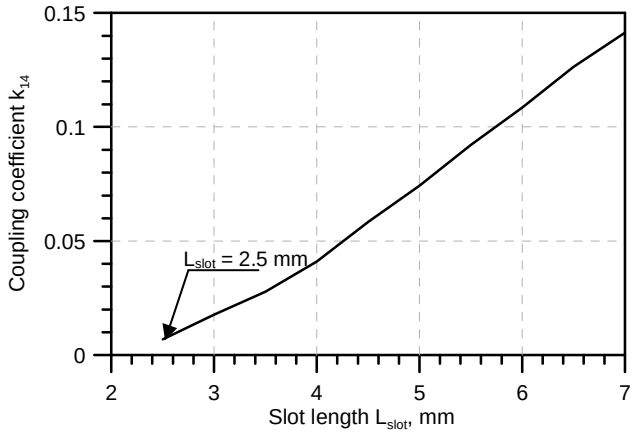

Figure 6-13: Coupling coefficient k_{14} against slot length L_{slot}.

It can be noticed from Figures 6-11, 6-12 and 6-13 that the wider the coupling elements, the stronger the couplings, and the larger the value of coupling coefficient. Such behaviour is characteristic to magnetically coupled cavities: in this case high-mode frequency drifts slightly, while low-mode frequency moves significantly with variation of the coupling value. In contrast, for electric coupling behaviour of low and high modes is opposite and thus coupling coefficient decreases with widening of coupling element, such as a capacitive gap.

Variation of input iris width W_{in} is used in order to control the external Q-factor. This parameter Q_{ext} can be extracted from the frequency response of doubly-loaded resonator using expression:

$$Q_{ext} = \frac{f_{res}}{\Delta f_{3dB}} \cdot 10^{\frac{|S_{21}|}{20}}, \tag{6.2-7}$$

where Δf_{3dB} is a 3dB-bandwidth of the resonator. The resultant plot of external quality factor against the input iris width W_{in} is presented in Figure 6-14.

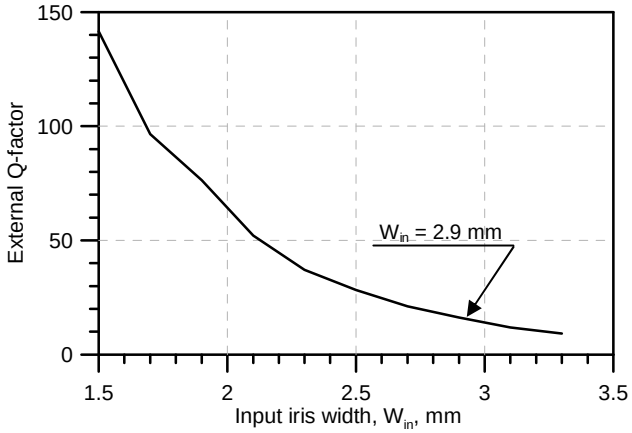

Figure 6-14: External *Q*-factor Q_{ext} against input iris width W_{in}.

6.2.3.3. Simulation and Experimental Results

The filter has been fabricated using two layers of Rogers Duroid RT/5880™ substrate (ε_r = 2.2, tanδ = 0.0009; thickness T_{diel} = 0.5 mm), where two λ/2-wavelength and two λ/4-wavelength FSIW resonators have been organized. Feeding of the filter has been realized by CPW input and output pads located on the top layer. These are connected to the middle layer stripline using a metallic post. The stripline is connected to the resonator 1; resonator 4 is connected to the output stripline respectively. Drawing of the filter structure with dimension markings is presented in Figure 6-10; corresponding dimensions are collected in Table 6-2; photograph of the fabricated filter is shown in Figure 6-15.

Parameter	Value, mm	Parameter	Value, mm
L_{hw}	10.9	W_{23}	1.7
L_{qw}	5.5	L_{slot}	2.8
W_{wg}	5.5	W_{total}	17
W_{in}	3.3	L_{total}	22
W_{12}	2.2	T_{diel}	0.5

Table 6-2: Dimensions of the designed FSIW filter (see Figure 6-10).

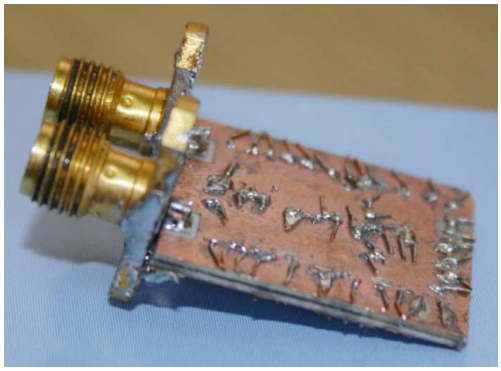

Figure 6-15: Photograph of the fabricated FSIW filter.

Transmission characteristics of the designed cross-coupled filter, simulated in Ansoft HFSS™, are presented in Figure 6-16. The filter exhibits about 0.95 dB insertion loss in passband, and its return loss is better than required 30 dB. Spurious passband of the filter appears at about 15 GHz, however it is suppressed by 23 dB. It can be noticed that an extra transmission zero has been obtained in upper stopband at about 13.8 GHz. Theoretical analysis shows that the transmission zero appears because of very weak coupling available between source and load. At the same time the source-load coupling creates another transmission zero in lower stopband below 5 GHz which could not be caught by the simulator. Increase of source-load coupling leads to drifting of the extra transmission zeros closer to passband.

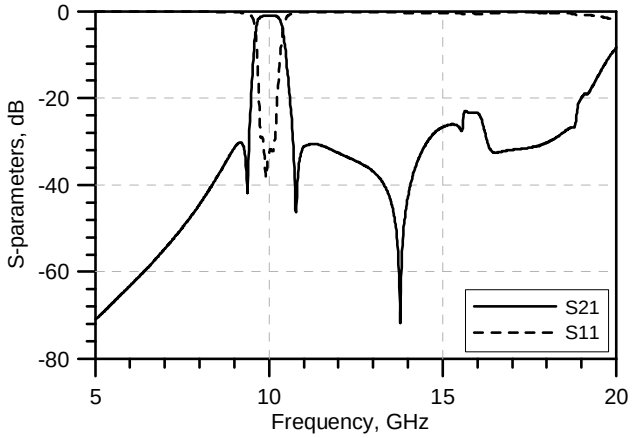

Figure 6-16: Simulated S-parameters of the FSIW cross-coupled filter.

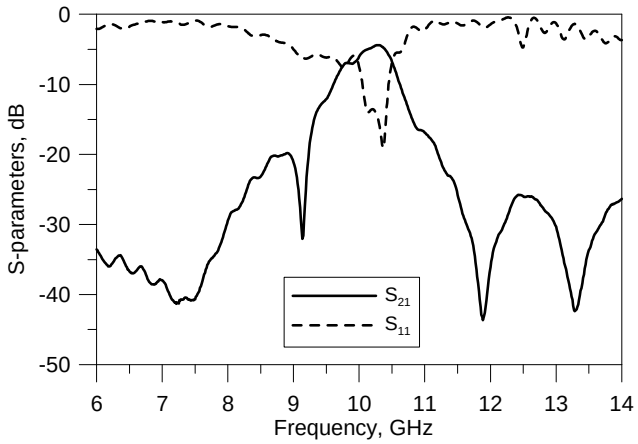

Figure 6-17: Measured S-parameters of the fabricated FSIW cross-coupled filter.

Measured S-parameters of the filter are shown in Figure 6-17. The experimental results show poor agreement with the simulated; however visible passband and good transmission zeros generally prove the concept and particularly applicability of the negative coupling structure. Measured insertion loss in passband is about 5 dB, return loss – 15 dB. The zero at 10.8 GHz has drifted to about 12 GHz. Two transmission zeros at 7.3 GHz and 13.3 GHz are the extra zeros generated by parasitic source-load coupling. The reason of the high losses is bad quality of fabrication; analysis of the failure has shown that electric contact between the vias and the middle metallization layer had not been established properly. This happened due to lack of practical experience at multilayer PCB fabrication and unavailability of special equipment for this type of fabrication. It should be emphasized that there were several attempts to fabricate this filter; however all of them had shown much poorer results than the presented one due to unavailability of electric contact between the vias connecting the input/output pads and the middle metallization layer. After obtaining the poor experimental results it has been decided to abandon further experimental verifications of the other circuits designed to be built using the multilayer PCB process and concentrate on the waveguide filters with E-plane inserts. It is expected that the proposed filter can be fabricated using the multilayer PCB process by experienced professionals or using alternative fabrication techniques as split-block waveguide housing with a horizontal all-metal insert or LTCC. These techniques will be attempted to prove feasibility of the filter in the future work.

6.3. Design of Modular SIW Filters

In this section, a modular solution for design of an inline pseudo-elliptic bandpass filter with three transmission zeros using double-layer substrate integrated waveguide (DLSIW) will be proposed. New approach which involves stripline resonators arranged in common wall of two stacked SIW is introduced. Singlet and doublet structures based on the stripline resonators are presented as basic units for modular design of a filter with non-resonating node.

6.3.1. SIW Filtering Modules

Singlets and doublets, the simplest filtering modules capable of generating and controlling individual transmission zeros, can be implemented using SIW technologies. In this section, DLSIW singlet and doublet structures will be introduced.

6.3.1.1. Singlet

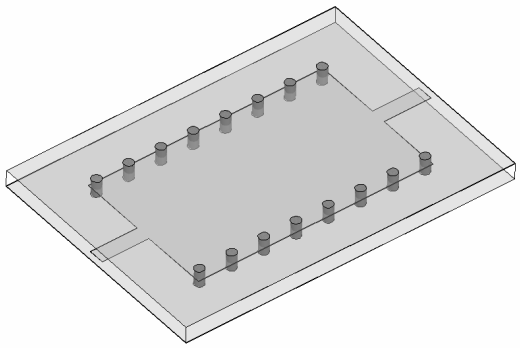

Figure 6-18: Configuration of a hollow DLSIW.

Let us consider two conventional SIW arranged in parallel, sharing top/bottom ground plane. Such configuration has half the characteristic impedance of the single layer SIW and a wave can be easily excited by a stripline connected to the common wall of the waveguides. It worth mentioning that having equal magnitudes, electromagnetic fields in top and bottom halves of the waveguide propagate out of phase as a result of mode conversion from the TEM in the stripline to the quasi-TE_{10} in both parallel SIW. The

structure can be manufactured by stacking two layers of dielectric substrates. View of a complete computer model of the DLSIW section with stripline transitions and cylindrical via connectors forming side metallic walls is presented in Figure 6-18.

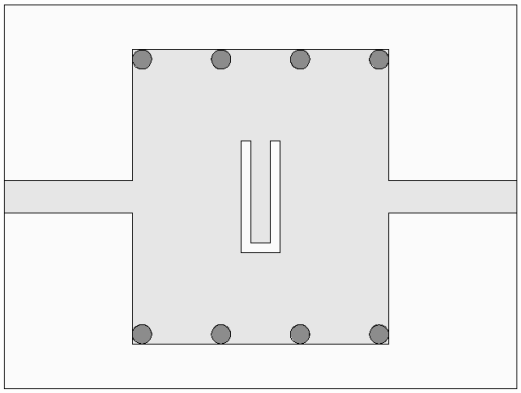

Figure 6-19: Configuration of a DLSIW singlet
with a λ/4-wavelength stripline resonator (top view).

Slots of arbitrary shapes cut out in the common metallic plane of DLSIW provide coupling between top and bottom waveguides. For example, FSIW resonator [6-5] can be considered as a section of the DLSIW with a longitudinal coupling slot which provides magnetic coupling between two conventional cavity resonators located in top and bottom layers. Slots of some particular dimensions and shapes may have resonant properties. Let us consider a hairpin-shaped slot cut out in the middle metallic layer of the DLSIW, shown in Figure 6-19. This slot creates a λ/4-wavelength stripline resonator, which interacts with a wave, propagating in the waveguide, providing source-resonator and resonator-load couplings. Also the wave bypasses the resonator, in such a way forming direct source-load coupling. Hence, the structure can be represented as a singlet which has been discussed in section 4.2.1. Frequency response of singlets contains a reflection zero and a transmission zero placed in either upper or lower stopband depending on the sign of the product of three coupling coefficients. In Figure 6-20, typical S-parameters of the DLSIW singlet are presented. Position of the transmission zero can be modified by moving the hairpin slot in transversal direction: if open end of the resonator moves closer to the side wall, the source-load coupling increases and the transmission zero drifts closer to the pole frequency.

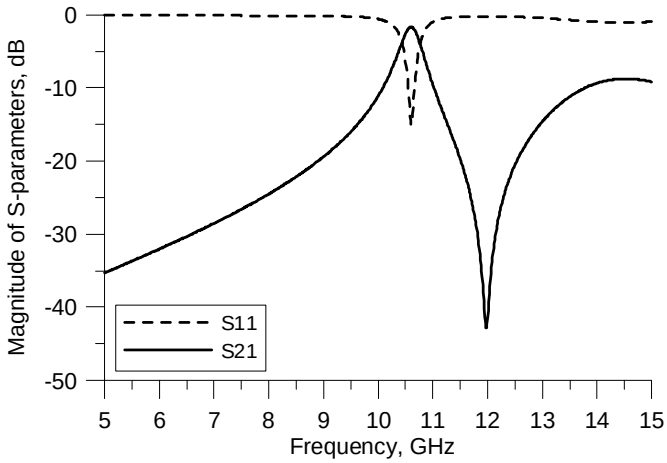

Figure 6-20: Typical S-parameters of a DLSIW singlet.

6.3.1.2. Doublet

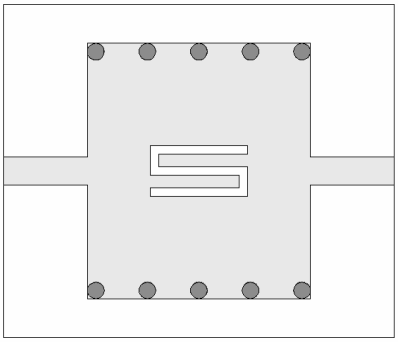

Figure 6-21: Configuration of a DLSIW doublet
with two λ/4-wavelength stripline resonators (top view).

Doublet configuration consists of two λ/4-wavelength stripline resonators which are formed in the middle layer of a DLSIW using an S-shaped slot arranged in longitudinal direction (see Figure 6-21). In the obtained structure source and load interact with both resonators and with each other, generating a bypass coupling. At the same time, two stripline resonators are electrically coupled, which implies that this coupling can be considered as negative. The structure acts as a doublet with asymmetrical frequency response, which has been previously considered in section 4.2.2. Typical frequency response of a DLSIW with two λ/4-wavelength stripline resonators is presented in Figure 6-22. The doublet has an asymmetrical frequency response with two reflection zeros forming its passband, and two transmission zeros in upper and lower stopbands. The upper transmission zero is observed

much further from passband than the lower one. Adjustment of the doublet's coupling coefficients in order to modify positions of the transmission and reflection zeros can be performed by changing gap width between two λ/4-wavelength stripline resonators and by introducing a coupling iris between source and load.

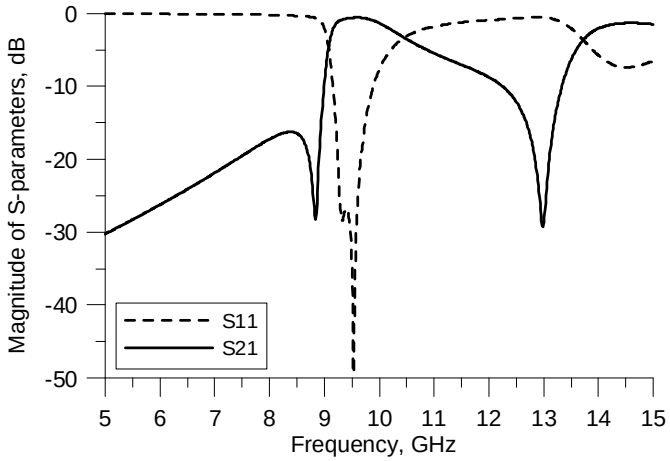

Figure 6-22: Typical S-parameters of a DLSIW doublet.

6.3.2. Filter Design Example

It is seen from Figure 6-22 that the introduced doublet can be used as a bandpass filter individually. However, it does not provide enough lower stopband rejection and upper slope appears to be very flat. In order to improve stopband performance of the doublet and add extra transmission and reflection zeros, a bandpass filter can be built by connecting the singlet and doublet modules in series.

To retain properties of the singlet and doublet in the modular filter configuration, these two sections must be connected through an NRN, which can be represented by a uniform section of the DLSIW with its length smaller than resonant wavelength at the centre frequency of the filter. Nevertheless, despite using the NRN, some parasitic effects leading to conflicting objectives take place. On the one hand, distance between singlet and doublet must be small enough to form an NRN; on the other hand, reduction of the distance increases parasitic coupling between the stripline resonators in singlet and doublet. This issue can be resolved by placing an inductive iris between singlet and doublet in order to provide certain reactance and reduce the level of parasitic coupling. Complete coupling scheme of the modular filter with NRN is presented in Figure 6-23.

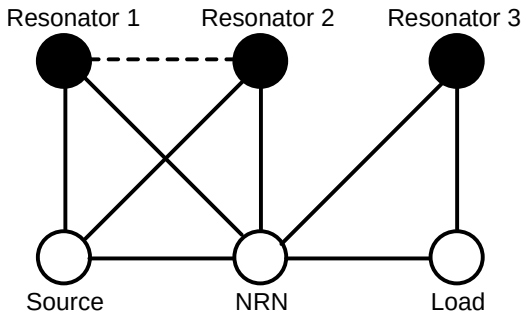

Figure 6-23: Coupling scheme of the proposed modular DLSIW filter.

Following specifications have been used for design of the modular DLSIW cross-coupled filter:

- centre frequency: 10 GHz;
- ripple passband: 9.6 – 10.4 GHz;
- return loss: 20 dB;
- transmission zeros: 8.8 GHz, 11.2 GHz and 13 GHz.

Generalized Chebyshev approximation and coupling matrix synthesis procedure yield the following coupling matrix for the required filter:

$$M = \begin{bmatrix} 0 & 1.389 & 0.031 & 0.156 & 0 & 0 \\ 1.389 & 0 & -2.421 & 0.373 & 0 & 0 \\ 0.031 & -2.421 & 0 & 0.71 & 0 & 0 \\ 0.156 & 0.373 & 0.71 & 0 & 0.543 & 0.399 \\ 0 & 0 & 0 & 0.543 & -1.934 & 0.659 \\ 0 & 0 & 0 & 0.399 & 0.659 & 0 \end{bmatrix} \quad (6.3\text{-}1)$$

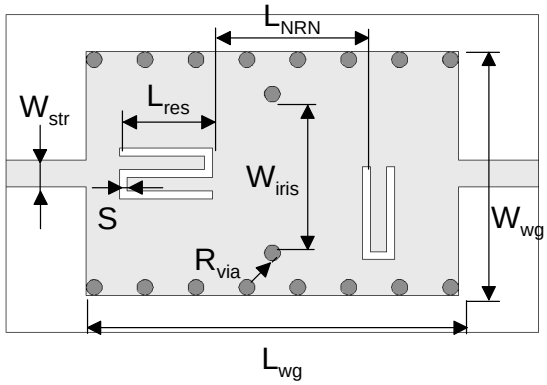

Figure 6-24: Layout of the proposed modular DLSIW filter (top view).

Layout of the filter comprises of two layers of Taconic RF-35™ (ε_r = 3.5; tanδ = 0.0018) in which a DLSIW with slots are organized. Top view of the filter's layout is presented in Figure 6-24. Input coplanar pad on top layer is connected to a stripline with the width of W_{str} = 1 mm in the middle metallic layer. The stripline provides transition to the DLSIW

with its width and length of W_{wg} = 8 mm and L_{wg} = 10 mm respectively. Widths of both slots in the middle metallization layer are S = 0.3 mm; lengths of the stripline resonators are L_{res} = 3.2 mm. Length of the NRN is L_{NRN} = 6 mm. Width of the iris formed by via cylinders between the S-shaped and hairpin-shaped slots is W_{iris} = 6 mm. Radii of the vias equal R_{via} = 0.3 mm.

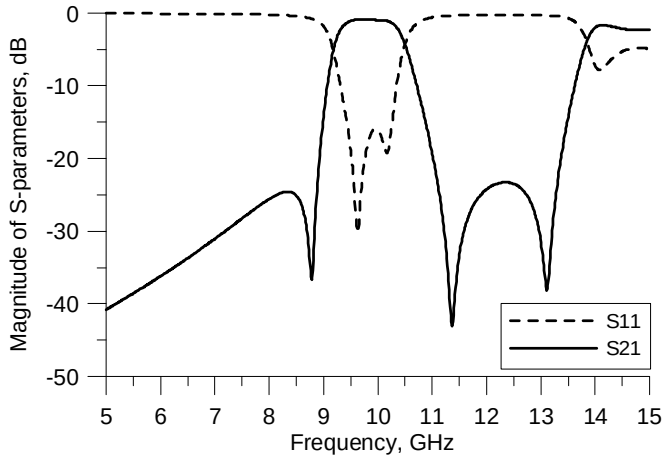

Figure 6-25: Simulated frequency response of the proposed modular DLSIW filter.

Transmission characteristics of the designed cross-coupled filter, simulated in Ansoft HFSS™, are presented in Figure 6-25. The filter exhibits insertion loss of about 0.9 dB and return loss better than 16 dB in passband. Adjacent channel rejection of 23 dB is achieved. The second passband of the filter appears at 14 GHz. The filter has not been verified experimentally due to inability of available fabrication process to guarantee electric contact between vias and middle metallization layer.

6.4. Design of Inline Extracted Pole SIW Filters

In chapter 5 it has been shown that use of EPS in design of inline extracted pole filters leads to significant size reduction and stopband performance improvement of bandpass filters. In this section, an EPS for inline extracted pole SIW filters will be proposed and an example of this filter will be presented.

6.4.1. SIW Extracted Pole Section

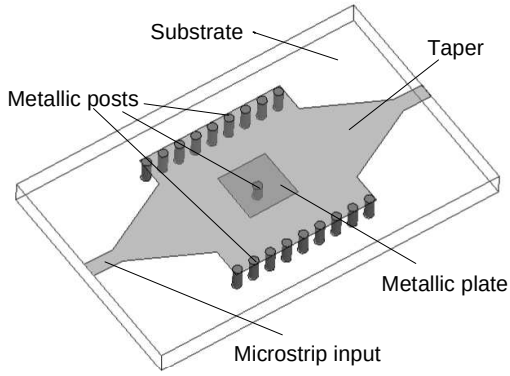

Figure 6-26: Configuration of a SIW EPS.

Configuration of a SIW EPS is presented in Figure 6-26. The proposed EPS consists of a mushroom-type resonator and an NRN arranged within a double-layer SIW. The resonator contains a rectangular metallic plate arranged on the middle metallization layer of the structure, and a metallized via hole which connects the plate with the SIW's bottom ground plane. The NRN is formed by a SIW section which self-resonant frequency is significantly detuned from the frequency range of interest. Complete EPS contains microstrip inputs and a taper which provides transition from the microstrip line to the SIW, and performs corresponding matching.

The proposed EPS, designed using double-layer Rogers Duroid RT/5880™ substrate (ε_r = 2.2, tanδ = 0.0009; thickness T_{diel} = 0.8 mm) with copper metallization (σ = 5.8·10^7 Sm/m), has been simulated in commercial EM simulator CST Microwave Studio™.

Simulated transmission characteristics of a single EPS are shown in Figure 6-27. It is clear from the figure that, in frequency domain, the proposed EPS retains the behaviour of EPS designed for conventional rectangular waveguides (see chapter 5) generating a pole-zero pair; the zero is located in upper stopband.

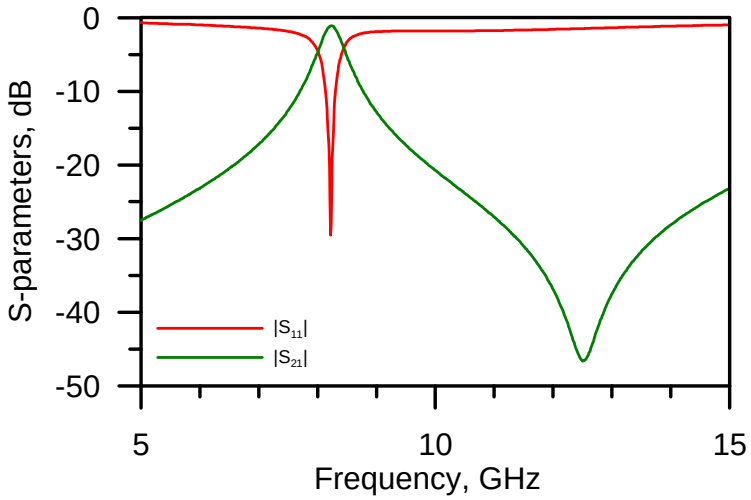

Figure 6-27: Typical frequency response of a SIW EPS.

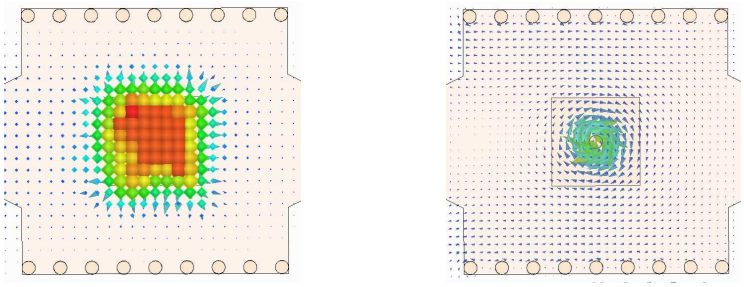

(a) (b)

Figure 6-28: Field distribution in the proposed EPS at pole frequency:
(a) electric field; (b) magnetic field.

Distribution of electric and magnetic fields in the EPS at the pole frequency is presented in Figure 6-28. It is seen that electric field is concentrated at the top layer of the EPS – between the metallic plate in the middle of the SIW and its top ground plane. Magnetic field oscillates at both top and bottom layers. Bottom layer magnetic field is caused by a current which flows in the post connecting the metallic plate with bottom ground plane.

The field reaches its maximum right near the post fading with approach to the resonator's edges. The same magnetic field distribution can be observed in coaxial resonator. At the top layer of the structure, magnetic field has its minimum in the middle, where maximum of the electric field occurs, and further increases reaching maximum near the resonator‘s edges. It should be noted that in Figure 6-28 magnitude of the magnetic field at the bottom layer is much larger than one at the top layer.

6.4.2. Filter Design Example

In order to prove feasibility of the proposed EPS, a 3rd-order inline SIW extracted pole filter has been designed using the generalized coupling coefficients approach introduced in chapter 5 for conventional rectangular waveguide E-plane extracted pole filters. The filter specifications are defined as follows:

- center frequency: 7.5 GHz;
- ripple passband: 7.25 – 7.75 GHz;
- return loss: 15 dB;
- transmission zero: 13.25 GHz (triple zero).

Development of the filter follows the design procedure used for the 3rd-order extracted pole filter presented in section 5.2.2. Therefore, coupling scheme of the filter can be found in Figure 5-37. However, in this design three identical EPS are used in order to miniaturize the filter. Each of these EPS generates a transmission zero at the same frequency, and the filter has a single zero repeated three times. Generalized Chebyshev approximation and subsequent synthesis procedure result in the following coupling matrix for the SIW filter to be implemented:

$$M = \begin{bmatrix} 0 & 1 & 0 & 0 & 0 & 0 & 0 & 0 \\ 1 & -11.633 & 14.475 & 1 & 0 & 0 & 0 & 0 \\ 0 & 14.475 & -18.01 & 0 & 0 & 0 & 0 & 0 \\ 0 & 1 & 0 & -17.819 & 17.91 & 1 & 0 & 0 \\ 0 & 0 & 0 & 17.91 & -18.01 & 0 & 0 & 0 \\ 0 & 0 & 0 & 1 & 0 & -11.5 & 14.393 & 1 \\ 0 & 0 & 0 & 0 & 0 & 14.393 & -18.01 & 0 \\ 0 & 0 & 0 & 0 & 0 & 1 & 0 & 0 \end{bmatrix} \quad (6.4\text{-}1)$$

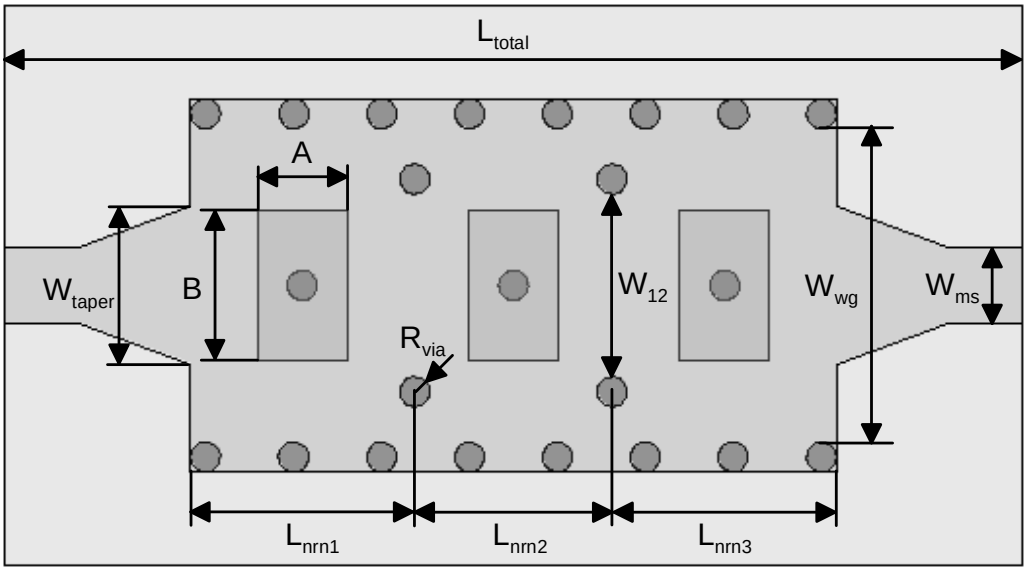

Figure 6-29: Layout of the inline SIW extracted pole filter (top view).

Parameter	Value, mm	Parameter	Value, mm
A	2.4	W_{12}	5
B	4	W_{ms}	2
W_{wg}	10	W_{taper}	4
L_{nrn1}	6	R_{via}	0.4
L_{nrn2}	5.3	L_{total}	27.3
L_{nrn3}	6	T_{diel}	0.8

Table 6-3: Dimensions of the inline SIW extracted pole filter (see Figure 6-28).

Top view of the filter's layout is presented in Figure 6-29 together with its main geometrical design parameters denoted; values of these parameters can be found in Table 6-3. The structure contains two stacked layers of Rogers Duroid RT/5880™ substrate ($\varepsilon_r = 2.2$, $\tan\delta = 0.0009$) with thickness of $T_{diel} = 0.8$ mm. Three identical mushroom resonators are organized within the bottom layer using rectangular metallic plates and via holes. Top wall metallization of the SIW with tapered microstrip-to-SIW transitions are formed on the top layer. Side walls of the SIW and inductive irises between adjacent EPS are represented by metallized via holes.

The filter has been simulated in Ansoft HFSS™ software; results of this simulation are shown in Figure 6-30. The filter shows about 1.4 dB insertion loss, and return loss better than 15 dB in passband. Adjacent channel 7.9 – 8.4 GHz is rejected by 20 dB. The filter exhibits wide upper stopband – the next passband occurs at about 17 GHz.

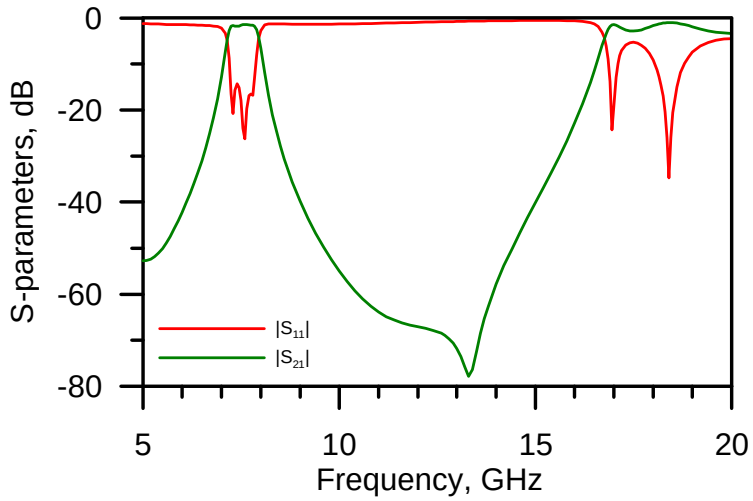

Figure 6-30: Simulated S-parameters of the inline SIW extracted pole filter.

6.5. Summary

In this chapter a problem of development of miniaturized SIW cross-coupled filters with improved performance using advanced design techniques, outlined in the previous chapters, has been discussed.

In section 6.2 compact FSIW resonators with high *Q*-factor have been introduced; a novel negative coupling structure for application in FSIW cross-coupled filters has been proposed. Performance of the negative coupling structure has been demonstrated in a 4^{th}-order cross-coupled filter with λ/2- and λ/4-wavelength FSIW resonators which has been designed, fabricated and tested. Experimental frequency response of the filter has shown poor agreement with the simulated one due to inaccurate fabrication. Particularly, failure analysis has shown that the middle metallization layer was not connected electrically to the vias. The main reason of this error is unavailability of practical experience at fabrication of the multilayer PCB. The experimental verification has been repeated several times; however the results did not show any further improvement. Therefore further fabrications of the multilayer SIW structures have been abandoned. Despite the unsatisfactory agreement of the curves, it can be concluded from the availability of good transmission that the proposed negative coupling structure shows adequate performance.

In section 6.3 design of modular filters using SIW technology has been considered. Singlet and doublet modules with embedded λ/4-wavelength stripline resonators have been proposed and implemented using DLSIW. A 3^{rd}-order modular filter with three transmission zeros in both stopbands has been designed by cascading the singlet and the doublet through an NRN.

Finally, in section 6.4 an EPS with mushroom resonator has been proposed for realization in double-layer SIW technology. Inline extracted pole filter with NRN using the proposed EPS has been designed by the GCC extraction technique which has been previously presented in this thesis. Performances of the filters have not been verified experimentally due to numerous problems occurred with the multilayer PCB fabrication process.

6.6. References

[6-1] D. Deslandes and K. Wu, "Integrated Microstrip and Rectangular Waveguide in Planar Form," *IEEE Microwave and Wireless Comp. Lett.*, vol. 1, pp. 68–70, Feb. 2001.

[6-2] X.-P. Chen and K. Wu, "Substrate Integrated Waveguide Cross-Coupled Filter With Negative Coupling Structure," *IEEE Trans. Microwave Theory Tech.*, vol. 56, pp. 142–149, Jan. 2008.

[6-3] A. Shelkovnikov and D. Budimir, "Novel Compact EBG Waveguide Resonators in Planar Form," *European Microwave Conference*, Vol. 2, 4-6 Oct. 2005.

[6-4] J. A. Ruiz-Cruz, M. A.E. Sabbagh, K. A. Zaki, J. M. Rebollar and Yunchi Zhang, "Canonical Ridge Waveguide Filters in LTCC or Metallic Resonators," *IEEE Trans. Microwave Theory Tech.*, vol. 53, pp. 174–182, Jan. 2005.

[6-5] N. Grigoropoulos, B. Sanz Izquierdo, and P. R. Young, "Substrate Integrated Folded Waveguides (SIFW) and filters," *IEEE Microw. And Wireless Comp. Lett.*, vol. 15, no. 12, pp. 829-831, December 2005.

[6-6] S. K. Alotaibi and J.-S. Hong, "Novel substrate integrated waveguide filter," *Microw. Opt. Technol. Lett.*, Vol. 50, No. 4, 1111–1114, Apr. 2008.

[6-7] H. Lin, "Novel folded resonators and filters," *IEEE MTT-S Digest*, pp. 1277–1280, 2007.

[6-8] R. Wang, L.-S. Wu, and X.-L. Zhou, "Compact Folded Substrate Integrated Waveguide Cavities and Bandpass Filter," *Progress in Electromagnetics Research*, PIER 84, pp. 135–147, 2008.

[6-9] D. Deslandes, "Design equations for tapered microstrip-to-Substrate Integrated Waveguide transitions," *IEEE MTT-S Int. Microwave Symp. Dig.*, pp. 704-707, 2010.

[6-10] N. Grigoropoulos and P. R. Young. "Compact Folded Waveguides," *34th European Microwave conference*, Amsterdam, 2004.

[6-11] W. Q. Che, L. Geng, K. Wu and Y. L. Chow, "Theoretical Investigation and Experimental Verification of Compact Folded Substrate Integrated Waveguide," *37th European Microwave conference*, Munich, Oct. 2007.

[6-12] J.-S. Hong, “Compact folded-waveguide resonators,” *IEEE MTT-S Int. Microwave Symp. Dig.*, pp. 213–216, 2004.

[6-13] D. Budimir, “Optimized E-plane bandpass filters with improved stopband performance,” *IEEE Trans. Microwave Theory Tech.*, vol. 45, pp. 212–220, Feb. 1997.

[6-14] J. B. Thomas, “Cross-coupling in coaxial cavity filters – a tutorial overview,” *IEEE Trans. Microwave Theory Tech.*, vol. 51, no. 4, pp. 1368-1376, April 2003.

[6-15] S. Amari, “Synthesis of cross-coupled resonator filters using an analytical gradient-based optimization technique,” *IEEE Trans. Microw. Theory Tech.*, vol. 48, no. 9, pp. 1559–1564, Sep. 2000.

CHAPTER 7

CONCLUSION AND FUTURE WORK

7.1. Conclusion

The aim of this work was to develop miniaturized, high performance, and easy-to-design and fabricate filters for wireless applications using conventional and substrate integrated waveguide technologies.

In chapter 2 an overview of electromagnetic theory with regards to wave propagation in rectangular waveguides has been given. Configurations, parameters and characteristics of conventional and substrate integrated waveguides have been briefly outlined.

Chapter 3 has provided an overview of the filter design flow. Methods of approximation, lowpass prototype and coupling matrix synthesis for direct- and cross-coupled filters and subsequent frequency mapping have been presented. Problems of filter implementation and optimization using CAD have been considered.

In chapter 4 a solution for inline modular filters implementation in conventional rectangular waveguide using E-plane metallo-dielectric inserts has been presented. Compact singlets, doublets and higher-order filtering modules, capable of improving filter stopband performance by generating transmission zeros have been introduced. Modular bandpass and dual-band filters using the filtering modules connected in cascade through NRN have been designed, fabricated and tested. Despite the fabrication errors occurred, the measurements have proven adequacy and applicability of the proposed solutions.

In chapter 5 inline extracted pole filters have been designed and implemented in conventional rectangular waveguide using E-plane all-metal and metallo-dielectric inserts. Theoretical model of E-plane EPS structures has been developed; several E-plane EPS have

been proposed for implementation; the individual EPS have been thoroughly investigated; dual-mode EPS capable of generating a transmission zero in lower stopband has been developed as a result of theoretical investigation. Generalized coupling coefficients have been introduced and applied in design of extracted pole filters with NRN. For this purpose, expressions for extraction of the GCC from frequency responses of single and coupled EPS have been derived using the schematic circuit model of the EPS. Several design examples of compact bandpass filters with improved stopband performance have been presented. The measured transmission characteristics of the filters have shown quite good agreement with the simulated ones. Particularly, the experimental response of the extracted pole filter realized by means of an all-metal insert has shown excellent agreement with the simulation. Therefore it can be concluded that the proposed GCC extraction technique provides good initial values for the further CAD optimization of the filters with cascaded EPS.

In chapter 6 attention has been paid to development of SIW filters using the design techniques employed in chapters 4 and 5 for conventional rectangular waveguide filters. FSIW cross-coupled filter with a new negative coupling structure has been designed, fabricated and tested. The obtained experimental results allow stating that the negative coupling structure performs adequately; however, agreement of the simulated and measured S-parameters has been clearly unsatisfactory due to repeating significant fabrication errors. Configurations of DLSIW singlet and doublet using stripline resonator have been proposed as filtering modules for SIW technology; modular filter with NRN using cascaded singlet and doublet has been developed. EPS with mushroom resonator for multilayer SIW has been presented; inline extracted pole bandpass filter with wide stopband has been successfully designed using the proposed GCC extraction technique. Performances of the latter filters have not been verified experimentally due to inability to fabricate the required multilayer PCB using the available equipment.

This chapter concludes the thesis contributions and offers recommendations for future work.

7.2. Contributions of the Thesis

The following contribution has been made in this thesis:

- Development of a new class of compact modular cross-coupled filters with improved stopband performance using NRN in conventional and substrate integrated waveguides. Singlets, doublets and higher-order module structures using stripline resonators and septa have been proposed. Coupling matrix extraction procedure by numerical optimization has been realized. Compact filters composed of the developed modules have been designed.

- Development of a model of improved E-plane resonators with embedded S-shaped resonators and SRR, and its representation as a single EPS. Application of GCC to the model of EPS with NRN has been performed. GCC extraction procedure from measured or simulated frequency responses of single or interacting EPS has been developed. New EPS with quarter-wavelength and SIR stripline resonators have been proposed for conventional rectangular waveguide; new EPS with mushroom resonator has been developed for SIW. Dual-mode EPS with a transmission zero in lower stopband has been designed. Several inline extracted pole bandpass filters with stopband performance improved by transmission zero have been designed using the GCC extraction technique.

- Development of a new negative coupling structure for FSIW cross-coupled resonator filters. The structure has been designed, investigated and successfully applied in design of a cross-coupled filter using FSIW resonators.

7.2.1. Modular Cross-Coupled Filters with NRN

Several examples of modular cross-coupled filters with NRN have been designed and implemented in conventional and substrate integrated waveguide technologies.

In conventional waveguide, a doublet with centre frequency of 8.15 GHz and passband of 7.9 – 8.4 GHz with two transmission zeros in both stopbands has been realized using two electrically coupled hairpin resonators and a septum arranged on a metallo-dielectric E-plane insert; a 4^{th}-order cross-coupled module with two hairpin, two I-shaped resonators and two parallel septa has been designed for centre frequency of 10.4 GHz and ripple passband of 10.1 – 10.7 GHz using several metallo-dielectric inserts. The filtering modules have been designed using the coupling coefficients extraction procedure by optimization; the program for this extraction procedure has been developed in MATLAB™ by author. Implementation of internal couplings between hairpin and I-shaped resonators in the 4^{th}-order filtering module has been performed by the traditional coupling coefficient extraction technique. 4^{th}-order inline modular E-plane filter with four transmission zeros has been designed by cascading two doublets through an NRN; a dual-band E-plane filter has been implemented taking advantage of parallel connection of two doublets shielded by a septum between them.

In SIW, singlet and doublet structures have been developed using quarter-wavelength stripline resonators arranged within the middle metallization layer of a DLSIW. 3^{rd}-order modular filter with three transmission zeros has been designed at centre frequency of 10 GHz with 800 MHz ripple bandwidth by cascading these two modules through an NRN represented by a waveguide section with an iris.

The presented filters exhibit enhanced stopband performance, improved by introducing transmission zeros, and compactness in comparison with their all-pole counterparts. However, this has been achieved at the cost of increased insertion loss due to use of basic stripline resonators with lower unloaded *Q*-factor.

7.2.2. E-plane and SIW Extracted Pole Filters

Recently proposed compact E-plane resonators improved by embedding S-shaped resonators and SRR between their input and output septa have been successfully represented by an EPS model which contains a resonator and an NRN connected through admittance inverters. GCC concept introduced for characterizing couplings between resonating and non-resonating nodes has been applied to the EPS model. New expressions for GCC extraction from simulated or measured frequency responses of individual EPS, cascaded pairs of EPS or cascaded EPS and resonators have been developed as a result of analysis of the proposed EPS model.

Several new EPS configurations have been proposed for use in conventional and substrate integrated waveguide filters. For conventional rectangular waveguide, compact E-plane inserts with embedded quarter-wavelength and SIR resonators have been developed. New dual-mode EPS for implementation of lower stopband transmission zero has been designed based upon analysis of the EPS model. For SIW applications, a multilayer mushroom resonator based EPS has been developed.

The proposed EPS have been employed in design of advanced inline extracted pole filters with NRN. A few design examples have been presented in order to cover the whole range of the presented EPS. 3^{rd}-order filter with three quarter-wavelength resonators based EPS connected in series has been designed for centre frequency of 9.45 GHz with 0.3 GHz ripple bandwidth using an all-metal E-plane insert in conventional waveguide; another 3^{rd}-order three-EPS filter with 0.4 GHz bandwidth at the same centre frequency has been implemented by employing EPS with embedded S-shaped resonators using a metallo-dielectric insert. Dimensions of these filter structures have been found by applying the new GCC extraction technique. Extracted pole filter with the dual-band EPS has been partially designed by optimization. Compact SIW inline extracted pole filter with centre frequency of 7.5 GHz and 0.5 GHz bandwidth, exhibiting a wide stopband, has been developed using the new mushroom resonator based EPS.

7.2.3. Negative Coupling Structure for FSIW Resonators

New configuration has been developed for implementation of negative coupling coefficient between adjacent FSIW resonators. The main advantage of the structure is that it allows diversifying a set of realizable cross-coupled topologies due to an opportunity to integrate the negative coupling element at all the regions where maximum amplitude of magnetic field is observed.

In order to demonstrate feasibility of the proposed element, a 4^{th}-order bandpass filter with centre frequency of 10 GHz and 500 MHz ripple bandwidth has been designed using half- and quarter-wavelength FSIW resonators. Implementation of the filter has been carried out by extraction of conventional coupling coefficients between pairs of adjacent resonators. Despite that the experimental frequency response has shown poor overall agreement with the simulated one, the evidently generated transmission zeros suggest that the presented configuration provides negative coupling between the corresponding resonators.

7.3. Suggestions for Future Work

Ideas for further improvement of filter performances using the structures proposed and investigated in this thesis are divided into three groups.

For modular filter design using conventional E-plane waveguide technology:

- Design of modular filters with NRN using singlets;
- Development of new singlets for generation of lower stopband transmission zeros using standard septa;
- Investigation of new modules with split septa which should generate an additional transmission zero due to introducing a frequency dependent source-load coupling;
- Investigation of possibility to use O-shaped resonators in higher-order modules with parallel septa in order to provide magnetic coupling with adjacent resonators at both input and output;
- Investigation of possibility to realize cross-coupled topologies in the main path of higher-order filtering modules with parallel septa in order to generate more transmission zeros in stopbands;
- Investigation of possibility to design multimode filter described by transverse matrix using a single septum.

For inline extracted pole filters with NRN:

- Investigation of properties of E-plane EPS with new resonators (O-shaped, I-shaped, *etc.*);
- Development of rigorous GCC extraction procedure for dual-mode EPS;
- Development of a GCC extraction procedure not requiring frequency normalization.

For SIW filters:

- Design, investigation and application of multimode FSIW cavity resonators;
- Investigation of possibility to design a balun filter using DLSIW and modular filter design principle.

PUBLICATIONS

[1] O. Glubokov and D. Budimir, "Compact E-plane Doublet Structures for Modular Filter Design", *40th European Microwave Conference*, 29 September – 1 October 2010, Paris, France.

[2] D. Budimir, O. Glubokov and M. Potrebic, "Novel waveguide filters using T-shaped resonators", *IET Electronics Letters*, Volume 47, Issue 1, 6th January 2011.

[3] A. Glubokov and D. Budimir, "Compact Substrate Integrated Waveguide Resonators on LCP Substrate for mm-wave Wireless Systems", *Asia Pacific Microwave Conference*, Hong Kong, 15-19 December 2008.

[4] O. Glubokov, S. Nagandiram, A. Tarczynski and D. Budimir, "Substrate Integrated Waveguide Cross-Coupled Filters for Wireless Applications," *IEEE International Symposium on Antennas and Propagation (AP-S) and 2011 USNC/CNC/URSI Meeting*, 3-8 July 2011, Spokane, Washington, USA.

[5] O. Glubokov and D. Budimir, "Compact Inline Substrate Integrated Waveguide Filter with Transmission Zeros", *IEEE International Symposium on Antennas and Propagation (AP-S) and 2010 USNC/CNC/URSI Meeting*, 11-17 July 2010, Toronto, Canada.

[6] O. Glubokov and D. Budimir, "Substrate Integrated Folded-Waveguide Cross-Coupled Filter with Negative Coupling Structure", *IEEE Antennas and Propagation Society International Symposium (APS'2009)*, 1-5 June 2009, Charleston, USA.

[7] A. Glubokov and D. Budimir, "Compact Multilayer SRR-loaded Integrated Waveguide Filters on Liquid Crystal Polymer Substrate", *IEEE Antennas and Propagation Society International Symposium (APS'2008)*, 5-11 July 2008, San Diego, USA.

[8] O. Glubokov, N. Suntheralingam, N. Mohottige and D. Budimir, "Electromagnetic Analysis of SRR and S-shaped Resonator Loaded Filters", *4th European Conference on Antennas and Propagation 2010 (EuCAP'2010)*, 12-16 April 2010, Barcelona, Spain.

[9] O. Glubokov and D. Budimir, “Compact CSRR-loaded Substrate Integrated Waveguide Resonators on LCP Substrate”, *3rd European Conference on Antennas and Propagation 2009 (EuCAP'2009)*, pp. 3167-3169, 23-27 March 2009, Berlin, Germany.

[10] O. Glubokov, M. Potrebic and D. Budimir**, “**Multilayer Substrate Integrated Waveguide Bandpass Filters”, *5th European Conference on Circuits and Systems for Communications (ECCSC’10)* ,23-25 November 2010, Belgrade, Serbia.

[11] D. Budimir and O. Glubokov, “Waveguide Structures and Filters for Millimetre-wave Applications*”, 5th ESA Workshop on Millimetre Wave Technology and Applications & 31st ESA Antenna Workshop*, 18-20 May 2009, ESA/ESTEC.

[12] O. Glubokov and D. Budimir, “Compact Quasi-Ridged Substrate Integrated Resonators on LCP Substrate”, 2009 *IEEE Wireless and Microwave Conference (WAMICON)*, 20-21 April 2009, Clearwater, USA.

[13] O. Glubokov, D. Budimir and B. Shelkovnikov, “Novel Compact Substrate Integrated Resonators at 60 GHz for LCP”, *18th International Crimean Conference on Microwave and Telecommunication Technology. CriMiCo’2008*, pp. 537-538, Sevastopol, Ukraine, 2008.

[14] A. A. Glubokov and B. N. Shelkovnikov, “Waveguide Filters Using Ring Resonators”, *16th International Crimean Conference on Microwave and Telecommunication Technology. CriMiCo’2006, Conf. Proc.*, Vol. 2, pp. 525-526, Sevastopol, Ukraine, 2006.

[15] O. A. Glubokov and B. N. Shelkovnikov, “Novel Compact Split Ring Resonators for LTCC”, 8*th International Conference on Telecommunications in Modern Satellite, Cable and Broadcasting Services, 2007*, pp. 291-292, Serbia, 2007.

[16] O. Glubokov, S. Nagandiram, A. Tarczynski and D. Budimir, “Folded Substrate Integrated Waveguide Cross-Coupled Filters with Negative Coupling Structure,” *Microwave and Optical Technology Letters*, (submitted).

[17] O. Glubokov and D. Budimir, “Compact Waveguide Filters Using Metal-Dielectric Inserts”, *IEEE Microwave and Wireless Components Letters*, (submitted).

[18] O. Glubokov and D. Budimir, “Extraction of Generalized Coupling Coefficients for Inline Extracted Pole Filters With Nonresonating Nodes,” *IEEE Trans. Microwave Theory Tech.*, Feb. 2011 (submitted).

[19] O. Glubokov and D. Budimir, “Novel Inline Waveguide E-plane Filter Using Dual-Mode Extracted Pole Section”, *41th European Microwave Conference*, 9-14 October 2011, Manchester, UK, (submitted).

[20] O. Glubokov, N. Suntheralingham, A. Shelkovnikov and D. Budimir, “Compact E-plane Resonators and Filters with Enhanced Stopband Performance,” *IEEE Trans. Microwave Theory Tech.*, (in preparation).